Dark matter annihilation and local warming in the core of a neutron star

M. Ángeles Pérez-García[1], *Joseph Silk*[2,3,4]

[1] Department of Fundamental Physics, University of Salamanca, Plaza de la Merced s/n 37008 Salamanca, Spain
[2]Institut d'Astrophysique, UMR 7095 CNRS, Université Pierre et Marie Curie, 98bis Blvd Arago, 75014 Paris, France
[3]Department of Physics and Astronomy, The Johns Hopkins University, Homewood Campus, Baltimore MD 21218, USA
[4]Beecroft Institute of Particle Astrophysics and Cosmology, Department of Physics, University of Oxford, Oxford OX1 3RH, UK,

DOI: http://dx.doi.org/10.3204/DESY-PROC-2014-04/30

In this contribution we propose that the possible existence of a component of self-annihilating dark matter in the universe may result in a local inner core warming of medium-age neutron stars on a time-scale of $\sim 10^2$ yr. The energy released from annihilation of a massive ($m_\chi \gtrsim$ TeV) dark matter particle in the central regions of the star could be capable of injecting an extra neutrino/photon component allowing a positive emissivity, opposed to the usual negative values for the standard cooling processes. As a result, an enhanced early warming era in the neutron star coolig scenario may result.

In the ΛCDM paradigm, current indications from recent Planck data [1] show that the current total matter content of the Universe is roughly 27%, more precisely Planck data yield (at 68% CL) a physical baryonic content $\Omega_b h^2 = 0.02207 \pm 0.00033$ and a physical dark matter (DM) content of $\Omega_c h^2 = 0.1196 \pm 0.0031$. DM, being about five times more abundant than baryonic matter, has not yet been thoroughly taken into account in our current understanding of microscopic processes occurring inside stars. Namely, for neutron stars (NSs), the physical description of the interior has mostly been attempted only taking into account ordinary standard model species. Even if a tiny fraction, it remains to be determined at what extent the DM component may play a role and, consequently, trigger observable effects that could have been missidentified entangled in the, already complex, description of these objects.

Provided DM could be a Majorana particle, the emission of radiation in the final states from self-annihilation could be used as indirect evidence of its existence as we will argue. Althouh we should keep in mind that there is not yet consensus on basic DM properties such as bosonic or fermionic nature or, as mentioned, whether it is a Majorana or Dirac particle. To try to shed light on these aspects there is an international multi-messenger effort involving collider, direct or indirect searches where DM signals may be detected. Typically, globular clusters or the galactic center seem regions where a vast amount of this type of matter is expected. Some partial hints of an extra photon component coming from the galactic center have already arised [2]. The actual interaction strength in this dark sector is not clearly determined so far

and candidates in the weak sector (WIMPs) seem favoured in light of cosmological arguments. Regarding fundamental properties such as the mass of the DM candidate, favoured values in the range $m_\chi \sim \mathcal{O}(\ 10\ \mathrm{GeV/c^2} - 10\,\mathrm{TeV/c^2})$ are under current scrutiny.

In our galaxy a DM density distribution can be described under the form of a power-law density profile as already pointed out in the seminal work of [3]. Assuming this prior, the possibility of gravitational accretion of the dark component into massive compact stars comes naturally. In particular, the very dense environments of planets and stars seem capable to resonantly capture DM [4].

More in detail, in a NS with radius R and baryonic number N_B the large opacity of its internal dense core to incoming WIMPs seems capable to stabilize an inner distribution of these, given a scattering cross-section with nucleons around the value of the geometrical cross-section $\sigma_{\mathrm{geom}} \simeq 2.4 \times 10^{-45}\ \mathrm{cm}^2 \left(\frac{1.4\mathrm{M}_\odot}{\mathrm{M}}\right)\left(\frac{\mathrm{R}}{11.5\,\mathrm{km}}\right)^2$. For possibly larger cross-sections than this and in order to preserve unitarity, the NS opacity saturates providing no enhancement of DM capture. On the other hand, for cross-sections smaller than the geometrical value there is a fundamental limit given by the escape velocity of the NS, that on the Newtonian approximation is $v_{esc} \simeq 0.6c\sqrt{2G\left(\frac{M}{1.4M_\odot}\right)\left(\frac{11.5\,\mathrm{km}}{R}\right)}$. In this case, the NS gravitational potential well could bound the WIMPs kinematically although to form an inner thermalized distribution they must further interact with a nucleus/nucleon with mass M' losing an energy fraction $\frac{\Delta E_k}{E_k} \lesssim \frac{4M'm_\chi}{(M'+m_\chi)^2}$ of the incoming kinetic energy E_k every time.

The internal thermalized DM distribution can be parametrized by a particle number density $n_\chi(r,T) = n_{0,\chi}e^{-\left(\frac{r}{r_{\mathrm{th}}}\right)^2}$ where r_{th} is the thermal radius and $n_{0,\chi}$ is the central value normalized to the DM population number inside the star of radius R [5] at a given time in a local environment density similar to our solar system value of about $\rho_\chi \simeq 0.3\ \mathrm{GeV/cm^3}$.

The population at a given time inside the NS, $N_\chi(t)$, is obtained from the solution of an ordinary differential equation $\dot{N}_\chi = C_\chi - C_a N_\chi^2$ including competing processes by means of a capture rate C_χ and an annihilation rate C_a yielding [4]

$$N_\chi(t) = \sqrt{\frac{C_\chi}{C_a}}\coth\left[\frac{(\mathrm{t}-\mathrm{t_{col}})}{\tau} + \coth^{-1}\left(\sqrt{\frac{\mathrm{C_a}}{\mathrm{C_\chi}}}\mathrm{N_\chi(t_{col})}\right)\right], \tag{1}$$

with $\tau^{-1} = \sqrt{C_\chi C_a}$ the relaxation time to achieve equilibrium and $N_\chi(t_{\mathrm{col}})$ is the number of DM particles inside the progenitor core at the time of the collapse (NS birth). This population is esentially inherited from the progenitor star in its lifetime.

The energetics of the dynamical microscopic processes must include the heating and cooling possibilities. First, considering the specific emissivity (energy released per unit volume and unit time) in the photon and neutrino channels arising from the annhilation channels it could be written as

$$\varepsilon_\chi(r,T) \simeq n_\chi^2(r,T) m_\chi \langle\sigma_a v\rangle \sum_{i=\nu,\gamma} f_i, \tag{2}$$

with $\langle\sigma_a v\rangle \simeq 3 \times 10^{-26}\,\mathrm{cm^3/s}$ the velocity averaged annihilation cross-section and $f_i \simeq \int \frac{E}{m_\chi}\frac{dN_i}{dE}dE$ the energy fraction from the spectrum $\frac{dN_i}{dE}$. We must note that the quantity $f = f_\nu + f_\gamma$ is a positive number, *injecting* net energy into the system.

In the typical scenarios for NS cooling [6] standard-model (anti)neutrinos and photons are in charge of cooling efficiently the system. From observations, effective external temperatures

can be measured for a dozen isolated NSs [7]. In the so-called direct URCA process a very efficient neutrino cooling mode is triggered if the proton fraction in the core is large enough, in excess of $(9-11)\%$. Since this requires large central densities it is uncertain whether this mode is switched on. However, if the existence of a spectator neutron is allowed, reactions $p+e+n \to n+n+\nu_e$, $n+n \to p+n+e+\bar{\nu}_e$ under the so-called modified URCA (MURCA) process can proceed. Its emissivity is given by

$$\varepsilon_\nu^{MURCA} \simeq -8.55 \times 10^{21} \left(\frac{T}{10^9\, K}\right)^8 \mathrm{erg\,s^{-1}cm^{-3}}, \tag{3}$$

where the minus sign means that they are cooling modes, effectively removing energy from the system. In addition to this mode and at late times ($\gtrsim 10^5$ yr) the standard photon mode overtakes the cooling as a black-body emitter with a luminosity $L_\gamma \simeq 4\pi R^2 \sigma_{SB} T_e^4$ and $T_e \simeq T^{0.5+\alpha}$, $\alpha \simeq 0.1$ is the effective temperature with $T_e \simeq 0.87 \times 10^6 (T/10^8\, K)^{0.55}$. This yields $\varepsilon_\gamma \simeq -L_\gamma / \frac{4}{3}\pi R^3$ [6].

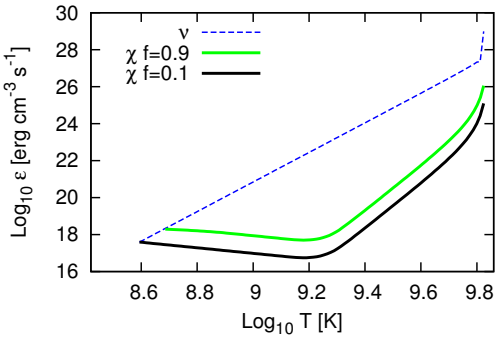

Figure 1: Emissivities in the inner NS core as a function of internal temperature for $m_\chi = 10$ TeV. Dashed line is the MURCA neutrino process while the solid green and black lines denote the effect of a DM energy deposit of $f = 0.9, 0.1$ respectively.

If we now consider the dynamical heat-energy flow the equations for the luminosity L and local temperature T (including redshift factors e^Φ in a curved static spacetime) read [8]

$$\frac{1}{4\pi r^2}\sqrt{1-\frac{r_s}{r}}\frac{\partial}{\partial r}\left(e^{2\Phi}L\right) = -\varepsilon - \frac{C_v}{e^\Phi}\frac{\partial T}{\partial t}, \quad \frac{L}{4\pi r^2} = \kappa\sqrt{1-\frac{r_s}{r}}e^{-\Phi}\frac{\partial}{\partial r}\left(Te^\Phi\right), \tag{4}$$

where $\varepsilon = \sum_{j=\nu,\gamma} \varepsilon_j$ is the contribution of the emissivities, $r_s = 2GM$ is the Schwarzschild radius, C_v is the heat capacity per unit volume and κ is the thermal conductivity. C_v is the sum of the contribution of partial heat capacities from particle constituents (we take protons, neutrons, electrons) $C_v = \sum_{i=p,n,e} C_{v,i}$. For a degenerate core with fermions we have (per unit volume) $C_{v,i} = N_i(0)\frac{\pi^2}{3}k_B^2 T$ and $N_i(0) = \frac{m_i^* c^2 p_{F,i}}{\pi^2}$ is the density of states for a degenerate quantum system, being $p_{F,i}$ the ith-Fermi momentum and $m_{p,n}^* < m_n$ the in-medium nucleon mass, that can be a reduced with respect to vacuum values due to many-body effects [9]. Consistently, we

take $m_e^* = m_e$. Let us note that in the Newtonian limit (the one we are going to analyze in this contribution) the solution is obtained from solving in the isothermally flat limit. This is a consequence of the large thermal conductivity in the system. Relativistic corrections to time and distance scales are set to unity. Then the equation simplifies to

$$C_v \frac{dT}{dt} = -|\varepsilon_\nu| - |\varepsilon_\gamma| + \varepsilon_\chi. \tag{5}$$

In Fig.(1) we show the emissivities in the NS inner core as a function of internal temperature T. We suppose neutrinos, photons and DM particles in a flat, Newtonian space. We assume an initial temperature of $T \simeq 1$ MeV. We depict with a dashed line the MURCA neutrino process while the solid green and black lines denote the effect of an energy deposit of $f = 0.9, 0.1$, respectively. We can see that at a $T \simeq 10^{8.6-8.7}$ K the emissivities are comparable. This T drop corresponds to $\sim 10^2$ yr assuming a central core density of 3.5 times that of nuclear saturation density for a 10 TeV particle. Let us remind here that we have supposed that the core is isothermal at very early times. Standard approaches show that isothermality in the core takes about $\Delta t \simeq 10$ yr to be achieved, however this correction should not change much the results obtained here. In a previous work [10] it was determined that the possible effect on the cooling pattern in a NS was a flattening of the temperature of the star around $\sim 10^4$ K at times larger than $\sim 10^7$ yrs, making this a challenging experimental confirmation, especially if looking towards central galactic locations where DM fraction may be enhanced. We find here that, for existing models of DM candidates with masses in the $\gtrsim$TeV range this is, in principle, a viable measurement that could test the proposed mechanism. This is subject of ongoing work and results will appear elsewhere. As a final remark let us mention that we have supposed that the fate of the NS is to remain as a nucleon-matter object, but if, however, a nucleation massive event is triggered, furhter consequences may result. This has been partially explored in [11][12][13]. M. A. P. G. would like to thank useful conversations with J. Pons and C. Kouvaris and the kind hospitality of IAP where part of this work was developed and the Spanish MICINN MULTIDARK, FIS2012-30926 projects.

References

[1] P. A. R. Ade et al. [Planck Collaboration], arXiv: 1303.5075.

[2] T. Daylan et al., arXiv:1402.6703.

[3] J. E. Gunn and J. R. Gott ApJ, **176** (1972) 1.

[4] A. Gould, ApJ **321** 571 (1987).

[5] M. A. Pérez-García and J. Silk, arXiv: 1403.6111, in press in Phys. Lett. B

[6] D. Page et al, ApJ **155** (2004) 623.

[7] D. G. Yakovlev et al, Advances in Space Research **33** (2004) 523.

[8] K. S. Thorne, *The General Relativistic Theory of Stellar Structure and Dynamics*, in C. Dewitt, E. Schatzman, P. Véron, editor, High Energy Astrophysics, Volume 3, (1967).

[9] M. A. Pérez-García , C. Providencia and A. Rabhi, Phys Rev C **84** (2011) 045803.

[10] C. Kouvaris, Phys. Rev. D **77** (2008) 023006.

[11] M. A. Pérez-García, Silk, J., Stone, J. R. , Phys. Rev. Lett. **105** (2010) 141101.

[12] M. A. Pérez-García and J. Silk, Physics Letters B **711** (2012) 6.

[13] M. A. Pérez-García, F. Daigne and J. Silk, ApJ **768** (2013) 145.

DarkSide-50: results from first argon run

Davide D'Angelo for the DarkSide collaboration

Università degli Studi di Milano e I.N.F.N., via Celoria 16, 20133 Milano, Italy

DOI: http://dx.doi.org/10.3204/DESY-PROC-2014-04/315

DarkSide (DS) at Gran Sasso underground laboratory is a direct dark matter search program based on TPCs with liquid argon from underground sources. The DS-50 TPC, with 50 kg of liquid argon is installed inside active neutron and muon detectors. DS-50 has been taking data since Nov 2013, collecting more than 10^7 events with atmospheric argon. This data represents an exposure to the largest background, beta decays of ^{39}Ar, comparable to the full 3 y run of DS-50 with underground argon. When analysed with a threshold that would give a sensitivity in the full run of about 10^{-45} cm^2 at a WIMP mass of 100 GeV, there is no ^{39}Ar background observed. We present the detector design and performance, the results from the atmospheric argon run and plans for an upscale to a multi-ton detector along with its sensitivity.

The DarkSide (DS) project [1] aims to direct Dark Matter detection via WIMP-nucleus scattering in liquid Argon. The detectors are dual phase Time Projection Chambers (TPCs) located at Laboratori Nazionali del Gran Sasso in central Italy under a rock coverage of $\sim$3800 m w.e. DS aims to a background-free exposure via three key concepts: (1) very low intrinsic background levels, (2) discrimination of electron recoils and (3) active suppression of neutron background.

DS has a multi-stage approach: after the operation of a 10 kg detector [2], we are now running DarkSide-50 (DS-50) detector with a 45 kg fiducial mass TPC and a projected sensitivity of $\sim 10^{-45}$ cm^2 for a 100 GeV WIMP. The project will continue with a multi-ton detector and a sensitivity improvement of two orders of magnitude.

The DS-50 TPC is depicted in Fig. 1. The scattering of WIMPs or background in the active volume induces a prompt scintillation light, called S1, and ionization. Electrons which do not recombine are drifted by an electric field applied along the z-axis. The maximum drift time across the 35.6 cm height is $\sim$375 μs at the operative field of 200 V/cm. Electrons are then extracted into gaseous argon above the extraction grid, where a secondary larger scintillation emission takes place, called S2. Two arrays of 19 3"-PMTs collect the light on each side of the TPC.

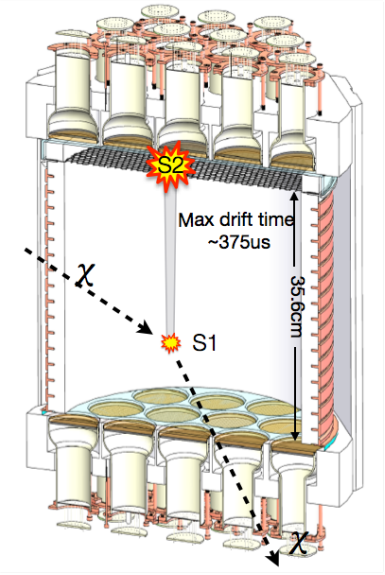

Figure 1: DS-50 TPC principle of operation.

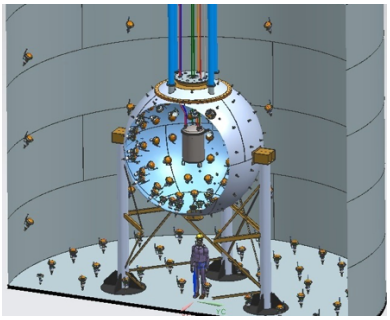

Figure 2: DS-50 Schematics. TPC, ND and MD are visible.

The TPC is housed inside an organic liquid scintillator Neutron Detector (ND) and a water Cherenkov Muon Detector (MD) [3], designed to host also a larger TPC with up to 5 t of Liquid Argon, see Fig. 2. The ND is made by a 4 m diameter steel sphere filled with a 1:1 mixture of Pseudocumene (PPO doped) and Trimethyl Borate (TMB) for enhanced neutron detection. The scintillation light is captured by 110 8"-PMTs mounted on the sphere inner surface. In addition of acting as a veto it also features independent trigger capabilities for an in-situ measurement of the neutron background. Boron has a high n-capture cross section which allows a compact veto size and reduces the capture time to 2.3 μs, two orders of magnitude below pure PC. The n-capture on ^{10}B results in recoiling ^{7}Li and α particle. In 94% of the cases a 0.48 MeV-γ accompanies the process and is brightly visible. In the remaining cases the recoil energy of 1.47 MeV must be detected and this is typically quenched to $\sim$ 50 keV. Simulations indicate an efficiency $>$ 99% for radiogenic neutrons and $>$ 95% for cosmogenic neutrons [4]. The MD is a cylindrical tank, 11 m in diameter and 10 m high, filled with ultra-pure water and instrumented with 80 8" PMTs on the floor and inner walls. In addition of acting as water Cherenkov detectors for through-going muons with >99% efficiency, it also serves as passive shielding again gammas and neutrons from the rocks. DS-50 has been commissioned and is taking data since Nov. 2013. After circulatimg Argon through charcoal filters for about 5 months, the electron lifetime was brought a stable value of $\sim$ 5 ms, much larger then the maximum drift time in the TPC.

Operating Argon detectors implies dealing with the intrinsic cosmogenic background from ^{39}Ar, a β-emitter with a Q=565 keV and $\tau_{1/2} = 269$ y. In Atmospheric Argon (AAr) its activity can be as high as $\sim$ 1 Bq/kg. However we have identified a source of Underground Argon (UAr) where the contamination is $<$ 6.5 mBq/kg. A cryogenic distillation plant is producing the UAr at a rate of $\sim$ 0.5 kg/d. We are currently operating with AAr and we will switch to UAr at the beginning of 2015. Argon has an intrinsic capability to distinguish Electron Recoils (ER) such as ^{39}Ar decays from Nuclear Recoils (NR). Prompt scintillation light in Argon comes from the de-excitation of singlet and triplet states of Ar_2^*, having very different mean lives: $\tau_{\text{singlet}} \sim 7$ ns while $\tau_{\text{triplet}} \sim 1.6\,\mu$s. Since NRs tend to populate more the singlet state, they result in significantly faster signals compared to ERs. We define the parameter F90 as the ratio of charge collected in the first 90ns over the total S1 charge. NRs are distributed around F90 $\sim$ 0.7 while ERs around F90 $\sim$ 0.3.

We have characterised our detector in terms of Light Yield (LY). At null field we have used the LY from the ^{39}Ar shoulder at 565 keV, obtaining $\text{LY}_{\text{null}} \sim 8$ pe/keV, assumed energy independent within 3%. With the application of the drift field, the LY becomes energy dependent and ^{39}Ar is way beyond or region of interest. Therefore we spiked argon by adding gaseous ^{83m}Kr in the recirculation system. ^{83m}Kr decays fast ($\tau_{1/2} \sim 1.8$ h) and yields a good monochromatic line at 41.5 keV. We have used the relative position of this line with and without drift field to scale the LY, obtaining $\text{LY}_{200V} \sim 7.2$ pe/keV at 200 V/cm.

Compared to ERs, NRs are quenched by a factor that depends on energy and field. We have used the data from SCENE [5] to determine the quenching factor. SCENE features a small TPC with a concept similar to DS and has been measuring recoils from a neutron beam, whose energy can be selected. SCENE has measured quenching factors at different neutron energies

and drift field with respect to ERs from ^{83m}Kr. We have processed SCENE raw data using the DS reconstruction code and we have obtained the quenching factors as well as the distributions of the F90 parameter.

The ND has been also commissioned. The LY has been estimated exploiting ^{60}Co contamination present in the cryostat. The LY has been found to be ~ 0.5 pe/keV, sufficient to detect recoils following a neutron capture on Boron of the order of 50 keV$_{ee}$. Unfortunately we have observed a high rate due to the intrinsic biogenic isotope ^{14}C in the TMB, at the level of $\sim 10^{-13}$ g/g. We have therefore successfully distilled the scintillator mixture and replaced TMB with pure Pseudocumene. Meanwhile we have identified a supplier of TMB coming from an underground oil batch which is low in ^{14}C, $< 10^{-15}$ g/g. We will restore the design scintillator mixture before the end of 2014.

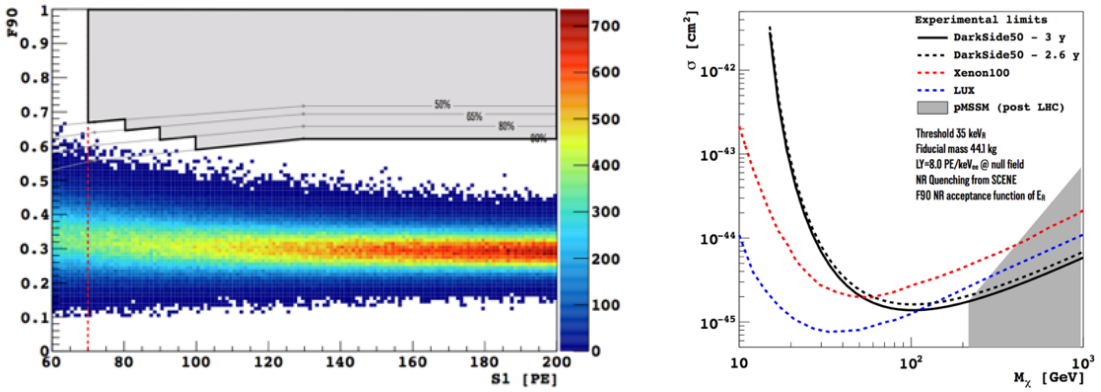

Figure 3: DS-50 exposure of 280 kg-days, F90 vs S1 energy in PE units with the NR acceptance curves and the WIMP search region superimposed (left). DS-50 projected sensitivity for 2.6 y and 3 y running with UAr compared to rejection curves from LUX and Xenon100 experiments (right).

In Fig. 3 (left) are shown events corresponding to 280 kg-days in the parameter plane of F90 vs S1 Energy in photoelectrons. Only single hit events are selected. A z-cut is applied to remove the regions close to the cathode and to the extraction grid. Events which show a coincident energy deposition in the ND are removed. The high ^{39}Ar content of AAr allows us to calibrate our S1-PSD with an exposure equivalent to 2.6 y of operation with UAr at a contamination as high as the present upper limit. In this energy scale 70 pe and 125 pe correspond to ~ 35 keV and ~ 57 keV NRs according to the quenching factors determined from the SCENE data. 70 pe is also our choice of energy threshold. We have also superimposed the F90 NR acceptance curves derived from SCENE, a conservative choice as DS has a higher LY and hence narrower F90 distributions. This plot proves that PSD at 200 V/cm can efficiently suppress the dominant ER background that we expect in 2.6 y of DS-50 UAr run, while maintaining high acceptance for WIMPs. We have then proceeded to define a WIMP search region as in Fig. 3. Assuming no candidate WIMP event, this allows us to project the sensitivity of DS-50 in the parameter plane of WIMP-nucleus cross-section vs WIMP mass, as it can be seen in Fig. 3 (right), and compare it to the existing Xenon100 and LUX rejection curves. Systematics on NR quenching factors and F90 curves contribute about 10% variation at 100 GeV WIMP mass.

We have also modelled F90 using the statistical distributions of the underlying processes with parameters taken from data. The model accounts for macroscopic effects related to argon micro-physics, detector properties, reconstruction and noise effects. We have simulated F90 distributions for a DS upgrade of 3.8 t fiducial mass and for 5 y of run, assuming the ER background will be dominated by ^{39}Ar at its present upper limit. Figure 4 shows the agreement of the simulated distribution for a sample energy bin to real DS-50 data, after normalization. Similar plots are obtained for all energy slices. Figure 5 (left) shows the simulated exposure in analogy to the DS-50 data plot of Fig. 3. In this case the energy threshold would be 120 pe although 100 pe could be considered too. The projected sensitivity is shown in Fig. 5 (right). An increase in sensitivity of two orders of magnitude is expected in comparison with DS-50.

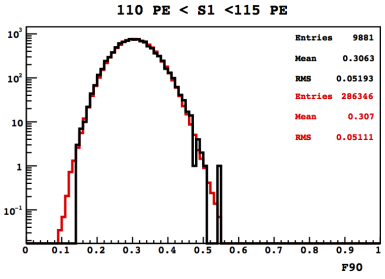

Figure 4: F90 distributions in the [110,115] pe sample energy bin. Simulation (red) compared to data (black) after normalization.

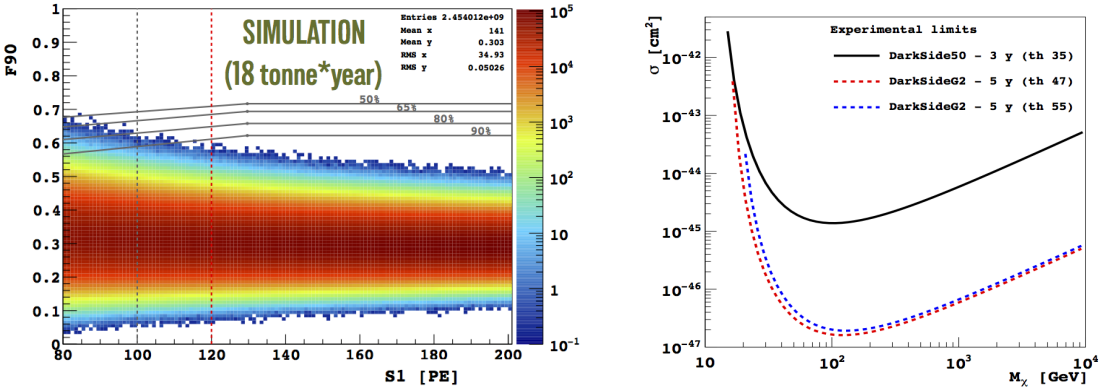

Figure 5: DS multi-ton upscale. Simulated exposure of 5 y, F90 vs S1 energy in PE units (left). Projected sensitivity with 120 pe (blue) and 100 pe (red) compared to DS-50 (right).

DS-50 has now acquired ∼5000 kg-day of AAr data. The analysis is ongoing [6] in order to improve your understanding of backgrounds and study the S2 signal. The latter would bring x-y position reconstruction, hence a full 3D volume fiducialization, and additional ER/NR discrimination from the S2/S1 ratio. We are also planning a detailed source calibration campaign in fall 2014. In January 2015 we foresee to switch to UAr and start the physics run.

References

[1] T. Alexander *et al.* [DarkSide Collaboration], JINST **8** (2013) C11021.
[2] T. Alexander *et al.* [DarkSide Collaboration], Astropart. Phys. **49** (2013) 44 [arXiv:1204.6218 [astro-ph.IM]].
[3] L. Pagani, D. D'Angelo and S. Davini, PoS EPS **-HEP2013** (2013) 062.
[4] A. Wright, P. Mosteiro, B. Loer and F. Calaprice, Nucl. Instrum. Meth. A **644** (2011) 18 [arXiv:1010.3609].
[5] H. Cao *et al.* [SCENE Collaboration], arXiv:1406.4825 [physics.ins-det].
[6] P. Agnes *et al.* [DarkSide Collaboration], arXiv:1410.0653 [astro-ph.CO].

Searching for Dark Matter with the LUX experiment

J. E. Y. Dobson[1] for LUX Collaboration

[1]School of Physics & Astronomy, University of Edinburgh, Edinburgh, UK, EH9 3JZ

DOI: http://dx.doi.org/10.3204/DESY-PROC-2014-04/95

The Large Underground Xenon (LUX) experiment completed its first physics run in 2013 and produced a world-leading limit for spin-independent scattering of Weakly Interacting Massive Particles using 85.3 live-days of data. After presenting these first results we discuss the detector development work and calibrations following the first physics run, the current status of LUX and plans for the future multi-ton LUX-ZEPLIN experiment.

1 Introduction

First postulated more than 80 years ago to address the missing mass of the Milky Way galaxy, dark matter remains one of the best motivations for physics beyond the Standard Model. The Λ-Cold Dark Matter standard model of Big Bang cosmology is now well established and presents a clear and consistent picture of a universe in which non-baryonic cold dark matter makes up around four fifths of the total matter content. The evidence in support of this is both abundant and varied and includes galactic rotation curves, precise measurements of the cosmic microwave background, weak lensing studies of galaxy clusters, primordial nucleosynthesis and the characteristics of large scale structure in the universe [1]. Despite considerable knowledge concerning the impact of dark matter on these astrophysical phenomena very little is known about its fundamental nature. Direct search experiments aim to change this by detecting individual interactions of particles of dark matter that are hypothesised to permeate our galaxy. Many experiments focus on the search for Weakly Interacting Massive Particles (WIMPs), the leading candidates for dark matter. They look for the low energy nuclear recoils expected when WIMPs scatter elastically off target nuclei in the experiment. The small interaction cross sections and low velocities expected for galactic WIMPs impose the challenging requirement that dark matter detectors need to be sensitive to ∼few keV recoiling nuclei and at the same time be capable of amassing exposures of many kg · years.

2 The LUX Experiment

The Large Underground Xenon (LUX) experiment [2] is a 370 kg dual-phase liquid xenon time projection chamber (TPC) located 4850 feet underground (4300 m w.e.) at the Sanford Underground Research Facility (SURF) in Lead, South Dakota. The active region of the TPC is 47 cm in diameter and 48 cm in height comprising 250 kg of xenon. Interactions in the liquid xenon produce both prompt scintillation light (S1) and ionisation electrons that drift in an applied

electric field (181 V/cm) to the liquid-gas interface at the top of the detector. The electrons are then extracted into the gas phase (6.0 kV/cm), where they produce electroluminescence (S2). The S1 and S2 signals are used to reconstruct the deposited energy and their ratio is used to discriminate WIMP-like nuclear recoils (NR) from background electron recoils (ER) at the 99.6% level at a 50% NR acceptance in the energy range of the LUX analysis. The TPC is read out from the top and bottom by two arrays of 61 photomultiplier tubes (PMTs) which image the central liquid xenon region and record the S1 and S2 signals. The x-y position of an interaction is determined to better than 4–6 mm from the localisation of the hit pattern of S2 light in the top PMT array. The depth of the interaction is given—to similar precision—based on the measured drift speed of the electrons (1.51 ± 0.01 mm/μs) and the time interval between the S1 and S2 light. This knowledge of the precise 3D position of an interaction means the full self-shielding capability of the liquid xenon can be utilised by only considering interactions in an inner radioactively-quiet fiducial volume.

An extensive screening campaign imposed stringent requirements on the levels of radioactivity for materials used to build the detector. Before being used in LUX, the full contingent of research grade xenon was purified at a dedicated research facility using a novel technique based on chromatographic separation. In addition to shielding against cosmic rays provided by the rock overburden, the LUX detector sits within a 6.1 m tall and 7.6 m in diameter water tank, instrumented with 20 8-inch PMTs, which acts as both an active veto for any penetrating cosmic rays and as a further shield to any remaining γ-rays and neutrons. Backgrounds from these particles are thereby rendered subdominant to those from radioactivity of internal detector components. A full description of LUX can be found in [2].

3 First results from LUX

LUX completed its first physics run in 2013, collecting a total of 85.3 live-days of WIMP search data between late April and early August. During this period the ER background rate inside the 118 kg fiducial volume was measured to be 3.6 ± 0.3 mDRU (mDRU= 10^{-3} counts/day/kg/keV) in the energy range of interest, to date the lowest achieved by any xenon TPC. Full details of the radiogenic and muon-induced backgrounds in LUX can be found in [3]. To reduce the scope for bias, a non-blind analysis was conducted in which only a minimal set of high-acceptance data quality cuts were used. Single scatter events containing exactly one S1 within the maximum drift time (324 μs) preceding a single S2 were selected for further analysis. The single scatter ER and NR acceptance was measured with dedicated tritium (β^-), AmBe, and ^{252}Cf (neutron) datasets. All the cuts and efficiencies combined to give an overall WIMP-detection efficiency of 17, 50 and $> 95\%$ at 3.0, 4.3 and 7.5 keV recoil energies respectively.

In total 160 events were observed in the energy range of interest for WIMPs, between 2–30 photoelectrons (phe) S1, with all observed events being consistent with the predicted background of electron recoils. The p-value for the background-only hypothesis was 0.35. Confidence intervals on the spin-independent WIMP-nucleon cross section were set using a profile likelihood ratio (PLR) test statistic which exploits the separation of signal and background distributions in radius, depth and S1 and S2. For the signal model we conservatively assumed no signal below 3 keV, the lowest energy for which direct light yield measurements in xenon existed. The 90% upper C.L. are shown in figure 1 (left) with a minimum of 7.6×10^{-46}cm^2 at a WIMP mass of 33 GeV/c^2, making LUX the first experiment to probe sub-zeptobarn WIMP-nucleon cross sections. We see in figure 1 (right) that the LUX limit fully excludes nearly all

the anomalous results at low WIMP masses claimed by a number of experiments. Full details of the analysis can be found in [4].

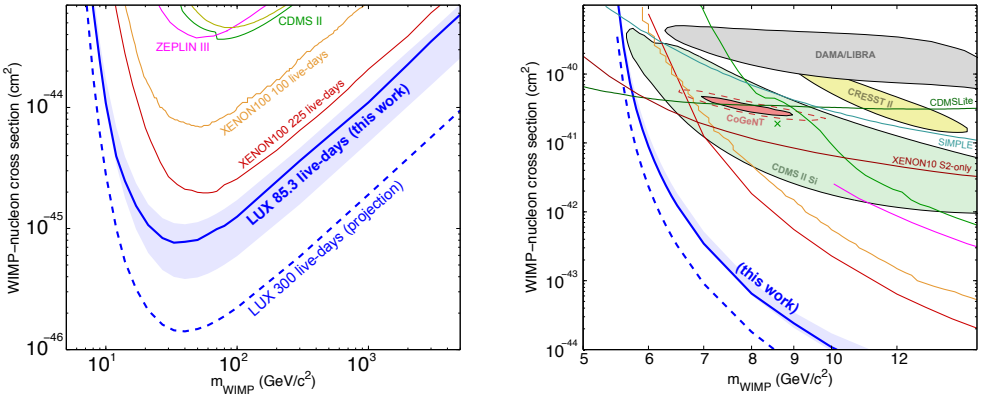

Figure 1: *Left:* The LUX 90% confidence limit on the spin-independent elastic WIMP-nucleon cross section for the 85.3 live-day exposure (blue) and projected limit for the upcoming 300-day run (dashed blue). *Right:* Close-up of low-mass region.

Following the first WIMP-search result LUX underwent a period of upgrades and maintenance in preparation for the final 300-day WIMP-search run. This included a campaign of cathode and grid wire conditioning aimed at increasing the applied drift and extraction fields and improvements to the krypton calibration system and the xenon controls and recovery system. Finally, a D-D neutron generator providing an almost monochromatic source of neutrons was used to make an in-situ calibration (down to 0.7 keV for the ionization channel) of the low-energy nuclear recoil response of LUX through an analysis of multiple-scatter events [5].

Final preparations for the 300-day run are now underway and it is expected to start before the end of 2014. The sensitivity for the 300-day run is expected to surpass that of the first WIMP-search result by a factor of around five and the sensitivity at low masses will benefit from the confirmation of the detector response to low-energy recoils.

4 LUX-ZEPLIN

Looking to the future, designs for the LUX-ZEPLIN (LZ) experiment are well underway. At the heart of LZ is a scaled up version of the LUX TPC with an active region containing about 7 tonnes (at least 5 tonnes fiducial). LZ will replace LUX on the 4850' level at SURF and will reuse the LUX water tank. Figure 2 shows the overall detector concept.

In addition to the considerable increase in target mass ($\sim$40 $\times$ LUX fiducial) LZ features a more sophisticated veto system which includes an optically separated and instrumented xenon *skin* layer between the inner TPC and the walls of the cryostat and an external liquid scintillator veto (gadolinium loaded linear alkyl benzene). The combination of skin readout and the outer detector creates a highly efficient integrated veto system providing powerful rejection of γ-rays and neutrons from internal sources (e.g. PMTs) that could otherwise scatter once in the TPC and then escape, thus potentially posing a problematic background.

With a projected sensitivity of 10^{-48}cm^2 for its full 1000-day exposure, LZ reaches faster and further than any competing experiment being proposed on a similar timescale, exploring

a significant fraction of the parameter space remaining above the irreducible background from coherent scattering of neutrinos from astrophysical sources [6]. Earlier this year LZ was selected by the US Department of Energy as one of three approved *Generation 2* dark matter experiments and plans to begin its construction phase in 2015 with a projected start of physics data taking in 2018.

5 Conclusions

With its first WIMP search data LUX set the world's most stringent limit for spin-independent WIMP-nucleon elastic scattering, becoming the first direct search experiment to probe the sub-zeptobarn regime. The LUX 300-day run is due to start soon and will further increase this sensitivity by a factor of five with discovery still possible. In the longer term the LUX-ZEPLIN experiment will improve on the LUX 300-day sensitivity by almost two orders of magnitude, enabling significantly deeper probing of parameter space for discovery if necessary, or giving the capability to characterise a dark matter signal if found.

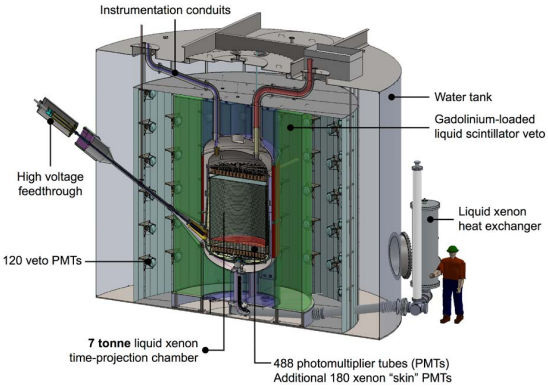

Figure 2: Schematic of the LZ experiment as housed in the reused LUX water-tank.

Acknowledgments

This work was partially supported by the U.S. Department of Energy (DOE) under award numbers DE-FG02-08ER41549, DE-FG02-91ER40688, DE-FG02-95ER40917, DE-FG02-91ER40674, DE-NA0000979, DE-FG02-11ER41738, DE-SC0006605, DE-AC02-05CH11231, DE-AC52-07NA27344, and DE-FG01-91ER40618; the U.S. National Science Foundation under award numbers PHYS-0750671, PHY-0801536, PHY-1004661, PHY-1102470, PHY-1003660, PHY-1312561, PHY-1347449; the Research Corporation grant RA0350; the Center for Ultra-low Background Experiments in the Dakotas (CUBED); and the South Dakota School of Mines and Technology (SDSMT). LIP-Coimbra acknowledges funding from Fundação para a Ciência e Tecnologia (FCT) through the project-grant CERN/FP/123610/2011. Imperial College and Brown University thank the UK Royal Society for travel funds under the International Exchange Scheme (IE120804). The UK groups acknowledge institutional support from Imperial College London, University College London and Edinburgh University, and from the Science & Technology Facilities Council for PhD studentship ST/K502042/1 (AB). The University of Edinburgh is a charitable body, registered in Scotland, with registration number SC005336.

References

[1] K.A. Olive et al. Review of Particle Physics. *Chin.Phys.*, C38:090001, 2014.

[2] D.S. Akerib et al. The Large Underground Xenon (LUX) Experiment. *Nucl.Instrum.Meth.*, A704:111–126, 2013.

[3] D.S. Akerib et al. Radiogenic and Muon-Induced Backgrounds in the LUX Dark Matter Detector. *Astropart.Phys.*, 62:33–46, 2014.

[4] D.S. Akerib et al. First results from the LUX dark matter experiment at the Sanford Underground Research Facility. *Phys.Rev.Lett.*, 112:091303, 2014.

[5] J. Verbus. Recent Results from the LUX Dark Matter Search, in: Lake Louise Winter Institute 2014.

[6] J. Billard, L. Strigari, and E. Figueroa-Feliciano. Implication of neutrino backgrounds on the reach of next generation dark matter direct detection experiments. *Phys.Rev.*, D89:023524, 2014.

The EDELWEISS-III Dark Matter Search: Status and Perspectives

Lukas Hehn[1] on behalf of the EDELWEISS Collaboration

[1]Karlsruhe Institute of Technology (KIT), Institut für Kernphysik

DOI: http://dx.doi.org/10.3204/DESY-PROC-2014-04/235

EDELWEISS is a direct Dark Matter search program looking for WIMPs in the GeV-TeV mass range. For that purpose, an array of cryogenic Ge mono-crystals read out simultaneously by NTD thermal sensors and by surface electrodes is installed in the Modane underground laboratory. We present a summary of EDELWEISS-II results including limits on axion couplings. For EDELWEISS-III a major upgrade of the setup was undertaken. 36 new FID800 Ge bolometers are currently installed, as well as a new DAQ system and improved shielding to lower the background.

1 The EDELWEISS experiment

1.1 Experimental setup at LSM

The EDELWEISS experiment is situated in the deepest underground laboratory in Europe, the *Laboratoire Souterrain de Modane* (LSM). A 4800 mwe rock overburden reduces the cosmic muon flux by a factor of $O(10^6)$ to only $5\,\mu/\mathrm{m}^2/\mathrm{day}$ [1]. In the LSM, the experiment is housed in a clean room with a deradonized air supply and a remaining activity from Rn-decay of a few tens of $\mathrm{mBq/m}^3$. The surrounding active muon veto system of 48 plastic scintillator modules and $100\,\mathrm{m}^2$ with a geometric coverage of $>98\,\%$ tags throughgoing muons. Next is a 50 cm thick polyethylene (PE) layer to moderate the neutron flux, followed by 20 cm lead for the suppression of γ-activity. Inside is a dilution copper cryostat which cools down several tens of kg of detectors to stable cryogenic temperatures of a few mK.

1.2 Cryogenic bolometer detectors

The detectors used in EDELWEISS are germanium mono-crystal bolometers (see Fig. 1 left). Particles can interact with the Ge atoms via elastic scattering on either the nucleus or the electron shell and thereby produce both $\mathrm{e}^-/\mathrm{h}^+$-pairs and phonons. By comparing the ionization yield Q, the fraction of created charge vs. heat energy, it is possible to discriminate *Electronic Recoils* (ER) from *Nuclear Recoils* (NR) on an event-by-event basis. *ER*s from β's and γ's have $Q = 1$ by definition while *NR*s from neutrons and expected from WIMPs produce significantly less charge with $Q \approx 0.3$. This allows to efficiently reject background radiation from possible WIMP candidate events. To read out the two signals, the cylindrical detectors are equipped with phonon sensors and electrodes on the surface. At an operating temperature of $T = 18\,\mathrm{mK}$ the

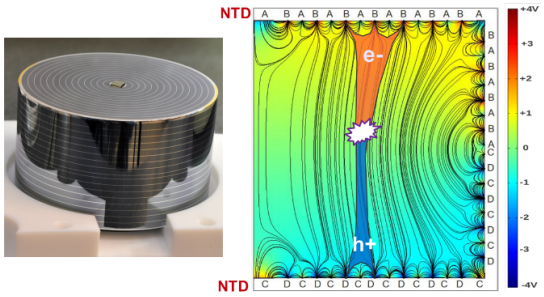

Figure 1: Left: FID800 detector with concentric ring electrodes and NTD phonon sensor. Width = 7 cm and height = 4 cm. Right: Axial symmetric electric field map with the charges of a fiducial event drifted to electrode sets B and D.

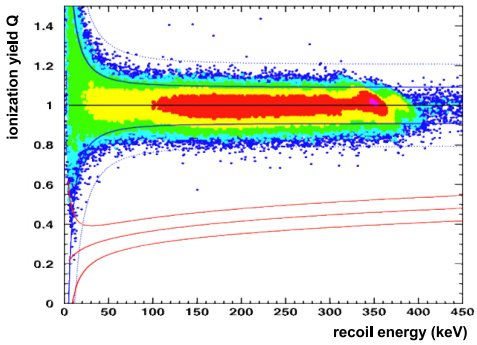

Figure 2: ^{133}Ba calibration data with electron recoils from $>400,000\,\gamma$'s. No event above 20 keV populates the 90 % C.L. nuclear recoil band.

Neutron Transmutation Doped (NTD) germanium transistors measure a minuscule temperature increase of $\approx 1\,\mu$K for a 10 keV recoil. Concentric rings of Al electrodes are connected such, that interleaved rings form two different sets on top and bottom [2]. These sets are biased with different voltages $O(1\,\text{V})$, drifting charges to top and bottom of the detector and along the surface (see Fig. 1 right). The set of *fiducial electrodes* (here B and D) has the higher potential difference and collects charges from the inner bulk volume of the crystal, while a signal on the *veto* electrodes (A,C) efficiently rejects events near the surface. Detectors used in EDELWEISS-II had masses of 400 g and a so called *InterDigit* (ID) design with ring electrodes only on top and bottom, while the outer sides had planar electrodes. The resulting electric field configuration led to an inner *fiducial mass* of 40 % or 160 g. For the 800 g crystals used in EDELWEISS-III a *Fully InterDigit* (FID) design with ring electrodes also on the sidewalls leads to a much higher fiducial mass of 75 % or 600 g, while at the same time improving the rejection of surface events due to better charge collection.

2 Results from the EDELWEISS-II phase

Phase II of the EDELWEISS experiment was running under stable low temperature conditions from April 2009 to May 2010, for a continuous data taking of more than 400 days. Installed were 10 ID-detectors with masses around 400 g each.

2.1 Standard WIMP analysis

The standard analysis [3], optimized for WIMPs of masses $O(100\,\text{GeV})$, used a total effective exposure of 384 kg.days after all cuts. In the 90 % C.L. nuclear recoil band [20, 200 keV] (the WIMP search region), 5 candidate events were observed, which was compatible with the expected background of 3.0 events. This result was interpreted in terms of a spin-independent WIMP-nucleon scattering cross section, leading to $\sigma_{\text{SI}} < 4.4 \times 10^{-8}$ pb (90 % C.L.) for a WIMP mass of 85 GeV. Constraints were also set on scenarios with inelastic scattering mechanisms.

Due to their similarities, the results of EDELWEISS-II and the CDMS experiment could be combined and the two collaborations published an exclusion limit of $\sigma_{\mathrm{SI}} < 3.3 \times 10^{-8}$ pb for a WIMP mass of 90 GeV, derived from a combined exposure of 614 kg.days [4].

2.2 Low mass WIMP analysis

A dedicated analysis was performed on a reduced data set to search for low mass WIMPs between 7 and 30 GeV [5]. The 4 ID detectors with the best resolutions were used and stronger quality cuts allowed to lower the analysis threshold to 5 $\mathrm{keV_{nr}}$, therefore making the experiment sensitive to low WIMP masses. With an upper recoil energy limit set to 20 keV, the results are independent from the standard WIMP analysis. For a reduced effective exposure of 113 kg.days a maximum of 3 candidate events (depending on the WIMP mass) were found, which was compatible with the expected background from neutrons and γ's of 2.9 events. At a WIMP mass of 10 GeV and with only one candidate event, the resulting limit derived with Poisson statistics is $\sigma_{\mathrm{SI}} < 1.0 \times 10^{-5}$ pb (90 % C.L.) which significantly constrains a possible CoGeNT signal and excludes signals reported by DAMA/LIBRA and CRESST.

2.3 Search for Axions and ALPs

Complimentary to WIMP search in nuclear recoil events, the search for axions in EDELWEISS-II was performed on data of electron recoils only [6]. Axions and *Axion Like Particles* (ALPs) could lead to such recoils after producing photons via the Primakoff effect (enhanced by Bragg diffraction in the mono-crystals) or electrons via the axio-electric effect. For these type of events the surface rejection with the ID design provided very low backgrounds down to 0.3 evts/kg/day/keV and energy thresholds down to 2.5 $\mathrm{keV_{ee}}$, in a data set with 484 kg.days exposure. For 3 different solar production mechanisms and the assumption of an axion Dark Matter halo limits could be set on axion-photon and axion-electron couplings to exclude mass ranges of $0.92\,\mathrm{eV} < m_{\mathrm{A}} < 80\,\mathrm{keV}$ for DFSZ axions and $5.78\,\mathrm{eV} < m_{\mathrm{A}} < 40\,\mathrm{keV}$ for KSVZ axions.

3 Improvements for EDELWEISS-III

The EDELWEISS-II sensitivity goal was reached in 2010 with the experiment eventually limited by backgrounds. To probe spin-independent cross sections down to $\sigma_{\mathrm{SI}} \approx 10^{-9}$ pb, EDELWEISS-III will employ a higher exposure at a significantly reduced background level.The 36 FID 800-g detectors currently installed in the cryostat do not only increase the fiducial mass from 1.6 kg in EDELWEISS-II to > 20 kg, but also have reduced background due to their improved design. The rejection of γ's was shown to be 5$\times$ better than for ID400 detectors. This was measured with calibration data from a ^{133}Ba γ-source (see Fig. 2). Out of $> 4 \times 10^5\,\gamma's$ no event leakage into the 90 % C.L. nuclear recoil band above 20 keV was observed, giving a rejection factor of $< 6 \times 10^{-6}$ NRs/γ. Rejection of surface events was also improved: With a ^{210}Pb source implanted in its copper casing, a detector was exposed to 10^5 α's, β's and γ's of the Pb decay chain. Only one event in the 90 % C.L. NR-band above 15 keV was observed after the fiducial volume cut, giving a rejection of 4×10^{-5} misidentified evts/kg.day. Both improvements are attributed to the better charge collection due to the additional electrode rings, which decreases the misreconstruction of double scatter events.

Enhancements were also made to the experimental setup. Within the cryostat additional PE at the 1 K stage has been added between detectors and cold electronics, while new PE pieces outside the shield against the warm electronics. Coaxial cabling in the cryostat has been replaced with more radiopure Kapton cabling. New thermal screens for the cryostat itself are now made from NOSV copper with higher radiopurity. The combined neutron suppression compared to EDELWEISS-II improved by a factor of 100. In order to reduce microphonic noise, the pulse tubes close to the cryostat have been replaced by GM thermal machines outside the complete shielding, which are connected by a cryoline. To avoid Johnson noise, resistors in the electronics have been removed and the active feedback system was replaced by a relay system. Altogether these changes lead to improvements of $\approx 30\,\%$ in resolutions, lowering the average FWHM baselines of the ionization channels from 900 eV to 600 eV and from 1.2 keV to 1.0 keV for the heat channel. Multiple R&D efforts are currently ongoing to improve the sensitivity of the experiment: Replacing the JFET based amplifiers with a HEMT readout could improve the resolution on the ionization channel down to 300 eV, with a significant benefit for low mass WIMP search. The recent installation of an integrated DAQ system is accompanied by tests with an event triggered 40 MHz readout of the ionization channel, which gives additional spatial information on the z-axis of the detector. The channel upscaling due to the new DAQ system is a crucial requirement for the next phase after EDELWEISS-III, the proposed cryogenic 1-ton scale multi-target experiment EURECA [7].
With the 36 FID800 detectors installed, EDELWEISS-III is currently on the way to take a first data set of 3000 kg.days exposure, expected to be background free. The final goal is then an exposure of 12 000 kg.days which should reach a sensitivity of $\sigma_{\mathrm{SI}} \approx 10^{-9}$ pb with background limitation setting in.

Acknowledgments

The help of the technical staff of the Laboratoire Souterrain de Modane and the participant laboratories is gratefully acknowledged. The EDELWEISS project is supported in part by the Helmholtz Association, by the French Agence Nationale pour la Recherche, by Science and Technology Facilities Council (UK) and the Russian Foundation for Basic Research (grant No. 07-02-00355-a). R&D activities towards EURECA are supported in part by the German ministry of science and education (BMBF Verbundforschung ATP Proj.-Nr. 05A11VK2) and by the Helmholtz Alliance for Astroparticle Phyics (HAP), funded by the Initiative and Networking Fund of the Helmholtz Association,

References

[1] B. Schmidt *et al.* Astrop. Phys. 44, 28 (2013).

[2] A. Broniatowski *et al.* Phys. Lett. **B681** 305 (2009)

[3] E. Armengaud *et al.* Phys. Lett. **B702** 329 (2011).

[4] Z. Ahmed *et al.* Phys. Rev. **D84** 011102(R) (2011).

[5] E. Armengaud *et al.* Phys. Rev. **D86** 051701(R) (2012).

[6] E. Armengaud *et al.* JCAP 11, 67 (2013).

[7] G. Angloher *et al.* Physics of the Dark Universe 3, 41 (2014)

Searching a Dark Photon with HADES

Romain Holzmann[1], *Malgorzata Gumberidze*[2] for the HADES collaboration

[1]GSI Helmholtzzentrum für Schwerionenforschung, 64291 Darmstadt, Germany
[2]Technical University Darmstadt, 64289 Darmstadt, Germany

DOI: http://dx.doi.org/10.3204/DESY-PROC-2014-04/9

The existence of a photon-like massive particle, the γ' or dark photon, is postulated in several extensions of the Standard Model. Such a particle could indeed help to explain the puzzling behavior of the observed cosmic-ray positron fraction as well as to solve the so far unexplained deviation between the measured and calculated values of the muon $g-2$ anomaly. The dark photon, unlike its conventional counterpart, would have mass and would be detectable via its mixing with the latter. We present a search for the e^+e^- decay of such a hypothetical dark photon, also named U boson, in inclusive dielectron spectra measured with HADES in the p (3.5 GeV) + p, Nb reactions, as well as in the Ar (1.756 GeV/u) + KCl reaction. A new upper limit on the kinetic mixing parameter squared (ϵ^2) at 90% CL has been obtained in the mass range $M_U = 0.02 - 0.55$ GeV and is compared here with the present world data set. For masses 0.03 – 0.1 GeV, the limit has been lowered with respect to previous results, allowing to exclude a large part of the parameter space favored by the muon $g-2$ anomaly.

1 Introduction

Observations of the cosmic-ray electron and/or positron flux by ATIC [1], PAMELA [2], HESS [3], Fermi [4], and recently the AMS02 collaboration [5] have revealed an unexpected excess at momenta above 10 GeV, in particular in the positron fraction $e^+/(e^- + e^+)$. These observations cannot easily be reconciled in a consistent way with known astrophysical sources [6] and alternative theoretical explanations have therefore been put forward. In particular, scenarios in which the excess radiation stems from the annihilation of weakly interacting dark matter particles [6, 7] might offer an enticing solution to the puzzle.

To accommodate DM in elementary particle theory and to allow it to interact with visible matter, it has been proposed to supplement the Standard Model (SM) with an additional sector characterized by another $U(1)'$ gauge symmetry [8, 9, 10]. The corresponding vector gauge boson — called U boson, A', γ', or simply dark photon — would thereby mediate the annihilation of DM particles into charged lepton pairs. Indeed, from theoretical arguments a kinetic mixing of the $U(1)'$ and $U(1)$ symmetry groups would follow [11], providing a natural connection between the dark and SM sectors. For that purpose, a mixing parameter ϵ has been introduced [8] relating the respective coupling strengths α‘ and α of the dark and SM photons to visible matter via $\epsilon^2 = \alpha'/\alpha$. Through the $U(1) - U(1)'$ mixing term the U boson would be involved in all processes which include real or virtual photons [12]. On the other hand, any search for a U boson will have to deal with the large unavoidable background from standard QED radiative processes [13], namely any electromagnetic decay leading to lepton pairs. In

recent years, a number of such searches have been conducted in various experiments done in the few-GeV beam energy regime, looking either at e^+e^- pair distributions produced in electron scattering [14, 15] or in the electromagnetic decays of the neutral pion [16] and the ϕ meson [17]. Analyzing data obtained from high-flux neutrino production experiments at CERN [18] and at Serpukhov [19], regions in parameter space ϵ^2 vs. M_U corresponding to a long-lived U have been excluded as well. Note finally, that from the very precisely measured value of the anomalous gyromagnetic factors $(g-2)$ of the muon and electron [20], additional constraints are put on the allowed range of the mixing parameter ϵ and the mass M_U [21, 22].

2 The HADES experiment

The High-Acceptance DiElectron Spectrometer (HADES) operates at the GSI Helmholtzzentrum für Schwerionenforschung in Darmstadt where it uses the few-GeV beams from the heavy-ion synchrotron SIS18. A detailed description of HADES can be found in [23]. In the experiments discussed here a proton beam with a kinetic energy of $E_p = 3.5$ GeV and an average intensity of about 2×10^6 particles per second was used to bombard either a solid 12-fold segmented niobium target (with 2.8% nuclear interaction probability) [24] or a liquid hydrogen target (1% interaction probability) [25]. Likewise, a 1.76 GeV/u Ar beam was used to bombard KCl targets [26]. In the data analysis, electrons and positrons were identified by applying selection cuts to the RICH patterns, pre-shower and energy-loss signals. Charged particles were tracked through the HADES magnetic field and indentified leptons were combined two-by-two to reconstruct the 4-momentum of e^+e^- pairs. A detailed description of this analysis is given in [23, 26].

3 The U-boson search

The search for the U boson can be performed with HADES using all electromagnetic decays typically populated in few-GeV hadronic interactions, that is mostly $\pi^0 \to \gamma U$, $\eta \to \gamma U$, and $\Delta \to NU$, followed by $U \to e^+e^-$. In contrast to previous experiments focusing on a specific decay channel, our search was based on the inclusive measurement of all e^+e^- pairs produced in a given mass range. Because of the expected long lifetime of the U boson, the width of an observable signal is solely determined by the detector resolution.

The present analysis is based on the raw dilepton mass spectra, i.e. spectra not corrected for efficiency and acceptance. The low invariant-mass region of the spectra ($M_{ee} < 0.13\ GeV/c^2$) is dominated by π^0 Dalitz decays, at intermediate masses ($0.13\ GeV/c^2 < M_{ee} < 0.55\ GeV/c^2$), η and Δ Dalitz decays prevail, and the high-mass region is populated mostly by low-energy tails of vector-meson decays [24, 25]. However, as the electromagnetic decay branching ratios decrease with increasing particle mass, resulting in low sensitivity, we restrict our search to $M_U < 0.6\ GeV/c^2$.

Our search for a narrow resonant state in the e^+e^- mass distributions has been conducted in the following way: The dN/dM_{ee} spectra, measured in either of the analyzed reactions, was fitted piece-wise with a model function consisting of a 5^{th}-order polynomial and a Gauss peak of fixed position M_{ee} and fixed width. The adjustment was done by sliding a fit window of width $\pm 4\sigma(M)$ over the spectrum in steps of 3 MeV/c^2. In each step, the fit delivered a parameterization of the local background in presence of a possible Gaussian signal of given width $\sigma(M)$. Consequently, a statistical likelihood-based test must be performed to determine

at a given Confidence Level (CL) an upper limit (UL) for a possible U-boson signal [27]. In our case, background and e^+e^- efficiency corrections are needed to extract an absolute signal yield, and as both are known with limited accuracy only, we have used the method proposed by Rolke, Lopez and Conrad [28] to compute the UL at a confidence level CL=90%. A pair efficiency and acceptance correction factor, $eff \times acc$, has been obtained from detailed simulations and, after having corrected the UL for this factor, the procedure detailed in [29] was used to compute a corresponding upper limit $UL(\epsilon^2)$ on the relative coupling strength ϵ^2 of a hypothetical dark vector boson. Finally, in Fig. 1 we show the HADES result together with a compilation of limits from the searches conducted by KLOE-2 [17], APEX [15], WASA at COSY [16], A1 at MAMI [14], and BaBar [30].

At low masses ($M_U < 0.1\ GeV/c^2$) we clearly improve on the recent result obtained by WASA [16], excluding now to a large degree the parameter range allowed by the muon $g-2$ anomaly. At higher masses, the sensitivity of our search is compatible with, albeit somewhat lower than the combined KLOE-2 analysis of ϕ decays. Our data probe, however, the U-boson coupling in η decays and add hence complementary information. At masses above the η mass, the inclusive dilepton pectrum is fed by Δ (and to some extent heavier baryon resonance) decays which offer only small sensitivity, partly due to the small electromagnetic branching ratio ($BR_{N\gamma} \simeq 10^{-3} - 10^{-2}$) and partly due to the decreasing $BR_{U\to ee}$ at high M_U. Recently, the UL in the high-mass region has been largely improved by an analysis of data obtained by the BaBar experiment, namely $e^+e^- \to e^+e^-$ and $e^+e^- \to \mu^+\mu^-$ [31] (not shown in Fig. 1). On the other hand, at low masses, we expect to lower substantially the UL by including recent HADES data from the 1.23 GeV/u Au+Au reaction in our search.

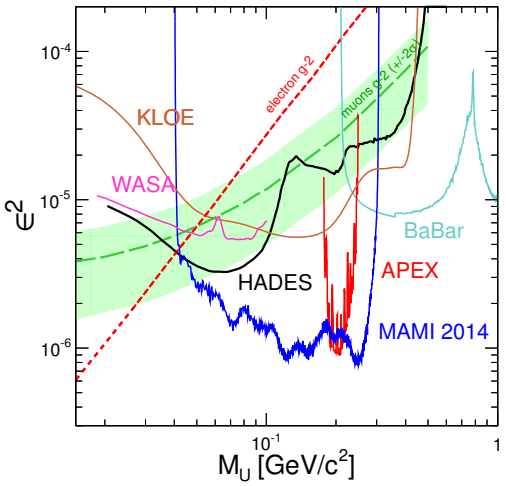

Figure 1: The 90% Cl upper limit on ϵ^2 versus the U-boson mass obtained from the combined analyses of the HADES data (solid black line) in comparison with existing limits from the MAMI/A1, APEX, BaBar, WASA, and KLOE-2 experiments (various colored lines). In addition, the constraints from the muon g-2 anomaly are indicated (green shaded band).

Acknowledgement

The HADES Collaboration gratefully acknowledges support by BMBF grants 06DR9059D, 05P12CRGHE, 06FY171, 06MT238 T5, and 06MT9156 TP5, by HGF VH-NG-330, by DFG

EClust 153, by GSI TMKRUE, by the Hessian LOEWE initiative through HIC for FAIR (Germany), by EMMI GSI, TU Darmstadt (Germany): VH-NG-823, Helmholtz Alliance HA216/ EMMI, by grant GA CR 13-067595 (Czech Rep.), by grant NN202198639 (Poland), Grant UCY/3411-23100 (Cyprus),by CNRS/IN2P3 (France), by INFN (Italy), and by EU contracts RII3-CT-2005-515876 and HP2 227431.

References

[1] J. Chang *et al.*, Nature **456**, 362 (2008).
[2] O. Adriani *et al.*, Nature **458**, 607 (2009).
[3] F. Aharonian *et al.*, Astron. Astrophys. **508**, 561 (2009).
[4] A. Abdo *et al.*, Phys. Rev. Lett. **102**, 181101 (2009).
[5] L. Accardo *et al.* (AMS Collaboration), Phys. Rev. Lett. **113**, 121101 (2014).
[6] I. Cholis, L. Goodenough, N. Weiner, Phys. Rev. D **79**, 123505 (2009).
[7] I. Cholis *et al.*, Phys. Rev. D **80**, 1123518 (2009).
[8] P. Fayet, Phys. Lett. B **95**, 285 (1980).
[9] C. Boehm, P. Fayet, Nucl. Phys. B **683**, 219 (2004).
[10] M. Pospelov, A. Ritz, M. B. Voloshin, Phys. Lett. B **662**, 53 (2008).
[11] B. Holdom, Phys. Lett. B **166**, 196 (1986).
[12] M. Reece, L.-T. Wang, JHEP **0907**, 051 (2009).
[13] L. Landsberg, Phys. Rept. **128**, 301 (1985).
[14] H. Merkel *et al.* (A1 Collaboration), Phys. Rev. Lett. **112**, 221802 (2014).
[15] S. Abrahamyan *et al.* (APEX Collaboration), Phys. Rev. Lett. **107**, 191804 (2011).
[16] P. Adlarson *et al.* (WASA-at-COSY Collaboration), Phys. Lett. B **726**, 187 (2013).
[17] D. Babuski *et al.* (KLOE-2 Collaboration), Phys. Lett. B **720**, 111 (2013).
[18] S. Gninenko, Phys. Rev. D **85**, 055027 (2012).
[19] J. Blümlein, J. Brunner, Phys. Lett. B **731**, 320 (2014).
[20] G.W. Bennett *et al.* (Muon (g-2) Collaboration), Phys. Rev. D **73**, 072003 (2006).
[21] M. Pospelov, Phys. Rev. D **80**, 095002 (2009).
[22] M. Endo, K. Hamaguchi, G. Mishima, Phys. Rev. D **86**, 095029 (2012).
[23] G. Agakishiev *et al.* (HADES Collaboration), Eur. Phys. J. A **41**, 243 (2009).
[24] G. Agakishiev *et al.* (HADES Collaboration), Phys. Lett. B **715**, 304 (2012).
[25] G. Agakishiev *et al.* (HADES Collaboration), Eur. Phys. J. A **48**, 64 (2012).
[26] G. Agakishiev *et al.* (HADES Collaboration), Phys. Rev. C **84**, 014902 (2011).
[27] G. Cowan, K. Cranmer, E. Gross, O. Vitells, Eur. Phys. J. C **71**, 1554 (2011).
[28] W.A. Rolke, A.M. Lopez, J. Conrad, Nucl. Inst. Meth. Phys. Res. A **551**, 493 (2005).
[29] G. Agakishiev *et al.* (HADES Collaboration), Phys. Lett. B **731**, 265 (2014).
[30] B. Aubert *et al.* (BaBar Collaboration), arXiv:0902.2176.
[31] J. P. Lees *et al.* (BaBar Collaboration), arXiv:1406.2980

Chapter 7

Nuclear and particle astrophysics

Magnetic horizons of ultra-high energy cosmic rays

Rafael Alves Batista, Günter Sigl

II. Institute for Theoretical Physics, University of Hamburg
Luruper Chaussee, 149, 22761 Hamburg, Germany

DOI: http://dx.doi.org/10.3204/DESY-PROC-2014-04/127

The propagation of ultra-high energy cosmic rays in extragalactic magnetic fields can be diffusive, depending on the strength and properties of the fields. In some cases the propagation time of the particles can be comparable to the age of the universe, causing a suppression in the flux measured on Earth. In this work we use magnetic field distributions from cosmological simulations to assess the existence of a magnetic horizon at energies around 10^{18} eV.

1 Introduction

During their propagation ultra-high energy cosmic rays (UHECRs) can be deflected by the intervening cosmic magnetic fields, namely the extragalactic and galactic. The extragalactic magnetic field has different strengths in different regions of the universe. For instance, in the center of clusters of galaxies it is $\sim$10 μG, with coherence length of the order of 10 kpc. The existence of magnetic fields in the voids is still controversial [1], but there are some indications that they can be $\sim 10^{-15}$-10^{-12} G, with typical coherence lengths of the order of 1 Mpc [1].

The propagation of cosmic rays in the extragalactic magnetic fields can be diffusive if the scattering length is much smaller than the distance from the source to the observer. Depending on the magnetic field strength and diffusion length, a significant fraction of these particles can have trajectory lengths comparable to the Hubble radius. In this case, a suppression in the flux of cosmic rays is expected compared to the case in which magnetic fields are absent, leading to the existence of a magnetic horizon for the propagation of cosmic rays. This effect has been previously studied by many authors, including Mollerach & Roulet [2], who developed a parametrization for it, under the assumption of Kolmogorov turbulence. In this work we generalize their result for the case of inhomogeneous extragalactic magnetic fields.

2 Magnetic suppression

The diffusive cosmic ray spectrum for an expanding universe can be written as [3]

$$j(E) = \frac{c}{4\pi} \int_0^{z_{max}} dz \left|\frac{dt}{dz}\right| Q(E_g(E,z),z) \frac{dE_g}{dE} \left(\int_0^{\infty} dB \frac{1}{N_s} \sum_{i=0}^{N_s} \frac{\exp\left(-\frac{r_g^2}{\lambda^2}\right)}{(4\pi\lambda^2)^{3/2}} p(B) \right), \quad (1)$$

where $p(B)$ is the probability distribution of the magnetic field strength B, r_g is the comoving distance of the source and λ is the so-called Syrovatskii variable, given by:

$$\lambda^2(E,z,B) = \int_0^z dz' \left|\frac{dt}{dz'}\right| \frac{1}{a^2(z')} \left[\frac{c l_c(z)}{3} \left(a_L \left(\frac{E}{E_c(z,B)} \right)^{\frac{1}{3}} + a_H \left(\frac{E}{E_c(z,B)} \right)^2 \right) \right], \quad (2)$$

with $a = 1/1+z$ being the scale factor of the universe and $l_c(z) = l_{c,0}a(z)$ the coherence length of the field at redshift z. The parameters a_L and a_H are, respectively, 0.3 and 4. E_c is the critical energy, defined as the energy for which a particle has a Larmor radius equal to the coherence length of the magnetic field. The probability distribution functions can be obtained from magnetohydrodynamical (MHD) simulations of the local universe. In this work we considered four different cosmological simulations, namely the ones performed by Miniati [4], Dolag *et al.* [5], Das *et al.* [6], Donnert *et al.* [7].

If the term in parentheses in equation 1 is equal to 1, then the magnetic field dependence will vanish and the shape of the spectrum will be independent of the modes of propagation. This result is known as the propagation theorem [8], and states that if the separation between the sources in a uniform distribution is much smaller than the characteristic propagation lengths, the UHECR spectrum will have a universal shape. This spectrum (j_0) will be henceforth called universal.

We have not considered the actual time evolution of these cosmological simulations. Instead we assume a magnetic field distribution at $z = 0$ and extrapolate it to higher redshifts: $B = B_0(1+z)^{2-m}$, with m designating the evolution parameter. Moreover, we assume a Kolmogorov magnetic field with strengths taken from the simulations.

The suppression factor G can be written as:

$$G = \frac{j(E)}{j_0(E)} \approx \exp\left[-\frac{(aX_s)^\alpha}{x^\alpha + bx^\beta} \right], \quad (3)$$

with $x \equiv E/\langle E_c \rangle$, α, β, a and b the best fit parameters obtained by fitting $j(E)/j_0(E)$ with the function in the right-hand side of the equation. The complete list of best fit parameters for these extragalactic magnetic field models can be found in ref. [9]. In this expression $X_s = d_s/\sqrt{R_H l_c}$, where d_s is the source separation and R_H the Hubble radius.

3 Magnetic horizons

In this work the magnetic horizon is defined as the mean distance that a cosmic ray can propagate away from the source in a Hubble time. In figure 1 $\lambda/\sqrt{R_H l_c}$ is displayed as a function of the redshift. In this case λ can be understood as the average distance a particle can

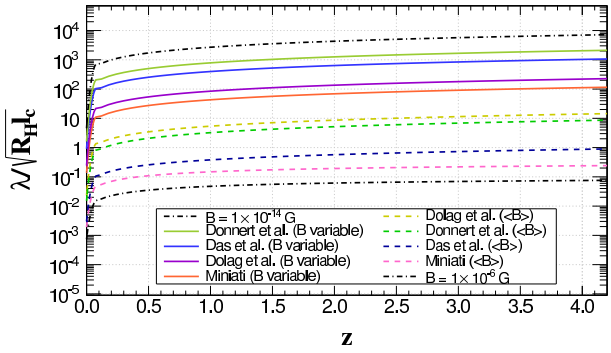

Figure 1: Volume-averaged Syrovatskii variable for an E/Z =10^{16} eV, m =1, γ =2 and z_{max} =4. Solid lines correspond to the extragalactic magnetic field distribution, dashed lines correspond to the values obtained using the mean magnetic field strengths obtained from these models, and dotted dashed lines are two limiting cases with high and low magnetic field strengths.

propagate away from the source in a time interval corresponding to a redshift z. In this figure we notice that the magnetic horizons for the case of extragalactic magnetic field distributions from cosmological simulations are larger compared to the case of a Kolmogorov turbulent field with B_{rms} equal to the mean magnetic field strength from the distributions. This happens due to the fact that the voids fill most of the volume, dominating the magnetic field distribution and hence the volume-averaged Syrovatskii variable.

We can calculate the energy (E_e) for which the suppression factor is $G = 1/e \approx 0.37$ of its original value, as a function of the coherence length. The results are shown in figure 2.

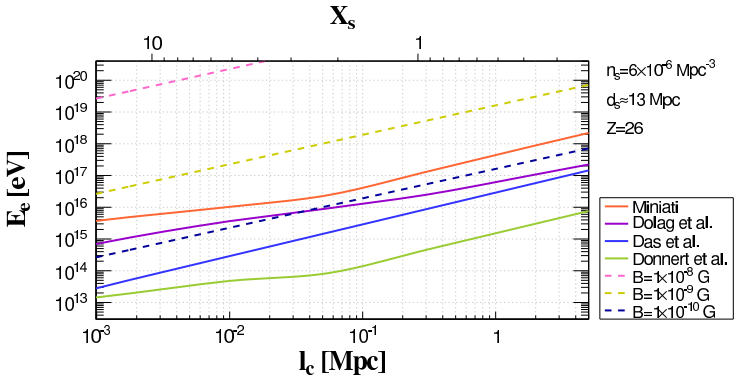

Figure 2: Upper limit on the energy for which the flux of cosmic rays is suppressed to $1/e$ (≈37%) of its former value, as a function of the coherence length. Solid lines correspond to the indicated extragalactic magnetic field model, and dashed lines to constant magnetic field strengths. This particular case is for a source density of 6×10^{-6} Mpc^{-3} and Z=26.

The magnetic suppression due to magnetic horizon effects starts to become relevant for $E \lesssim 10^{17}$ eV, for the most optimistic choice of parameters (heavy composition, large coherence

length and low source density). The curves in figure 2 reflect the behavior of the diffusion coefficient, shown in equation 2 within square brackets, which is proportional to l_c^{-1} for small values of the coherence length, and to $l_c^{2/3}$ for large l_c.

4 Discussion and outlook

We have parametrized the suppression of the cosmic ray flux at energies $\lesssim$Z$\times 10^{18}$ eV. The method to obtain this parametrization can be adapted to any magnetic field distribution from cosmological simulations (for details see ref. [9]). Moreover, we have also derived upper limits for this suppression to occur, as a function of the coherence length.

The results here described suggest that the suppression sets in at energies below $\sim 10^{17}$ eV. This has profound implications for the interpretation of current experimental data. For instance, recently there has been several attempts [10, 11] to perform a combined spectrum-composition fit to data from the Pierre Auger Observatory [12, 13]. These results indicate that the spectral indexes of the sources are hard ($\gamma \sim$1.0-1.6), which contradicts the current acceleration paradigm, in which UHECRs are accelerated to the highest energies through Fermi-like mechanisms ($\gamma \sim$2.0-2.2). In ref. [2] it was shown that the existence of a magnetic horizon around 10^{18} eV can affect the results of these combined fits, softening the spectral index to $\gamma \sim 2$. We have shown that if one considers a more realistic extragalactic magnetic field model, the contribution of the voids is dominant and since the field strengths in these regions are low, the suppression will also be small compared to the case of a simple Kolmogorov turbulent magnetic field. In this case, the combined spectrum-composition fits would again favor scenarios in which the sources have hard spectral index.

Acknowledgements

RAB acknowledges the support from the Forschungs- und Wissenschaftsstiftung Hamburg. GS was supported by the State of Hamburg, through the Collaborative Research program "Connecting Particles with the Cosmos" and by BMBF under grant 05A11GU1.

References

[1] A. Neronov and I. Vovk, Science **328** 73 (2010)
[2] S. Mollerach and E. Roulet, JCAP **10** 13 (2013)
[3] V. Berezinsky and A. Z. Gazizov, Astrophys. J. **643** 8 (2013)
[4] F. Miniati, MNRAS **337** 199 (2002)
[5] K. Dolag *et al.*, JCAP **1** 9 (2005)
[6] S. Das *et al.*, Astrophys. J. **682** 29 (2008)
[7] J. Donnert *et al.*, MNRAS **392** 1008 (2009)
[8] R. Aloisio and V. Berezinsky, Astrophys. J. **612** 900 (2004)
[9] R. Alves Batista and G. Sigl, JCAP **11** 031 (2014)
[10] R. Aloisio, V. Berezinsky and P. Blasi. JCAP **10** 020 (2014)
[11] A. Taylor, Astropart. Phys. **54** 48 (2014)
[12] Pierre Auger Collaboration, Phys. Lett. B **685** 239 (2010)
[13] Pierre Auger Collaboration. arXiv:1409.5083 (*to appear in Phys. Rev. D*)

Core-collapse supernova simulation using Λ hyperon EoS with density-dependent couplings

Sarmistha Banik[1], *Prasanta Char*[2]

[1]BITS Pilani, Hyderabad Campus, Shamirpet Mondal, Hyderabad-500078, India
[2]Astroparticle Physics & Cosmology Division,Saha Institute of Nuclear Physics, 1/AF Bidhan nagar, Kolkata-700064, India.

DOI: http://dx.doi.org/10.3204/DEFY-KROC-2014-04/115

Recently we generated an equation of state (EoS) table of dense matter relevant to neutron star and supernova with Λ hyperons. We use this EoS to investigate the role of strange hyperons in the dynamical collapse of a non-rotating massive star to a black hole(BH) using 1D General relativistic simulation $GR1D$. We follow the dynamical formation and collapse of the protoneutron star (PNS) from the gravitational collapse of a massive progenitor, adopting this EoS table.

1 Introduction

Neutron stars are born in the aftermath of massive stars ($> 8M_{\odot}$) through the core-collapse supernova (CCSN) explosions in the penultimate stage of their evolution. The fate of the compact object depends on the EoS and the amount of infalling material. In addition to the nucleons and nuclear matter, several novel phases with large strangeness fraction such as, hyperon matter, and quark phase, and Bose-Einstein condensates of antikaons are theoretically predicted in the early post-bounce phase of a core-collapse supernova. There are several exotic EoS, including quark and hyperons, for supernova simulations. However, none of them are within the observational constraints of $2M_{\odot}$ neutron stars [1, 2].

The Banik, Hempel and Bandyopadhyay (BHB) EoS is the first realistic EoS table involving hyperons [3] that is compatible with the recent observations. It is based on the density-dependent relativistic mean field model (DD2). The model is exploited to describe the uniform and non-uniform matter in a consistent manner. Further, light and heavy nuclei along with interacting nucleons are treated in the nuclear statistical equilibrium (NSE) model of Hempel and Schaffner-Bielich (HS) which includes excluded volume effects and DD relativistic interactions [4]. We considered only Λ hyperons and exclude other hyperons such as Σ and Ξ, due to scarcity of experimental data about their potential depth values in nuclear matter.

The presence of exotic particles may have considerable effect on the core collapse supernova explosions. It was earlier reported that hyperons appear just after the core bounce. And they trigger the BH formation, but fail to generate the second shock because the EoS is softened too much with their appearance [5]. These studies were carried out with the hyperonic EoS of Shen et. al. [6], which do not conform to the the observational mass limit of neutron star.

In this paper, we follow the dynamical formation and evolution of a PNS beginning from the onset of core collapse adopting our BHB EoS table[3]. We report the effect of hyperons on the

black hole formation using the spherically-symmetric general relativistic hydrodynamic code, $GR1D$[7]. We use both the variants of BHB hyperonic EoS tables. In one case the repulsive hyperon-hyperon interaction is mediated by the strange ϕ mesons [BHB$\Lambda\phi$] and in the second case ϕ mesons are not considered [BHBΛ]. We also compare these results with nucleon-only EoS, that we denote by HS(DD2).

2 The equation of state and the numerical simulations

The BHB EoS table is based on a density dependent (DD2) relativistic hadron field theory [8, 9], where baryon-baryon interaction is mediated by σ, ω, ρ mesons. The additional ϕ mesons take care of the hyperon-hyperon couplings. The density-dependence of the couplings gives rise to a rearrangement term in baryon chemical potential that on the other hand, changes the pressure. Thus the EoS is significantly changed at higher densities. Nuclear symmetry energy is another important parameter that controls the stiffness of the EoS. The symmetry energy and its density dependence near the saturation density n_0 are denoted by $S_\nu = E_{sym}(n_0)$ and slope parameter $L = 3n_0 dE_{sym}/dn|_{n=n_0,T=0}$. The DD2 model, with $S_\nu = 31.67$ MeV and $L = 55.04$ MeV, are fully consistent with the experimental and observational constraints [8]. The BHB$\Lambda(\phi)$ EoS table covers a broad range of density ($\sim 10^{3.22} - 10^{15.22(15.3)}$ g/cm^3), temperature($T =$ 0.01 to 158.48 MeV) and charge-to-baryon number ratio ($Y_p = 0$ to 0.60) [3].

The matter consists of nuclei, (anti)neutrons , (anti)protons, (anti) Λ hyperons, and photons at different regions. Electrons and positrons form a uniform background; contribution of neutrinos and muons are not taken into account in the calculations. In the DD2 parameter set, the nuclear matter saturation density is 0.149065fm^{-3}, binding energy 16.02MeV, incompressibility of matter 242.7MeV and symmetry energy 31.67MeV. The effective Dirac mass (m*/m) of neutron and proton are 0.5628 and 0.5622 respectively. For the Λ, the experimental mass value is 1115.7MeV, and the potential depth in nuclear matter is -30MeV.

We use the open source code $GR1D$ [7] for the supernova simulations. $GR1D$ is a spherically-symmetric, general-relativistic Eulerian hydrodynamics code for low and intermediate mass progenitors. It is designed to follow the evolution of stars beginning from the onset of core collapse to black hole formation for different zero age main sequence(ZAMS) progenitors.

3 Result & Discussions

We report our simulation results for a $40M_\odot$ progenitor model of Woosley et. al [10] using GR1D [7] for BHB EoS. We solved the Tolman-Oppenheimer-Volkov equation for zero temperature (T=0) β-equilibrated matter. The maximum mass of the neutron star for nucleon-only HS(DD2) EoS is $2.42M_\odot$, whereas for BHB$\Lambda(\phi)$ EoS, the maximum mass reduces to $1.95(2.1)M_\odot$. The corresponding radii are 11.9 km and 11.7(11.6) km respectively [9, 3].

Fig. 1 shows the plot of the baryonic and gravitational mass of PNS, obtained from simulations. The maximum mass is higher than that of NS. When accretion pushes PNS over its maximum mass, a BH is formed. The spike in the gravitational mass correspond to a blow-up and the BH formation. For the HS(DD2) EoS(solid line), this happens for a $2.47M_\odot$ star at 0.94 sec after bounce, whereas for BHB$\Lambda(\phi)$ EoS (the dashed line, colour online) this happens much earlier at 0.55 sec after bounce for a $2.25M_\odot$ star.

Figs. 2 and 3 show the evolution of central density (ρ_c) and temperature (T) for the nucleon-only HS(DD2) (solid lines) and BHB$\Lambda(\phi)$ EoS (dashed lines) respectively. The bounce

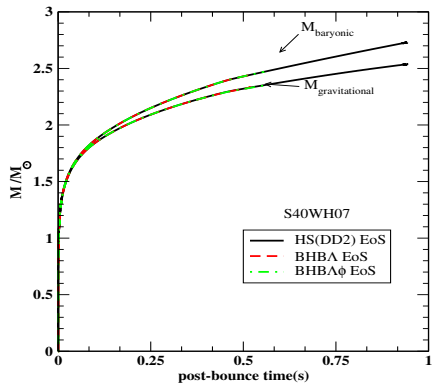

Figure 1: Post-bounce evolution of baryonic mass and gravitational mass.

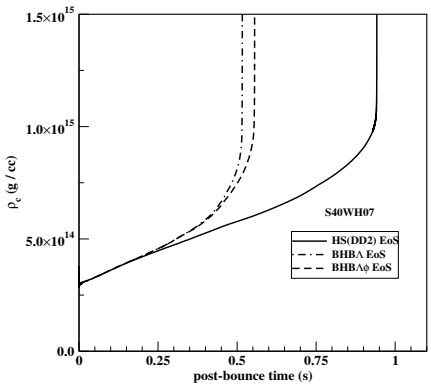

Figure 2: Central density as a function of post-bounce time.

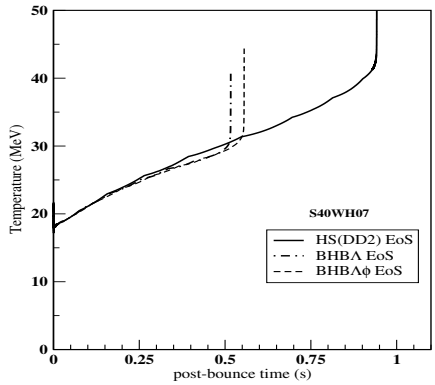

Figure 3: Temperature as a function of post-bounce time.

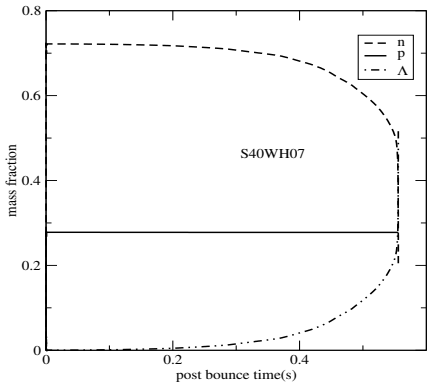

Figure 4: Mass fractions of various species are plotted as a function of post-bounce time.

corresponds to the spikes at real timeline $t_{bounce} = 0.321$sec, which we take as t=0 in the figure. The value of t_{bounce} is same for the HS(DD2) and BHBΛ(ϕ) cases; the hyperons do not appear at that density as evident from the mass fraction graph (Fig. 3). The onset of BH formation is marked by a sharp rise in the value of central density as well as the temperature profile. Owing to the hyperon emergence, the contraction of PNS is accelerated, which leads to quicker rise in temperature and central density. Or in other words, the stiffer EoS leads to larger post-bounce time to BH-formation.

In Fig. 4, we show the compositions of PNS. Initially at core bounce the system consists of neutron and protons only, hyperons appears first at 0.16 sec after core bounce. As soon as the Λ hyperons populate, they replace the neutrons. And the central density that was just above normal nuclear matter density at bounce rises to $\sim 4 \times 10^{14} gm/cm^{-3}$ and the temperature rises to $\sim$ 23MeV.

4 Summary

We studied the effect of hadron-hyperon phase transition in core-collapse supernova using general relativistic hydrodynamic simulation GR1D [7]. By following the dynamical collapse of a new-born proto-neutron star from the gravitational collapse of a $40M_{\odot}$ star adopting the BHB hyperonic EoS table [3], we noticed that hyperons appear just before bounce. It appears off center at first due to high temperature and prevails at the center just before the black hole formation, when the density becomes quite high. Also the presence of hyperons triggers the early BH formation, compared to nucleon-only case.

Acknowledgments

SB acknowledges the financial support from Department of Science & Technology, India, BITS Pilani, Hyderabad and Alexander von Humboldt Foundation.

References

[1] P. B. Demorest, T. Pennucci,S. M. Ransom, M. S. E. Roberts & J. W. T. Hessels, Nature **467** 1081 (2010).

[2] J. Antoniadis et. al., Science **340**, 6131 (2013).

[3] S. Banik, M. Hempel, D. Bandyopadhyay, Astrophy. Suppl. J, **214** 22 (2014).

[4] M. Hempel and J. Schaffner-Bielich, Nucl. Phys. A **837** 210 (2010).

[5] S. Banik, Phy. Rev. **C 89** 035807 (2014).

[6] H. Shen, H. Toki, K. Oyamatsu, K. Sumiyoshi, Astrophy. Suppl. J, **197**, Issue 2, 14 pp. (2011).

[7] C. D. Ott and E. O'Connor, Class. Quant. Grav.**27** 114103 (2010).

[8] S. Typel, G. Röpke, T. Klähn, D. Blaschke and H.H. Wolter, Phys. Rev.**C 81** 015803 (2010).

[9] P. Char, S. Banik, Phy Rev **C90** 015801 (2014).

[10] S. E. Woosley, A. Heger, and T. A. Weaver, Rev. Mod. Phys. **74** 1015 (2002).

Investigation of the rotation effects on high–density matter in hybrid stars

Tomoki Endo

Division of Physics, Department of General Education, National Institute of Technology, Kagawa College, 355 Chokushi-cho, Takamatu, Kagawa 761-8058, Japan

DOI: http://dx.doi.org/10.3204/DESY-PROC-2014-04/98

The equation of state (EOS) of high-density matter is still not clear and several recent observations indicate restrictions to EOSs. Theoretical studies should thus elucidate EOSs at high density and/or high temperature. Many theoretical studies have attempted to account for the effect of rotation of rapidly rotating neutron stars (pulsars), which are commonly observed astronomical objects having high-density interiors. Furthermore, neutron stars generate a strong magnetic field. Several recent studies indicate that this magnetic field exerts some restrictions on the EOS. Theoretical studies should thus incorporate these effects. In this paper, we focus on the effect of rotation. We find that one of our EOSs is consistent with these observations, and another is inconsistent. We also find an important relation between radius and rotation.

1 Introduction

It is widely believed that quark matter exists in high-temperature and/or high-density environments such as those of relativistic heavy-ion collisions [1] or the cores of neutron stars [2, 3], and the "deconfinement transition" has been actively searched. Theoretical studies using model calculations or based on the first principle, lattice QCD [4] have been also carried out by many authors to find the critical temperature of the deconfinement transition. Although many exciting results have been reported, the deconfinement transition is not yet clearly understood. Many theoretical studies have suggested that the deconfinement transition is of first order in high-density cold matter [5, 6]. We thus assume that it is a first-order phase transition in the present work. We have given the equation of state (EOS) for the hadron–quark mixed phase taking into account the charge screening effect [7] without making any approximations. We have investigated the inner structures of neutron stars as environments of quark matter [8, 9]. Recently, many theoretical studies have attempted to account for the effect of the rotation of neutron stars [10, 11, 12, 13]. The results suggest that observations restrict the EOSs of theoretical calculations. Other studies have given the effect of the magnetic field [14, 15, 16, 17] and it would thus be interesting to account for the magnetic effect in our EOS. However, as a first step, we focus on the effect of rotation. We thus apply our EOS to a stationary rotating star in this paper.

2 Formalism and Numerical Results

Our formulation was presented in detail in Ref. [7, 8] and is only briefly explained here. The quark phase consists of u, d, and s quarks and the electron. We incorporate the MIT bag model and assume a sharp boundary at the hadron–quark interface. u and d quarks are treated as massless and s as having mass ($m_s = 150$MeV), and the quarks interact with each other via a one-gluon-exchange interaction inside the bag. The hadron phase consists of the proton, neutron and electron. The effective potential is used to describe the interaction between nucleons and to reproduce the saturation properties of nuclear matter. In treating the phase transition, we have to consider the thermodynamic potential. The total thermodynamic potential ($\Omega_{\rm total}$) consists of hadron, quark and electron contributions and the surface contribution:

$$\Omega_{\rm total} = \Omega_{\rm H} + \Omega_{\rm Q} + \Omega_{\rm S}, \tag{1}$$

where $\Omega_{\rm H(Q)}$ denotes the contribution of the hadron (quark) phase. We here introduce the surface contribution $\Omega_{\rm S}$, parameterized by the surface tension parameter σ, $\Omega_{\rm S} = \sigma S$, with S being the area of the interface. Note that $\Omega_{\rm S}$ may be closely related with the confining mechanism and unfortunately we have no definite idea about how to incorporate it. Many authors have treated its strength as a free parameter and investigated how its value affects results [18, 19, 20]. We take the same approach in this study. To determine the charge screening effect, we also make calculations without the screening effect [7, 21, 22]. We then apply the EOS derived in our paper [7] to the Tolman–Oppenheimer–Volkoff equation [8, 9]. We finally apply our EOS to a stationary rotating star. However, it is difficult to consider the rotation effect in general relativity. We therefore make assumptions of 1) stationary rigid rotation ("uniform rotation"), 2) axial symmetry with respect to the spin axis; and 3) the matter being a perfect fluid. Stationary rotation in general relativity has been reviewed in [23] and [10]; we follow their calculation. We then apply our EOS to a stationary rotating star.

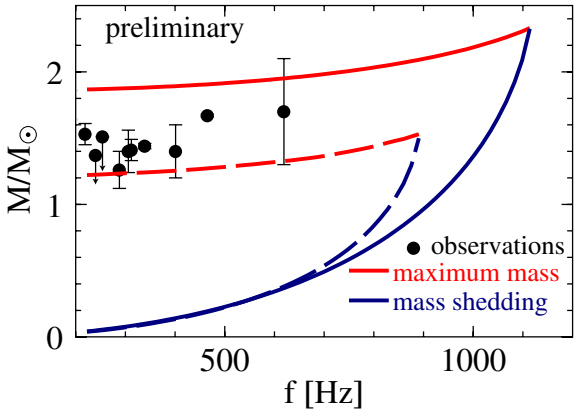

Figure 1: (Color online) Mass–frequency relation obtained with our models plotted against the observational data listed in [10]. The solid and dashed curves represent the results obtained with and without screening, respectively.

Figure 1 shows the result for a rotating star obtained using our EOSs with and without screening. The red curve shows the maximum mass of the star and the blue curve shows

the mass-shedding curve, which corresponds to the Kepler frequency. The Kepler frequency indicates that the centrifugal force is equal in magnitude to gravity. Therefore, the area on the right-hand side of the blue curve is physically invalid. If the red curve is lower than the observations, the EOS should be ruled out. Our EOS in the screening case is thus consistent with these observations. However, our EOS without screening is not consistent and therefore inappropriate. This could be due to the softness of the EOS [10], although further studies are required.

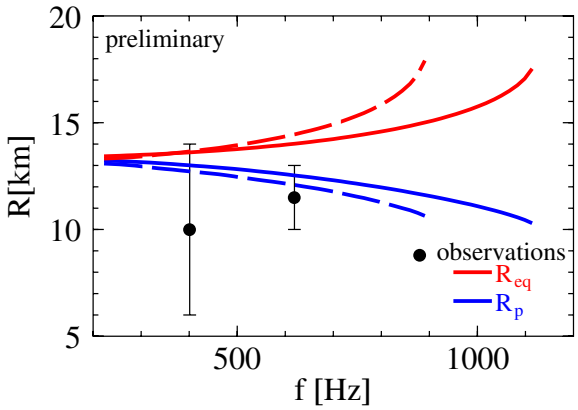

Figure 2: (Color online) Radius–frequency relation of our model plotted against observational data (SAXJ1808.4-3658 and 4U1608-52). The solid and dashed curves represent the results obtained with and without screening, respectively.

Figure 2 suggests an important relation between the radius and rotation. The radius of a star is considered a single value because we ordinarily consider a star approximately spherical. However, if the star is rapidly rotating, it is an ellipse rather than a sphere, and we have to recognize the different radii. Therefore, we introduce two values, R_{eq} and $R_{\rm p}$, which are the equatorial radius and polar radius, respectively. Figure 2 shows R_{eq} and $R_{\rm p}$ with respect to rotation. If the rotation rate is 400 Hz or higher, the two radii are different. We thus have to note the effects of rotation on rapidly rotating stars.

3 Summary and Concluding Remarks

We presented the difference between EOSs with and without charge screening taking into account rotation effects. We used a simple model for quark matter and hadron matter. To obtain a more realistic picture of the hadron–quark phase transition, we need to take into account color superconductivity [20, 24, 25] and relativistic mean field theory [26]. A neutron star has another interesting feature—its magnetic field. The origin of the magnetic field is still unknown. A magnetic field can be explained by the spin-polarization of quark matter [27, 28], but whether quark matter exists strongly depends on the EOS. In this paper, we did not include magnetic fields. Several recent studies have investigated the effect of the magnetic field on the EOS [14, 15, 16, 17]. Interesting results would be obtained if we took into account both the magnetic field and rotation effects.

Acknowledgments

This work was supported in part by a Principal Grant from the National Institute of Technology, Kagawa College.

References

[1] K. Adcox *et al.*, (PHENIX collaboration), Phys. Rev. Lett. **88** 022301 (2002); C. Adler *et al.*, (STAR collaboration), Phys. Rev. Lett. **90** 082302 (2003).

[2] J. Madsen, Lect. Notes Phys. **516** 162 (1999).

[3] K. S. Cheng, Z. G. Dai and T. Lu, Int. Mod. Phys. **D7** 139 (1998).

[4] For review, D. H. Rischke, Prog. Part. Nucl. Phys. **52** (2004) 197; J. Macher and J. Schaffner-Bielich, Eur. J. Phys. **26** 341 (2005) and references therein.

[5] R. D. Pisalski and F. Wilczek, Phys. Rev. Lett. **29** 338 (1984).

[6] R. V. Gavai, J. Potvin and S. Sanielevici, Phys. Rev. Lett. **58** 2519 (1987).

[7] T. Endo, T. Maruyama, S. Chiba and T. Tatsumi, Prog. Theor. Phys. **115** 337 (2006); hep-ph/0510279.

[8] T. Endo, Phys. Rev. **C83** 068801 (2011).

[9] T. Endo, arXiv:1310.0913[astro-ph.HE].

[10] A. Kurkela, P. Romatschke, A. Vuorinen and B. Wu, arXiv:1006.4062[astro-ph.HE].

[11] M. Orsaria, H. Rodrigues, F. Weber and G.A. Contrera, Phys. Rev. **D87** 023001 (2013).

[12] F. Weber, M. Orsaria and R. Negreiros, arXiv:1307.1103[astro-ph.SR]

[13] R. Belvedere, K. Boshkayev, J. A. Rueda, and R. Ruffini, arXiv:1307.2836[astro-ph.SR]

[14] V. Dexheimer, R. Negreiros and S. Schramm, arXiv:1108.4479[astro-ph.HE].

[15] C. Chirenti, and J. Skakalala, Phys. Rev. **D88** 104018 (2013).

[16] R. Aguirre, E. Bauer and I. Vidana, Phys. Rev. **C89** 035809 (2014).

[17] R. Mallick and S. Schramm, Phys. Rev. **C89** 045805 (2014).

[18] H. Heiselberg, C. J. Pethick and E. F. Staubo, Phys. Rev. Lett. **70** 1355 (1993).

[19] N. K. Glendenning and S. Pei, Phys. Rev. **C52** 2250 (1995).

[20] M. Alford, K. Rajagopal, S. Reddy, and F. Wilczek, Phys. Rev. **D64** 074017 (2001).

[21] Toshiki Maruyama, T. Tatsumi, D.N. Voskresensky, T. Tanigawa, T. Endo and S. Chiba, Phys. Rev. **C73** 035802 (2006); nucl-th/0505063.

[22] T. Maruyama, T. Tatsumi, T. Endo and S. Chiba, Recent Res. Devel. Phys. **7** 1 (2006); nucl-th/0605075

[23] N. Stergioulas and J.L. Friedman, Astrophys. J. **444** 306 (1995).

[24] For reviews, M. Alford, A. Schmitt, K. Rajagopal and T. Schäfer, Rev. Mord. Phys. **80** 1455 (2008).

[25] M. Alford and S. Reddy, Phys. Rev. **D67** 074024 (2003).

[26] H. Shen, H. Toki, K. Oyamatsu and K. Sumiyoshi, Nucl. Phys. **A637** 435 (1998).

[27] T. Tatsumi, Phys. Lett. **B489** 280 (2000).

[28] T. Tatsumi, arXiv:1107.0807[hep-ph].

LHCf: Very forward measurement at LHC p-p and p-Pb

H. Menjo[1], *O. Adriani*[2,3], *E. Berti*[2,3], *L. Bonechi*[2], *M. Bongi*[2,3], *G. Castellini*[4], *R. D'Alessandro*[2,3], *M. Del Prete*[2,3], *M. Haguenauer*[5], *Y. Itow*[6,7], *K. Kasahara*[8], *K. Kawade*[6], *Y. Makino*[6], *K. Masuda*[6], *E. Matsubayashi*[6], *G. Mitsuka*[6], *Y. Muraki*[6], *P. Papini*[2], *A-L. Perrot*[9], *D. Pfeiffer*[9], *S. Ricciarini*[2,4], *T. Sako*[6,7], *Y. Shimizu*[10], *Y. Sugiura*[6], *T. Suzuki*[8], *T.Tamura*[11], *A. Tiberio*[2,3], *S. Torii*[8], *A. Tricomi*[12,13], *W.C. Turner*[14], *Q. Zhou*[6]

[1] Graduate school of Science, Nagoya University, Japan
[2] INFN Section of Florence, Italy
[3] Physics and Astronomy Department, University of Florence, Italy
[4] IFAC-CNR, Italy
[5] Ecole-Polytechnique, France
[6] Solar-Terrestrial Environment Laboratory, Nagoya University, Japan
[7] Kobayashi-Maskawa Institute for the Origin of Particles and the Universe, Nagoya University, Japan
[8] RISE, Waseda University, Japan
[9] CERN, Switzerland
[10] JAXA, Japan
[11] Kanagawa University, Japan
[12] INFN Section of Catania, Italy
[13] University of Catania, Italy
[14] LBNL, Berkeley, USA

DOI: http://dx.doi.org/10.3204/DESY-PROC-2014-04/94

The LHCf experiment is an LHC experiment dedicated to measurement of very forward neutral-particle spectra with the aim of improving hadronic interaction model used in MC simulation of cosmic-ray induced air showers. The LHCf have completed the physics plans for $\sqrt{s}$ = 0.9 and 7 TeV p-p collisions in 2010 and for $\sqrt{s_{NN}}$ = 5.02 p-Pb collisions in 2013. The LHCf have another operation with the increased collision energy of 13 TeV in 2015. The recent LHCf result of forward neutron energy spectra at 7 TeV p-p and forward π^0 spectra at p-Pb are presented in this paper.

1 LHCf experiment

The LHCf experiment is one of the LHC forward experiments. The aim is to provide critical calibration data of hadronic interaction models used in MC simulation of air showers induced by cosmic-rays with measuring the production spectra of neutral secondary particles at the very forward region of LHC collisions. The most of energetic particles produced at collisions emit into the forward region and the energy flux of secondaries concentrates on the region although the multiplicity concentrates on the central region of collisions which are covered by the central

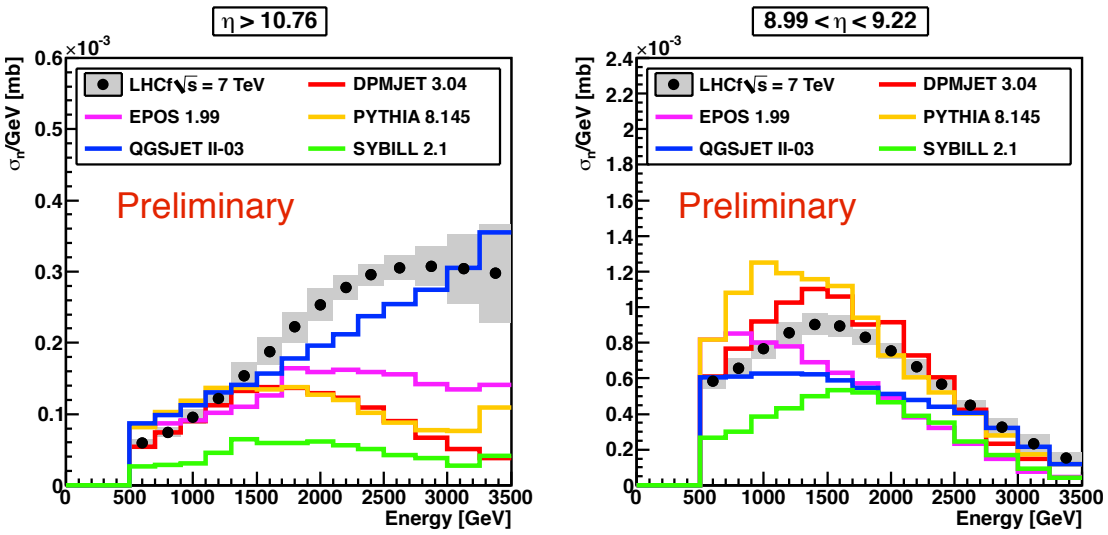

Figure 1: Forward neutron energy spectra at $\sqrt{s} = 7$ TeV p-p collisions measured in $\eta > 10.76$ (left) and $8.99 < \eta < 9.22$ (right) [6]. The black dots and the shaded area show LHCf data and the uncertainties. The color lines indicate the predictions by several hadron interaction models[7, 8, 9, 10, 11].

detectors like ATLAS.
The LHCf have two independent detectors, so called Arm1 and Arm2, which were installed +/- 140m from the ATLAS interaction point (IP1). Each detector has two sampling and imaging calorimeter towers which are consisted of tungsten plates, 16 scintillator layers for shower sampling and four position sensitive layers for measurement of shower position. The position sensitive layers were developed with deferent techniques of X-Y scintillating fiber hodoscopes and X-Y silicon strip detectors for Arm1 and Arm2, respectively. The transverse cross sections of calorimeters are $20{\times}20\,\mathrm{mm}^2$ and $40{\times}40\,\mathrm{mm}^2$ in Arm1 and $25{\times}25\,\mathrm{mm}^2$ and $32{\times}32\,\mathrm{mm}^2$ in Arm2. The energy resolution of detectors are about 5 % for photons and 40 % for neutrons. The position resolution is better than $200\,\mu$m for photons and a few mm for neutrons. More details of the detector performance were reported elsewhere [1, 2].
The LHCf have successfully completed the operation with proton-proton collisions at $\sqrt{s} = 0.9$, 7 TeV in 2010 and the operation with proton-lead collisions at $\sqrt{s_{NN}} = 5.02$ TeV in 2013. The forward photon and π^0 spectra at proton-proton collisions has been published [3, 4, 5].

2 Neutron spectrum in $\sqrt{s} = 7$ TeV p-p collisions

The measurement of neutron energy spectum is a way to access one of the key parameters for air-shower development, inelasticity of hadronic interaction. The parameter is estimated from the energy of leading baryons in collisions. The LHCf detectors are able to measure neutral hadrons, mostly neutrons, with 40% energy resolution and 1 mm position resolution. Events with hadron induced showers are well identified with parameters calculated from longitudinal developments of showers. Figure 1 shows the preliminary result of neutron energy spectra after

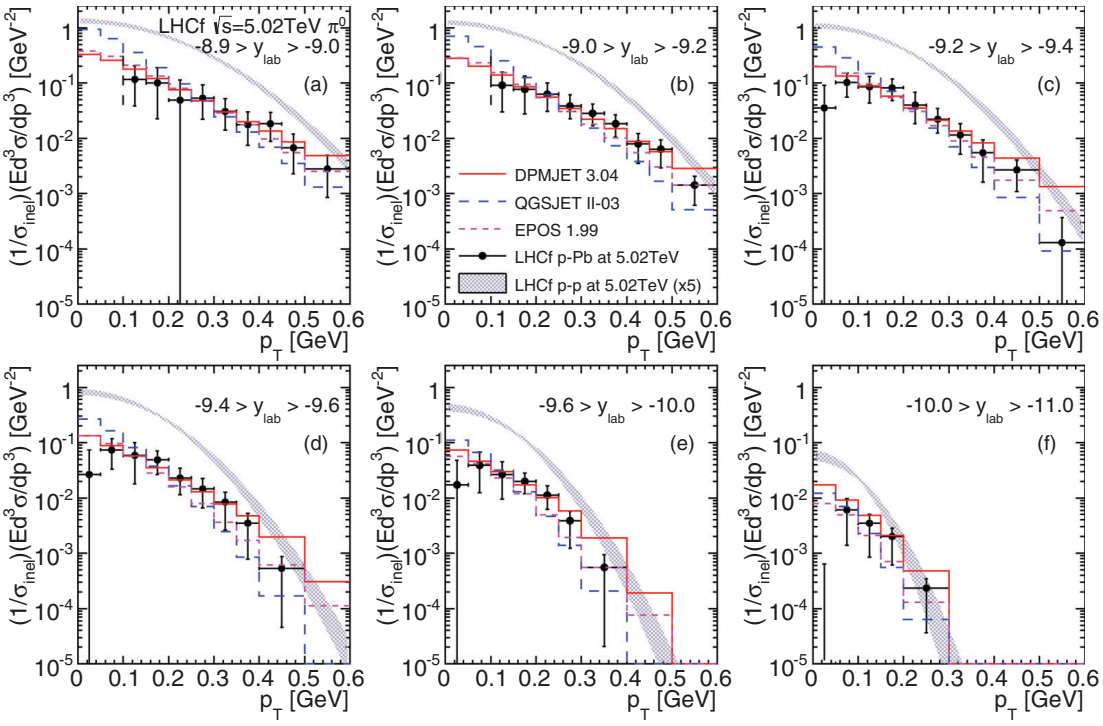

Figure 2: Transverse momentum spectra of forward π^0s at p-Pb [12]. The black dots and the shaded area show LHCf data and the uncertainties. The color lines indicate the predictions by several hadron interaction models[7, 8, 9, 10, 11].

unfolding procedure for detector response [6]. The left and the right figures are for the pseudo-rapidity bins of $\eta > 10.76$ and $8.99 < \eta < 9.22$, respectively. The colored lines indicate the predictions of several hadronic interaction models [7, 8, 9, 10, 11]. We found that the spectrum in $\eta > 10.76$ was very hard like QGSJET2 and the spectrum in $8.99 < \eta < 9.22$ was in the middle of model predictions.

3 π^0 P_T spectrum in $\sqrt{s_{NN}} = 5.02$ TeV p-Pb collisions

In the bingeing of 2013, LHC had proton-lead collisions at the center-of-mass collision energy per nucleus of $\sqrt{s_{NN}} = 5.02$ TeV. LHCf have installed one of the LHCf detectors (Arm2) into the LHC tunnel and had an operation. In the most of our operation time, the Arm2 detector was located on the p-remnant side where proton beams passed from IP1. The LHCf had an operation at the Pb-remnant side only for some hours. In that time, the detector was located 4 cm up from zero degree of collisions to avoid too high multiplicity on the calorimeter towers. Figure 2 shows the transverse momentum spectra of π^0s in p-Pb collisions (the p-remnant side) [12]. The expected contribution of ultra peripheral collisions (UPCs) was already subtracted in these spectra. The thin lines indicate the predictions from the hadronic interaction models, DPMJET3, QGSJET2 and EPOS1.99. The transverse momentum spectra at proton-

proton collisions with the equivalent energy of $\sqrt{s} = 5.02\,\mathrm{TeV}$ were derived from the LHCf data taken at $\sqrt{s} =$ 0.9 2.76 and 7 TeV proton-proton collisions and are shown as the gray hatched lines in Fig.2. Comparing the measured transverse momenta with the estimated spectra in proton-proton collisions give us new information of nuclear modification effect. The nuclear modification factor, $\mathbf{R_{pPb}}$, was defined as the ratio of the p-Pb result to the p-p result. $\mathbf{R}_{pPb}$ varies from 0.1 at P_T 0.1 GeV/c to 0.3 at P_T 0.3 GeV/c. This tendency is found in the all rapidity bins of Fig2. The hadronic interaction model reproduce the small factor of $\mathbf{R_{pPb}}$ 0.1 constantly in the P_T range. They are in good agreement with the LHCf result within the errors.

4 Future prospects

The LHC will restart the operation in 2015. In the beginning of LHC physics run, a run with very low-luminosity of $10^{30} cm^2 s^{-1}$ is planed. The LHCf will have an operation for one week in that period at proton-proton collisions with $\sqrt{s} = 13\,\mathrm{TeV}$. The collision energy is about 10^{17} eV. It will be unique data point of forward spectra at the highest collision-energy of collider experiment in the next decades. Comparing with the date taken at proton-proton collisions of $\sqrt{s} = 0.9$, 2.76 and 7 TeV in the past operations, the energy scaling of forward particle production can be checked. The test with the wide collision energy of $10^{14} - 10^{17}$ eV in the laboratory frame is important because it covers the energy of well-known Knee kink of the cosmic-ray spectrum around 10^{15} eV. Additionally the operation in 2015 will be important to study the diffractive physics thanks to the common operation with the ATLAS experiment. The LHCf sends its final trigger signals to ATLAS trigger system and they trigger ALTAS after pre-scaling of the signals. It was confirmed by a simple simulation study that an event cut with the number of particle tracks in the ATLAS central tracker works well to select only diffractive events. Forward production spectra with such event categorization help us to understand the particle production mechanism in the soft hadronic interactions.
After the operation in 2015, we are proposing to bring one of the detectors to RHIC and to have an operation at proton-proton collisions with $\sqrt{s} = 0.5\,\mathrm{TeV}$. It provides an opportunity of measuring forward production spectra with much wider P_T coverage than the operation at LHC 0.9 TeV proton-proton collisions. It will be much useful to test the energy scaling.

References

[1] O. Adriani, et al., JINST **3** (2008) S08006.
[2] K. Kawade, et al., JINST **9** (2014) P03016.
[3] O. Adriani, et al., PLB 715 (2012) p. 298-303.
[4] O. Adriani, et al., Phys. Lett. B **703** (2011) 128.
[5] O. Adriani, et al., PRD **86** (2012) 092001.
[6] O. Adriani, et al., in preparation.
[7] F. W. Bopp, J. Ranft R. Engel and S. Roesler, Phys. Rev. C **77** (2008) 014904.
[8] T. Sjostand, S. Mrenna and P. Skands, JHEP **05** (2006) 026.
[9] K. Werner, F.-M. Liu and T. Pierog, Phys. Rev. C **74** (2006) 044902.
[10] S. Ostapchenko, Phys. Rev. D **74** (2006) 014026.
[11] E.-J. Ahn, et al., Phys. Rev. D **80** (2009) 094003.
[12] O. Adriani, et al., Phys. Rev. C **89** (2014) 065209.

Numerical Analysis of the $^1S_0$ Pairing Gap in Neutron Matter

S. Maurizio[1], *J. W. Holt*[2], *P. Finelli*[3]

[1] Albert Einstein Center for Fundamental Physics, Institute for Theoretical Physics, CH-3012 Bern, Switzerland
[2] Department of Physics, University of Washington, Seattle, WA 98195-1560
[3] Department of Physics and Astronomy, University of Bologna, I-40126 Bologna, Italy and INFN, Bologna section, I-40127 Bologna, Italy

DOI: http://dx.doi.org/10.3204/DESY-PROC-2014-04/66

In a recent paper [1] we studied the behavior of the pairing gaps Δ_F as a function of the Fermi momentum k_F for neutron and nuclear matter in all relevant angular momentum channels where superfluidity is believed to naturally emerge. The calculations employed realistic chiral nucleon-nucleon potentials [2, 3] with the inclusion of three-body forces and self-energy effects. In this contribution we perform a numerical analysis of Khodel's method [6] for the singlet case.

1 Khodel's method

In this section we explain the method employed to solve the BCS equations by partial-wave decomposition. The BCS equation reads in terms of the NN potential $V(\mathbf{k},\mathbf{k}') = \langle \mathbf{k}\,|V|\,\mathbf{k}'\rangle$ as follows

$$\Delta\left(\mathbf{k}\right) = -\sum_{\mathbf{k}'}\langle \mathbf{k}\,|V|\,\mathbf{k}'\rangle \frac{\Delta\left(\mathbf{k}'\right)}{2E\left(\mathbf{k}'\right)}\,, \tag{1}$$

with $E(\mathbf{k})^2 = \xi(\mathbf{k})^2 + |\Delta(\mathbf{k})|^2$ and where $\xi(\mathbf{k}) = \varepsilon(\mathbf{k}) - \mu$, $\varepsilon(\mathbf{k})$ denotes the single-particle energy and μ is the chemical potential. We can decompose both the interaction and the gap function

$$\langle \mathbf{k}\,|V|\,\mathbf{k}'\rangle = 4\pi\sum_l (2l+1) P_l(\hat{\mathbf{k}}\cdot\hat{\mathbf{k}}') V_l(k,k') \tag{2}$$

$$\Delta(\mathbf{k}) = \sum_{lm}\sqrt{\frac{4\pi}{2l+1}} Y_{lm}(\hat{\mathbf{k}})\Delta_{lm}(k)\,, \tag{3}$$

where $Y_{lm}(\hat{\mathbf{k}})$ denotes the spherical harmonics, l and m are the quantum numbers associated with the orbital angular momentum and its projection along the z axis and $P_l(\hat{\mathbf{k}}\cdot\hat{\mathbf{k}}')$ refers to the Legendre polynomials. After performing an angle-average approximation we have the following equation for any value of l

$$\Delta_l^j(k) = \sum_{l'}\frac{(-1)^\Lambda}{\pi}\int dk'\; V_{ll'}^j(k,k')\frac{\Delta_{l'}^j(k')}{E(k')}k'^2\,, \tag{4}$$

where $\Lambda = 1 + (l - l')/2$, j refers to the total angular momentum ($\boldsymbol{J} = \boldsymbol{l} + \boldsymbol{S}$) quantum number including spin $\boldsymbol{S}$ and now $E(k)^2 = \xi(k)^2 + \sum_{jl} \Delta_l^j(k)^2$. Gaps with different l and j are coupled due to the energy denominator but we assume that different components of the interaction mainly act on non-overlapping intervals in density. To solve Eq. (4), we follow the approach suggested by Khodel *et al.* [6] that has been proven to be stable even for small values of the gap and to require only the initial assumption of a scale factor δ (results will be δ-independent, as will be shown in Sect. 2). We define an auxiliary potential W according to

$$W_{ll'}(k,k') = V_{ll'}(k,k') - v_{ll'}\phi_{ll'}(k)\phi_{ll'}(k') \,, \tag{5}$$

where $\phi_{ll'}(k) = V_{ll'}(k,k_F)/V_{ll'}(k_F,k_F)$ and $v_{ll'} = V_{ll'}(k_F,k_F)$ so that $W_{ll'}(k,k')$ vanishes on the Fermi surface. The coupled gap equations can be rewritten as

$$\Delta_l(k) - \sum_{l'} (-1)^{\Lambda} \int d\tau' \; W_{ll'}(k,k') \frac{\Delta_{l'}(k')}{E(k')} = \sum_{l'} D_{ll'}\phi_{ll'}(k) \,, \tag{6}$$

where $d\tau = k^2 dk/\pi$ and the coefficients $D_{ll'}$ satisfy

$$D_{ll'} = (-1)^{\Lambda} v_{ll'} \int d\tau \; \phi_{ll'}(k) \frac{\Delta_{l'}(k)}{E(k)} \,. \tag{7}$$

The gap is defined as follows

$$\Delta_l(k) = \sum_{l_1 l_2} D_{l_1 l_2} \chi_l^{l_1 l_2}(k) \,, \tag{8}$$

where

$$\chi_l^{l_1 l_2}(k) - \sum_{l'} (-1)^{\Lambda} \int d\tau' \; W_{ll'}(k,k') \frac{\chi_{l'}^{l_1 l_2}(k')}{E(k')} = \delta_{ll_1}\phi_{l_1 l_2}(k) \,, \tag{9}$$

and $\delta_{ll'}$ is the scale factor. The property that $W_{ll'}(k,k')$ vanishes on the Fermi surface ensures a very weak dependence of $\chi_l^{l_1 l_2}(k)$ on the exact value of the gap so that, in first approximation, it is possible to rewrite the previous equation (9) as

$$\chi_l^{l_1 l_2}(k) - \sum_{l'} (-1)^{\Lambda} \int d\tau' \; W_{ll'}(k,k') \frac{\chi_{l'}^{l_1 l_2}(k')}{\sqrt{\xi^2(k') + \delta^2}} = \delta_{ll_1}\phi_{l_1 l_2}(k) \,. \tag{10}$$

We use this equation to evaluate $\chi_l^{l_1 l_2}(k)$ initially by matrix inversion, then we use this function to self-consistently evaluate $D_{ll'}$. Finally, we solve the system given by Eqs. (7)–(9) in a self-consistent procedure as shown in Fig. 1 (left panel). We always assumed $\mu = \varepsilon_F$ and adopted the relativistic version of the single-particle energy $\varepsilon(k) = \sqrt{k^2 + M_N^2}$, where M_N is the nucleon mass. For the pairing potential $V(p,k)$ we introduce the following ansatz:

$$V(p,k) = V_{2\mathrm{B}}(p,k) + \sum_m V_{3\mathrm{B}}(p,k,m) \simeq V_{2\mathrm{B}}(p,k) + V_{2\mathrm{B}}^{\mathrm{eff}}(k_F,p,k) \,, \tag{11}$$

where $V_{2\mathrm{B}}$ is the NN potential [2] at N3LO order in the chiral expansion and the three-body potential is approximated by an effective two-body density-dependent potential V_{2B}^{eff} derived by Holt *et al.* in Refs. [4, 5]. When considering self-energy effects, we simply perform the transformation $M_N \to M_N^*$ using the effective mass obtained by Holt *et al.* in Ref. [7] using a density matrix expansion technique.

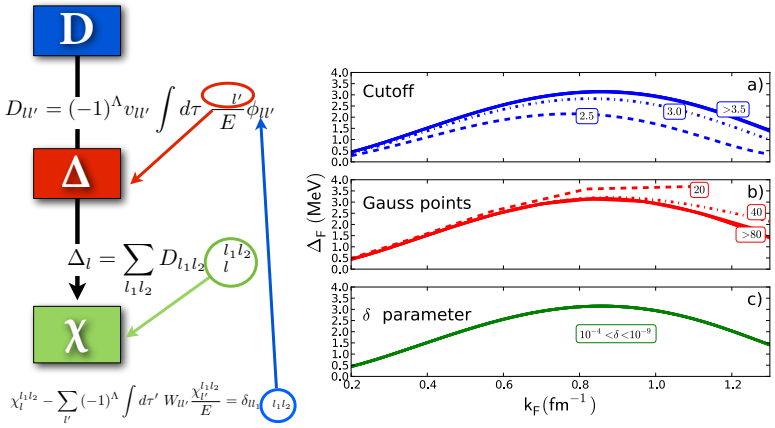

Figure 1: **Left**: Self-consistent procedure (Eqs. 7–9) for the solution of the gap equation according to Khodel's prescription [6]. **Right**: Numerical analysis of Khodel's procedure for the singlet channel in neutron matter: **a)** cutoff, **b)** Gaussian integration points and **c)** δ dependence. This method is a very stable procedure if satisfactory values of n_{gauss} and Λ_k are employed.

2 Results and Numerical analysis

In the neutron matter case, at the two-body level, there is good agreement with the gap computed from well known realistic potentials like the CD-Bonn or Nijmegen interactions [9], except for larger densities where the N3LO gap exhibits a higher value (phase shifts from the chiral N3LO potential exhibit more attraction than the CD-Bonn potential for high momenta [8]). We tested Khodel's method [6] against the variation of the following three parameters: n_{gauss} (number of Gauss integration points), Λ_k (cutoff for integrals in the momentum space, see Eq. (4)) and δ (the scale factor). In Fig. 1 (right side) we summarise our results. In the upper panel (**a**) we calculated Δ_F for different values of the momentum cutoff (using $n_{gauss} = 200$ and $\delta = 1 \times 10^{-10}$ MeV) where in the second panel (**b**) we varied n_{gauss} (keeping $\Lambda_k = 4.5$ fm^{-1} and $\delta = 1 \times 10^{-10}$ MeV) and in the lower panel (**c**) we changed δ (with $n_{gauss} = 200$ and $\Lambda_k = 4.5$ fm^{-1}) by orders of magnitude. Our conclusion is that the method proposed by Khodel [6] is a very stable procedure to study nuclear superfluidity if a reasonable number of Gaussian points (≥ 100) and a realistic momentum cutoff (≥ 4 fm^{-1}) are employed. In Fig. 2 we compare our full calculation for the gap, i.e., with the complete potential in Eq. (11) and the density-dependent effective mass, with recent results by Hebeler *et al.* [8], where the authors started from a chiral N3LO interaction and evolved to a sharp low-momentum interaction. Also presented for comparison are *ab-initio* results obtained in the last several years: Auxiliary Field Diffusion Monte Carlo (AFDMC) [10] with AV8' + UIX potentials, Quantum Monte Carlo (QMC) [11], where the authors have retained the S-wave part of the AV18 interaction, and Correlated Basis Functions (CBF) [12] still with AV8' plus UIX. We observe that at low densities the gap behaviors are very similar, with the exception of QMC, but beyond Fermi momenta

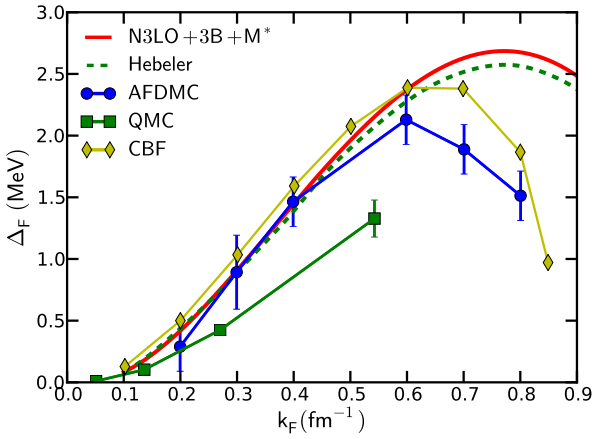

Figure 2: The $^1S_0$ gap for neutron matter computed with the realistic chiral potential of [2] at N3LO plus the three-body contribution of Eq. (11) and the inclusion of the effective mass in comparison with *ab-initio* simulations.

of $k_F \approx 0.6$ fm^{-1} the gaps computed with the Argonne potentials decrease rapidly in contrast to those from chiral interactions. At the present time, it is hard to assess if disagreement is due to different choices in the nuclear Hamiltonian or different many-body methods.

Acknowledgments

Work supported in part by US DOE Grant No. DE-FG02-97ER-41014.

References

[1] S. Maurizio, J. W. Holt and P. Finelli, Phys. Rev. C **90** (2014) 044003.
[2] R. Machleidt and D. R. Entem, Phys. Rept. **503** (2011) 1 and references therein.
[3] E. Epelbaum, H.-W.Hammer and Ulf-G. Meissner, Rev. Mod. Phys. **81** (2009) 1773 and references therein.
[4] J. W. Holt, N. Kaiser and W. Weise, Phys. Rev. C **79** (2009) 054331.
[5] J. W. Holt, N. Kaiser and W. Weise, Phys. Rev. C **81** (2010) 024002.
[6] V. V. Khodel, V. A. Khodel and J. W. Clark, Nucl. Phys. A **598** (1996) 390.
[7] J. W. Holt, N. Kaiser, and W. Weise, Eur. Phys. J. A **47** (2011) 128.
[8] K. Hebeler, A. Schwenk and B. Friman, Phys. Lett. B **648** (2007) 176.
[9] M. Hjorth-Jensen and D. J. Dean, Rev. Mod. Phys. **75** (2003) 607.
[10] S. Gandolfi, A. Y. .Illarionov, F. Pederiva, K. E. Schmidt and S. Fantoni, Phys. Rev. C **80** (2009) 045802.
[11] A. Gezerlis and J. Carlson, Phys. Rev. C **77** (2008) 032801(R).
[12] A. Fabrocini, S. Fantoni, A. Y. Illarionov and K. E. Schmidt, Phys. Rev. Lett. **95** (2005) 192501.

Recent Results from the Telescope Array Experiment

Thomas Stroman for the Telescope Array Collaboration
University of Utah, Salt Lake City, United States

DOI: http://dx.doi.org/10.3204/DESY-PROC-2014-04/62

The Telescope Array Experiment (TA) is the northern hemisphere's largest detector of ultra-high-energy cosmic rays (UHECRs). Built to measure the UHECR chemical composition, arrival-direction anisotropy, and energy spectrum for $E > 1$ EeV, TA's instrumentation includes both an array of scintillator-based particle counters and three fluorescence detector stations overlooking the ground array. This presentation highlights recent composition, spectrum, and anisotropy measurements based on UHECR data collected since TA operations began in 2007, including preliminary results for $E > 10$ PeV from the newly commissioned TA Low-energy Extension (TALE). The expected impact of planned expansions to the experiment will also be described.

1 Introduction

Ultra-high-energy cosmic rays (UHECRs) are subatomic particles that have been accelerated elsewhere in the cosmos to energies in excess of 10^{18} eV. Primary UHECR particles incident on Earth's atmosphere undergo inelastic collisions with gas nuclei, producing extensive air showers. These cascades of secondary particles produce ultraviolet light (via fluorescence emissions of excited nitrogen as well as the Cherenkov mechanism) en route to the ground, where the shower's electromagnetic and muonic footprint can be several kilometers wide in the case of the most energetic primary interactions.

The cosmic-ray flux is a steeply falling function over many orders of magnitude in energy, so that a detector with very large exposure is necessary for any experimental investigation of especially the highest-energy UHECRs' properties. The Telescope Array (TA) experiment is the northern hemisphere's largest UHECR detector, built on over 700 km^2 centered at approximately 39.3° N, 112.9° W in west-central Utah. The original TA instrumentation consists of 38 ultraviolet telescopes located at three fluorescence detector (FD) stations, operating since 2007, and 507 surface detectors (SDs) located every 1.2 km on a square grid, operating since 2008. The SD array and each FD station operate independently, as well as allowing hybrid SD+FD or stereoscopic FD+FD observation of individual showers.

Telescope Array's design facilitates the study of several distinct but interrelated aspects of the nature of UHECRs, and we present some recent highlights of these investigations here. After a brief review of the data analysis in Section 2, we report measurements of an intermediate-scale anisotropy we call the *hotspot* (Section 3), a proton-dominated chemical composition at all energies $E > 10^{18.2}$ eV (Section 4), and the differential energy spectrum manifesting four

distinct spectral features in the range $15.9 \leq \log_{10}(E/\mathrm{eV}) < 20.5$ (Section 5). Finally, we preview the present and future operations to enlarge the TA scientific program in Section 6.

2 Data analysis

The principle underlying TA data analysis is the reconstruction of the air shower properties responsible for the observed signal. The shower trajectory is first determined from an appropriate combination of signal timing and/or detector geometry, which enables the reconstruction of shower energy and, in the case of FD observations, the longitudinal development. The details of the analysis depend on whether the data being analyzed originated in SD or FD observation [1, 2].

A shower observed via direct detection of secondary particles by SDs has its impact position and zenith angle θ determined from the respective distribution of signal sizes and times. The observed signals are then projected onto a lateral distribution model, from which the shower density 800 m from the axis (s_{800}) is interpolated. A lookup table provides an estimate, determined from Monte Carlo simulation and calibrated to the FD energy scale via common events, of the primary shower energy for the observed combination of s_{800} and θ.

In the case of a shower observed via atmospheric fluorescence, the pattern of illuminated photomultiplier tubes (PMTs) constrains the shower trajectory to a plane including the position of the FD. Within this shower-detector plane, the shower's inclination angle and impact parameter determine the relative timing of the signals observed in each PMT.

An inverse-Monte Carlo technique determines the energy and atmospheric slant depth of shower maximum (X_{max}) by varying the longitudinal profile parameters of simulated showers, until reaching the best agreement in detector response between simulation and data.

3 Anisotropy above 57 EeV

Based on five years of SD observation, a directional excess in the flux of UHECRs with $E >$ 57 EeV has been observed in the constellation Ursa Major [3]. Given the exposure of the SD array, the expected number of events within a 20° radius was 4.5, but 19 were observed, a 5.1σ excess (see Fig. 1). The chance probability of our observing an excess of this size from an isotropic flux, given intermediate-scale event oversampling in 5° steps from 15° to 35°, is 3.7×10^{-4}, for a post-trials significance of 3.4σ. Preliminary analysis including a sixth year of data increases the significance of the observation to 4.0σ.

4 Mass composition

It is possible to estimate the mean mass of primary cosmic rays as a function of energy by comparison of the observed X_{max} distribution to model predictions for known compositions. Using the hybrid combination of data from the SD array and the Middle Drum FD (consisting of equipment refurbished from the High Resolution Fly's Eye experiment), we find our observations compatible with a predominantly protonic composition at all energies $E > 10^{18.2}$ eV regardless of the choice of hadronic interaction model used in simulation [4].

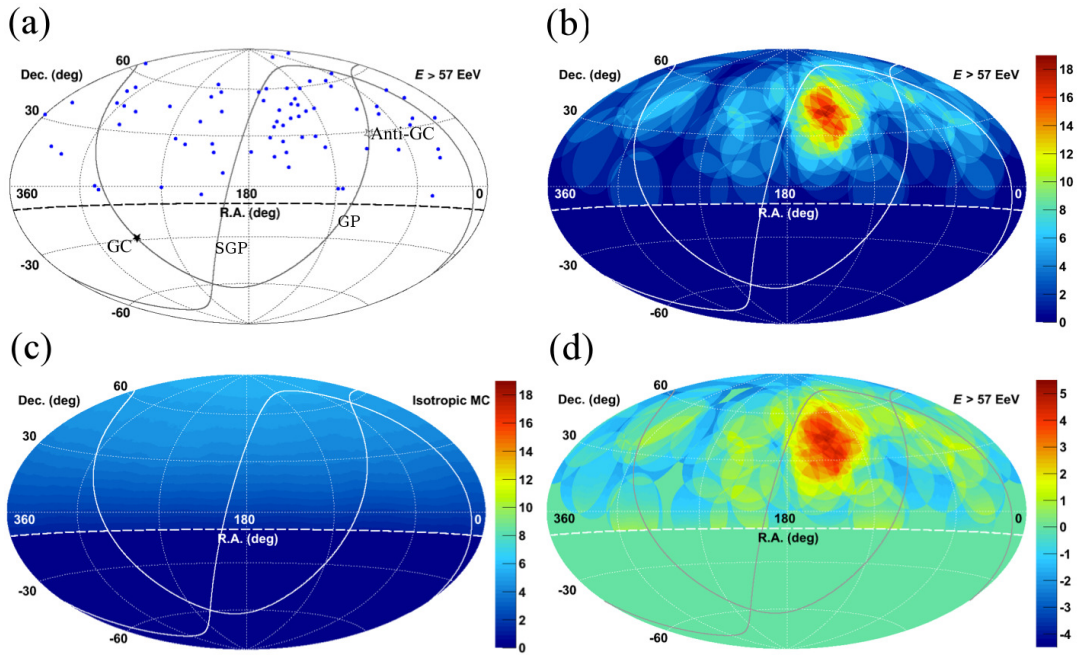

Figure 1: Anisotropy above 57 EeV: (**a**) arrival directions; (**b**) arrival directions with 20° oversampling; (**c**) expected number of events assuming isotropic null hypothesis; (**d**) Li-Ma significance of excess.

5 Energy spectrum

Using six years of data from the SD array, we observe two features in the UHECR spectrum: a hardening *ankle* at $10^{18.70\pm0.02}$ eV and a suppression above $10^{19.74\pm0.04}$ eV compatible with the *GZK cutoff* predicted for protons. The suppression represents a 6.59σ deficit relative to a spectrum maintaining the post-ankle spectral slope without cutoff.

The newly commissioned TA Low-energy Extension (TALE) includes ten FD telescopes observing at higher elevation angles than the main FD configuration, complemented by an array of closely-spaced ($\sim$ 400 m) SDs, to reduce the energy threshold for shower detection [5]. A preliminary analysis using fluorescence and Cherenkov light seen by the TALE FD extends the observed spectrum to below 10 PeV and reveals two additional spectral breaks.

6 Future operations

A number of operations are being pursued to upgrade Telescope Array in the coming years. A quadrupling of the TA exposure above 10^{19} eV (TA$\times$4) will be accomplished by adding another 500 SDs with greater spacing, overlooked by two additional FD stations. The detection threshold will be pushed further down into the PeV decade via a Non-Imaging Cherenkov Experiment (NICHE [6]) cross-calibrated with TALE events. Progress continues toward UHECR detection via bistatic radar (TARA [7]), and we are exploring claims of a connection between thun-

derstorms and high-energy radiation with a lightning-mapping array (TALMA). The science program at Telescope Array continues to grow increasingly expansive and robust.

Acknowledgments

The Telescope Array experiment is supported by the Japan Society for the Promotion of Science through Grants-in-Aid for Scientific Research on Specially Promoted Research (21000002) "Extreme Phenomena in the Universe Explored by Highest Energy Cosmic Rays," and the Inter-University Research Program of the Institute for Cosmic Ray Research; by the U.S. National Science Foundation awards PHY-0307098, PHY-0601915, PHY-0703893, PHY-0758342, PHY-0848320, PHY-1069280, and PHY-1069286 (Utah) and PHY-0649681 (Rutgers), and through TeraGrid resources provided by Purdue University and Indiana University [8]; by the National Research Foundation of Korea (2006-0050031, 2007-0056005, 2007-0093860, 2010-0011378, 2010-0028071, R32-10130); by the Russian Academy of Sciences, RFBR grants 10-02-01406a and 11-02-01528a (INR), IISN project No. 4.4509.10, and Belgian Science Policy under IUAP VI/11 (ULB). The foundations of Dr. Ezekiel R. and Edna Wattis Dumke, Willard L. Eccles, and George S. and Dolores Doré Eccles all helped with generous donations. The State of Utah supported the project through its Economic Development Board, and the University of Utah through the Office of the Vice President for Research. The experimental site became available through the cooperation of the Utah School and Institutional Trust Lands Administration (SITLA), the U.S. Bureau of Land Management, and the U.S. Air Force. We also wish to thank the people and the officials of Millard County, Utah, for their steadfast and warm support. We gratefully acknowledge the contributions from the technical staffs of our home institutions as well as the University of Utah Center for High Performance Computing (CHPC).

References

[1] T. Abu-Zayyad et al. The Cosmic-Ray Energy Spectrum Observed with the Surface Detector of the Telescope Array Experiment. *Astrophys. J. Letters*, 768:L1, May 2013.

[2] T. Abu-Zayyad et al. The energy spectrum of ultra-high-energy cosmic rays measured by the Telescope Array FADC fluorescence detectors in monocular mode. *Astroparticle Physics*, 48:16–24, August 2013.

[3] R. U. Abbasi et al. Indications of Intermediate-scale Anisotropy of Cosmic Rays with Energy Greater Than 57 EeV in the Northern Sky Measured with the Surface Detector of the Telescope Array Experiment. *Astrophys. J. Letters*, 790:L21, August 2014.

[4] R. U. Abbasi et al. Study of Ultra-High Energy Cosmic Ray Composition Using Telescope Array's Middle Drum Detector and Surface Array in Hybrid Mode. *ArXiv e-prints*, August 2014.

[5] G. Thomson. The Telescope Array Low Energy Extension (TALE). *International Cosmic Ray Conference*, 3:338, 2011.

[6] J. Krizmanic, D. Bergman, and Pierre Sokolsky for the TA/TALE Collaboration. The Non-Imaging CHErenkov Array (NICHE): A TA/TALE Extension to Measure the Flux and Composition of Very-High Energy Cosmic Rays. *ArXiv e-prints*, July 2013.

[7] R. Abbasi et al. Telescope Array Radar (TARA) observatory for Ultra-High Energy Cosmic Rays. *Nuclear Instruments and Methods in Physics Research A*, 767:322–338, December 2014.

[8] C. Catlett et al. *TeraGrid: Analysis of Organization, System Architecture, and Middleware Enabling New Types of Applications*. IOS Press, 2007.

Results and prospects on registration of reflected Cherenkov light of EAS from cosmic particles above 10^{15} eV

R.A. Antonov[1], *T.V. Aulova*[1], *E.A. Bonvech*[1], *D.V. Chernov*[1], *T.A. Dzhatdoev*[1,*], *Mich. Finger*[2,3], *Mir. Finger*[2,3], *V.I. Galkin*[4,1], *D.A. Podgrudkov*[4,1], *T.M. Roganova* [1]

[1] Skobeltsyn Institute of Nuclear Physics, Lomonosov Moscow State University, Leninskie gory 1-2, 119991 Moscow, Russia

[2] Charles University in Prague, Faculty of Mathematics and Physics, V Holesovickach 2, 18000 Prague, Czech Republic

[3] Joint Institute for Nuclear Research, Joliot-Curie 6, 141980 Dubna, Moscow region, Russia

[4] Faculty of Physics, Lomonosov Moscow State University, Leninskie gory 1-2, 119991 Moscow, Russia

[*] timur1606@gmail.com

DOI: http://dx.doi.org/10.3204/DESY-PROC-2014-04/152

We give an overview of the SPHERE experiment based on detection of reflected Vavilov-Cherenkov radiation ("Cherenkov light") from extensive air showers in the energy region E>10^{15} eV. A brief history of the reflected Cherenkov light technique is given; the observations carried out with the SPHERE-2 detector are summarized; the methods of the experimental datasample analysis are described. The first results on the primary cosmic ray all-nuclei energy spectrum and mass composition are presented. Finally, the prospects of the SPHERE experiment and the reflected Cherenkov light technique are given.

1 Introduction

Despite several decades of intensive research, experimental results on the superhigh energy ($E > 10^{15}$ eV = 1 PeV) cosmic ray spectrum and composition are still somewhat controversial. An uncertainty of the spectral shape is considerable (see, e.g., [1]), and the results on the nuclear composition obtained by different experiments are often contradictory (e.g. [2]). A scatter of results is especially large for the composition studies: various measurements of the mean logarithmic mass number, $< lnA >$, at some energy region span almost the full range of masses from proton to Iron. For some extensive air shower (EAS) experimental techniques the uncertainty of the primary composition might translate into an additional error of the reconstructed all-nuclei spectrum, and this latter systematic uncertainty may dominate the total error of the spectrum measurement.

The experimental situation clearly calls for development of new EAS observation and data analysis methods. In the present paper we describe one such method based on reflected Vavilov-Cherenkov radiation ("Cherenkov light") registration. Many details could be found in [3].

The first proposal to use a compact device lifted over a snow surface to observe reflected

Cherenkov light of EAS was made by A.E. Chudakov [4]. The first detector of such kind was developed by C. Castagnoli et al. [5]. The first balloon-borne apparatus capable of reflected Cherenkov light observation was the SPHERE-1 detector [6]; it had a mosaic of only 19 PMTs and could not register details of light impulse shape. The next generation, and currently the most advanced experiment with reflected Cherenkov light, employed the SPHERE-2 detector.

2 The SPHERE-2 detector and the datasample

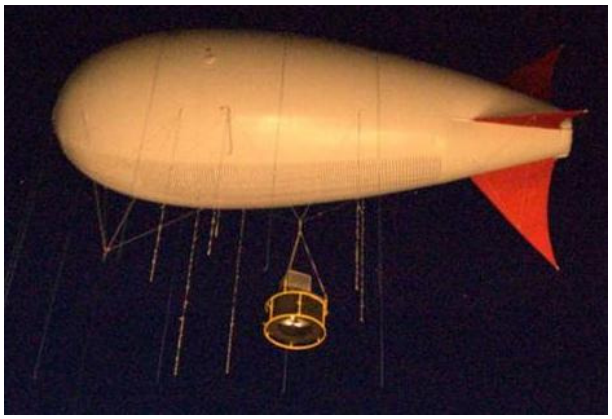

Figure 1: The SPHERE-2 detector carried by the BAPA tethered balloon.

The SPHERE-2 balloon-borne detector [3] had a mosaic of 109 PMTs and 12.5 ns time sampling (25 ns until the 2012 experimental run). A general view of the SPHERE-2 detector together with by the BAPA tethered balloon is shown in Fig. 1. Observations were typically carried out in February-March at altitude H= 400–900 m above the surface of Lake Baikal. Total observation time for the 2008–2013 runs was about 140 h; about 1100 EAS were detected.

3 Simulations, data analysis and results

The detector response simulations were carried out by means of Monte Carlo (MC) approach using the CORSIKA code with the QGSJET-I high energy hadronic model and the GHEISHA low energy hadronic model [7], and the Geant4 code [8]. The first step of experimental data analysis is reconstruction of lateral distribution function (LDF) of detected showers. An example of reconstructed LDF is shown in Fig. 2, left. LDF reconstruction is a quite complex procedure; it is important to have several independent techniques to ensure robustness of this procedure. An example of LDF obtained with the second technique is shown in Fig. 2, right. The next step of analysis, estimation of EAS primary energy, was performed by normalising the experimental LDFs to the model LDFs with known energy [9]. Finally, the sample of the estimated primary energy values together with the model of the instrumental acceptance allowed the all-nuclei spectrum reconstruction [10],[3].

Simulated energy distributions for the 2013 experimental run data, power-law primary spectrum $J \sim E^{-\gamma}$ with slope $\gamma = 3$, and different types of primary nuclei, are shown in Fig. 3,

left. The lowest curve corresponds to the primary Iron case, upper concentric curves are calculated for the Nitrogen, Helium and proton cases, correspondingly. The thick curve that fits the experimental histogram (circles) is drawn for the energy distribution with mixed composition. Information about the LDF steepness, that is sensitive to the primary composition, was utilized to build a model of energy distribution for mixed composition (see [10],[3] for more details).

The combined all-nuclei spectrum for the 2011–2013 runs is shown in Fig. 3 (right) by stars with statistical uncertainies (bars); systematic uncertainties are shown as well. For comparison the results of the KASCADE-Grande (triangles with associated statistical and systematic uncertainties) [11] and the Akeno (circles) [12] experiments are shown. For the Akeno case statistical uncertainties are small and comparable to the diameter of the circles, and systematic uncertainties are unknown. For other results on the all-nuclei spectrum see [13].

The primary composition for the 2012 run was reconstructed using the LDF steepness parameter [14],[3], that allows an event-by-event composition study. The reconstructed composition for the 2012 run is shown in Fig. 2 of [14]. It is in general agreement to the KASCADE-Grande result [15]; the estimated fraction of light nuclei averaged over the 30–150 PeV energy region is 0.21 ± 0.11.

4 Prospects and conclusions

Uncertainty of results on the primary spectrum and composition discussed in sec. 3 at E>50 PeV is dominated by statistical errors. Two possible extensions of the SPHERE experiment to the energy region E>100 PeV were proposed [3]:
1) A SPHERE-type detector with $N>10^3$ channels that would allow to perform an event-by-event study of the primary CR composition at E>100 PeV with statistical uncertainty comparable to the KASCADE-Grande's one given ∼500 h of exposition at H= 2–3 km;
2) A detector with $N>10^3$ channels aimed for study of the all-nuclei spectrum of Ultrahigh Energy Cosmic Rays (UHECR, $E>10^{18}$ eV) during a long-duration high-altitude (H≈30–40 km) Antarctic flight, or, alternatively, a detector with $N>10^4$ channels that would allow to study the UHECR primary composition under similar experimental conditions.

To conclude, we have reviewed a novel technique to study CR at E>1 PeV using reflected Cherenkov light. The method is currently mature enough to be competitive with other EAS observation methods, given sufficient observation time. For the first time, a detailed reconstruction of the all-particle CR spectrum at E= 3-300 PeV was performed using reflected Cherenkov light. This technique allows the CR nuclear composition study on event-by-event basis. Reflected Cherenkov light is a promising signal to study CR at E>100 PeV, either with tethered balloon at H= 2–3 km, or during a high-altitude Antarctic flight.

Acknowledgements

The authors are grateful to the technical collaborators of the SPHERE-2 experiment. The work was supported by the Russian Foundation for Basic Research (grants 11-02-01475-a, 12-02-10015-k, 13-02-00470-); the Russian President grants LSS-871.2012.2; LSS-3110.2014.2; the Program of basic researches of Presidium of Russian Academy of Sciences "Fundamental properties of a matter and astrophysics". Calculations were performed using the SINP MSU space monitoring data center computer cluster; we are grateful to Dr. V.V. Kalegaev for permission to use the hardware and to V.O. Barinova, M.D. Nguen, D.A. Parunakyan for technical support.

References

[1] R. Abbasi et al. (ICETOP), astro-ph/1202.3039 (2012).

[2] Y. Tsunesada et al. (BASJE), Proc. 30th ICRC **4** 127 (2008); K.-H. Kampert & M. Unger, APh **35** 660 (2012).

[3] R.A. Antonov et al., Phys. Part. Nucl. (2015) (In press).

[4] A.E. Chudakov, Proc. All-USSR Symp. on Exp. Meth. of UHECR (Yakutsk) (In Russian) 69 (1974).

[5] C. Castagnoli et al., Proc. 17th ICRC **6** 103 (1981).

[6] R.A. Antonov et al., Nucl. Phys. (Proc. Suppl.) **B52** 182 (1997); R.A. Antonov et al., Proc. 27th ICRC **1** 59 (2001).

[7] D. Heck et al., FZKA Report 6019 (1998); N. Kalmykov et al., Nucl. Phys. (Proc. Suppl.) **B52** 17 (1997); H.C. Fesefeldt, Technical Report No. PITHA 85-02 RWTH (1985).

[8] S. Agostinelli et al., NIM **A506** 250 (2003).

[9] L.G. Dedenko et al., Nucl. Phys. (Proc. Suppl.) **B136** 1217 (2004).

[10] R.A. Antonov et al., 33^{rd} ICRC (Rio), id. 1185 (2013).

[11] W.D. Apel et al. (KASCADE-Grande), APh **36** 183 (2012).

[12] M. Nagano et al., J. Phys. G **18** 423 (1992).

[13] M.G. Aartsen et al., Phys. Rev. D **88** 042004 (2013); S.P. Knurenko et al., 33^{rd} ICRC (Rio), id. 53 (2013); S.P. Knurenko, A. Sabourov, EPJ Web of Conf. **53** 04004 (2013); M. Fukushima, Talk at ISVHECRI-2014 (2014).

[14] Antonov et al., J. Phys. Conf.Ser. **409** 012088 (2013).

[15] W.D. Apel et al. (KASCADE-Grande), Phys. Rev. D. (2013).

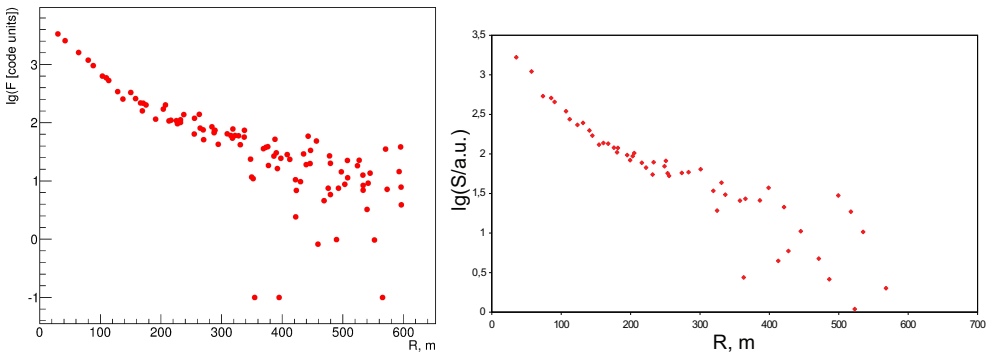

Figure 2: Two examples of reconstructed experimental LDFs: left — for the first analysis, right — for the second analysis.

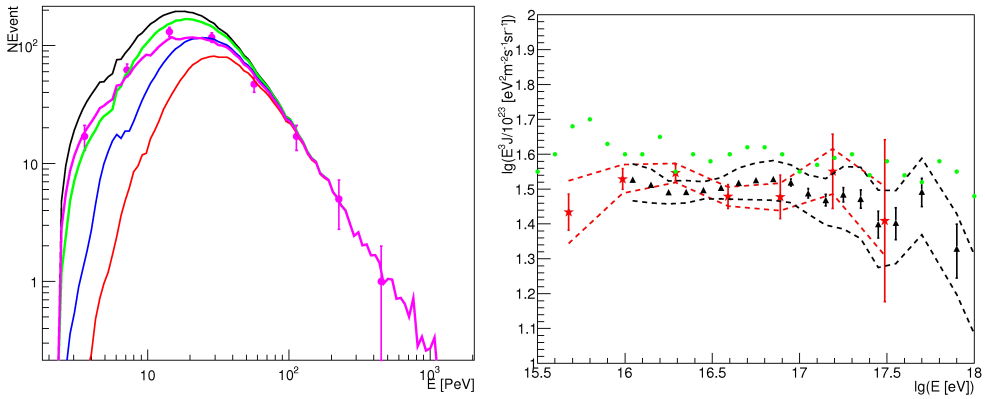

Figure 3: Left — model energy distribution for different composition assumptions (curves) and experimental energy distribution for the 2013 run data (circles). Right — the all-nuclei spectrum reconstructed for the 2011–2013 runs (stars) along with the KASKADE-Grande and Akeno results.

Chapter 8

Tests of symmetries and conservation laws

^{3}He/^{129}Xe Clock Comparison Experiment: Search for Spin-Dependent Short-Range Interaction

Kathlynne Tullney[1], *Fabian Allmendinger*[2], *Werner Heil*[1], *Sergei Karpuk*[1], *Yuri Sobolev*[1], *Ulrich Schmidt*[2]

[1]Institut für Physik, Johannes Gutenberg-Universität Mainz, Germany
[2]Physikalisches Institut, Ruprecht-Karls-Universität Heidelberg, Germany

DOI: http://dx.doi.org/10.3204/DESY-PROC-2014-04/69

We report on the search for a new spin–dependent interaction $\vec{\sigma}\cdot\hat{r}$ which causes a shift in the precession frequency of nuclear spin polarized gases. Therefore we use a comagnetometer that is based on the detection of freely precessing nuclear spins from ^{3}He and ^{129}Xe gas samples using SQUIDs as low–noise magnetic flux detectors. As result we could improve the upper bounds of the dimensionless product $g_s g_p$ of the monopole–dipole coupling of an axion to the spin of a bound neutron in the mass range between 2 μeV and 500 μeV (corresponding to force ranges between $3 \cdot 10^{-4}$ m and 10^{-1} m) by up to 4 orders of magnitude.

The existence of a new spin–dependent short–range force may be a signature of pseudoscalar boson particles like the axion, which was proposed by Peccei and Quinn to solve the strong *CP* problem [1]. This hypothetical particle could have been created in early stages of the universe and since it is a light and weak interacting particle, it is an attractive candidate to the cold dark matter that could compose up to 1/3 of the ingredients of the universe [2]. An axion or any axion–like particle mediates an interaction between a fermion f and the spin of another fermion f_σ which in case of monopole-dipole coupling violates parity and time symmetries. The Yukawa-type potential of this monopole-dipole interaction with range λ is given by [3]

$$V_{\mathrm{sp}}(r) = \frac{\hbar^2 g_s^f g_p^{f_\sigma}}{8\pi m}(\vec{\sigma}\cdot\hat{r})\left(\frac{1}{\lambda r}+\frac{1}{r^2}\right)e^{-r/\lambda}\ , \tag{1}$$

where g_s^f and $g_p^{f_\sigma}$ are dimensionless scalar and pseudoscalar constants for the axion-fermion vertices, which in our case correspond to the scalar coupling of an axion or an axion-like particle to a nucleon ($g_s^f = g_s^N$) and its pseudoscalar coupling to a polarized bound neutron ($g_p^{f_\sigma} = g_p^n$). $\hat{r}$ is the unit distance vector pointing from the polarized fermion to the unpolarized fermion, respectively from the polarized sample to the unpolarized sample. λ is the range of the Yukawa force with $\lambda = \hbar/m_a c$, m_a is the mass of the axion and m is the mass of the fermion which carries the spin $\vec{\sigma}$. The potential given by Eq. 1 effectively acts near the surface of a massive unpolarized sample ($r \leq \lambda$) as a pseudo-magnetic field and gives rise to a shift $\Delta\omega_{\mathrm{sp}} = 2\pi\Delta\nu_{\mathrm{sp}} = V_\Sigma/\hbar$ in the precession frequency of nuclear spin polarized gases. The potential V_Σ is obtained by integration of $V_{\mathrm{sp}}(r)$ from Eq. 1 over the volume of the massive unpolarized sample averaged over the volume of the polarized sample.

Our approach to search for non-magnetic spin-dependent interactions is to use an ultrasensitive low-field comagnetometer which is based on simultaneous detection of free spin precession of

gaseous, nuclear spin polarized ^{3}He and ^{129}Xe atoms. The Larmor frequencies of helium and xenon in a constant magnetic guiding field B are given by $\omega_{\mathrm{L,He(Xe)}} = \gamma_{\mathrm{He(Xe)}} \cdot B$, whereby $\gamma_{\mathrm{He(Xe)}}$ are the gyromagnetic ratios of the according gas species. Hence, the influence of ambient magnetic fields cancels in the weighted difference of Larmor frequencies, respectively, the corresponding time integral, the weighted difference of Larmor phases

$$\Delta\omega = \omega_{\mathrm{He}} - \frac{\gamma_{\mathrm{He}}}{\gamma_{\mathrm{Xe}}} \cdot \omega_{\mathrm{Xe}} = 0\,, \quad \Delta\Phi(t) = \Phi_{\mathrm{He}}(t) - \frac{\gamma_{\mathrm{He}}}{\gamma_{\mathrm{Xe}}} \cdot \Phi_{\mathrm{Xe}}(t) = const\,. \tag{2}$$

For the gyromagnetic ratios of helium and xenon we took the literature values given by $\gamma_{\mathrm{He}}/\gamma_{\mathrm{Xe}} = 2.75408159(20)$ [5, 6]. The quantities $\Delta\omega$ and $\Delta\Phi(t)$ are sensitive to anomalous frequency shifts due to non–magnetic spin interactions. According to the Schmidt model [4], in the nuclei of helium and xenon the spin of 1/2 is carried by a neutron only. Thus, the frequency shift $\Delta\nu_{\mathrm{sp}}$ due to the spin–dependent short–range force (Eq. 1) is expected to be similar for ^{3}He and ^{129}Xe. Hence, the frequency shift $\Delta\nu_{\mathrm{sp}}$ does not drop out in the the weighted frequency, respectively, weighted phase difference (Eq. 2). A detailed description of this comagnetometer can be found in [7].

1 Experimental Setup and Principle of Measurements

The experiment was performed inside the magnetically shielded room BMSR-2 at the Physikalisch Technische Bundesanstalt Berlin (PTB). BMSR-2 has a passive shielding factor, which exceeds 10^8 above 6 Hz. A homogeneous guiding magnetic field of about 350 nT - with maximum field gradients of about 33 pT/cm - was provided inside the shielded room by means of a square coil pair (B_x-coils). With a second square coil pair (B_y-coils) which was arranged perpendicular to the first one it was possible to manipulate the precession of the spin samples, e.g., $\pi/2$ spin flip by nonadiabatic switching [7]. For detection of the spin precession we used a low-T_c DC–SQUID vector magnetometer system [8, 9]. The pick-up coils of the SQUIDs were sensitive to the vertical magnetic field component of the two precessing nuclear spin species (^{3}He, ^{129}Xe). The system noise of the SQUIDs was about 2.3 fT/$\sqrt{\mathrm{Hz}}$ in the range of the precession frequencies. Most part of the environmental noise was caused by dewar vibrations relative to the B_x-coils. Here, combining two SQUIDs to a gradiometer helps to suppress this effect down to a level of 2.5 fT/$\sqrt{\mathrm{Hz}}$. As gas container we used a cylindrical cell made of aluminosilicate glass (GE180) with a diameter of 58 mm and a length of 60 mm. ^{3}He and ^{129}Xe were nuclear spin polarized outside the shielding by means of optical pumping. Afterwards the cell was filled with a mixture of polarized ^{3}He, polarized ^{129}Xe (≈ 2 mbar, ≈ 8 mbar) and N_2 (≈ 35 mbar). The nitrogen was added to suppress xenon relaxation due to the van der Waals molecular coupling. After transportation of the measurement cell into the BMSR-2 the cell was mounted directly beneath the dewar which houses the SQUIDs. A cylindrical glass tube with a length of 1 m and an inner diameter of 60 mm was placed on a separate support with its axis aligned with the axis of the cylindrical measurement cell. At its open end towards the polarized sample cell a BGO–crystal (BGO = $Bi_4Ge_3O_{12}$, ρ=7.13 g/cm^3, diameter 60 mm and length 70 mm) was installed. The tube and with it the BGO–crystal could be moved horizontally from "close"–position to "distant"–position and vice versa, whereby the movement of the glass tube was possible without opening the door of the magnetic shielded room, i.e., without interruption of the ^{3}He and ^{129}Xe spin precession. At "close"–position we had a minimum gap of 2.2 mm between the BGO–crystal and the polarized gases. The BGO–crystal was used, since a non-conducting material prevented us from additional noise sources.

If the spin–dependent axion fermion interaction exist it will cause a shift $\Delta\omega_{\rm sp}^{w}$ in the weighted precession frequency difference (Eq. 2) when the BGO–crystal is close ("close"–position) to the measurement cell. If the BGO–crystal is far away ("distant"–position) from the measurement cell this frequency shift should vanish. To measure this frequency shift $\Delta\omega_{\rm sp}^{w}$ the measurement procedure was as follows: The spin precession signals were measured whereby the BGO-crystal was installed close to the cell ("close"–position). After 10800 s the BGO–crystal was moved away ("distant"–position). The spin precession signals were then measured again for about 21500 s. It was also possible to do measurements where the BGO-crystal was first in the "distant"–position and in the second part of the measurement in the "close"-position. These measurements were repeated several times whereby for systematic checks, the BGO–crystal could be placed left and right with respect to the ^{3}He/^{129}Xe sample cell.

2 Data Analysis and Results

A detailed despription of the data analysis is described in [10, 11]. Briefly, for each measurement run – in total we did 10 runs – the accumulated phases and with it the corresponding phase difference $\Delta\Phi(t)$ was determined, which is not a constant in time, as Eq. 2 may suggest. Instead higher order effects, as Earth rotation, chemical shift and the generalized Ramsey-Bloch-Siegert-Shift [11], have to be taken into account. These effects can be parameterized by

$$\Delta\Phi(t) = \Phi_0 + \Delta\omega_{\rm lin}\cdot t - \epsilon_{\rm He}\cdot T^{*}_{2,\rm He}\cdot A_{\rm He}\cdot e^{-\frac{t}{T^{*}_{2,\rm He}}} + \epsilon_{\rm Xe}\cdot T^{*}_{2,\rm Xe}\cdot A_{\rm Xe}\cdot e^{-\frac{t}{T^{*}_{2,\rm Xe}}} \ . \qquad (3)$$

If the pseudoscalar Yukawa potential $V_{\rm sp}(r)$ would occur at an instant $t = t_0$ due to the movement of the BGO–crystal, an additional linear phase drift $\Delta\omega_{\rm sp}^{w}\cdot(t-t_0) = 2\pi\cdot\Delta\nu_{\rm sp}^{w}\cdot\Theta(\pm(t-t_0))\cdot(t-t_0)$ in Eq. 3 is expected[1]. The frequency shift $\Delta\nu_{\rm sp}$ is then extracted from

$$\Delta\nu_{\rm sp} = \frac{\Delta\omega_{\rm sp}^{w}}{2\pi\cdot(1-\frac{\gamma_{\rm He}}{\gamma_{\rm Xe}})} \ . \qquad (4)$$

For each measurement run $\Delta\nu_{\rm sp}$ was determinded. From the calculation of the weighted mean, one gets $\overline{\Delta\nu}_{\rm sp} = (-2.9\pm2.3\pm0.1)$ nHz. The last value corresponds to the systematic error[2]. The $\chi^2/d.o.f$ of the data to their weighted mean $\overline{\Delta\nu}_{\rm sp}$ gives 2.29, indicating that the errors on the measured frequency shifts are somewhat underestimated. In order to take this into account, the errors were scaled to obtain a χ^2/d.o.f of one, as recommended, e.g., by [12, 13]. At the 95% C.L., our result for the measured frequency shift is

$$\overline{\Delta\nu}_{\rm sp} = (-2.9\pm6.9\pm0.2)\ \text{nHz}\ . \qquad (5)$$

The result of $\overline{\Delta\nu}_{\rm sp}$ indicates that we find no evidence for a pseudoscalar short–range interaction mediated by axions or axion–like particles.
From the total error $\delta(\overline{\Delta\nu}_{\rm sp}) = \pm7.1$ nHz exclusion bounds for $\left|g_s^N g_p^n\right|$ can be derived by calculating V_Σ and using $|\delta(\overline{\Delta\nu}_{\rm sp})| \geq 2\cdot V_\Sigma/h$. The results are shown in Fig.1. We substantially improved the bounds on a spin–dependent short–range interaction between polarized (bound) neutrons and unpolarized nucleons over most of the axion window. Existing constraints on axions or axion–like particles heavier than 20 μeV could be tightened by up to four orders of magnitudes.

[1] $(\pm)$ in the argument of the Heaviside step function has to be set (-) for the sequence c→d and (+) for the reverse one d→c.

[2] A detailed description of the calculation of the systematic error is given in [11].

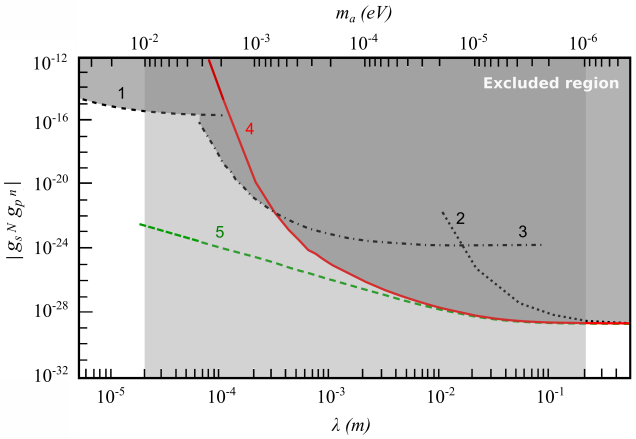

Figure 1: The experimental 95% confidence upper limit on $\left|g_s^N g_p^n\right|$ plotted versus the range λ of the Yukawa-force with $\lambda = \hbar/(m_a c)$. The light gray area indicates the axion window. (1): result of [14], (2): result of [15], (3): result of [16], (4): this experiment ($\Delta x = 2.2$ mm), (5): expected results for Δx≈ 0 mm using $\delta(\overline{\Delta\nu}_{\rm sp}) = \pm 7.1$ nHz demonstrates the gain in measurement sensitivity for $\lambda < 10^{-3}$ m. For bounds on the pseudoscalar short–range force between polarized electrons and unpolarized nucleons see [17].

References

[1] C.D. Peccei, H.R. Quinn, Phys. Rev. Lett. **38**, 1440 (1977)

[2] J. Jaeckel, A. Ringwald, Annu. Rev. Nucl. Part. Sci. **60**, 405 (2010)

[3] J.E. Moody, F. Wilczek, Phys. Rev. D **30**, 130 (1984)

[4] Th. Schmidt, Zeitschrift für Physik A Hadronen und Kerne **10**6, 358 (1937)

[5] International council for Science: Committee on Data for Science and Technology (CODATA), www.codata.org (2007)

[6] M. Pfeffer and O. Lutz, J. Magn. Res. A **108**, 106 (1994)

[7] C. Gemmel *et al.*, Eur. Phys. Journal D **57**, 303 (2010)

[8] D. Drung, Physica C **368**, 134 (2002)

[9] M. Burghoff *et al.* IEEE Trans. App. Supercon. **17**, 846 (2007)

[10] C. Gemmel *et al.* Phys. Rev. D **82**, 111901(R) (2010).

[11] K. Tullney *et al.* Phys. Rev. Lett. **111**, 100801 (2013)

[12] The Particle Data Group Phys. Lett. B **592**, 14 (2004)

[13] W.H. Press, S.A. Tenkolsky, W.T. Vetterling and B.P. Flannery *Numerical Recipes 3rd Edition: The Art of Scientific Computing.*, Cambridge University Press, New York (2007)

[14] T. Jenke *et al.* Phys. Rev. Lett. **112**, 151105 (2014)

[15] A.N. Youdin *et al.* Phys. Rev. Lett. **77**, 2170 (1996)

[16] M. Bulatowicz *et al.* Phys. Rev. Lett. **111**, 102001 (2013)

[17] S.A. Hoedel Phys. Rev. Lett. **106**, 041801 (2011)

Search for T-invariance Violation in the Proton-Deuteron Scattering

Azamat Temerbayev[1], *Yury Uzikov*[2]

[1]ENU, Kazhymukhan 5, Astana, 010008 Kazakhstan
[2]JINR, Joliott-Curie 6, Dubna, 141890 Russia

DOI: http://dx.doi.org/10.3204/DESY-PROC-2014-04/86

The spin-dependent Glauber theory is used to calculate differential observables and integrated polarized cross sections of the *pd* scattering at proton beam energy 135 MeV. In addition to the pure strong NN interactions, the Coulomb effects and T-invariance violating but P-parity conserving interactions are considered. This study is motivated by the TRIC experiment planned at COSY to test time-reversal symmetry.

1 Introduction

Under assumption of CPT-symmetry, CP violation established in physics of kaons and B-mesons implies existence of T-odd P-odd interactions. These interactions are parametrized in the standard model by CP violating phase of the Cabibbo-Kobayashi-Maskawa matrix. On the contrary, time-invariance-violating (T-odd) P-parity conserving (P-even) flavor conserving (TVPC) interactions do not arise on the fundamental level within the standard model. This type of interaction can be generated by radiative corrections to the T-odd P-odd interaction. However in such a case its intensity is too small to be observed in experiments at present [1]. Thus, observation of TVPC effects would be considered as indication to physics beyond the standard model.

The goal of the TRIC experiment [2] is the measurement of the total polarized cross section $\widetilde{\sigma}$ of the proton-deuteron scattering with vector polarization of the proton p_y^p and tensor polarization of the deuteron P_{xz} (see below Eq. (4)). As it was shown in Ref. [3], this observable constitutes a null-test of TVPC effects. According to [4], the experiment [2] will be done at beam energy 135 MeV. The aim of this experiment is to improve the results of previous measurement [5] on $\vec{n}^{167}$Ho scattering by one order of magnitude. In this case, detailed information on the ordinary T-even P-even spin observables at this energy is required in order to determine magnitude of possible false-effects caused by pure strong and Coulomb interaction due to non-ideal conditions of the experiment. However, experimental data on these observables at this energy are not complete. In the present work we use the Glauber theory to calculate unpolarized differential cross section and spin observables of the elastic *pd* scattering and total polarized *pd* cross sections. The spin-dependent formalism of the pd-elastic scattering is recently developed in Ref. [6]. The formalism includes full spin dependence of elementary pN-amplitudes and S- and D-components of the deuteron wave function. We further develop the formalism to account for Coulomb effects and TVPC interactions.

2 Elements of formalism

Assuming P-invariance the transition operator for the process $pd \to pd$ can be written as [7]

$$\begin{aligned} M = (A_1 + A_2\boldsymbol{\sigma}\hat{\mathbf{n}}) + (A_3 + A_4\boldsymbol{\sigma}\hat{\mathbf{n}})(\mathbf{S}\hat{\mathbf{q}})^2 + (A_5 + A_6\boldsymbol{\sigma}\hat{\mathbf{n}})(\mathbf{S}\hat{\mathbf{n}})^2 + A_7(\boldsymbol{\sigma}\hat{\mathbf{k}})(\mathbf{S}\hat{\mathbf{k}}) + \\ A_8(\boldsymbol{\sigma}\hat{\mathbf{q}})\left[(\mathbf{S}\hat{\mathbf{q}})(\mathbf{S}\hat{\mathbf{n}}) + (\mathbf{S}\hat{\mathbf{n}})(\mathbf{S}\hat{\mathbf{q}})\right] + (A_9 + A_{10}\boldsymbol{\sigma}\hat{\mathbf{n}})(\mathbf{S}\hat{\mathbf{n}}) + A_{11}(\boldsymbol{\sigma}\hat{\mathbf{q}})(\mathbf{S}\hat{\mathbf{q}}) + \\ A_{12}(\boldsymbol{\sigma}\hat{\mathbf{k}})\left[(\mathbf{S}\hat{\mathbf{k}})(\mathbf{S}\hat{\mathbf{n}}) + (\mathbf{S}\hat{\mathbf{n}})(\mathbf{S}\hat{\mathbf{k}})\right] \\ +(T_{13} + T_{14}\boldsymbol{\sigma}\hat{\mathbf{n}})\left[(\mathbf{S}\hat{\mathbf{k}})(\mathbf{S}\hat{\mathbf{q}}) + (\mathbf{S}\hat{\mathbf{q}})(\mathbf{S}\hat{\mathbf{k}})\right] + T_{15}(\boldsymbol{\sigma}\hat{\mathbf{q}})(\mathbf{S}\hat{\mathbf{k}}) + T_{16}(\boldsymbol{\sigma}\hat{\mathbf{k}})(\mathbf{S}\hat{\mathbf{q}}) + \\ T_{17}(\boldsymbol{\sigma}\hat{\mathbf{k}})\left[(\mathbf{S}\hat{\mathbf{q}})(\mathbf{S}\hat{\mathbf{n}}) + (\mathbf{S}\hat{\mathbf{n}})(\mathbf{S}\hat{\mathbf{q}})\right] + T_{18}(\boldsymbol{\sigma}\hat{\mathbf{q}})\left[(\mathbf{S}\hat{\mathbf{k}})(\mathbf{S}\hat{\mathbf{n}}) + (\mathbf{S}\hat{\mathbf{n}})(\mathbf{S}\hat{\mathbf{k}})\right], \end{aligned} \tag{1}$$

were $\boldsymbol{\sigma}$ is the Pauli matrix acting on the spin state of the proton beam, $\mathbf{S}$ is the spin operator of the deuteron; the unit vectors $\hat{\mathbf{q}}$, $\hat{\mathbf{k}}$, $\hat{\mathbf{n}}$ are defined through initial $\mathbf{p}$ and final $\mathbf{p}'$ momenta as $\hat{\mathbf{q}} = (\mathbf{p} - \mathbf{p}')/|\mathbf{p} - \mathbf{p}'|$, $\hat{\mathbf{k}} = (\mathbf{p} + \mathbf{p}')/|\mathbf{p} + \mathbf{p}'|$, $\hat{\mathbf{n}} = [\hat{\mathbf{k}} \times \hat{\mathbf{q}}]/|[\hat{\mathbf{k}} \times \hat{\mathbf{q}}]|$; $A_1 \div A_{12}$ are T-even P-even invariant amplitudes introduced in Ref. [6], $T_{13} \div T_{18}$ are T-odd P-even (TVPC) amplitudes. The reference frame is defined as $OZ \uparrow\uparrow \hat{\mathbf{k}}$, $OX \uparrow\uparrow \hat{\mathbf{q}}$, $OY \uparrow\uparrow \hat{\mathbf{n}}$. Under T-invariance conditions $T_{13} = T_{14} = T_{15} = T_{16} = T_{17} = T_{18} = 0$ the following relations between spin transfer coefficients are valid [7]

$$\begin{aligned} K_x^z(\vec{p} \to \vec{p}) = -K_z^x(\vec{p} \to \vec{p}),\ K_x^z(\vec{p} \to \vec{d}) = -K_z^x(\vec{d} \to \vec{p}), \\ K_x^z(\vec{d} \to \vec{p}) = -K_z^x(\vec{p} \to \vec{d}),\ K_x^z(\vec{d} \to \vec{d}) = -K_z^x(\vec{d} \to \vec{d}). \end{aligned} \tag{2}$$

In addition the relations $A_y^p = P_y^p$ and $A_y^d = P_y^d$ are also valid, where A_y^p (A_y^d) is the vector analyzing power for the proton (deuteron) and P_y^p (P_y^d) is the polarization of the final proton (deuteron) for the case of unpolarized initial particles.

In general case TVPC NN interaction contains 18 different terms [8]. We consider here only following terms which were under discussion in Ref. [4]:

$$\begin{aligned} t_{pN} = h[(\boldsymbol{\sigma} \cdot \mathbf{p})(\boldsymbol{\sigma}_N \cdot \mathbf{q}) + (\boldsymbol{\sigma}_N \cdot \mathbf{p})(\boldsymbol{\sigma} \cdot \mathbf{q}) - (\boldsymbol{\sigma}_N \cdot \boldsymbol{\sigma})(\mathbf{p} \cdot \mathbf{q})] + \\ +g[\boldsymbol{\sigma} \times \boldsymbol{\sigma}_N] \cdot [\mathbf{q} \times \mathbf{p}] + g'(\boldsymbol{\sigma} - \boldsymbol{\sigma}_N) \cdot i\,[\mathbf{q} \times \mathbf{p}][\boldsymbol{\tau} \times \boldsymbol{\tau}_N]_z. \end{aligned} \tag{3}$$

Here $\boldsymbol{\sigma}$ ($\boldsymbol{\sigma}_N$) is the Pauli matrix acting on the spin state of the proton (nucleon $N = p, n$), $\boldsymbol{\tau}$ ($\boldsymbol{\tau}_N$) is the corresponding matrix acting on the isospin state, $\mathbf{q} = \mathbf{p} - \mathbf{p}'$. In the framework of the phenomenological meson exchange interaction the term g' corresponds to $\rho-$meson exchange, and h-term provides the axial meson exchange. In the single scattering approximation accounting S- and D- waves of the deuteron we obtain only two non-zero amplitudes: T_{15} and T_{16} [7]. Other TVPC amplitudes vanish in this case: $T_{13} = T_{14} = T_{17} = T_{18} = 0$. The charge-exchange g'-term gives zero-contribution because the corresponding isospin matrix element equals zero for the single scattering mechanism of the $pd \to pd$ process.

In collinear kinematics the transition operator (1) contains only four terms (invariant spin amplitudes) for the case of T-even P-even interaction and one additional term for T-odd P-even interactions. Consequently, the total cross section of the pd interaction takes the form

$$\sigma_{tot} = \sigma_0 + \sigma_1 \mathbf{p}^p \cdot \mathbf{p}^d + \sigma_2 (\mathbf{p}^p \cdot \hat{\mathbf{k}})(\mathbf{p}^d \cdot \hat{\mathbf{k}}) + \sigma_3 P_{zz} + \widetilde{\sigma} p_y^p P_{xz}^d, \tag{4}$$

where $\mathbf{p}^p$ ($\mathbf{p}^d$) is the vector polarization of the initial proton (deuteron) and P_{zz} and P_{xz} are the tensor polarizations of the deuteron. The OZ axis is directed along the proton beam

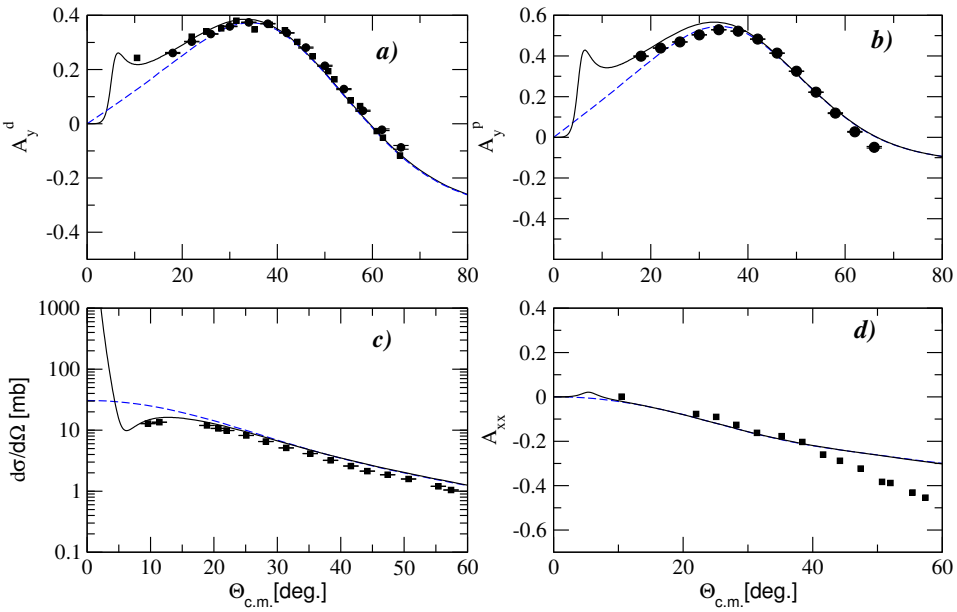

Figure 1: Result of our calculations [10] of spin observables A_y^d(a), A_y^p (b), $d\sigma/d\Omega$ (c) and A_{xx} (d) of the *pd* elastic scattering in comparison with the data [11] (squares) and [12] (circles) at 135 MeV: without Coulomb (dashed line) and with Coulomb included (full).

momentum. In Eq. (4) the terms σ_i with $i = 0, 1, 2, 3$ are non-zero only for T-even P-even interaction and the last term $\widetilde{\sigma}$ is non-zero if the T-odd P-even interaction effects occur. Thus, this term constitutes a null-test signal of T-invariance violation with P-parity conservation. The total hadronic polarized cross sections σ_1 and σ_3 are calculated using the optical theorem, whereas Coulomb effects are taken into account in the line of Ref. [9].

3 Numerical results and discussion

The detailed formalism for T-even P-even amplitudes $A_1 \div A_{12}$ was developed within the Glauber model in Ref. [6] taking into account single and double scattering mechanisms, S- and D-components of the deuteron wave function and full spin dependence of the elementary pN scattering amplitudes. We use this formalism to calculate spin observables of the *pd*-elastic scattering at energy of the TRIC experiment, i.e. $T = 135$ MeV. In addition to Ref. [6] we take into account the Coulomb interaction, as explained in [10] within the single scattering mechanism. Some results of numerical calculations performed with the Cd Bonn wave function of the deuteron are shown in Fig. 1. One can see from this figure, that the Glauber model allows to explain data on unpolarized cross section, vector analyzing powers A_y^p, A_y^d and tensor analyzing power in forward hemisphere. Accounting for the Coulomb interaction is very important at these energies and considerably improves the agreement with the experimental data [11, 12] at small c.m.s. scattering angles $\theta_{cm} < 20^\circ - 30^\circ$. We can show [10] that good agreement was obtained also between this theory and the data [12] on spin-correlation coefficients $C_{xz,y}$, $C_{y,y}$,

$C_{x,z}$, and $C_{z,x}$ of the pd elastic scattering at 135 MeV in forward hemisphere.

The constants g and h in Eq. (3) are chosen here in such a way that the absolute value of the integrated cross section $\tilde{\sigma}$ in Eq. (4) would be $\tilde{\sigma}/\sigma_0 = 10^{-6}$. One should note that the aim of the TRIC experiment is to get an upper limit for the TVPC signal $\tilde{\sigma}$ just at this level. We show [7] that in this case the maximal magnitudes of the violation of the relations (2) (in forward hemisphere, $\theta_{cm} < 50^\circ$) are $2 \div 3 \times 10^{-4}$ for $|K_x^z(p \to d) + K_z^x(d \to p)|$, $|A_y^p - P_y^p| \sim 3 \times 10^{-5}$ and much more lower for others relations. Thus, $|K_x^z(p \to d) + K_z^x(d \to p)|$ is by two orders of magnitude higher than $\tilde{\sigma}/\sigma_0$. Nevertheless, the null-test observable $\tilde{\sigma}$ can be measured in one experiment, whereas measurement of $|A_y^p - P_y^p|$ and $|K_x^z(pd) + K_z^x(dp)|$ requires two or more experiments with measurement of polarizations of final particles.

Let us consider possible problems in measurement of the null-test observable $\widetilde{\sigma}$. One source of false-effects is connected with non-zero projection of the vector polarization of the deuteron $p_y^d \neq 0$ onto direction of the vector polarization of the proton beam p_y^p. In this case the term $\sigma_1 p_y^p p_y^d$ in Eq. (4) contributes to the asymmetry $A_{xz,y}$ which is planned to be measured in the TRIC experiment [2] and corresponds to the cases $p_y^p P_{xz}^d > 0$ and $p_y^p P_{xz}^d < 0$. According to our calculation, at beam energy 135 MeV the total cross sections are $\sigma_0 = 78.5$ mb, $\sigma_1 = 3.7$ mb, $\sigma_2 = 17.4$ mb, and $\sigma_3 = -1.1$ mb. Therefore, the ratio $r = \sigma_1/\sigma_0$ is equal to ≈ 0.05. If the TRIC project is going to measure the ratio $R_T = \widetilde{\sigma}/\sigma_0$ with an uncertainty about $\leq 10^{-6}$ (an upper limit for R_T), then one can find from this ratio r that the vector polarization of the deuteron p_y^d has to be less than $\approx 2 \times 10^{-6}$. When making this estimation, we assume that the ratio of the background-to-signal is $p_y^d \sigma_1/\widetilde{\sigma} \sim 10^{-1}$.

4 Summary

We found that the Glauber model with Coulomb interaction taken into account reasonably explains existing data on unpolarized differential cross section and some spin observables of pd elastic scattering at 135 MeV in forward hemisphere. This provides a theoretical basis for estimation of possible false-effects in the TRIC experiment [2] planned at this energy.

References

[1] I.B. Khriplovich, Nucl. Phys. **B352** 385 (1991).

[2] COSY Proposal N 215, "Test of Time reversal invariance in proton-deuteron scattering at COSY", Spokespersons: D. Eversheim, B. Lorentz, Yu. Valdau, available from http://donald.cc.kfa-juelich.de/wochenplan/List of all COSY-Proposals.shtml.

[3] H.E. Conzett, Phys. Rev. **C48** 423 (1993).

[4] M. Beyer, Nucl. Phys. **A560** 906 (1993).

[5] P.R. Huffman *et al.*, Phys. Rev. **C55** 2684 (1997).

[6] M.N. Platonova, V.I. Kukulin, Phys. Rev. **C81** 014004 (2010).

[7] A.A. Temerbayev, Yu.N. Uzikov, Izv. Ross. Akad. Nauk Ser. Fiz. (2015) (in press).

[8] P. Herczeg, Nucl. Phys. **75** 655 (1966).

[9] Yu.N. Uzikov, J. Haidenbauer, Phys. Rev. **C79** (2009) 024617.

[10] A.A. Temerbayev, Yu.N. Uzikov, Yad. Fiz. **78** 38 (2015).

[11] K. Sekiguchi *et al.*, Phys. Rev. **C65** 034003 (2002).

[12] B. von Przewoski *et al.*, Phys. Rev. **C74** 064003 (2006).

Parity Violation Inelastic Scattering Experiments at 6 GeV and 12 GeV Jefferson Lab

Vincent Sulkosky[1] for the JLab PVDIS and SoLID collaborations

[1]University of Virginia, Charlottesville, Virginia 22904, USA

DOI: http://dx.doi.org/10.3204/DESY-PROC-2014-04/257

We report on the measurement of parity-violating asymmetries in the deep inelastic scattering and nucleon resonance regions using inclusive scattering of longitudinally polarized electrons from an unpolarized deuterium target. The effective weak couplings C_{2q} are accessible through the deep-inelastic scattering measurements. Here we report a measurement of the parity-violating asymmetry, which yields a determination of $2C_{2u}$ - C_{2d} with an improved precision of a factor of five relative to the previous result. This result indicates evidence with 95% confidence that the $2C_{2u}$ - C_{2d} is non-zero. This experiment also provides the first parity-violation data covering the whole resonance region, which provide constraints on nucleon resonance models. Finally, the program to extend these measurements at Jefferson Lab in the 12 GeV era using the Solenoidal Large Intensity Device was also discussed.

1 Introduction

In parity-violating electron scattering (PVES), the PV asymmetry is given by the expression: $A_{PV} = \frac{\sigma_R - \sigma_L}{\sigma_R + \sigma_L}$, where σ_R (σ_L) represents the cross-section for scattering longitudinally polarized right-handed (left-handed) electrons. This observable is highly sensitive to studies beyond the standard model physics and the structure of both nuclei and nucleons [1]. In deep inelastic scattering (DIS), the asymmetry can be expressed (mostly model-independent) in terms of the variables $a_{1,3}\left(x, Q^2\right)$, which are related to the subatomic structure of the nucleus and the neutral-weak axial and vector coupling of the electron and the quark. Here, x is the Bjorken scaling variable, and Q^2 is the four-momentum transferred squared.

In the approximation where the electron exchanges only a single photon or Z boson with the target, simple expressions for $a_{1,3}$ can be expressed for a deuteron target in the valence quark model:

$$a_1 = \frac{6}{5}\left(2C_{1u} - C_{1d}\right), a_3 = \frac{6}{5}\left(2C_{2u} - C_{2d}\right).$$

The $C_{1u(1d)}$ and $C_{2u(2d)}$ represent the effective weak couplings between electrons and up (down) quarks. Sometimes, they are collectively expressed as C_{1q} and C_{2q}. The indices 1 and 2 correspond to if the coupling to the electron or quark is vector or axial-vector. C_{1q} is the (AV) combination of the electron's axial-vector weak charge and the quark's vector weak charge. Then C_{2q} is the (VA) combination of the electron's vector weak charge and the quark's axial-vector weak charge. The C_{2q} is sensitive to PV due to the quark chiral states and can only be direclty accessed in DIS, whereas, C_{1q} can also be obtained from elastic PVES. SLAC E122 [2] was

the first PVES experiment and provided the first measurement for $\sin^2\theta_w$. It also established the gauge model of Weinberg, Glashow, and Salam as the correct theory for the electroweak interactions.

2 Experimental Procedure

The measurements reported at the conference were conducted using a 5−6 GeV longitudinally-polarized electron beam at Jefferson Lab. The beam current was ~ 100 μA with approximately 90% polarization. The electron beam was incident on a 20-cm long liquid deuterium target controlled at a temperature of 22 K. The scattered electrons were detected in a pair of spectrometers [3] that provided high precision measurements of their momentum and angle. For the majority of the run period, the spectrometers were set to detect DIS electrons [4]. However, additional data were also collected in four kinematic settings, which covered the entire nucleon resonance region [5]. Besides providing constraints on nucleon resonance models, these data also exhibited a feature known as "quark-hadron duality" [6] for electroweak observables for the first time.

3 Results

3.1 Nucleon resonance region

Figure 1 shows the measured PV asymmetries, scaled by $1/Q^2$, from $\vec{e}$-^{2}H scattering in the resonance region versus W. The vertical error bars represent the statistical uncertainties, whereas the horizontal bars indicate the RMS value of the W coverage for each bin. The shaded band near the bottom of the graph shows the experimental systematic uncertainties. The measured asymmetries are consistent with the three resonance models [7, 8, 9]. In Fig. 1, theory A (dashed lines), theory B (dotted lines) and theory C (solid lines) correspond to Refs. [7], [8] and [9], respectively. In the case of Theories B and C, there are three curves, which indicate the upper and lower bands and central values of the two calculations. These data also agree well with the DIS estimation (dash-double-dotted lines) using CTEQ-Jefferson Lab (CJ) [10] parton distribution fuction (PDF) fits. This agreement with the DIS calculation indicates that quark-hadron duality holds at the 10−15% level throughout the entire resonance region.

3.2 Deep inelastic region

In Fig. 2, the correlation plot of $2C_{2u}$ - C_{2d} versus $2C_{1u}$ - C_{1d} at $Q^2 = 0$ is shown as extracted from the measured asymmetry. The details of the extraction are presented in Ref. [4]. The new results are represented by the ellipse labeled "This measurement", and the results on $2C_{2u}$ - C_{2d} deviate from zero by 2σ. The yellow ellipse shows the results from the SLAC 122 experiment. The vertical band is the latest C_{1q} results [11]. The red ellipse is the combined result from all published measurements. The standard model expected value is represented by the black dot, which is in good agreement with all measured results.

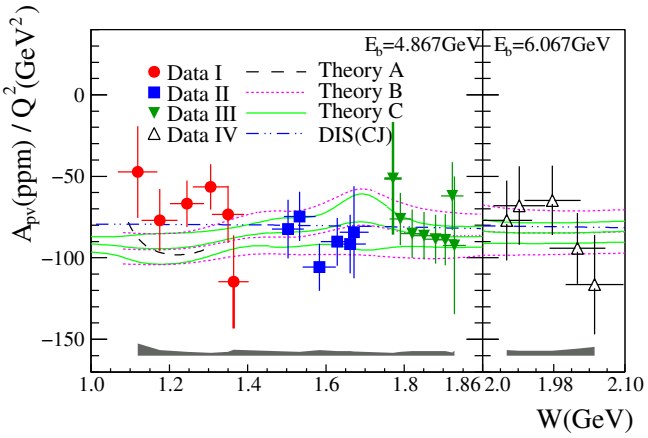

Figure 1: Invariant mass dependence of the measured $\vec{e}$-^{2}H parity-violating asymmetries in the nucleon resonance region. See text for details. Reproduced from Ref. [5].

4 Future Perspectives

With the upgrade of the Jefferson Lab electron beam, the PVDIS program will continue with the Solenoidal Large Intensity Device (SoLID) [12]. This device is a multi-purpose spectrometer with physics topics including PVDIS on proton and deuteron targets, semi-inclusive DIS on polarized proton and ^{3}He targets and threshold J/ψ production. The main motivation for the PVDIS experiment is to investigate possible new interactions beyond the Standard Model and to measure the PDF ratio d/u at high x. The experiment will obtain data over a wide kinematic range: $x > 0.2$, 2 GeV^2 $< Q^2 <$ 10 GeV^2 and will improve the measurement of the effective weak couplings by one order of magnitude compared with the 6 GeV results presented here.

5 Summary

In conclusion, recent results on the parity-violating asymmetries over the whole nucleon resonance region and in the deep-inelastic regime are reported. We have improved our knowledge on the electron-quark VA effective coupling term $2C_{2u}$ - C_{2d} by a factor of five. Our result is in agreement with the standard model prediction and is the first evidence that $2C_{2u}$ - C_{2d} deviates from zero at the 2σ level. Additionally, the nucleon resonance asymmetries agree with DIS-based calculations, indicating for the first time that quark-hadron duality may also exists in electroweak observables. The resonance data provide constraints on nucleon resonance models, which are relevant for background estimations to elastic PVES measurements. Finally, the construction of SoLID, to be used with the upgraded Jefferson Lab 12-GeV electron beam, will allow us to continue these measurements and improve our knowledge on C_{2q} by another order of magnitude.

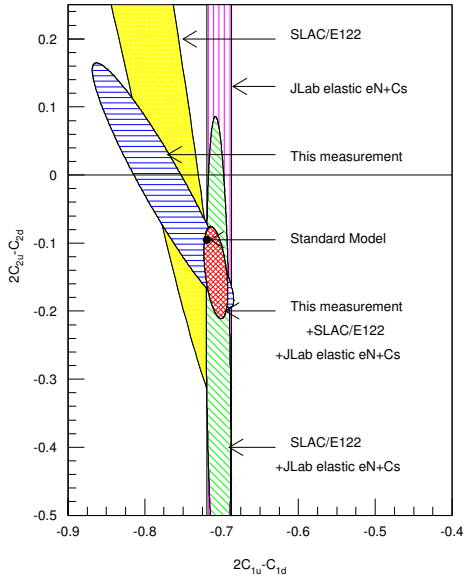

Figure 2: (color online) Comparison of current results (blue ellipse) compared with earlier experiments for the effective weak couplings. See text for details. Reproduced from Ref. [4].

Acknowledgments

This work was supported in part by the Jeffress Memorial Trust under Grant no. J-836, the U.S. National Science Foundation under grant no. 0653347, and the U.S. Department of Energy under award nos. DE-SC0003885 and DE-AC02-06CH11357. This work was authored by Jefferson Science Associates, LLC under U.S DOE contract no. DE-AC05-06OR23177. The U.S. Government retains a nonexclusive, paid-up irrevocable, world-wide license to publish or reproduce this manuscript for U.S. Government purposes.

References

[1] D.S. Armstrong and R.D. McKeown, Annu. Rev. Nucl. Part. Sci. **62** 337 (2012).
[2] C.Y. Prescott *et al.*, Phys. Lett. B **77** 347 (1978); C.Y. Prescott *et al.*, Phys. Lett. B **84** 524 (1979).
[3] J. Alcorn *et al.*, Nucl. Instrum. Meth. **A522** (2004) 294.
[4] D. Wang *et al.*, Nature **506** 7486 67 (2014).
[5] D. Wang *et al.*, Phys. Rev. Lett. **111** 082501 (2013).
[6] E.D. Bloom and F.J. Gilman, Phys. Rev. Lett. **25** (1970) 1140.
[7] K. Matsui, T. Sato, and T.-S.H. Lee, Phys. Rev. C **72** 025204 (2005).
[8] M. Gorchtein, C.J. Horowitz, and M.J. Ramsey-Musolf, Phys. Rev. C **84** 015502 (2011).
[9] N.L. Hall, P.G. Blunden, W. Melnitchouk, A.W. Thomas, and R.D. Young, Phys. Rev. D **88** 013011 (2013).
[10] J.F. Owens, A. Accardi, and W. Melnitchouk, Phys. Rev. D. **87** 094012 (2013).
[11] D. Androic *et al.*, Phys. Rev. Lett. **111** 141803 (2013).
[12] J.-P. Chen *et al.*, arXiv:1409.7741.

Latest results of MEG and status of MEG-II

Francesco Renga[1] for the MEG Collaboration

[1]INFN - Sez. di Roma, P.le A. Moro 2, 00185 Roma, Italy

DOI: http://dx.doi.org/10.3204/DESY-PROC-2014-04/38

Within the Standard Model, in spite of neutrino oscillations, the flavor of charged leptons is conserved in very good approximation, and therefore charged Lepton Flavor Violation is expected to be unobservable. On the other hand, most new physics models predict charged Lepton Flavor Violation within the experimental reach, and processes like the $\mu \to e\gamma$ decay became standard probes for physics beyond the Standard model. The MEG experiment, at the Paul Scherrer Institute (Switzerland), searches for the $\mu \to e\gamma$ decay, down to a Branching Ratio of about 5×10^{-13}, exploiting the most intense continuous muon beam in the world and innovative detectors. In this talk I will present the latest results from MEG, and the status of its upgrade (MEG-II), aiming at an improvement of the sensitivity by one order of magnitude within this decade.

1 Introduction

Charged lepton flavor conservation is an accidental symmetry in the standard model (SM), not related to the gauge structure of the theory, but following from the particle content of the model. As a consequence, this conservation is naturally violated in most of the extensions of the standard model. Indeed, LFV in the charged lepton sector (cLFV) is expected in the SM due to neutrino oscillations, but the expected branching ratios for LFV decays ($< 10^{-40}$) are predicted to be well below the current experimental sensitivities. Hence, an observation of cLFV would be an unambiguous evidence of new physics (NP) beyond the SM.

Among the NP models predicting cLFV at observable levels, Supersymmetry (SUSY) is of particular interest: even if the theory is developed to be flavor blind at the high energy scale, cLFV arises at the electroweak scale through renormalization group equations, and hence it is essentially unavoidable. Moreover, many SUSY models predict a strong correlation between cLFV and the possible deviation of the muon $g-2$ from its SM prediction. Anyway, the expected branching ratios strongly depend on the specific flavor structure of the model. Recent limits on $\mu \to e\gamma$ already rule out several scenarios still allowed by direct searches at LHC but nonetheless, even within the same models, a different flavor structure can predict rates not yet explored, and within the reach of the next generation of cLFV experiments (see [1] for a specific model with flavored gauge mediation).

I will report here the latest results for the search of $\mu \to e\gamma$ with the MEG experiment, and the status of its upgrade MEG-II.

2 The quest for $\mu^+ \to e^+\gamma$ with the MEG experiment

The MEG experiment [2], at the Paul Scherrer Institut (PSI, Switzerland), exploits the most intense continuous muon beam in the world (up to 10^8 muons per second) to search for the $\mu^+ \to e^+\gamma$ decay. Positive muons are stopped in a thin plastic target, and hence the signature of the $\mu^+ \to e^+\gamma$ decay is given by a positron and a photon, monochromatic (~ 52.8 MeV), emitted at the same time, and back-to-back. Although a prompt background is given by the radiative $\mu \to e\nu\overline{\nu}\gamma$ decay, the largely dominant background, when operating with with very high muon beam intensity, is given by the accidental coincidence of a positron from a muon decay with a photon from another muon decay (radiative decay or annihilation in flight of the positron). The background rate is then proportional to the square of the muon rate, making useless a further increase of the muon rate as soon as the background expected in the signal region becomes relevant. For this reason, the MEG experiment is operated with $\sim 3 \times 10^7$ muons per second, which is found to be an optimal value for our setup.

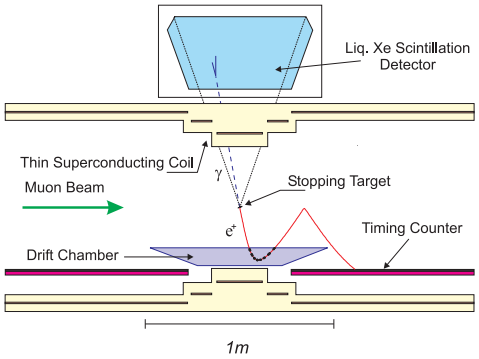

Figure 1: The MEG detector.

The MEG detector is shown in Figure 1. Positron are reconstructed in MEG by a system of 16 planar drift chamber in a gradient magnetic field, with its main component along the beam axis, and a system of 30 scintillating bars for timing and trigger. The gradient magnetic field is necessary to prevent tracks emitted at almost 90 degrees with respect to the beam axis to make several turns within the spectrometer before exiting the detector. The drift chambers reached a resolution of ~ 300 μm in the radial direction and ~ 1 mm along the beam axis, resulting into a core momentum resolution of ~ 330 keV and angular resolutions of ~ 10 mrad. The timing counter allows to measure the positron time with a resolution of ~ 70 ps. The overall positron efficiency is $\sim 30\%$, and it is largely dominated by the loss of positrons in the path from the drift chamber system to the timing counter.

Photons are reconstructed by a liquid Xenon detector instrumented with 856 PMTs. It measures the energy, the time and the conversion point of the photon, with resolutions of ~ 900 keV in the bulk region of the detector, 70 ps and $\lesssim 6$ mm.

The decay vertex is defined by the intersection of the positron track with the target, while the direction from the vertex to the photon conversion point is taken as the photon direction to determine the relative $e\gamma$ angle.

Electronic waveforms from all detectors are fully digitized at GS/s rates thanks to the DRS4 chip developed at PSI. A fully digital trigger system has been developed, exploiting energy, time and position measurements in the Xenon detector and time measurement in the timing counter.

Several calibrations are necessary to reach and measure the mentioned resolutions. Among them, it is worth to mention the use of a pion beam, along with an ancillary photon detector to select back to back photon pairs in the reaction chain $\pi^- + p \to \pi^0 + n$, $\pi^0 \to \gamma\gamma$. Kinematics make the selected positrons almost monochromatic, with an energy of about 55 MeV, very near to the signal photon energy. This is used to calibrate the absolute energy scale of the calorimeter, which is then monitored periodically with low energy photons from proton-induced nuclear reactions, in order to finally get a 0.2% accuracy on the energy scale.

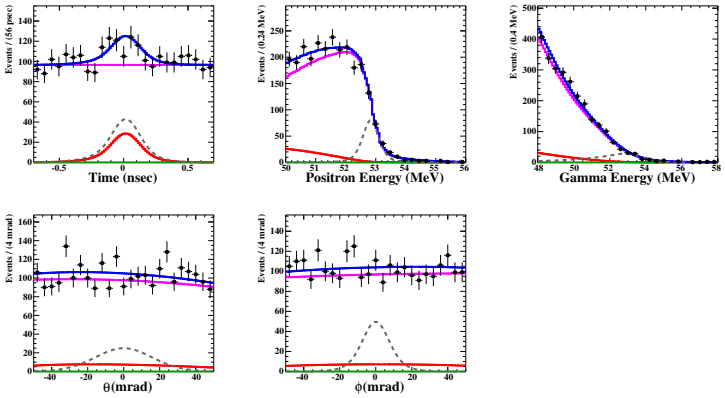

Figure 2: Result of the fit (blue) to the 2009-2011 data (black dots with error bars). Contributions from accidental background (blue), radiative decay background (red) and signal (green) are shown. The signal PDFs for a branching ratio of 3×10^{-11} are also shown for reference (gray).

A likelihood analysis is used for the search of $\mu \to e\gamma$. Five discriminating variables are used: the positron energy E_e, the photon energy E_γ, the relative time $T_{e\gamma}$ and the projections of the relative angle angle $\phi_{e\gamma}$ and $\theta_{e\gamma}$. The signal Probability Distribution Functions (PDFs) are obtained by combining the measured resolution, as well as the PDFs for the radiative muon decays. Conversely, the PDFs for the accidental background are fully extracted from data, using sideband regions defined in the E_γ vs. $T_{e\gamma}$ plane. In the construction of the PDFs we take into account several correlations in the positron PDFs, which emerge from geometrical effects and are well understood both qualitatively and quantitatively. The results of the likelihood fit, based on the data collected in the 2009-2011 period ($\sim 36 \times 10^{13}$ muons stopped in the target), are shown in Figure 2 [3]. No significant signal is observed, and an upper limit on the number of signal events has been extracted at 90% confidence level, with a frequentistic approach based on a profile likelihood ratio. This is combined with a normalization factor obtained by counting the number of Michel positrons reconstructed in the spectrometer and, including all systematics (dominated by the uncertainties on the PDFs for the relative angle), an upper limit of 5.7×10^{-13} is obtained for the $\mu \to e\gamma$ branching ratio, to be compared with an expected limit of 7.7×10^{-13} (from toy Monte Carlo studies).

The MEG experiment collected data in 2012 and 2013, and doubled the available statistics. Several improvements have been included in the on going analysis of these data: refined algorithms allowed to increase the efficiency for tracks making several turns within the spectrometer; a more accurate measurement if the magnetic field has been performed in order to

reduce the corresponding systematic uncertainties; an algorithm for the recognition of photons coming from positron annihilation in flight has been introduced, in order to suppress the main contribution to the background at large photon energies. Although the determination of the final sensitivity is still ongoing, an expected upper limit below 5×10^{-13} is foreseen.

3 Status of MEG-II

As already mentioned, many NP models predict a $\mu \to e\gamma$ branching ratio not far from the current limit. Hence, a short term upgrade to improve the sensitivity of MEG of about one order of magnitude is worth the effort. As shown in [4], the upgraded experiment will be competitive with the first phase of the experiments searching for $\mu \to e$ conversion in the field of nuclei, if cLFV arises from magnetic-moment operators, $\mathcal{L} \propto \overline{\mu}_R \sigma_{\mu\nu} e_L F^{\mu\nu}$, like in supersymmetry.

The upgrade of the MEG experiment will involve all the subdetectors. The system of 16 drift chambers will be replaced with a unique cylindrical drift chamber with stereo wires. The chamber will be operated with a light mixture of Helium and Isobutane (85%:15%) to reduce the material budget, and will cover all the path of the track to the timing counter, in order to recover the large inefficiency observed in MEG. A single hit resolution of about 120 μm is expected and confirmed by measurements with different prototypes in different environments (cosmic rays and positron beams). Given the stereo angle, it will give a resolution below 1 mm along the beam axis. A momentum resolution of 130 keV and angular resolutions of about 5 mrad are expected.

The Timing Counter will be replaced by about 500 scintillating tiles read out by Silicon Photomultipliers (SiPM). Tests with positron beams confirmed that a time resolution of about 30 ps can be reached combining the time measurements of the tiles hit by each track.

The PMTs in the inner face of the liquid Xenon calorimeter will be replaced with SiPMs, specifically developed to be sensitive to ultra-violet scintillation light of Xenon. The improved granularity will allow to improve the resolutions for photons converting just after entering the calorimeter (*shallow events*) and the capability of detecting pileup photons. Moreover, the geometry of the lateral faces will be changed in order to increase the fiducial volume and better control the reflection of the scintillation light. The energy resolution is expected to go down to 1%. Finally, a new DAQ board is under development, still based on the DRS4 chip, in order to handle the increased number of channels within the limited space of the MEG experimental hall.

The upgraded detectors are presently under construction and are expected to be ready for an engineering run at the end of 2015 and for physics runs in 2016. A three-year data taking campaign is foreseen, with an optimal muon rate which should reach 7×10^7 muons per second, thanks to the improved resolutions. An expected upper limit of about 4×10^{-14} is finally envisaged.

References

[1] L. Calibbi *et al.*, arXiv:1408.0754 [hep-ph] (2014).

[2] J. Adam *et al.*, Eur. Phys. J. **C73** 2365 (2013).

[3] J. Adam *et al.*, Phys. Rev. Lett. 110 201801 (2013).

[4] A. M. Baldini *et al.*, arXiv:1301.7225 [physics.ins-det] (2013).

Parity-Violating Electron Scattering

Krishna S. Kumar for the MOLLER collaboration

Department of Physics and Astronomy, Stony Brook University, USA

DOI: http://dx.doi.org/10.3204/DESY-PROC-2014-04/255

Measurements of parity-violating asymmetries in the scattering of longitudinally polarized electrons off unpolarized fixed targets are used to access leptonic and semi-leptonic weak neutral current amplitudes. One thrust of the current program is the measurement the elastic neutral weak amplitude at very low Q^2 from scattering off a heavy spinless nucleus, which is sensitive to the presence of a neutron skin. A second major thrust is the neutral current elastic amplitude at very low Q^2 off protons and electrons and in the DIS regime off deuterium, which allows precision measurements of the weak mixing angle at low energy and is thus sensitive to new physics beyond the Standard Model.

1 Introduction

The technique of electron scattering has been used for more than sixty years to study nuclear and nucleon structure using the experimental cleanliness and well-understood theory of electromagnetic interactions. Soon after parity-violation in the weak interactions was demonstrated, Zel'dovich noted that if an analogous neutral interaction existed, then parity violation would be manifested in longitudinally polarized lepton scattering off unpolarized nucleons due to the interference between the weak and electromagnetic amplitudes. He estimated that the parity-vioating asymmetry A_{PV} would be of order $10^{-4}Q^2$ (GeV)^2.

For typical fixed target experiments, A_{PV} ranges from roughly 10^{-4} to as small as 10^{-7}. Parity violation in deep inelastic electron nucleon scattering was first observed at SLAC [1], consituting an important test of the SU(2)×U(1) gauge theory of electroweak interactions. Over the past 30 years, the experimental techniques employed to measure these tiny left-right asymmetries have been steadily refined such that statistical and systematic errors better than 1 part per billion (ppb) are possible [2, 3].With judiciously chosen targets and kinematics, this has facilitated measurements in several important physics topics, such as many-body nuclear physics, nucleon structure and searches for physics beyond the standard model at the TeV scale. In this review, we discuss the ongoing research program and future prospects.

2 Neutron Skin of a Heavy Nucleus

In a heavy nucleus such as ^{208}Pb, the fractional difference between neutron radius R_n and proton radius R_p is believed to be several percent. Analogous to the classic measurement of R_p via elastic electron electromagnetic scattering, R_n can be measured via parity-violating electron scattering [4]. The parity violating asymmetry in elastic scattering off a heavy spinless nucleus is proportional to the ratio of the neutron to proton form factors since the weak neutral current

coupling of protons is much smaller than that of neutrons. Experimentally, there is some controversy as to how well R_n is known [5]; the best guess is $\sim 5\%$. A precise measurement of R_n can have impact on nuclear theory, atomic parity violation [6] and neutron star structure [7].

With the improvements made on the control of helicity-correlated beam fluctuations, it became feasible to make a measurement of $A_{\rm PV}$ in elastic scattering off a ^{208}Pb target. For a beam energy of 1.05 GeV and a scattering angle of 6° and $Q^2 \sim 0.01$ GeV^2, A_{PV} is of order 0.6 ppm. A 3% measurement of A_{PV} leads to a 1% measurement of R_n. A new experimental project known as PREX was approved and carried out a first data run at Jefferson Laboratory in 2010. The experiment ran for about 10 weeks in the spring of 2010. Statistics for a 9% A_{PV} measurement and a 3% R_n determination was accumulated [8]. After corrections for beam fluctuations, the grand average was found to be 594 ± 50 parts per billion (ppb). After normalizing to the beam polarization and subtracting background, the PREX result is $A_{PV} = 656 \pm 60$ (stat) ± 14 (syst) ppb.

The measured result corresponds to a value for the neutron skin of $R_n - R_p = +0.33^{+0.16}_{-0.18}$ fm. While the result demonstrates that the neutron RMS radius is 2σ larger than that of the protons the result is not yet precise enough to discriminate between various models based on mean field theory and other observables. A followup proposal to obtain the remaining statistics required for a 1% R_n measurement by the PREX collaboration has been approved and will likely run in 2016. Two other attractive nuclei to explore R_n measurements are ^{48}Ca and $^{120/124}$Sn. In general low Z nuclei tend to have a higher figure of merit due to the fact that the optimum Q^2 at which one must make the A_{PV} measurement tends to increase, and the figure of merit rises with the square of the asymmetry times the count rate [9]. ^{48}Ca is particularly interesting because microscopic calculations may soon be feasible, which would allow R_n to be related to poorly studied 3-neutron forces. It turns out that ^{48}Ca is an ideal measurement at Jefferson Laboratory with a similar configuration to that used for PREX, except that the beam energy would be raised to 2.2 GeV, and an experimental proposal has recently been approved.

It is interesting to consider measurements of Pb and Sn at Mainz in the future, adapting the apparatus that would be required for a high precision proton weak charge measurement (see Sec. 3). It looks feasible to design the require apparatus for a 0.5% R_n measurement of ^{208}Pb [10]. The loss in rate due to the lower beam energy is roughly compensated by the larger available solid angle. The momentum resolution that would be required is about 1%, and a system of baffles could be used to isolate elastic events while rejecting background from inelastics as well as from neutrals [11].

3 Precision Weak Neutral Current Measurements

Precision measurements of the properties of W and Z bosons and their couplings to leptons and quarks have allowed sensitive tests of the electroweak theory. No significant deviation from Standard Model predictions have been found. Nevertheless, experiments continue to probe for the indirect effects of new physics at the TeV scale by making more and more precise measurements of electroweak parameters. Weak neutral current (WNC) interactions at $Q^2 \ll M_Z^2$ can probe for heavy Z$'$ bosons or leptoquarks whose effects might be highly suppressed in measurements on the Z pole [12], and for dark sector mediators that have small admixtures to the Z boson [13]. Since the neutral current amplitude at the Z pole is imaginary, there are no interference terms with new, real four-fermion amplitudes. At low Q^2 on the other hand, interference effects might be measurable if sufficient accuracy is achieved [2, 3, 14, 15].

A general, model-independent way to parametrize the contributions of contact interactions of high-mass particles to low-energy measurements of electron scattering off target fermions f is to use a Lagrangian [16] parametrized by coupling constants g_{ij} (i, $j = R$, L), and a mass scale Λ. The goal of low energy neutral current measurements is to reach sufficient sensitivity to access $\Lambda/g_{ij} \geq 1$ TeV for as many different initial and final state fermions and chiral combinations as possible, similar sensitivity yet complementary to that of the highest energy colliders.

Over the past couple of decades, the three published measurements with sufficient sensitive to probe the TeV-scale were the weak charge measurement in ^{133}Cs [17], the NuTeV neutrino deep-inelastic scattering measurement [18] and the measurement of $A_{\rm PV}$ in electron-electron (Møller) scattering [19] at SLAC. As we await the restart of the Large Hadron Collider (LHC) at full beam energy and design luminosity, improving these constraints and expanding their reach to include more fermion scattering combinations takes on increased significance. This is because such measurements will help narrow down the physics mechanisms that are responsible for any observed anomalies at the LHC.

The interactions of the Z-boson at low Q^2 can be approximated by four-fermion contact interactions. The parity-violating part of the electron-hadron interaction can then be given in terms of phenomenological couplings C_{ij}, where C_{1j} (C_{2j}) gives the vector (axial-vector) coupling to the j^{th} quark. In the Standard Model, all four couplings are functions of a single parameter: the weak mixing angle $\sin^2\theta_W$. The atomic Cesium weak charge measurement measured one combination of C_{1u} and C_{1d} precisely.

At sufficiently forward angles and low Q^2, the hadronic structure uncertainty in the WNC elastic electron-proton amplitude becomes small enough such that one can measure the underlying coherent $2u + d$ e-q amplitude combination to high precision, thus precisely constraining $2C_{1u}+C_{1d}$. This combination is proportional to $1-4\sin^2\theta_W$. A 4% measurement of A_{PV} would achieve a precision of $\delta(\sin^2\theta_W) = 0.0007$. This is the goal of the Qweak experiment [20] in Hall C at Jefferson Lab, which is reported on separately in these proceedings. The experiment has completed data-taking and published their first result based on commissioning data [21].

It would be highly complementary to obtain a new measurement of the proton weak charge with a new apparatus where the beam energy is smaller than 200 MeV. The dominant theoretical uncertainty in the prediction of A_{PV} is due to higher-order radiative corrections involving $\gamma - Z$ box diagrams. In order to compensate for the lower energy, it will be necessary to obtain data over the full range of the azimuth using a solenoidal spectrometer [11]. Such an experiment would be a flagship measurement of the proposed new MESA facility at Mainz. A measurement of A_{PV} with an ultimate goal of 2% overall error is compelling and seems feasible [22]

The upgrade of Jefferson Laboratory to 11 GeV will allow precision measurements in parity-violating deep inelastic scattering (PV DIS). One measurement using a 6 GeV beam and the existing high resolution spectrometers in Hall A has recently been published, and helped establish that the axial-quark couplings of light quarks to the Z boson are indeed non-zero [23]. A new dedicated high luminosity apparatus has been propopsed centered around a large superconducting solenoidal magnet [24]. This project, known as SoLID (Solenoidal Large Intensity Device), would allow $\sim 1\%$ measurements of A_{PV} for the first time over a range of x and Q^2 values, as high as $x \sim 0.7$ (x is the fraction of the nucleon momentum carried by the struck quark). PV DIS measurements with such accuracy and kinematic range provides access to novel aspects of nucleon structure, such as charge symmetry violation and investigation of higher-twist effects. Most importantly, PV DIS allows the isolation of the linear combination $2C_{2u} + C_{2d}$, which is difficult to measure using elastic scattering. A_{PV} in DIS can be written as as functions of two parameters $a(x)$ and $b(x)$, which are functions of the parton distributions $f_i(x)$ and the elec-

tromagnetic charges. For an isoscalar target such as deuterium, the dependence on structure largely cancels out in the A_{PV} ratio of the weak and electromagnetic amplitudes.

The measurement would test the WNC amplitude in the lepton-quark sector, where there is currently a discrepancy with the theoretical prediction in the NuTeV result. Secondly, combined with other measurements in elastic electron-proton scattering, precise constraints would be possible on the lesser known axial-vector quark couplings C_{2i}. This would, among other things, provide complementary constraints on various models with new heavy leptophobic Z' bosons [25] and leptoquarks [12]. More generally, the projected result for A_{PV}^D of 0.6% translates into a measurement of a specific linear combination of the phenomenological couplings C_{ij} to an accuracy of ± 0.0083, more than a factor of 30 better than the best current constraints. This translates into contact interaction scale reach $\gtrsim 2.5$ TeV.

The Feynman diagrams for electron-electron (Møller) scattering involve both direct and exchange diagrams that interfere with each other. A_{PV} for this process was first calculated in the late 70's [26] The electroweak theory prediction at tree level in terms of the weak mixing angle is $Q_W^e = 1 - 4\sin^2\theta_W$; this is modified at the 1-loop level [27, 28] and becomes dependent on the energy scale at which the measurement is carried out, *i.e.* $\sin^2\theta_W$ "runs". It increases by $\sim$3% compared to its value at the scale of the Z^0 boson mass, M_Z. The SLAC E158 experiment carried out the first measurement of parity violation in Møller scattering [19]. The grand average result for the parity-violating asymmetry in Møller scattering at $Q^2 = 0.03$ GeV^2 was found to be: $A_{\rm PV} = -131 \pm 14(\text{stat}) \pm 10(\text{syst})$ (ppb).. From the measured result, and assuming that the only contributing chiral structure comes from the $\Lambda_{\rm LL}$ term, the 95% C.L. limit is 7 TeV or 16 TeV depending on the sign of the contact interaction term.

There is strong motivation to make further improvements in the accuracy of weak neutral current coupling constants at low energy. Improved measurements would keep pace with the improved sensitivity for discovery at the multi-TeV scale by experiments at the Large Hadron Collider. With the upgrade of Jefferson Laboratory to 12 GeV, a new project called MOLLER (Measurement of Lepton-Lepton Electroweak Reaction) is being designed to improve on the SLAC E158 measurement of the weak charge of the electron Q_W^e by a factor of five. For the 2.3% total uncertainty envisioned, the sensitivity reach is $\frac{\Lambda}{\sqrt{|g_{RR}^2 - g_{LL}^2|}} = 7.5$ TeV. The strongest constraints on four-lepton contact interactions come from LEP 2, approaching 5 TeV for specific chiral combinations. However, the parity-conserving cross-sections and forward-backward asymmetries studied at LEP 2 are blind to the parity-violating combination $g_{RR}^2 - g_{LL}^2$ probed by MOLLER.

The prediction for MOLLER A_{PV} is 35.6 parts per billion (ppb). The goal is to measure this quantity to a statistical precision of 0.74 ppb and keep systematic errors to be significantly smaller, in order to achieve a 2.3% measurement of Q_W^e. MOLLER will greatly benefit from the steady improvement in the techniques employed to measure parity-violating asymmetries to sub-ppb systematic precision and to also achieve normalization control at the sub-% level. The MOLLER collaboration, a group of $\sim$ 100 authors, is currently developing the technical design of the apparatus, and is in the process of seeking project funding of order 20M$ from IS DoE, NSF and international funding agencies. The goal is to obtain construction funding by 2017 so that experiment commissioning and first data collection can take place by 2020.

4 Summary

Parity-violating electron scattering is a mature field and addresses fundamental questions in a variety of different topics. The E158 experiment at SLAC has produced the most precise measurement of the weak mixing angle at low energy. The Qweak experiment at Jefferson Laboratory is on track to make an improved weak mixing angle measurement. The two future proposals at Jefferson Laboratory, SoLID and MOLLER, will lead to important new insights on the structure of the nucleon and yield new and more precise measurements of the weak mixing angle and constitute flagship projects after the 12 GeV upgrade. It will be greatly beneficial to design and carry out a new measurement of the proton weak charge at Mainz that will improve on the Qweak experiment by a factor of 2.

In parallel, it is greatly motivated to carry out new measurements of A_{PV} on heavy nuclei to measure the ground-state neutron distribution. The PREX measurement is on-going and should produce a 1% measurement of the neutron radius in ^{208}Pb in a few years. In the long run, it will be very important to produce comparable measurements using Ca and Sn isotopes at Jefferson Laboratory and at Mainz. Finally, the proposed new MESA facility at Mainz has the potential to add important new measurements to the impressive list of parity-violation experiments in order to probe nuclear and nucleon structure and to search for physics beyond the Standard Model.

Acknowledgments

This work has been funded by a grant from the Division of Nuclear Physics at the US Department of Energy's Office of Science.

References

[1] C.Y. Prescott, W.B. Atwood, R. Leslie Cottrell, H.C. DeStaebler, Edward L. Garwin, et al. Parity Non-conservation in Inelastic Electron Scattering. *Phys.Lett.*, B77:347–352, 1978.

[2] K.S. Kumar, Sonny Mantry, W.J. Marciano, and P.A. Souder. Low Energy Measurements of the Weak Mixing Angle. *Ann.Rev.Nucl.Part.Sci.*, 63:237–267, 2013.

[3] Jens Erler, Charles J. Horowitz, Sonny Mantry, and Paul A. Souder. Weak Polarized Electron Scattering. 2014.

[4] T.W. Donnelly, J. Dubach, and Ingo Sick. Isospin Dependences in Parity Violating Electron Scattering. *Nucl.Phys.*, A503:589, 1989.

[5] C.J. Horowitz, S.J. Pollock, P.A. Souder, and R. Michaels. Parity violating measurements of neutron densities. *Phys.Rev.*, C63:025501, 2001.

[6] S.J. Pollock, E.N. Fortson, and L. Wilets. Atomic parity nonconservation: Electroweak parameters and nuclear structure. *Phys.Rev.*, C46:2587–2600, 1992.

[7] C.J. Horowitz and J. Piekarewicz. Neutron star structure and the neutron radius of Pb-208. *Phys.Rev.Lett.*, 86:5647, 2001.

[8] S. Abrahamyan, Z. Ahmed, H. Albataineh, K. Aniol, D.S. Armstrong, et al. Measurement of the Neutron Radius of 208Pb Through Parity-Violation in Electron Scattering. *Phys.Rev.Lett.*, 108:112502, 2012.

[9] Shufang Ban, C.J. Horowitz, and R. Michaels. Parity Violating Electron Scattering Measurements of Neutron Densities. *J.Phys.*, 39:015104, 2012.

[10] M. Thiel, D. Becker, M. Ferretti, K. Kumar, and C. Sfienti. Neutron skin studies of medium and heavy nuclei. *EPJ Web Conf.*, 73:07007, 2014.

[11] P.A. Souder and R. Holmes. New spectrometers for precision measurements of parity violation with polarized electrons. 1990.

[12] M.J. Ramsey-Musolf. Low-energy parity violation and new physics. *Phys.Rev.*, C60:015501, 1999.

[13] Hooman Davoudiasl, Hye-Sung Lee, and William J. Marciano. Muon g-2, Rare Kaon Decays, and Parity Violation from Dark Bosons. *Phys.Rev.*, D89:095006, 2014.

[14] Vincenzo Cirigliano and Michael J. Ramsey-Musolf. Low Energy Probes of Physics Beyond the Standard Model. *Prog.Part.Nucl.Phys.*, 71:2–20, 2013.

[15] Jens Erler and Shufang Su. The Weak Neutral Current. *Prog.Part.Nucl.Phys.*, 71:119–149, 2013.

[16] E. Eichten, Kenneth D. Lane, and Michael E. Peskin. New Tests for Quark and Lepton Substructure. *Phys.Rev.Lett.*, 50:811–814, 1983.

[17] S.C. Bennett and Carl E. Wieman. Measurement of the 6S to 7S transition polarizability in atomic cesium and an improved test of the Standard Model. *Phys.Rev.Lett.*, 82:2484–2487, 1999.

[18] G.P. Zeller et al. A Precise determination of electroweak parameters in neutrino nucleon scattering. *Phys.Rev.Lett.*, 88:091802, 2002.

[19] P.L. Anthony et al. Precision measurement of the weak mixing angle in Moller scattering. *Phys.Rev.Lett.*, 95:081601, 2005.

[20] D.S. Armstrong, A. Asaturyan, T. Averett, J. Benesch, J. Birchall, et al. The Qweak Experiment: A Search for New Physics at the TeV Scale via a Measurement of the Proton's Weak Charge. 2012.

[21] D. Androic et al. First Determination of the Weak Charge of the Proton. *Phys.Rev.Lett.*, 111(14):141803, 2013.

[22] D. Becker, K. Gerz, S. Baunack, K.S. Kumar, and F.E. Maas. P2 - The weak charge of the proton. *AIP Conf.Proc.*, 1563:78–81, 2013.

[23] D. Wang et al. Measurement of parity violation in electron–quark scattering. *Nature*, 506(7486):67–70, 2014.

[24] J.P. Chen, H. Gao, T.K. Hemmick, Z. E. Meziani, and P.A. Souder. A White Paper on SoLID (Solenoidal Large Intensity Device). 2014.

[25] Matthew R. Buckley and Michael J. Ramsey-Musolf. Precision Probes of a Leptophobic Z' Boson. *Phys.Lett.*, B712:261–265, 2012.

[26] Emanuel Derman and William J. Marciano. Parity Violating Asymmetries in Polarized Electron Scattering. *Annals Phys.*, 121:147, 1979.

[27] Andrzej Czarnecki and William J. Marciano. Electroweak radiative corrections to polarized Moller scattering asymmetries. *Phys.Rev.*, D53:1066–1072, 1996.

[28] Jens Erler and Michael J. Ramsey-Musolf. The Weak mixing angle at low energies. *Phys.Rev.*, D72:073003, 2005.

Precision Tests of the Standard Model with Kaon Decays at CERN

Tommaso Spadaro[1] for the NA62 collaboration

[1]Laboratori Nazionali di Frascati dell'INFN, Via E. Fermi 40, 00044 Frascati, Italy

DOI: http://dx.doi.org/10.3204/DESY-PROC-2014-04/14

Selected precision Standard Model tests performed in the recent past or possible in the near future using kaon decays are discussed, with a focus on unambiguous signatures, such as those for Lepton-Flavor violation (LFV) and Lepton-Number violation (LNV) transitions, and on the physics reach at the high-intensity beams produced at the CERN SPS for the NA48/2 and NA62 experiments. Recent results on the search for the LNV process $K^{\pm} \to \pi^{\mp}\mu^{\pm}\mu^{\pm}$ and for LFV-induced deviations from the SM expectation for the ratio of decays widths for $K^{+} \to e^{+}\nu$ and $K^{+} \to \mu^{+}\nu$ are briefly discussed. Sensitivity improvements with the new phase of NA62 on a variety of observables are outlined.

1 The Kaon physics framework

The Standard Model appears remarkably simple at a c.m. energy around the kaon mass, with few unknown parameters in the QCD dynamics, namely light and strange quark masses and e.m.- or QCD-induced isospin-breaking effects. This leaved room for a thouough study of the symmetry of the electro-weak lagrangian performed in the last decades. Searches with kaons have been competitive with those with B-mesons for lepton-flavor (LF) or CP violation transitions (most notably, the precise measurements of CPV in the mixing ϵ [1] and of the direct CPV in the decay [2]) and reached the highest sensitivity in the search for CPT and quantum mechanics violation effects. The most precise gauge-universality test comes for the unitarity of the first row of the CKM matrix, thanks to the results from kaon decays giving V_{us}, and from super-allowed nuclear transitions giving V_{ud} [3]. This translated into a severe constraint for every new-physics extension of the SM [4].

2 Search for lepton number violation from kaon decays

The lepton-number violation transition $K^{\pm} \to \pi^{\mp}\mu^{\pm}\mu^{\pm}$ is forbidden in the SM. It might be possible in new-physics models, if mediated by a Majorana neutrino. For neutrino masses ranging from 100 to 300 MeV, the cited channel would be that with the highest sensitivity [5].

The search for this decay has been performed at the NA48/2 experiment. The main goal of NA48/2 was the search for direct CPV from precise measurement of the charge asymmetry in the Dalitz-plot density slopes between the decays $K^{+} \to \pi^{+}\pi^{0\pm}\pi^{0,\mp}$ and their charge conjugates [6]. NA48/2 operated with high-intensity, unseparated, simultaneous, highly-collimated, 60-GeV momentum $K^{\pm}$ beams, with a 3.8% momentum bite. The beams entered a decay region in

vacuum instrumented with a magnetic spectrometer to measure the momentum of charged decay products, a fast scintillator hodoscope establishing the event time and initiating the trigger, and a liquid Krypton calorimeter downstream the hodoscope with high transversal segmentation and an excellent energy and spatial resolution. The LKr calorimeter was followed by a hadron calorimeter and a muon-veto system (MUV) used both for muon identification and for muon triggering. For details on the apparatus, see [7].

Samples were acquired in 2003-2004 by requiring the presence of three tracks at the trigger level using both the hodoscope and the spectrometer information. A single vertex was reconstructed from the three tracks, and for two of them associated hits in the MUV were required. The sample left for normalization had the same angular acceptance and vertex requests for the three tracks as the two-muon sample, while no request was made on the MUV system, and was equivalent to about 1.4×10^{11} kaon decays in a given fiducial volume.

Two-muon samples were divided into correct-sign (wrong-sign), candidates for the LN conserving (violating) decay $K^{\pm} \to \pi^{\pm}\mu^{\pm}\mu^{\mp}$ ($K^{\pm} \to \pi^{\mp}\mu^{\pm}\mu^{\pm}$). The three-track invariant mass distribution for the correct (wrong) sign sample, is shown in the left (right) panel of Fig. 1. A clear peak around the kaon mass is present for the correct sign events, while no peak is observed for the wrong sign sample. The number of events counted in the signal region agrees with the pure-background expectation. The corresponding upper limit, $BR(K^{\pm} \to \pi^{\mp}\mu^{\pm}\mu^{\pm}) < 1.1 \times 10^{-9}$ at 90% CL [8], improves on previous results by a factor of 3.

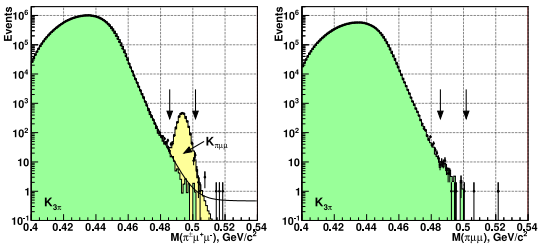

Figure 1: Three-track invariant mass from correct-sign (left-panel) and wrong-sign (right panel) $K \to \pi\mu\mu$ samples. The vertical arrows define the signal region.

3 Search for lepton flavor violation from kaon decays

Thanks to the cancellation of hadronic uncertainties, the ratio R_K of decay widths for kaon decays to $e\nu$ and $\mu\nu$ final states can be predicted with extremely high accuracy in the SM: $R_K = 2.477 \pm 0.001 \times 10^{-5}$ [9]. In large-tan β super-symmetric models R_K might deviate from the SM estimate by up to the percent [10, 11] and this NP effect should be dominated by a LFV contribution from $e\nu_\tau$ final states. After the Higgs discovery made the large-tan β scenario less probable and after the constraints from the $B \to \tau\nu$ and $B_{(s)} -> \mu^+\mu^-$ are taken into account, NP effects on R_K above the per-mil level are disfavoured [12]. Nevertheless, NP effects at the percent level might still be envisaged in scenarios with SM extensions including sterile fermions and inverse see-saw [13].

A data taking at the NA62 experiment was performed in 2007-2008, dedicated to the measurement of R_K. At that time, the most precise measurement of R_K had a total uncertainty

of 1.3% [14]. The design of NA62 was optimized for the R_K measurement with respect to that used for NA48/2, by increasing the beam momentum to 74 GeV, decreasing the momentum bite to 2.5%, and by increasing the momentum kick provided by the spectrometer magnet.The resolution on the missing mass from kaon decays from a single track was therefore significantly improved, thus increasing the kinematic separation of $K \to e\nu$ (a.k.a. K_{e2}) decays with respect to $K \to \mu\nu$ decays ($K_{\mu 2}$). Beam particles with a single charge were used and the majority of the data taking was devoted to a positively charged beam.

The main trigger for $K_{\mu 2}$ events required a single track observed at the hodoscope together with activity in the drift chambers corresponding to a single track. To trigger K_{e2} events, the request of having an energy deposition of at least 10 GeV in the LKr calorimeter was added. In the offline analysis, K_{e2} decays were identified by requiring a cluster of energy in the LKr calorimeter, geometrically associated to the kaon daughter track, and by selecting events with a ratio of energy measured by the calorimeter to momentum measured by the spectrometer around unity. Events with a squared missing mass at the K decay point around zero are considered K_{e2} candidates, see the left panel of Fig 2. The misidentification probability of high-energy muons mimicking the electron energy release in the calorimeter has been precisely evaluated comparing a muon-enriched control sample acquired by interspersing a lead bar between the two hodoscope planes. The probability was measured to be at the level of 4×10^{-6} and depends on the muon energy.

NA62 selected the largest K_{e2} data set ever, with almost 150000 events. The total background amounts to almost 11%, dominated by $K_{\mu 2}$ decays with muons mimicking the electron energy release in the calorimeter (5.64±0.20%). Radiative structure-dependent $K_{e2\gamma}$ decays contribute for 2.60±0.11%, while the beam halo due to muons from upstream in flight decay of beam pions constitute the third background source, 2.11±0.09%. The analysis for R_K was per-

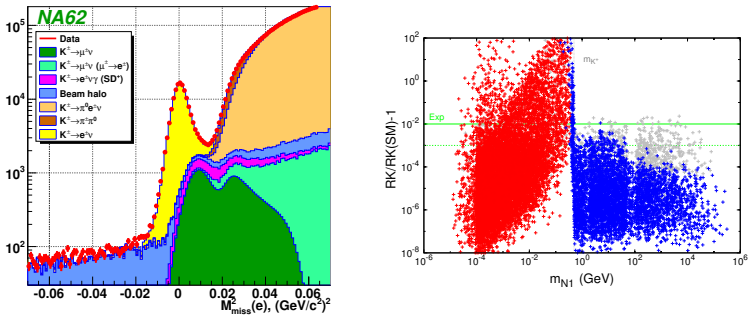

Figure 2: Left: Squared missing mass at the K decay vertex, evaluated assuming the daughter track has the electron mass, for K_{e2} candidate events. Right: fractional deviation of R_K with respect to its SM expectation as a function of the lightest sterile neutrino mass for NP models with sterile neutrinos with inverse see-saw (from Ref. [13]). Models above the solid green line representing the upper bound from the NA62 result of Eq. 1 are excluded.

formed in 10 bins of lepton momentum and separating runs according to the beam charge and to the setup (with and without the lead bar). The results are found to be mutually compatible and average to

$$R_K = (2.488 \pm 0.007_{\text{stat}} \pm 0.007_{\text{syst}}) \times 10^{-5}. \quad (1)$$

	K Mode	UL at 90% CL	Experiment
LFV	$K^+ \to \pi^+\mu^+e^-$	1.3×10^{-11}	E777/E865 [17]
LFV	$K^+ \to \pi^+\mu^-e^+$	5.2×10^{-10}	E865 [18]
LNV	$K^+ \to \pi^-\mu^+e^+$	5.0×10^{-10}	E865 [18]
LNV	$K^+ \to \pi^-e^+e^+$	6.4×10^{-10}	E865 [18]
LNV	$K^+ \to \pi^-\mu^+\mu^+$	1.1×10^{-9}	NA48/2 [8]
LNV	$K^+ \to \mu^-\nu e^+e^+$	2.0×10^{-8}	Geneva-Saclay [19]
LNV	$K^+ \to e^-\nu\mu^+\mu^+$	no data	

	π^0 Mode	Status	Experiment
LFV, ν_R	$\pi^0 \to$ inv.	$< 3 \times 10^{-7}$	E949 [20]
LFV	$\pi^0 \to e\mu$	$< 4 \times 10^{-10}$	KTeV [21]
NP scalars	$\pi^0 \to 4\gamma$	$< 2 \times 10^{-8}$ at 90% CL	Crystal box [22]
NP scalars	$\pi^0 \to e^+e^-e^+e^-$	$3.34(16)10^{-5}$	KTeV [21]
NP vectors	$\pi^0 \to U\gamma$, $U \to e^+e^-$	Various exclusions	see [23]
C violation	$\pi^0 \to 3\gamma$	$< 3.1 \times 10^{-8}$ at 90% CL	Crystal box [22]

Table 1: Upper (lower) panel: LFV/LNV K-decay modes (π^0 decay modes) possibly studied at the imminent run of NA62: the single-event sensitivity is expected to reach 10^{-12} (10^{-10}).

The residual systematic uncertainty is due to a number of different contributions [15]. Notwithstanding an uncertainty improvement on the previous data by a factor of 4, the result is in agreement with the SM expectation. Exclusion plots for NP contributions can be obtained: the right panel of Fig. 2 refers to models with sterile neutrino and inverse see-saw.

4 Near-future sensitivity from NA62 on NP searches

The NA62 collaboration developed a new detector setup, including the trigger and data acquisition systems, optimized to measure the branching fraction for the rare flavor-changing neutral current decay $K^+ \to \pi^+\nu\bar{\nu}$ with a 10% total uncertainty. For a detailed description of the new setup and of the measurement itself, see [16]. The data taking will begin in 2014 and will last for at least two years. Higher proton intensity and much larger beam accepted solid angle compared to the NA48/2 setup will allow 1.2×10^{13} K decays in a 60-meter long fiducial region to be studied, an improvement by a factor of 50. This, together with the possibility to apply flexible and dedicated trigger strategies using PID information and multi-track requests, will allow a single-event sensitivity at the level of 10^{-12} for the lepton-flavor violation channels listed in the upper panel of Table 1. The background rejection for the identification of the cited LNV decay $K^\pm \to \pi^\mp\mu^\pm\mu^\pm$ will be increased hugely, thanks to the redundant PID capability of the new setup and to the lowering of the invariant mass resolution by more than a factor of 2. The expected sentitivity will increase by a factor from 100 to 1000. Major impact on other topics are foreseen. One year of data taking at the new NA62 corresponds to more than 10^{11} π^0's produced from $K^+ \to \pi^+\pi^0$. This intense and possibly tagged π^0 *beam* will allow other interesting studies, as listed in the lower panel of Table 1. Among these, we cite the search for NP vectors, also called *dark photons* [24]. In one year of data taking $\sim 10^{15}$ $D^\pm$ will be produced, thus allowing interesting searches for long-lived exotic particles reaching the NA62 apparatus, such as the heavy neutral leptons of the NP model by Shaposhnikov and others [25].

References

[1] A. J. Buras, D. Guadagnoli and G. Isidori, Phys. Lett. B **688** (2010) 309 and references therein.

[2] V. Fanti *et al.* [NA48 Collaboration], Phys. Lett. B **465** (1999) 335 [hep-ex/9909022]. J. R. Batley *et al.* [NA48 Collaboration], Phys. Lett. B **544** (2002) 97 [hep-ex/0208009]. A. Alavi-Harati *et al.* [KTeV Collaboration], Phys. Rev. Lett. **83** (1999) 22 [hep-ex/9905060].

[3] M. Antonelli *et al.*, Phys. Rept. **494** (2010) 197 [arXiv:0907.5386 [hep-ph]].

[4] A. Czarnecki, W. J. Marciano and A. Sirlin, Phys. Rev. D **70** (2004) 093006 [hep-ph/0406324].

[5] A. Atre, T. Han, S. Pascoli and B. Zhang, JHEP **0905** (2009) 030 [arXiv:0901.3589 [hep-ph]].

[6] J. R. Batley *et al.* [NA48/2 Collaboration], EPJ C52 (2007) 875.

[7] V. Fanti *et al.* [NA48 Collaboration], Nucl. Instrum. Meth. A **574** (2007) 433.

[8] J. R. Batley *et al.* [NA48/2 Collaboration], Phys. Lett. B **697** (2011) 107.

[9] V. Cirigliano, I. Rosell, Phys. Rev. Lett. **99** (2007) 231801.

[10] A. Masiero, P. Paradisi, R. Petronzio, Phys. Rev. D **74** (2006) 011701 and JHEP 0811 (2008) 042.

[11] J. Girrbach, U. Nierste, arXiv:1202.4906.

[12] R. M. Fonseca, J. C. Romao and A. M. Teixeira Eur. Phys. J. C **72** (2012) 2228.

[13] A. Abada, *et al.* JHEP **1402** (2014) 091 [arXiv:1311.2830v2 [hep-ph]]

[14] F. Ambrosino, *et al.* [KLOE Collaboration], Eur. Phys. J. C **64** (2009) 627.

[15] C. Lazzeroni, *et al.* [NA62 Collaboration], Phys. Lett. B **719** (2013) 326.

[16] G. Ruggiero [NA62 Collaboration], proceedings of PANIC 2014 conference.

[17] A. Sher, *et al.*, Phys. Rev. D **72** (2005) 012005 [hep-ex/0502020].

[18] R. Appel, *et al.*, Phys. Rev. Lett. **85** (2000) 2877 [hep-ex/0006003].

[19] A. M. Diamant-Berger, *et al.*, Phys. Lett. B **62** (1976) 485.

[20] A.V. Artamonov, *et al.* [E949 Collaboration], [arXiv:hep-ex/0506028v2] (2005).

[21] E. Abouzaid, *et al.* [KTeV Collaboration], Phys. Rev. Lett. **100** (2008) 182001 [arXiv:0802.2064 [hep-ex]].

[22] J. McDonough, *et al.*, Phys. Rev. D 38 (1988) 2121.

[23] see Fig. 6 in arXiv:1311.0029v1 [hep-ph] and references therein.

[24] B. Holdom, Phys. Lett. B 166 (1986) 196; P. Galison and A. Manohar, Phys. Lett. B 136 (1984) 279.

[25] L. Canetti *et al.* [arXiv:1208.4607v2 [hep-ph]].

Ultracold Neutron Physics at the Los Alamos National Laboratory

Leah Broussard[1] for the UCNA, UCNB, UCNτ, and LANL nEDM collaborations

[1]Los Alamos National Laboratory, Los Alamos, NM, USA 87545

DOI: http://dx.doi.org/10.3204/DESY-PROC-2014-04/116

Los Alamos National Laboratory uses one of the highest density sources of ultracold neutrons in the world to perform precision measurements in neutron decay. The UCNA experiment's most recent dataset is expected to determine the beta asymmetry with half-percent uncertainty. Currently in progress are the UCNB experiment to measure the neutrino asymmetry, and the UCNτ experiment to measure the neutron lifetime. Finally, a new effort is underway to improve the sensitivity to the neutron EDM by an order of magnitude.

1 The UCN source at LANSCE

The ultracold neutron (UCN) facility at the Los Alamos Neutron Science Center (LANSCE) is used for a number of precision studies of the electroweak interaction through the decay of the neutron and the search for symmetry violations that could generate an electric dipole moment. UCN have energies of less than about 300 neV or 4 mK temperature, rendering them sensitive to all four of the fundamental forces at levels achievable in the laboratory. They are completely reflected by some material potentials, are constrained to heights of about 3 m by gravity, can be completely polarized by magnetic fields of about 6 T due to the neutron's magnetic moment, and decay due to the weak interaction with an experimentally convenient lifetime of about 15 minutes.

The pulsed 800 MeV proton beam from the LANSCE linear accelerator incident on a tungsten target produces spallation neutrons, which are moderated in graphite and cold polyethylene. The resulting cold neutrons can then single scatter in a solid deuterium crystal and convert into UCN. The UCN then escape the source, which is subsequently closed off by a butterfly valve, and are transported by a stainless steel guide system out of the biological shielding into the experimental area, where densities of up to 50 UCN/cc have been achieved [1].

2 UCNA

One of the most important tests of our understanding of the electroweak interaction is the unitarity of the Cabibbo-Kobayashi-Maskawa (CKM) quark-mixing matrix, which is sensitive to new physics beyond the Standard Model [2]. The matrix element V_{ud} contributes to the most precise such test. In neutron decay, two measurements are required to extract V_{ud}: the lifetime and a correlation coefficient, such as the asymmetry between the neutron spin and the emitted electron, A, to set the value of λ, the ratio of axial-vector to vector couplings. Currently, V_{ud}

is determined most precisely from the set of superallowed $0^+ \rightarrow 0^+$ Fermi decays [3]. It is extracted from neutron decay with about an order of magnitude greater uncertainty, primarily due to the uncertainty in λ. However, as the neutron is not sensitive to nuclear-structure dependent corrections, with reduced experimental error this system should be able to achieve a lower ultimate uncertainty.

The UCNA experiment is the first to determine the beta asymmetry A using UCN. The UCN are 100% polarized by a 6 T superconducting magnet and adiabatic fast passage spin flipper. The UCN are bottled by a copper guide with thin, beryllium foil end caps inside a 1 T decay spectrometer, which aligns their spins along the spectrometer axis. The decay electrons are guided along the magnetic field lines to a detection system consisting of multi-wire proportional chambers for position sensitivity and fast timing for backscatter reconstruction, and plastic scintillators for energy determination.

The most recent published result, resulting in the extraction of $\lambda = -1.2756(30)$, includes 20M beta decay events after all cuts applied, and a total systematic uncertainty of 0.8% and statistical uncertainty of 0.5% [4]. The most important uncertainties include the rate of depolarization of UCN, the backscattered fraction of electrons, and the determination of the electron energy as a function of angle. Several improvements significantly reduced the uncertainty of the 2011-2013 data set, now in analysis. A shutter installed between the polarizing 6 T magnet and the decay trap allowed for an improved determination of depolarization fraction. Thinner foils for the end caps on the decay trap reduced both the backscatter correction and uncertainty. A fast timing source using an avalanche photodiode to detect the Auger from ^{113}Sn in coincidence with the monoenergetic conversion electrons detected by the UCNA detectors improved characterization of scattering and energy loss as a function of pitch angle. Finally, calibrations using xenon and LED studies improved the uncertainty of the energy reconstruction. The systematic uncertainty is expected to improve by almost a factor of 3 in this data set, and is statistics limited. Future ventures to improve the determination of A would require a significant improvement in the neutron decay rate.

3 UCNτ

The lifetime of the neutron is a necessary input to extract V_{ud} along with the beta asymmetry, and is also a critical input for predicting the primordial helium abundance in the early universe. The accuracy of the determination of the lifetime is called into question by the current discrepancy between the lifetime as measured by either beam or bottle experiments, of about 8 s out of $\sim$880 s [5]. One important uncertainty in previous material bottle traps is the determination of the wall loss due to the material interactions. A magneto-gravitational trap eliminates all material interactions and significantly reduces this effect. The asymmetric shape also mitigates the effect of quasi-bound orbits which are not quickly cleaned and are not completely trapped, and can be lost at similar time scales to the decay lifetime. A storage time of $\tau_{store} = 860 \pm 19$ s has recently been demonstrated in the trap [6], and new methods for UCN detection within the trap are being developed. The current apparatus is being developed for a 1 s measurement of the neutron lifetime, ultimately leading to the design of a sub-1-s experiment.

4 UCNB

The correlation between the neutron spin and the neutrino direction B is sensitive to possible scalar and tensor currents predicted by theories beyond the Standard Model [7]. The neutrino direction must be determined from the decay proton and electron detected in coincidence. A greater sensitivity to b_ν, the electron energy dependent component of a scalar/tensor contribution to B, can be obtained by taking the ratio of the proton and electron asymmetry. By performing a simultaneous fit to the observed electron energy spectra for each proton/electron direction, the proton/electron asymmetries, and the spin-averaged electron energy spectrum, b, b_ν and λ can be extracted simultaneously with precision at the 10^{-3} level from 10^8 total decays [8].

The UCNB experiment uses novel 2 mm thick, large area (12 cm diameter active area), highly segmented (127 hexagonal pixels) silicon detectors installed in the UCNA spectrometer to detect the electron and proton from neutron beta decay in coincidence [9]. The detection system was developed in collaboration with the Nab experiment [10], which will measure the electron-neutrino correlation and Fierz interference term b at the Spallation Neutron Source. Custom preamplifiers are being developed which must meet the requirements of fast timing ($\sim$10 ns) for distinguishing electron backscatter events and very low noise to detect the protons. The protons are emitted with less than 800 eV and could not pass the deadlayer of the detector. Therefore they are accelerated by a -30kV high voltage bias applied to the detection system, including detector and mounting structure, preamplifiers and data acquisition system.

This detector has achieved the first direct observation of both the proton and electron from neutron beta decay in coincidence, using an 8 channel prototype preamplifier. The system can clearly resolve signals above 20 keV with 3 keV (σ) resolution, sufficient for triggering on proton events. A 24 channel prototype has been developed with improved noise characteristics and faster rise time of 20 ns, and after successful demonstration with neutron beta decay, the full 128 channel (127 pixels + ganged partial pixels) system will be implemented. The system has been operated stably at -30 kV and in the 0.6 T expansion region for 100 hours without damage to detectors or electronics. The detector connections can be mechanically damaged during installation, however. A new design using pogo-pin style connectors similar to those used in KATRIN [11] has been tested using 1 cm diameter prototype silicon detectors and have been demonstrated to be robust with many mechanical and cooling cycles. Full-size detectors fully instrumented with pogo-pins are now in development.

5 LANL nEDM

The existence of an electric dipole moment (EDM) in a non-degenerate system requires a violation of time and parity and is a clear indication of the presence of new physics, especially regarding the important question of the observed baryon asymmetry in the universe. Searches for EDMs provide sensitive tests of Beyond the Standard Model theories well beyond the reach of the LHC [12]. The most precise search for an EDM in the neutron was performed at the ILL, using Ramsey's method of separated oscillatory fields. The UCN spins were rotated into the plane perpendicular to the magnetic field, allowed to precess with an electric field aligned parallel and anti-parallel to the magnetic field, then rotated to complete the spin flip. This experiment achieved the limit $d_n < 2.9 \times 10^{-26}$ e-cm (90% C.L.) [13]. To improve this limit, an increase in density to about 100 UCN/cc is required.

With modest improvement to the LANSCE UCN source, the required UCN density for a 10^{-27} e-cm sensitivity is achievable. The most straightforward gains, of about a factor 3, come from improvement in the proton beam delivery and in increasing the current. Currently the proton pulse structure consists of a large burst every 5 s, resulting in significant UCN losses as UCN that fail to escape the source volume before the next beam burst fall back into the solid deuterium crystal when the butterfly valve reopens. Increasing the period to 30 s significantly reduces this loss, but requires an upgrade to beam safety hardware that inaccurately measures the average current, which still falls short of the design specification of 10 μA. A redesign of the UCN source, including better modeling of the moderator configuration, improved cooling, and moving the deuterium closer to the tungsten target is expected to deliver another factor of 2 improvement. Improved transport of the UCN out of the source volume and through the guide system should increase the density by a factor of 3 or more. To take advantage of the increased density, further improvements to the ILL design will be implemented. A prototype high voltage chamber is currently being constructed to test improvements to the geometry and materials used in the electrodes to permit an electric field greater than 10 kV/cm during precession. The PSI collaboration has demonstrated the required improvements to the magnetometry using a ^{199}Hg co-magnetometer to look for variations in the magnetic field over time [14].

6 Summary

The LANSCE UCN facility has a vibrant program for fundamental symmetries and precision searches for physics beyond the Standard Model. The facility was designed to allow for very low background measurements of polarized neutron decay correlations, especially the beta-asymmetry and neutrino-asymmetry, and has expanded to support efforts to determine the neutron lifetime and a search for an electric dipole moment. Planned upgrades to proton beam delivery and source performance will ensure this facility remains one of the most competitive UCN sources in the world.

References

[1] A. Saunders *et al.*, Rev. Sci. Instrum. **84** 013304 (2013).

[2] M. Antonelli *et al.*, Phys. Rep. **494**, 197 (2010).

[3] J. C. Hardy and I. S. Towner, Phys. Rev. C **79** 055502 (2009).

[4] M. P. Mendenhall *et al.*, Phys. Rev. C **87** 032501(R) (2013).

[5] A. T. Yue *et al.*, Phys. Rev. Lett. **111** 222501 (2013).

[6] D. J. Salvat *et al.*, Phys. Rev. C **89** 052501(R) (2014).

[7] T. Bhattacharya *et al.*, Phys. Rev. D **85** 054512 (2012).

[8] B. Plaster, S. J. Sjue and A. R. Young, (2014) in prep.

[9] A. Salas-Bacci *et al.*, Nucl. Instr. and Meth. in Phys. Rev. A **735** 408 (2014).

[10] S. Baessler *et al.*, AIP Conf. Proc. **1560** 114 (2013).

[11] B. A. VanDevender *et al.*, Nucl. Instr. and Meth. in Phys. Rev. A **673** 46 (2012).

[12] J. Engel, M. J. Ramsey-Musolf and U. van Kolck, Prog. Part. Nucl. Phys **71** 21 (2013).

[13] C. A. Baker *et al.*, Phys. Rev. Lett. **97** 131801 (2006).

[14] B. M. Horras, Ph.D. thesis, ETH Zürich (2012).

Measurements of Electric Dipole Moments of Charged Particles at Storage Rings

Volker Hejny for the JEDI Collaboration

Institut für Kernphysik and Jülich Center for Hadron Physics, Forschungszentrum Jülich, 52425 Jülich, Germany

DOI: http://dx.doi.org/10.3204/DESY-PROC-2014-04/156

Electric Dipole Moments (EDM) of elementary particles are considered to be one of the most powerful tools to investigate CP violation beyond the Standard Model and to find an explanation for the dominance of matter over antimatter in our universe. Up to now experiments concentrated on neutral systems (neutrons, atoms, molecules). Storage rings offer the possibility to measure EDMs of charged particles by observing the influence of the EDM on the spin motion. The Cooler Synchrotron COSY at the Forschungszentrum Jülich provides polarized protons and deuterons up to a momentum of 3.7 GeV/c and is thus an ideal starting point for such an experimental program. The JEDI (Jülich Electric Dipole moment Investigations) Collaboration has been formed to exploit the COSY facility to demonstrate the feasibility of such a measurement and to perform all the necessary investigations towards the design of a dedicated storage ring.

1 Introduction

Electric dipole moments (EDM) break parity (P), time-reversal (T) symmetry, and — via the CPT-theorem — charge-parity (CP) symmetry. The established Kobayashi-Maskawa mechanism of CP violation predicts EDMs orders of magnitude below the current experimental limits. In addition, the Standard Model Lagrangian contains a possible source of CP violation in strong interaction, which, however, does not seem to be realized in nature: the experimental bound from neutron EDM experiments (for an overview see e.g. Ref. [1]) on the strength parametrized by the vacuum angle θ_{QCD} is $|\theta_{\mathrm{QCD}}| \lesssim 10^{-10}$ and, thus, unexpectedly small. Furthermore, the universal matter/antimatter asymmetry implies that there should be CP violation from physics besides the Kobayashi-Maskawa mechanism and beyond the Standard Model. EDMs are excellent probes for these new CP-violating sources [2, 3, 4].

Once an EDM has been measured, the next goal is to identify its source. Is it, for example, caused by strong CP violation or from physics beyond the Standard Model? Experimental data on the EDMs of several light nuclei could provide an answer to this question: different classes of models predict different hierarchies of EDMs and thus can be disentangled once several light-nuclear EDM experiments (protons, deuterons and possibly ^{3}He) have been performed.

2 Basic Concept

The basic concept of measuring a permanent electric dipole moment is to place the test object into a strong electric field and to monitor the spin precession caused by the electric dipole moment. For neutral systems this can be done in a quasi-static, localized setup. Charged particles, however, are accelerated by the electric field. Therefore, it has been suggested in Ref. [5] (at that time for muons) to utilize a storage ring for such a measurement. The goal of the US-based srEDM collaboration [6] and the Jülich-based JEDI collaboration [7] is to apply this concept to protons, deuterons and ^{3}He [8].

The spin motion of a particle in a storage ring due to magnetic and electric dipole moments is described by the Thomas-BMT equation [9]

$$\frac{\mathrm{d}\vec{S}}{\mathrm{d}t} = \left(\vec{\Omega}_{\mathrm{MDM}} + \vec{\Omega}_{\mathrm{EDM}}\right) \times \vec{S} \tag{1}$$

$$\vec{\Omega}_{\mathrm{MDM}} = -\frac{q}{m_0}\left[G\vec{B} + \left(\frac{1}{\gamma^2-1} - G\right)\frac{\vec{\beta}\times\vec{E}}{c}\right] \tag{2}$$

$$\vec{\Omega}_{\mathrm{EDM}} = -\frac{dc}{\hbar S}\left[\frac{\vec{E}}{c} + \vec{\beta}\times\vec{B}\right] \tag{3}$$

with S denoting the spin of the particle, t the time in the laboratory system, q and m_0 the charge and the mass of the particle, β and γ the relativistic Lorentz factors, G the magnetic anomaly and d the electric dipole moment. Terms proportional to $\vec{\beta}\cdot\vec{E}$ and $\vec{\beta}\cdot\vec{B}$ (*i.e.*, the effect of longitudinal field components) are omitted. The general idea of the measurement is to adjust the electric and magnetic fields as well as the particle momentum such, that the term $\vec{\Omega}_{\mathrm{MDM}}$ — sensitive to the magnetic dipole moment — vanishes. For the proton with a positive anomalous magnetic moment this can be achieved with a purely electric ring by setting the momentum to $p = \frac{m_0}{\sqrt{G}}$, for deuterons and ^{3}He a suitable combination of electric and magnetic fields is necessary. Thereby, starting with the spin aligned to particle momentum, the precession caused by the transverse electric and magnetic fields (the latter creating a motional electric field $\vec{\beta}\times\vec{B}$) will lead to a vertical polarization build-up.

Assuming high intensity beams of $4\cdot10^{10}$ particles per fill, a polarization degree of 80%, electric fields of $E = 10\,\mathrm{MV/m}$, and spin coherence times of 1000 s (see below) a statistical error for an EDM of $10^{-29}\,e$cm is in reach for one year of measurement. The remaining challenge is to get the systematic uncertainty down to the same level.

While the effects from the magnetic dipole moment can only be canceled in a dedicated storage ring yet to be designed and built, the Cooler Synchrotron COSY at the Forschungszentrum Jülich is an ideal place for the necessary R&D work and a proof-of-principle experiment [7, 10]. COSY is a unique facility for spin physics with hadronic probes on a world-wide scale: it has a history of a highly successful operation of cooled polarized proton and deuteron beams and polarized targets. As a purely magnetic ring the spin precession caused by the magnetic dipole moment of the particles cannot be canceled. Instead, this spin motion is utilized to develop tools and equipment for the design and operation of the final ring. Furthermore, using an rf Wien filter the spin precession due to the magnetic dipole moment can be manipulated such that the motional electric field generates a net EDM effect [8, 10].

3 R&D at COSY

Currently various developments are under way at COSY: improved beam position monitors, electrostatic deflectors, polarimetry, the rf Wien filter, systematic studies of the influence of sextupoles, steerers and solenoids, etc. One major goal was to increase the spin coherence time of the particles: as an ensemble of about 10^{10} particles is under observation, the length of one experimental cycle is determined by the time the spins of all particles precess coherently with the same angular velocity. For this purpose a time marking system using the EDDA detector as polarimeter has been developed to monitor the horizontal spin precession — i.e. the in-plane polarization — of a deuteron beam at 0.97 GeV/c. Further information on the method, the data analysis and the results on the spin coherence time can be found in Refs. [11, 12]. Here a short summary: for deuterons in a pure magnetic ring with vertical bending fields the Thomas-BMT equation reduces to

$$\frac{\mathrm{d}S}{\mathrm{d}t} = \frac{qB}{m_0} \cdot G. \tag{4}$$

Dividing this by the cyclotron frequency $\omega_{\mathrm{cyc}} = \frac{qB}{m_0\gamma}$ one gets $\nu = \gamma G$. ν is called the spin tune and describes the number of spin revolutions per turn relative to the particle momentum. For an unbunched beam decoherence is expected within less than one second due to the spread in momentum (and, thus, in γ). To first order this spread can be compensated by a bunched beam and spin coherence times of several seconds can be achieved. Higher orders (e.g. synchrotron oscillations, dispersion effects) can be corrected by means of sextupoles. Here, spin coherence times of several hundred seconds could already be reached.

Another tool to be used for studying the effect of various ring elements like solenoids, steerer and the rf Wien filter on the spin motion is the precise measurement of the spin tune with a precision close to $\Delta\nu \approx 10^{-10}$. This has been used successfully during the last beam times and a corresponding publication is currently under preparation.

4 Summary and Outlook

At the Cooler Synchrotron COSY of the Forschungszentrum Jülich R&D work has been started towards a dedicated storage ring for measuring electric dipole moments of charged hadrons. A time marking system together with the EDDA detector has been setup to allow for high precision studies of the spin motion in COSY. As a first result large spin coherence times in the order of several hundred seconds have been achieved by tuning the standard ring sextupole magnets. There are two major milestones for the next five years: a proof-of-principle experiment at COSY with limited sensitivity and a conceptual design report for the final EDM ring.

Acknowledgments

We would like to thank the technical and administrative staff at the Forschungszentrum Jülich, especially at the COoler SYnchrotron COSY and at the participating institutes.

References

[1] S.K. Lamoreaux and R. Golub, J. Phys. G **36** 104002 (2009).

[2] J.M. Pendlebury *et al.*, Nucl. Inst. Meth. **A440** 471 (2000).

[3] T. Fukuyama, Int. J. Mod. Phys. **A27** 1230015 (2012).

[4] K. Jungmann, Ann. Phys. **525** 550 (2013).

[5] F.J.M. Farley *et al.*, Phys. Rev. Lett. **93** 052001 (2004).

[6] srEDM Collaboration, *http://www.bnl.gov/edm*

[7] JEDI Collaboration, *http://collaborations.fz-juelich.de/ikp/jedi*

[8] F. Rathmann, A. Saleev and N.N. Nikolaev, J. Phys. Conf. Ser. **447** 012011 (2013).

[9] V. Bargmann, L. Michel, and V.L. Telegdi, Phys. Rev. Lett. **2** 435 (1959).

[10] A. Lehrach *et al.*, *Search for Permanent Electric Dipole Moments at COSY Step 1: Spin coherence and systematic error studies*, COSY proposals #216 (2012) and #216.1 (2014).

[11] P. Benati *et al*, Phys. Rev. STAB **15** 124202 (2012).

[12] Z. Bagdasarian *et al.*, Phys. Rev. STAB **17** 052803 (2014).

Latest results from the *a*SPECT experiment

Alexander Wunderle[1], *Oliver Zimmer*[2], *Romain Virot*[2], *Camille Theroine*[3], *Torsten Soldner*[2], *Martin Simson*[2], *Christian Schmidt*[1], *Romain Maisonobe*[2], *Gertrud Konrad*[4], *Werner Heil*[1], *Ferenc Glück*[5], *Marcus Beck*[1], *Stefan Baeßler*[6]

[1]Johannes Gutenberg-Universität, Staudingerweg 7, 55128 Mainz, Germany
[2]Institut Laue-Langevin, 71 avenue des Martyrs, 38000 Grenoble, France
[3]European Spallation Source, Box 176, S221 00 Lund, Sweden
[4]Technische Universität Wien, Stadionallee 2, 1020 Wien, Austria
[5]Karlsruher Institut für Technologie, Hermann-von-Helmholtz-Platz 1, 76344 Eggenstein, Germany
[6]University of Virginia, 382 McCommick Rd. Charlottesville, VA, USA

DOI: http://dx.doi.org/10.3204/DESY-PROC-2014-04/72

The *a*SPECT retardation spectrometer measures the $\beta - \bar{\nu}_e$ angular correlation coefficient a in the β-decay of the free neutron. This measurement can be used to determine the ratio $\lambda = \frac{g_A}{g_V}$ of the weak coupling constants, as well as to search for physics beyond the standard electroweak model. In spring/summer 2013 *a*SPECT had a successful beam time at the Institut Laue-Langevin (ILL), Grenoble/France. The goal of this beam time is to improve the current uncertainty of a from $\frac{\Delta a}{a} \sim 5\%$ to about 1%. To achieve this goal the systematic uncertainties of *a*SPECT have to be understood accordingly. This is achieved via systematic tests, measurements of a with different systematic parameter settings during the beam time and measurements afterwards, like the work-function fluctuations of electrodes or the magnetic field ratio of our spectrometer. Sophisticated simulations of our spectrometer are used to understand and reduce the systematic uncertainties further.

1 Motivation

The β-decay of the free neutron is an ideal system to search for physics beyond the standard model. Its daughter nucleus, the proton, is the simplest possible, so no complicated nuclear corrections are necessary. Further, the system is overdetermined, which opens the possibility to determine one parameter of the standard model, λ, by measuring different correlations. With this complementarity a reduction of the systematic uncertainties of the parameter, as well as a test of the standard model itself is possible.

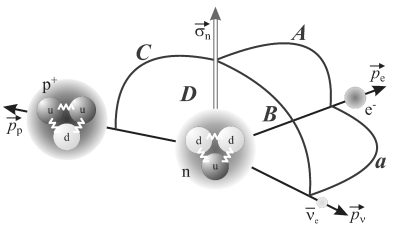

Figure 1: Graphical representation of the important angular correlations in the β-decay of the free neutron.

One of these correlations is the $\beta - \bar{\nu}_e$ angular correlation coefficient a. It describes the angular distribution between the emitted electron and electron-antineutrino and is linked to λ by $a = \frac{1-|\lambda|^2}{1+3|\lambda|^2}$. For further information about the physics of the

neutron, the reader is referred to [1].

2 The *a*SPECT Experiment

*a*SPECT is a MAC-E-filter (**M**agnetic **A**diabatic **C**ollimation combined with an **E**lectrostatic potential). In the following an overview of the measurement principle of a MAC-E filter and the systematic of *a*SPECT is given.

2.1 Measurement Principle

A schematic of the experimental setup of *a*SPECT can be seen in Fig. 2. The neutrons are collimated and guided through the Decay Volume (DV) at high magnetic field (B = 2.2 T). The protons from decays in the DV are adiabatically guided by the magnetic field to a region of 0.44 T, the Analysing Plane (AP). This adiabatic change of the magnetic field causes a momentum transfer from transversal momentum to longitudinal momentum, known as the inverse magnetic mirror effect. Between the electrodes in the DV and the AP a voltage is applied, which acts as a retardation voltage for the protons. This retardation potential performs the energy analysis of the protons. The resolution of a MAC-E filter is determined by the ratio of the magnetic field in the DV and in the AP, in case of *a*SPECT the resolution is about 20 %.

Protons with enough kinetic energy to overcome the potential barrier in the AP are accelerated by typically -15 kV and are detected by a silicon-drift-detector [2]. In this way *a*SPECT measures the integral recoil spectrum of the protons with high precision. This spectrum can be used to determine a and therefore λ with high precision.

For a detailed description of *a*SPECT the reader is referred to [3, 4].

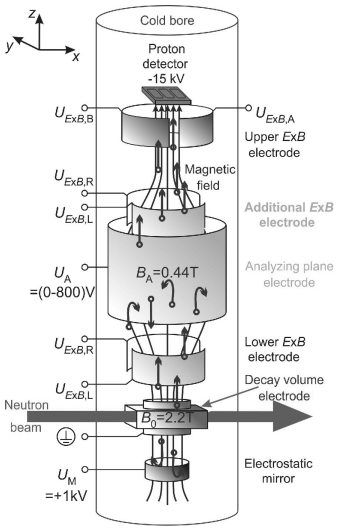

Figure 2: Schematic of the spectrometer *a*SPECT.

2.2 Beam Times and Improvements

*a*SPECT has had several beam times in the past, leading to significant improvements of the system and finally a successful beamtime in 2013. In the following a short overview of these improvements is given. A data acquisition system (DAQ) with logarithmic amplification has been designed and tested to avoid any saturation effects, as seen in 2008. The vacuum has been improved by better cleaning procedures, exchange of materials in the UHV system and the installation of additional turbo molecular and getter pumps. Further, the edges of our electrode system have been smoothed and the whole system has been recoated to reduce field emission. Also an additional dipole electrode has been installed to remove trapped charged particles from a penning-like trap in our spectrometer. These improvements proved to solve the problematic of discharges in the spectrometer and to reduce the background to a sufficiently

low level to determine a with $\frac{\Delta a}{a} \sim 1$ %. The system has been further improved by a new neutron collimation made of conductive boron nitride. Furthermore, a system to measure the beam profile inside of the DV has been designed for investigations of the so-called edge effect with high precision. This system also allows ti introduce radioactive sources into the DV, for alignment and background studies. The DV and AP have been redesigned out of flat electrode plates to obtain well-defined surfaces, which is important to determine the exact potential inside the electrodes.

In 2013 a beam time of 100 days took place with the improved system. This run includes 40 days of pure data taking. During these days no discharges occurred and a sufficiently low background has been observed. No saturation effects in the DAQ have been observed and an additional DAQ without a shaper, but with a high resolution FlashADC has been tested. With a statistical sensitivity of about 1.3 % per day and detector pad (a 3 pad detector was used) many in-depth systematic tests of the system were possible. The analysis of the data and the systematics is currently ongoing.

3 First Results

A thorough investigation of the systematic uncertainties is necessary to achieve the goal of aSPECT of $\frac{\Delta a}{a} \sim 1$ %. One of the main contributions to the systematic error is the uncertainty of the transmission-function of the MAC-E filter. The transmission-function is a function of the ratio of the magnetic field in the AP region and the DV region, as well as the potential difference between AP and DV electrodes [3]

$$f_{Trans} = f\left(\frac{B_{AP}}{B_{DV}}, \Phi_{AP} - \Phi_{DV}\right).$$

3.1 Magnetic field ratio

The magnetic field ratio $r_B = \frac{B_{AP}}{B_{DV}}$ has to be know to a level of $\frac{\Delta r_b}{r_b} \leq 10^{-4}$, which corresponds to an error contribution of $\frac{\Delta a}{a} \sim 0.1\%$ [4]. To achieve this level of precision a nuclear magnetic resonance system (NMR) has been designed, since a standard hall probe can not reach the required precision under lab conditions. The measurement of the magnetic field ratio took place immediately after the beam time at the beam place. The NMR system measured the magnetic field in the DV and AP simultaneously, determining the ratio of the magnetic fields. A small drift has been observed over time for the magnetic field in the single regions, as well as systematic influences of surrounding materials. However, the ratio of the magnetic field stays stable at a level of $\frac{\Delta r_b}{r_b} < 10^{-4}$, see Fig. 3. This is more than sufficient for our goal of $\frac{\Delta a}{a} \sim 1\%$.

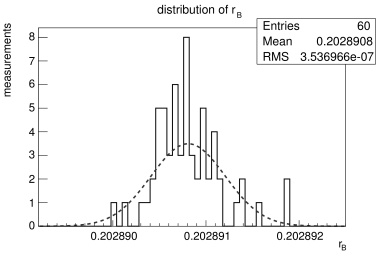

Figure 3: Histogram of the distribution of the r_B values for different settings and over time. The dashed line shows a Gaussian fit to the measured data.

3.2 Potential difference

An accuracy of the retardation potential for the decay protons $U_A = \Phi_{AP} - \Phi_{DV}$ of ~ 10 mV corresponds to an error in a of $\frac{\Delta a}{a} \sim 0.1\%$ [4]. The determination of the potential difference between the AP electrode and the DV electrode is not a trivial task. The retardation voltage is applied by a stable power supply (FUG HCN 0,8M 800) and measured by a precision digital multimeter (Agilent 3458A). However, the applied potential seen by the decay protons is changed by the shape of the electrode, field leakage from outside of the electrode and the work function of the surface material of the electrode.

The shape of the potential due to the electrode design can be simulated. The field leakage can be simulated and measured partially by changing the voltage difference between the electrode and its surrounding during the beam time. The work function, more precisely, the surface contact potential, has to be measured afterwards using eg. a Kelvin Probe. In Fig. 4 a scan of the surface contact potential at air of one of the aSPECT electrodes is shown. Clearly three different areas of different contact potential can be distinguished. These 'patches' are caused by the different crystal orientations of the gold coating of the electrodes [5]. The scanning of the electrodes with a Kelvin Probe is ongoing. First results show an average fluctuation across an electrode of 19 mV and differences of the average between different electrodes of 35 mV. The surface contact potential does not reflect the potential fluctuations, as seen by the protons, which have to be determined by simulations of the electric potential inside the electrodes. But these first results can be used for a worst case scenario, since a fluctuation of 54 mV in the retardation voltage corresponds to $\frac{\Delta a}{a} \sim 0.5\%$, which is compatible with an overall precision of $\frac{\Delta a}{a} \sim 1\%$.

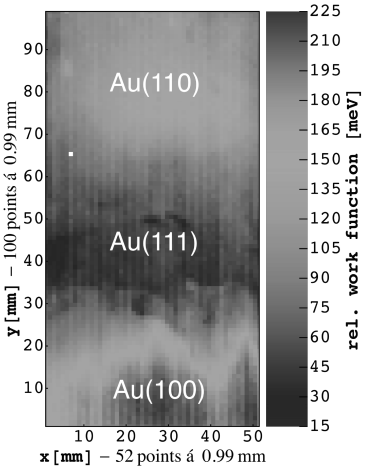

Figure 4: Scan of the surface contact potential with a Kelvin Probe of one of the aSPECT electrodes. For more details see text.

Acknowledgements

This work has been supported by the joint priority program 1491 of the Deutsche Forschungsgemeinschaft and the Austrian Science Fund, project HE2308/9-1, HE2308/9-2, ZI816/1-1, ZI816/4-1, SO1058/2-1 and I534-N20, the University of Mainz, the ILL and the Technische Universität Vienna.

References

[1] H. Abele, Prog. Part. Nucl. Phys., **60** 1 (2008).

[2] M. Simson *et al.*, NIM A, **581** 3 (2007).

[3] O. Zimmer *et al.*, NIM A, **440** 3 (2000).

[4] F. Glück *et al.*, Eur. Phys. J. A, **23** 1 (2005).

[5] Handbook of Chemistry and Physics, 95th edition, **ISBN 9781482208672**, (2014).

Limit on Lorentz-Invariance- and CPT-Violating Neutron Spin Interactions Using a ^{3}He-^{129}Xe Comagnetometer

Fabian Allmendinger[1], *Ulrich Schmidt*[1], *Werner Heil*[2], *Sergei Karpuk*[2], *Yury Sobolev*[2], *Kathlynne Tullney*[2]

[1]Physikalisches Institut, Ruprecht-Karls-Universität Heidelberg, Germany
[2]Institut für Physik, Johannes Gutenberg-Universität Mainz, Germany

DOI: http://dx.doi.org/10.3204/DESY-PROC-2014-04/41

We performed a search for a Lorentz-invariance- and CPT-violating coupling of the ^{3}He and ^{129}Xe nuclear spins to posited background fields. Our experimental approach is to measure the free precession of nuclear spin polarized ^{3}He and ^{129}Xe atoms using SQUIDs as detectors. As the laboratory reference frame rotates with respect to distant stars, we look for a sidereal modulation of the Larmor frequencies of the co-located spin samples. As a result we obtain an upper limit on the equatorial component of the background field $\tilde{b}^n_\perp < 8.4 \cdot 10^{-34}$ GeV (68% C.L.). This experiment is currently the most precise test of spin anisotropy due to the excellent long spin-coherence time.

1 Introduction and Experimental Setup

In the context of the Standard-Model Extension (SME)[1, 2, 3], couplings of the neutron or proton spin $\boldsymbol{\sigma}^{\boldsymbol{n,p}}$ to relic background fields $\tilde{\boldsymbol{b}}^{\boldsymbol{n,p}}$ are discussed. The background fields have distinct directions in space and correspond to preferred spin directions. These couplings with the potential $V = \tilde{\boldsymbol{b}}^{\boldsymbol{n,p}} \cdot \boldsymbol{\sigma}^{\boldsymbol{n,p}}$ are purely non-magnetic, but change the energy levels of spins in a magnetic field, which can be detected by changes in the Larmor frequency of precessing spins.

Nuclear spin clocks, based on the detection of free spin precession of gaseous nuclear polarized ^{3}He and ^{129}Xe atoms with LT$_C$ SQUIDs as low-noise magnetic flux detectors are used as ultra-sensitive probe for nonmagnetic spin interactions, since the magnetic interaction (Zeeman term) drops out in the case of co-located spin samples (comagnetometry). Measurements of uninterrupted precession of $T \sim 1$ day can be achieved at the present stage of investigation due to long spin-coherence times. The principle of measurement is to search for sidereal variations of the precession frequency of co-located spin species while the Earth and hence the laboratory reference frame rotates with respect to distant stars.

To give a short overview of the setup (details are given in Ref. [4]): The two polarized gas species (and N_2 as a buffer gas) are filled into a low-relaxation spherical glass cell with radius $R = 5$ cm. Typically, the optimum conditions in terms of long transverse relaxation times (T_2^*) and high Signal-to-Noise Ratio are met at a gas mixture with pressures of $p_{He} = 3$ mbar, $p_{Xe} = 5$ mbar, $p_{N2} = 25$ mbar. The cell is positioned in a homogeneous static magnetic field (about 400 nT)

that is generated by Helmholtz coils mounted inside the strongly magnetically shielded room *BMSR-2* at the *Physikalisch-Technische Bundesanstalt* in Berlin. At that field strength, the Larmor frequencies of ^{3}He and ^{129}Xe are about $\omega_{He} \approx 2\pi \cdot 13$ Hz and $\omega_{Xe} \approx 2\pi \cdot 4.7$ Hz, respectively. To measure these precession frequencies very precisely, low-noise low-temperature DC-SQUID gradiometers are used as magnetic flux detectors. Due to the very low field gradients in the order of pT/cm at the location of the cell, the transverse relaxation times reached $T_2^* = 8.5$ h for ^{129}Xe and up to $T_2^* = 100$ h for ^{3}He [4]. The measured signal amplitudes at the beginning of the measurement were up to $A_{\mathrm{He}} = 20$ pT and $A_{\mathrm{Xe}} = 8$ pT for ^{3}He and ^{129}Xe, respectively. The noise level (combination of four gradiometers) was $\rho = 3\ \mathrm{fT}/\sqrt{\mathrm{Hz}}$. Due to the long spin-coherence time and the high initial Signal-to-Noise Ratio, the spin precession could be monitored for more than one day, which improves the sensitivity remarkably (see below).

2 Data Evaluation and Results

To be sensitive to tiny nonmagnetic interactions, one has to consider the weighted difference of the respective Larmor frequencies of the co-located spin samples, or the corresponding time integral (weighted phase difference), which are defined by

$$\Delta\omega = \omega_{\mathrm{He}} - \frac{\gamma_{\mathrm{He}}}{\gamma_{\mathrm{Xe}}}\omega_{\mathrm{Xe}} \quad \text{and} \quad \Delta\Phi = \Phi_{\mathrm{He}} - \frac{\gamma_{\mathrm{He}}}{\gamma_{\mathrm{Xe}}}\Phi_{\mathrm{Xe}} \quad . \tag{1}$$

In doing so, magnetic field fluctuations are canceled, i.e. in principle $\Delta\omega = 0$ and $\Delta\Phi$ =const. if there are no further interactions. However, on a closer look, $\Delta\Phi$ is not constant in time, as higher order effects have to be take into account. These can be parameterized by

$$\Delta\Phi(t) \quad = \quad c_0 + c_1 t + E_{\mathrm{He}} e^{-t/T^*_{2,\mathrm{He}}} + E_{\mathrm{Xe}} e^{-t/T^*_{2,\mathrm{Xe}}} + F_{\mathrm{He}} e^{-2t/T^*_{2,\mathrm{He}}} + F_{\mathrm{Xe}} e^{-2t/T^*_{2,\mathrm{Xe}}} \quad . \tag{2}$$

The linear contribution stems from Earth's rotation and from chemical shift. The four exponential terms account for the Ramsey-Bloch-Siegert shift [5, 6]. These effects are discussed in Ref. [4]. Finally, the function in Eq. (2) together with the appropriate parameterization of the Lorentz-invariance-violating effect - in this case a sidereal modulation $\propto \tilde{b} \cdot \sin(\Omega_S \cdot t + \varphi_0)$ - is fitted to the combined weighted phase difference data of all measurement runs (7 in total). The resulting estimate on sidereal modulation is compatible with zero within the correlated and uncorrelated uncertainties and can be expressed as an upper limit on the magnitude of the hypothetical background field:

$$\tilde{b}^{\mathrm{n}}_{\perp} \quad < \quad 6.7 \cdot 10^{-34}\ \mathrm{GeV}\ (68\%\ \mathrm{C.L.}) \quad . \tag{3}$$

3 Frequency Stability

The benefit of long spin-coherence times can be explained on the basis of the Cramer-Rao Lower Bound (CRLB). The CRLB gives the minimum variance of an unbiased estimator of a deterministic parameter. In this case, the sensitivity of frequency measurements depends on the measurement time with coherent spin precession T, the signal amplitude at the beginning of the measurement A decaying with a time constant T_2^* and the noise level ρ (assuming white noise)[7]. The frequency uncertainty is:

$$\sigma_f \quad \geq \quad \frac{\sqrt{3}}{\pi}\frac{\rho}{A} \cdot T^{-3/2} \cdot \sqrt{C(T, T_2^*)} \tag{4}$$

with the dimensionless factor $C(T, T_2^*)$ accounting for the exponential decay of the Signal-to-Noise Ratio. The remarkable result is that the frequency uncertainty decreases with $T^{-3/2}$ for white (Gaussian) noise. The Allan Standard Deviation (ASD) is the appropriate measure to study the temporal characteristics of the ^{3}He-^{129}Xe comagnetometer with respect to phase or frequency determination. The ASD method is an established analysis technique for studying the low-frequency component of a time series and is a measure of phase and frequency stability of clocks and oscillators. In the case of the ^{3}He-^{129}Xe comagnetometer, one compares the ^{3}He precession frequency to the "scaled" ^{129}Xe precession frequency. These two oscillator frequencies are supposed to be the same if all deterministic phase shifts (chemical shift, Earth's rotation, Ramsey-Bloch-Siegert shift etc.) have been incorporated correctly. The behavior of the frequency uncertainty in the ASD plot is shown in Fig. 1 (black symbols) for two different runs. With increasing integration times τ the uncertainty in frequency decreases with $\sigma_{\mathrm{ASD}} \propto \tau^{-\frac{3}{2}}$ as expected by the CRLB in Eq. (4). This indicates the presence of pure white (Gaussian) noise. In other words: All deterministic phase shifts (chemical shift, Earth's rotation, Ramsey-Bloch-Siegert shift etc.) have been incorporated correctly. This has been tested for all measurement runs with different experimental conditions (e.g. different sample cells, partial pressures, magnetic field directions, T_2^*) and the ASD plot shows the expected behavior, leading to the conclusion that the fit model in Eq. (2) describes the behavior of the comagnetometer correctly. An incorrect fit model would immediately lead to a deviation from the CRLB power law. This is also demonstrated in Fig. 1 (gray symbols) showing the ASD as a function of τ for the residuals of a fit model where the $F_{\mathrm{He,\,Xe}}$ terms (called "cross-talk") of Eq. (2) are omitted. For run 6 (the run with largest cross-talk effect), the large deviation from the CRLB power law above $\tau \approx 500$ s is impressive. For run 3 (the run with the smallest cross-talk effect) the deviation in the ASD plot is smaller.

4 Conclusion

Freely precessing gaseous, nuclear polarized ^{3}He and ^{129}Xe samples can be used as ultra-sensitive probe for nonmagnetic spin interactions, since the magnetic interaction (Zeeman term) drops out in the case of co-located spin samples. Long spin-coherence times are highly beneficial as the uncertainty in frequency estimation decreases with $T^{-3/2}$ for Gaussian noise according to the CRLB. The ASD method can be used to verify the CRLB power law and thereby rule out the presence of further noise sources (i.e. further deterministic frequency shifts). With a similar setup, upper limits on interactions mediated by axion-like particles were obtained [8]. The next challenging step is to apply this method in the search for an electric dipole moment of ^{129}Xe.

References

[1] V. A. Kostelecký and S. Samuel, Phys. Rev. D **39**, 683 (1989).
[2] D. Colladay and V. A. Kostelecký, Phys. Rev. D **58**, 116002 (1998).
[3] V. A. Kostelecký and C. D. Lane, Phys. Rev. D **60**, 116010 (1999).
[4] F. Allmendinger *et. al*, Phys. Rev. Lett. **112**, 110801 (2014).
[5] F. Bloch and A. Siegert, Phys. Rev. **57**, 522 (1940).
[6] N. F. Ramsey, Phys. Rev. **100**, 1191 (1955).
[7] W. Heil *et al.*, Ann. Phys. (Berlin) **525**, 539 (2013).
[8] K. Tullney *et al.*, Phys. Rev. Lett. **111**, 100801 (2013).

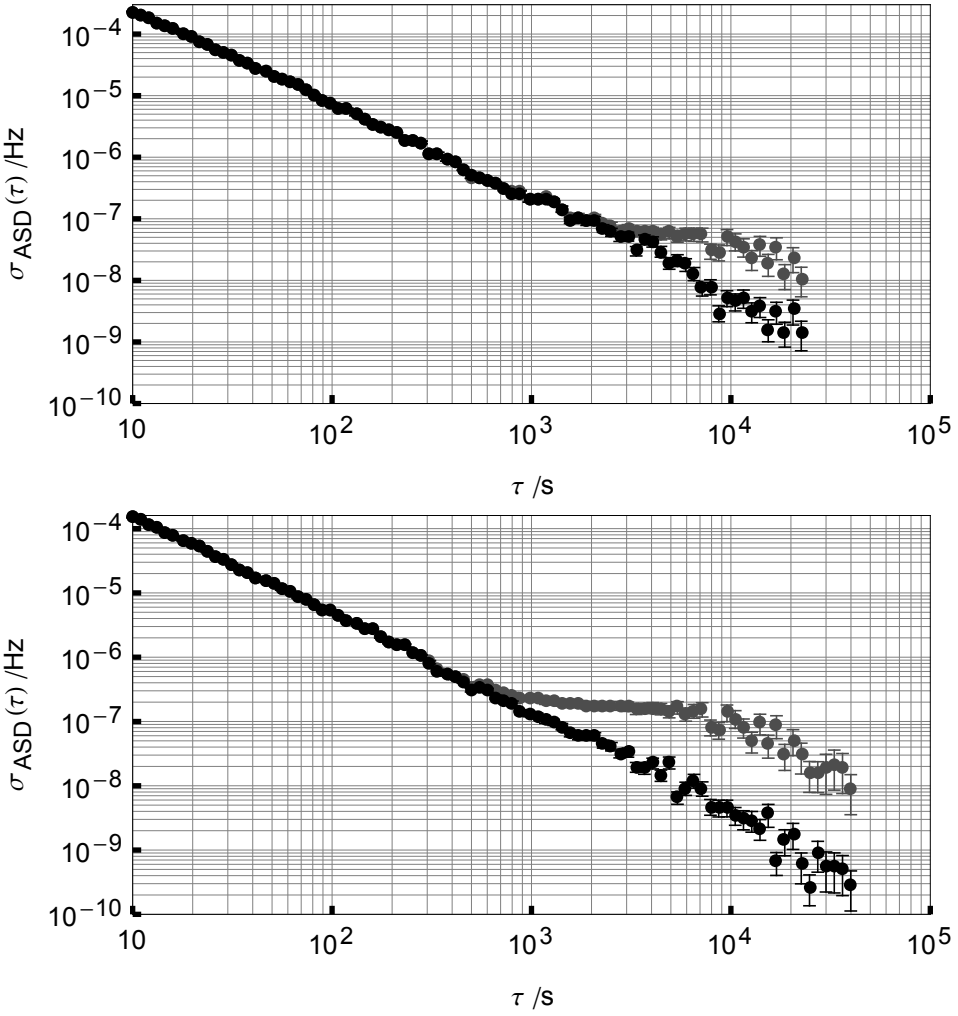

Figure 1: ASD plot of the residual frequency noise of two independent runs (Top: Run 3, Bottom: Run 6). Black symbols: ASD for the correct fit model (Eq. (2)). With increasing integration times τ the uncertainty in frequency decreases as $\sigma \propto \tau^{-\frac{3}{2}}$ indicating the presence of white (Gaussian) noise. Gray symbols: ASD for an incorrect fit model (omitting the Cross-Talk term). For run 6 (the run with largest cross-talk effect), the large deviation from the CRLB power law above a few hundred seconds is impressive. For run 3 (the run with the smallest cross-talk effect) the deviation in the ASD plot is smaller.

Laser spectroscopy of the hyperfine splitting energy in the ground state of muonic hydrogen

Masaharu Sato[1], *Katsuhiko Ishida*[1], *Masahiko Iwasaki*[1,2], *Sohtaro Kanda*[3], *Yue Ma*[1], *Yasuyuki Matsuda*[4], *Teiichiro Matsuzaki*[1], *Katsumi Midorikawa*[5], *Yu Oishi*[1], *Shinji Okada*[1], *Norihito Saito*[5], *Kazuo Tanaka*[1,4], *Satoshi Wada*[5]

[1]RIKEN Nishina Center, RIKEN, Wako, Saitama 351-0198, Japan
[2]Department of Physics, Tokyo Institute of Technology, Meguro, Tokyo 152-8551, Japan
[3]Department of Physics, The University of Tokyo, Bunkyo, Tokyo 113-0033, Japan
[4]Graduate School of Arts and Sciences, The University of Tokyo, Meguro, Tokyo 153-8902, Japan
[5]RIKEN Center for Advanced Photonics, RIKEN, Wako, Saitama 351-0198, Japan

DOI: http://dx.doi.org/10.3204/DESY-PROC-2014-04/67

A new measurement has been proposed to determine the proton Zemach radius from the ground-state hyperfine splitting energy of muonic hydrogen by mean of a laser spectroscopy. The resonance frequency corresponding to the hyperfine splitting energy difference is searched with a recently-developed mid-infrared laser. We have studied the experimental feasibility in the RIKEN-RAL muon facility.

1 Physics motivation

One of the recent hot topics in the present physics is *the proton radius puzzle*, which was stimulated by a measurement of the muonic hydrogen Lamb shift at Paul Scherrer Institute [1]. It is a discrepancy of the proton charge radius obtained by the muonic hydrogen Lamb shift from those by the ordinary methods such as electron-proton scattering and hydrogen spectroscopy [2]. The difference seems not to be attributed to the experimental uncertainty because it is more than 7σ by taking into account the new precise measurements in both sides [3, 4, 5]. To explain the discrepancy, there are several interpretations including hypotheses for physics beyond the standard model. However, none of them are still conclusive.

Meanwhile, the proton internal structure is not only related with the electric distribution, as defined as charge radius, but also with the magnetism distribution. It is a very interesting question how the magnetic distribution of the proton is determined by muons and it may give a definitive answer to understand proton radius puzzle. Therefore, we focus on the proton Zemach radius R_Z, which is defined as,

$$R_Z = \int d^3\mathbf{r}|\mathbf{r}| \int d^3\mathbf{r}' \rho_E(\mathbf{r}')\rho_M(\mathbf{r}-\mathbf{r}'), \tag{1}$$

where ρ_E and ρ_M denote the spatial distribution of the proton charge and the magnetism, respectively. To derive the proton Zemach radius, we measure the hyperfine splitting energy of

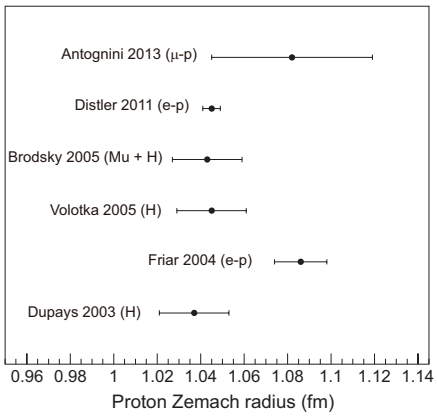

Figure 1: Summary of proton Zemach radius measurements.

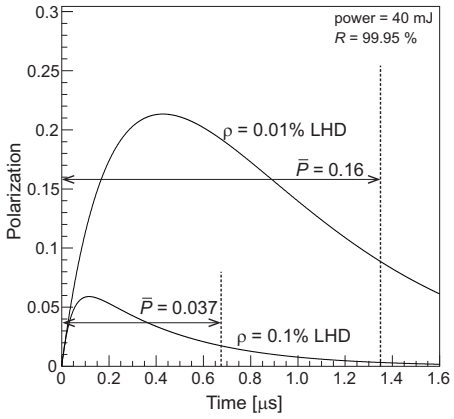

Figure 2: Time population of the muon spin polarization.

the muonic hydrogen. Theoretically, the hyperfine splitting energy is described as [6],

$$\Delta E_{HFS} = E_F(1 + \delta^{QED} + \delta^{FF} + \delta^{rec} + \delta^{pol} + \delta^{hvp}), \tag{2}$$

where E_F denotes the Fermi energy. The terms δ^{QED}, δ^{FF}, δ^{rec}, δ^{pol} and δ^{hvp} indicate the corrections related with higher order QED, proton electromagnetic form factor, recoil effect, proton polarizability and hadronic vacuum polarization, respectively. The dominant contribution is δ^{FF} and is as large as ∼7500 ppm [7]. Its leading contribution is expressed with the proton Zemach radius as, $\delta^{FF} = -2\alpha m_{\mu p} R_Z + O(\alpha^2)$, where α and $m_{\mu p}$ is the fine structure constant and the reduced mass of the muon and the proton. As same with the charge radius, the proton Zemach radius has been determined by $e - p$ scattering and the hydrogen spectroscopy [7, 8, 9, 10, 11]. Very recently, the PSI group has determined the Zemach radius from the two transitions in the 2S to 2P states of muonic hydrogen [5]. That is the first determination of the proton Zemach radius from the muonic system, however, the accuracy is still lower than the electronic determinations. A summary of the proton Zemach radius measurements is plotted in Fig. 1. Our goal is to determine proton Zemach radius from muonic hydrogen with much higher precision.

2 Principle

The experimental principle is as follows.

- *Formation of the muonic hydrogen*
  Negative muons are stopped in the hydrogen target. In the initial capture, an excited state of the muonic hydrogen is formed with a high principle quantum number of ~ 14, however, the state is quickly de-excited to the ground state. Since the nuclear capture rate in the muonic hydrogen is extremely small, muons in the atomic ground state decay with almost the same lifetime of free muons ($\tau = 2.197$ μs).

- *Laser-induced hyperfine sublevel transition*
  We irradiate a laser before muon decays to induce a transition from $^1S_0$ to $^3S_1$. The ground state hyperfine splitting energy is 0.183 eV, which corresponds to the mid-infrared wavelength of 6.78 μm. A selective excitation in a specific $^3S_1$ state ($m_Z = +1$ or -1) is realized by using a circularly-polarized laser due to the conservation rule of total angular momentum. Then the muon spin in $^3S_1$ is polarized.

- *Detection of the muon decay asymmetry*
  If polarized muons in the $^3S_1$ state decay, the emission of electrons has an asymmetry in the spatial distribution by V-A theory. Therefore, the electron emission asymmetry will be a signal to search for the resonance during the frequency scan. We detect asymmetry in the number of decay electrons in the forward and backward directions along with the laser direction.

These are the brief principle of the proposed measurement. The feasibility with the above procedure is discussed in the next section.

3 Feasibility

To accomplish the measurement, we study the two key issues; the laser-induced transition probability from $^1S_0$ to $^3S_1$ and the collisional quench rate in the $^3S_1$ state.

To detect muon decay asymmetry in the $^3S_1$ state with a limited beam time, the transition probability has to be sufficiently high to scan over a wide range of the frequency. The laser-induced transition probability P is evaluated with the laser power E [J], the cross sectional area S [m^2] and the temperature T [K] as, $P = 2\times10^{-5}E/S/\sqrt{T}$ [12]. The probability is proportional to the laser power, thus the intense mid-infrared laser is important for this measurement. Very recently mid-infrared laser system with intense and narrow band-width has been developed in RIKEN [13]. The precision of the hyperfine splitting energy is expected to be $\sim$2 ppm due to the narrow band-width. With realistic parameters of $E = 40$ mJ, $S = 4$ cm^2 and $T = 20$ K, the probability is calculated to be 4.4×10^{-4}. Since this probability is too small to perform the measurement, we adopt a multi-pass cavity installed in the hydrogen target to enhance the effective laser power by a reflection with mirrors facing each other. We assume the reflectivity of the mirror to be 99.95%. Then achievable polarization is estimated with the effect of the collisional quench rate discussed below.

The second issue is the collisional quench rate. It is known that the muon in the $^3S_1$ state is quickly de-excited to the $^1S_0$ state by a collision with a neighboring hydrogen atom and lose the polarization. If the collisional quench rate is much larger than that of the muon decay, the muon polarization made by the laser excitation is mostly lost before muon decays. Therefore, this quench rate is essential and should be comparable with the muon decay rate. Theoretically, this quench rate is calculated in Ref. [14], and it is proportional to the hydrogen density. A typical quench rate is 20 MHz with the density (ρ) of 0.1% of the liquid hydrogen density (LHD), which corresponds to the $^3S_1$ lifetime of 50 ns.

With the discussion above, we estimate the muon spin polarization taking into account the transition and quench rates. Figure 2 shows the time population of the muon spin polarization. After laser injection, the polarization increases slowly due to the small transition probability caused by each laser pass, but eventually decreases with the attenuation of the laser after the multiple reflection. The averaged polarization during the optimized time gate is 3.7 % with

ρ = 0.1% LHD. If we decease the hydrogen density to be 0.01% LHD, the polarization is increased to be 16% due to the longer lifetime of the $^3S_1$ state as shown in the figure.

Finally, we estimate the beam time for the measurement in the RIKEN-RAL muon facility. A typical intensity of 40 MeV/c negative muon beam is 2×10^4 s^{-1} with double pulse operation [15]. With the density of ρ = 0.1% LHD, about 0.1% of muons stop in the hydrogen target. For the electron counter, the acceptance and the sensitivity of spin polarization are 28% and 23%, respectively. Then the time to find the resonance with the significance of 3σ is 25 hours, where the standard deviation is defined by the statistical fluctuation in the electron counts.

We simply set the range of the scan region to be $\pm$5.7 GHz, taken from a convolution of theoretical uncertainty of δ^{FF} and δ^{pol} in Ref. [7]. The scan interval is assumed to be 100 MHz which is comparable with the resonance width of $\sim$80 MHz. We follow the three-stage scan over the frequency range above. The first and second scans are devoted to finding the resonance frequency with 3σ and 5σ significance, respectively. In the third scan, we determine the resonance frequency with fine step of 50 MHz. In total, we need 220 days for the scan sequence. With lower hydrogen density of 0.01% LHD, the time is reduced to 26 days because of the higher spin polarization. However it is very challenging to perform with such a low-density gas target against the background. We plan to follow stepwise beam studies to optimize the experimental condition in RIKEN-RAL.

4 Summary

We propose a new measurement of the hypdrefine splitting energy in the ground-state muonic hydrogen. A newly-developed intense mid-infrared laser enables us to measure it with an unprecedented accuracy of $\sim$ 2 ppm. The spin polarization in the spin triplet state is populated by a circularly-polarized laser. We search for the resonance frequency by detecting the spatial asymmetry in the polarized muon decay. From the measurement of the hyperfine splitting energy, we can derive the proton Zemach radius. The measurement is feasible at the RIKEN-RAL pulsed-muon facility.

References

[1] R. Pohl *et al.*, Nature **466** (2010) 213.
[2] P.J. Mohr, B.N. Taylor, and D.B. Newell, Rev. Mod. Phys. **80** (2008) 633.
[3] J. C. Bernauer *et al.*, Phys. Rev. Lett. **105** (2010) 242001.
[4] X. Zhan *et al.*, Phys. Lett. B**705** (2011) 59.
[5] A. Antognini *et al.*, Science **339** (2013) 417.
[6] M. I. Eides *et al.*, Phys. Rep. **342** (2001) 63.
[7] A. Dupays *et al.*, Phys. Rev. A**68** (2003) 052503.
[8] J. L. Friar and I. Sick, Phys. Lett. B**579** (2004) 285.
[9] A. V. Volotka *et al.*, Eur. Phys. J. D**33** (2005) 23.
[10] S. J. Brodsky *et al.*, Phys. Rev. Lett. **94** (2005) 022001, errutum Phys. Rev. Lett. **94** (2005) 169902.
[11] M. O. Distler *et al.*, Phys. Lett. B**696** (2011) 343.
[12] A. Adamczak *et al.*, Nucl. Instrum. Meth. B**281** (2012) 72, D. Bakalov, private communication.
[13] N. Saito *et al.*, Proc. of SPIE, vol **8526** (2012) 852605-1.
[14] J. S. Cohen, Phys. Rev. A**43** (1991) 4668.
[15] T. Matsuzaki *et al.*, Nucl. Instrum. Meth. A**465** (2001) 365.

Chapter 9

Standard model physics at the TeV scale

Recent electroweak results from ATLAS

Jochen Meyer[1] on behalf of the ATLAS collaboration

[1]CERN, 1211 Geneve 23, Switzerland

DOI: http://dx.doi.org/10.3204/DESY-PROC-2014-04/215

ATLAS measurements of multi-boson production processes involving combinations of W, Z and isolated photons are summarized. Production processes sensitive to vector-boson fusion and vector-boson scattering such as electroweak production of single vector bosons associated with two forward jets and the di-boson production at 8 TeV pp collisions are also presented. Measurements of the cross section and branching ratio for Z to four leptons are described. Standard Model parameters, such as the weak mixing angle, are measured with high precision by ATLAS and are compared to world averages. Prospects at HL-LHC are discussed as an outlook.

1 Introduction

The LHC gives amongst others the opportunity to probe the validity of the electroweak (EW) sector of the Standard Model (SM) at energies not accessible before. Deviations from the SM could indicate new physics like anomalous gauge couplings. Pair production of heavy gauge bosons are of special interest because there is an intersection with Higgs physics.

The ATLAS detector [1] installed at the LHC is able to measure and identify objects like leptons, photons and jets with its inner detector (ID) [2], hadronic and electromagnetic calorimetry [3] and muon spectrometer [4]. Neutrinos escape without any signal and are reconstructed in the transverse plane as missing energy E_T^{miss}.

2 Electroweak parameters

There are many predictions by the SM derived from just a small set of input parameters to be provided by measurements. The effective weak mixing angle, accessible via the forward-backward asymmetry A_{FB} of Z boson decays, is one of these parameters. The $Z \to e^+e^-$ (resp. $Z \to \mu^+\mu^-$) decays are analyzed with 4.8 (resp. 4.7) fb^{-1} of pp collisions at a center of mass energy of $\sqrt{s} = 7$ TeV [5]. The sensitivity of this measurement is greatly enhanced by the use of candidate electrons measured only by the calorimeters beyond the inner detector acceptance, i.e. with $2.5 < |\eta| < 4.9$. In general the invariant mass of lepton pairs is required to be 66 GeV $< m_{\ell\ell} <$ 1 TeV while if a forward electron is involved the upper bound is 250 GeV.

The background is very small with a dominant component arising from multi-jet events misidentified as prompt lepton pairs. This background is derived with data-driven techniques and is three (four) orders of magnitude smaller than the ee ($\mu\mu$) signal. Backgrounds from di-boson, $Z \to \tau\tau$ and $t\bar{t}$ are taken from Monte Carlo (MC). The angle $\cos\theta^*_{CS}$ in the Collins-Soper frame relates the final state leptons to the initial state and defines the forward ($A_{FB} > 0$)

and backward ($A_{FB} < 0$) directions. The ratio of the difference between forward and backward cross sections in a given bin of $m_{\ell\ell}$, divided by the total cross section in that bin, quantifies A_{FB}. It is determined as a function of $m_{\ell\ell}$ and unfolded for detector effects, with the main systematic uncertainties originating from the parton distribution functions (PDF) and limited MC statistics. Good agreement with the theoretical calculations is found.

The leptonic effective weak mixing angle $\sin^2\theta_W^{\text{eff}}$ is extracted from the raw A_{FB} distributions by performing χ^2 fits of templates constructed for different values of $\sin^2\theta_W^{\text{eff}}$. Only events with 70 GeV $< m_{\ell\ell} <$ 250 GeV are used. The combination of all channels results in $\sin^2\theta_W^{\text{eff}} = 0.2297 \pm 0.0004(\text{stat}) \pm 0.0009(\text{syst})$ and is the first such measurement at the Z pole from a hadron collider that combines electron and muon final states. Figure 1 presents results from other experiments as well as the ATLAS measurement separated into channels. Their combination deviates 1.8 standard deviations from the PDG best fit value.

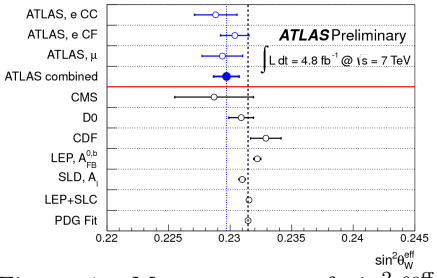

Figure 1: Measurements of $\sin^2\theta_W^{\text{eff}}$ from various experiments [5].

3 Single resonant decay to four leptons

The main contribution to the single resonant decay to four leptons at the Z pole is s-channel $Z \to \ell^+\ell^-$ production with one of the leptons emitting an off-shell Z or photon that creates another lepton pair. This final state provides a cross check for the performance of Higgs to ZZ^* to 4-lepton measurements and the branching of the Z boson to four leptons can be determined.

A dataset of pp collisions recorded at $\sqrt{s} = 7$ TeV ($\sqrt{s} = 8$ TeV) with 4.5 fb^{-1} (20.3 fb^{-1}) is analyzed [6]. Events are required with either one pair of electrons and one pair of muons, four electrons or four muons with the appropriate charge assignments. The four lepton invariant mass, $m_{4\ell}$, has to fulfill 80 GeV $< m_{4\ell} <$ 100 GeV. Each lepton pair must have an invariant mass above 5 GeV. In the same flavor modes this requirement must be fulfilled by any pairing of opposite charge. The largest dilepton invariant mass is required to be larger than 20 GeV. The overall background is determined to $< 1\%$ while there is a non resonant fraction of t-channel and gluon initial state production amounting to about 4%.

To measure $\frac{\Gamma_{Z\to 4\ell}}{\Gamma_Z}$, the expected background and non resonant contribution are subtracted from the number of observed events. Corrections for reconstruction efficiency are applied and an extrapolation to the full phase space is performed. The resulting yield is normalized to the $Z \to \mu\mu$ yield in the same dataset. The combined result $(3.20 \pm 0.25(\text{stat}) \pm 0.13(\text{syst})) \times 10^{-6}$ is in agreement with the SM value $(3.33 \pm 0.01) \times 10^{-6}$. The measurement was repeated in a fiducial volume previously introduced by CMS [7]. The results are in agreement and there is no deviation from the SM. Also cross sections at the two center of mass energies are measured and agree with the SM.

4 Di-boson production

The most recent result by ATLAS is the measurement of the W^+W^- production cross section in pp collisions at $\sqrt{s} = 8$ TeV [8]. The analyzed data amounts to 20.3 fb^{-1}. Considered events contain either one electron and one muon with $m_{e\mu} > 10$ GeV or two electrons or two muons

with $m_{ee/\mu\mu} > 15$ GeV and a deviation of 15 GeV from the Z mass. In all channels, the events are required to have opposite charge and substantial E_T^{miss}. Events with any jet with transverse momentum greater than 25 GeV reconstructed by the anti-k_t algorithm are rejected.

The main background components are W boson production with jets, Drell-Yan and $t\bar{t}$, and other di-boson modes. They are fully obtained from data, normalized to data in specific control regions, or, for the smaller components taken from MC. The total cross section is measured for all channels separately by correcting for the reconstruction efficiency and an extrapolation to the full phase space. The results are presented in Fig. 2. It shows in particular the combined cross section $71.4 \pm 1.2(\text{stat})^{+5.0}_{-4.4}(\text{syst})^{+2.2}_{-2.1}(\text{lumi})$pb, together with the theoretical predictions at NLO in QCD which are somewhat lower than the data.

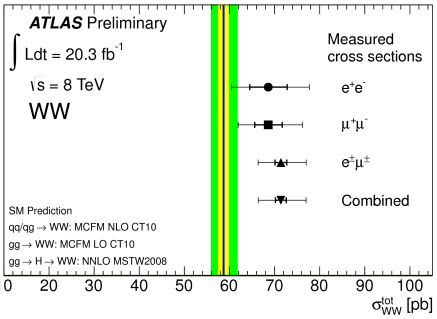

Figure 2: W^+W^- cross section [8].

5 Z boson production through vector-boson fusion

In addition to standard QCD production of Z bosons accompanied by at least two hard jets, there is the interesting production mode via vector-boson fusion referred to as EW production. This is of special interest since it gives insights into the gauge coupling structure of the EW sector of the SM.

A dataset of $20.3\,\text{fb}^{-1}$ of pp collisions recorded at $\sqrt{s} = 8$ TeV is analyzed [9]. Selected events contain a pair of electrons or muons forming an on-shell Z. At least two jets reconstructed with the anti-k_t algorithm have to be present. Five fiducial regions with different sensitivity to the EW component are studied. In the control region EW production is suppressed while the search region is optimized for this mode. The dominant background is $t\bar{t}$ which is taken from MC like WW, Wt and W plus jets. Background from multi-jet events is estimated using data driven techniques. Figure 3 presents the measured cross sections in the fiducial regions and the corresponding theory predictions.

The search region requires a di-jet invariant mass m_{jj} of at least 1 TeV and is used to probe for the EW component. The resulting m_{jj} distribution is fitted with templates to extract the EW component. The template for strong Z production is constrained by data selected in the control region. The measured cross section for the EW production is $10.7 \pm 0.9(\text{stat}) \pm 1.9(\text{syst}) \pm 0.3(\text{lumi})$fb and agrees well with the theory value of $9.38 \pm 0.5(\text{stat})^{+0.15}_{-0.24}(\text{scale}) \pm 0.24(\text{PDF}) \pm 0.09(\text{model})$fb. The background only hypothesis is rejected with more than 5 standard deviations.

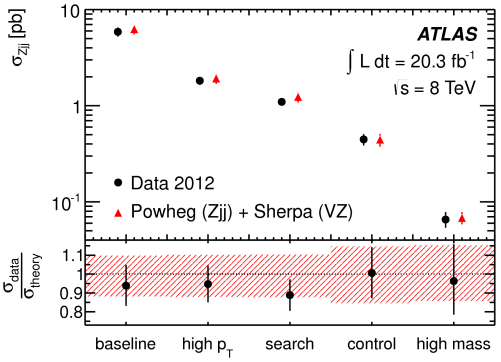

Figure 3: Z plus jets cross section [9].

The Z boson production associated with two jets gives insights into the triple gauge coupling parameters Δg_1^Z and λ_Z for which one-dimensional limits can be found in Ref. [9]. Because here the W bosons may be far off-shell the probing is complementary compared to studies in W^+W^- analyses.

6 $W^{\pm}W^{\pm}$ production via vector-boson scattering

The production of two W bosons of same charge is highly suppressed in the SM and even at the LHC only barely accessible. The final state can be created through strong production or vector-boson scattering which gives the possibility to study quartic gauge couplings.

A dataset of $20.3\,\mathrm{fb}^{-1}$ of pp collisions recorded at $\sqrt{s} = 8$ TeV is studied in two fiducial regions [10]: An inclusive region and a region where vector-boson scattering is enhanced. The inclusive region gathers events with exactly two electrons or muons of same charge and an invariant mass > 20 GeV while those with an invariant mass deviating less than 10 GeV from the Z mass are rejected. Besides substantial E_T^{miss}, there must be at least two jets reconstructed by the anti-k_t algorithm with $m_{jj} > 500$ GeV for the jets with highest transverse momentum. The region optimized for vector-boson scattering requires in addition a rapidity separation $|\Delta y_{jj}| > 2.4$ for those two jets. In both selections no jet must be identified as a b-jet.

The dominant background source arises from WZ, $W\gamma^*$ and $W\gamma$ production with photons converting into electron pairs in the ID material in the latter case. Most of the backgrounds are taken from MC and therefore the main uncertainty apart from jet reconstruction uncertainties of $11 - 15\%$ are theory uncertainties which amount to $4 - 11\%$. The combined measured cross section in the inclusive region (VBS region) is $2.1 \pm 0.5(\mathrm{stat}) \pm 0.3(\mathrm{syst})$fb ($1.3 \pm 0.4(\mathrm{stat}) \pm 0.2(\mathrm{syst})$fb) and within uncertainties compatible with the theory value of 1.52 ± 0.11fb (0.95 ± 0.06fb). The combined significance rejecting the background only hypothesis is 4.5 (3.6). The analysis provides one-dimensional as well as two-dimensional limits for quartic gauge couplings for several operator bases.

7 Prospects for HL-LHC

Facing future upgrade scenarios there are several studies for ATLAS physics performance at a high luminosity LHC at $\sqrt{s} = 14$ TeV. A variety of multi-boson channels is analyzed in their fiducial regions [11] and effective Lagrangian parameters for triple and quartic gauge couplings with cutoff unitarization are studied. Potential discovery values and expected limits are given for integrated luminosities of $300\,\mathrm{fb}^{-1}$ and $3\,\mathrm{ab}^{-1}$.

References

[1] ATLAS Collaboration, JINST **3** (2008) S08003.

[2] ATLAS Collaboration, CERN-LHCC-97-16, CERN-LHCC-97-17.

[3] ATLAS Collaboration, CERN-LHCC-96-40, CERN-LHCC-96-41, CERN-LHCC-96-42.

[4] ATLAS Collaboration, CERN-LHCC-97-22.

[5] ATLAS Collaboration, ATLAS-CONF-2013-043, http://cds.cern.ch/record/1544035.

[6] ATLAS Collaboration, Phys. Rev. Lett. **112** (2014) 231806 [arXiv:1403.5657 [hep-ex]].

[7] CMS Collaboration, JHEP **1212** (2012) 034 [arXiv:1210.3844 [hep-ex]].

[8] ATLAS Collaboration, ATLAS-CONF-2014-033, http://cdsweb.cern.ch/record/1728248.

[9] ATLAS Collaboration, JHEP **1404** (2014) 031 [arXiv:1401.7610 [hep-ex]].

[10] ATLAS Collaboration, arXiv:1405.6241 [hep-ex].

[11] ATLAS Collaboration, ATL-PHYS-PUB-2013-006, http://cdsweb.cern.ch/record/1558703.

Recent QCD Results from ATLAS

Tibor Ženiš[1] on behalf of the ATLAS collaboration

[1]Comenius University Bratislava, Slovakia

DOI: http://dx.doi.org/10.3204/DESY-PROC-2014-04/212

The ATLAS collaboration has performed studies of a wide range of QCD phenomena, from soft particle to hard photon and jet production. Recent soft-QCD measurements include studies of underlying event, vector meson production and quark confinement effects. Differential measurements of inclusive and multi-jet production provide stringent tests of high-order QCD predictions and provide input for determination of parton density functions. Measurements of isolated inclusive and di-photons cross sections for high p_{T} photons test various theoretical predictions and constrain parton density functions. In addition the total pp cross section at 7 TeV, together with the elastic and inelastic contributions, is measured and compared to various models. An overview of these results is given.

1 Introduction

The measurements described in this overview cover wide range of quantum chromodynamics (QCD) processes. The soft part of these processes characterized by low momentum transfer, comprehend processes with underlying events and is important at the total pp cross section determination. These processes cannot be calculated by the perturbative approach within the Standard Model (SM) however the obtained results test and constrain phenomenological models. The hard processes like jets, isolated prompt photon, photon and jet production provide a stringent tests for high-order theoretical QCD calculations.

The results were obtained using data produced in pp collisions at $\sqrt{s} = 7$ and 8 TeV collected by the ATLAS detector in years 2010, 2011 and 2012.

2 The ATLAS detector

The ATLAS detector is described in detail elsewhere [1]. The beam-line is surrounded by a tracking detector that uses silicon pixel, silicon strip and straw tube technologies and is embedded in a 2 T magnetic field. The tracking system covers the pseudorapidity range $|\eta| < 2.5$. It is surrounded by electromagnetic and hadronic calorimeters covering $|\eta| < 3.2$ which are complemented by a forward calorimeter covering $3.1 < |\eta| < 4.9$.

The Minimum Bias Trigger Scintillator (MBTS) detectors, the detectors used in the soft QCD measurements, are mounted in front of the endcap calorimeters on both sides of the interaction point at $z = \pm 3.56$ m and cover the range $2.09 < |\eta| < 3.84$.

The Absolute Luminosity for ATLAS (ALFA) sub-detector is located at 240 m from the interaction point in Roman Pots, its purpose is the measurement of elastic pp-scattering and small angles in the Coulomb-Nuclear Interference region.

3 Results of the ATLAS measurements

Underlying events (UE) comprise soft processes accompanying hard parton-parton interaction in pp collisions. There is no way to unambiguously distinguish between signals from the hard processes and from the UE.

The η, φ plane[1] can be divided into regions around the leading object (the highest p_{T} track or cluster in the event). Three regions are defined. The *toward* one ($\Delta\phi < 60°$) containing the leading object, the *away* one ($\Delta\phi > 120°$) containing the second leading jet in the di-jet events and the *transverse* one. The transverse region is the region most sensitive to the UE. One can distinguish the transverse region according to the leading object in this region with the maximum value of an observable into the *trans-min* and the *trans-max* sides on the event-by-event basis. Each observable has its definition of the sides.

ATLAS measured distributions sensitive to the underlying event in QCD jet events [2] using data collected at $\sqrt{s} = 7\,\mathrm{TeV}$ separately for inclusive jets and exclusive di-jet events. A sample of results is shown in Fig. 1. Comparisons to the predictions of different Monte-Carlo (MC) models show a need for further model tuning, but in general the standard approach is found to reproduce the features of the underlying event in both types of event selection.

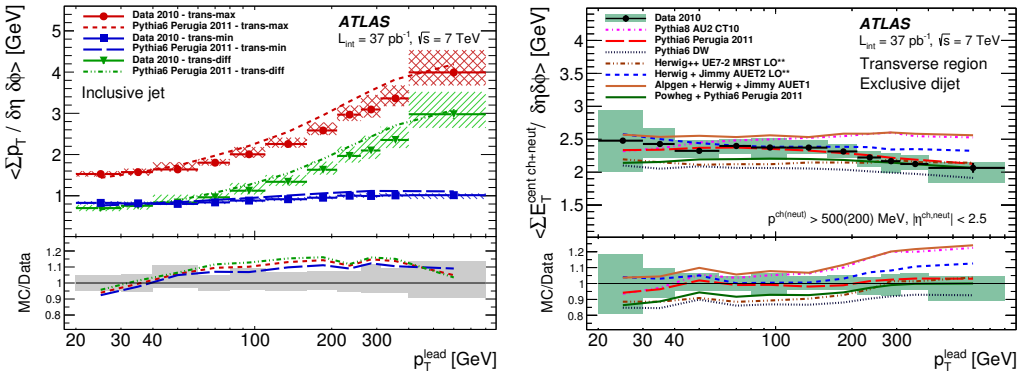

Figure 1: Comparison of profiles of charged-particle $\sum p_{\mathrm{T}}$ left (neutral and charged $\sum E_{\mathrm{T}}$ right) as a function of $p_{\mathrm{T}}^{\mathrm{lead}}$ in transverse regions for ATLAS measurements and MC predictions.

A measurement of charged-particle distributions sensitive to the properties of the underlying event for an inclusive sample of events containing a Z-boson decaying to an electron or muon pair [3] was performed using the ATLAS detector. The measured distributions are compared to the similar ones measured in jet events and to the predictions of various MC generators implementing different underlying event models.

ATLAS measured the inealistic pp cross section using the MBTS detector [4] for an acceptance region $\xi = M_{\mathrm{X}}^2/s > 5\times10^{-6}$ (M_{X} is a mass of the dissociation system) and the differential cross section for the rapidity gap size $\Delta\eta$ (central part of detector without activity) for $\Delta\eta < 8$ and $|\eta| < 4.9$ [5]. Fig. 2 left shows the ATLAS measurements with the TOTEM measurements and model predictions. The ATLAS results are consistent.

The total pp cross section measurement [6] was performed using the ALFA subdetector of

[1] ATLAS uses cylindrical coordinates (η, φ) in the transverse plane. η is the pseudorapidity, φ the azimuthal angle around the beam pipe.

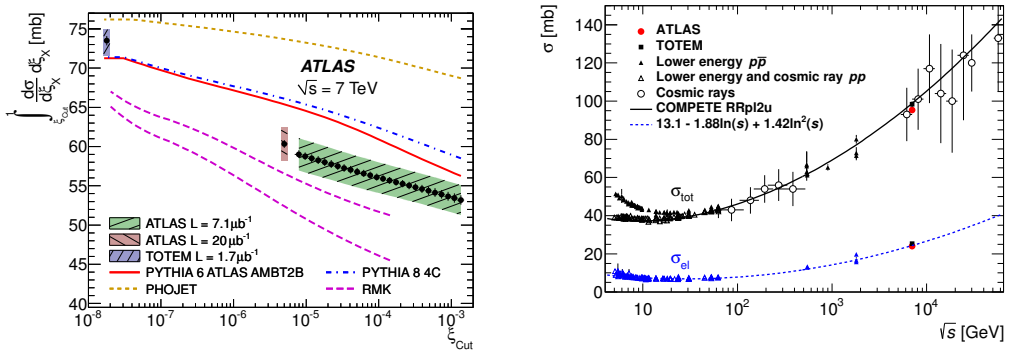

Figure 2: The differential inelastic (left) and total/elastic (right) pp cross section.

ATLAS. The total cross section is extracted using the optical theorem and its value is $\sigma_{\rm tt}(pp \to X) = 95.35 \pm 0.38(\text{stat.}) \pm 1.25(\text{exp.}) \pm 0.37(\text{extr.})\,\text{mb}$. Fig. 2 right shows this measurement compared with other published measurements.

The measurement of the $\varphi(1020)$ [7] probes strangeness production at a soft scale $Q = 1\,\text{GeV}$. It is sensitive to s-quark and low-x gluon densities. It is also sensitive to the fragmentation details. The $\varphi(1020)$ measurements can constrain phenomenological hadroproduction models.

Additional jet activity in di-jet events was measured using pp collisions at ATLAS [8]. The measurement tests the perturbative QCD theoretical predictions in extreme regions of phase space. In cases of large rapidity separation of jets or when a veto of additional jet activity is applied, higher order corrections become increasingly important. No theoretical prediction provides good agreement with the data in all observables over the whole phase space.

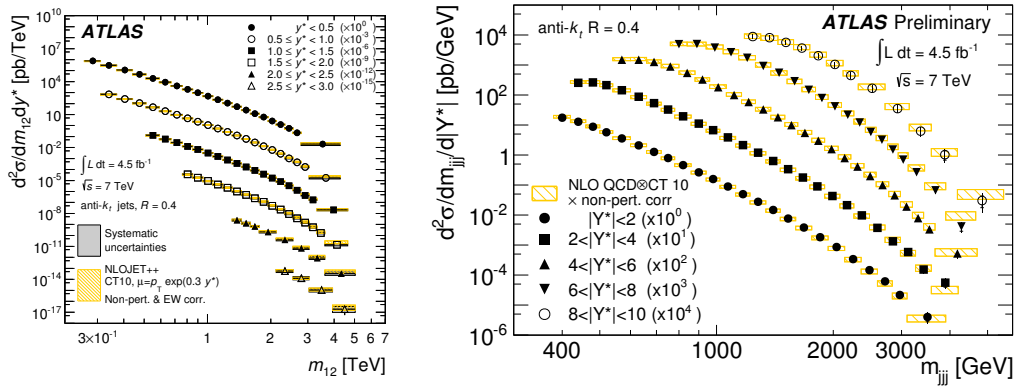

Figure 3: The differential di-jet (left) and three-jet (right) production cross section measured by the ATLAS detector compared to the NLOJet++ calculations.

ATLAS measured the inclusive-jet (not yet published) di-jet [9] and three-jet [10] production cross sections in pp collisions at $\sqrt{s} = 7\,\text{TeV}$. The measurements are in good agreement with the the NLOJet++ theoretical predictions when using the CT10, NNPDF2.1 and MSTW 2008 PDF sets as shown in Fig. 3.

An ATLAS measurement of the cross section for the production of isolated prompt photons in pp collisions at $\sqrt{s} = 7\,\text{TeV}$ [11] is compared to the LO parton-shower MC models and to the NLO perturbative QCD calculations. The prompt photon production is sensitive to the gluon content of the proton ($qg \to q\gamma$) and can be used to constrain gluon PDFs. The NLO QCD calculations agree with the ATLAS measurements.

The dynamics of isolated-photon plus jet production in pp collisions at $\sqrt{s} = 7\,\text{TeV}$ has been studied with the ATLAS detector at the LHC [12]. The production of prompt photons in association with a jet in pp collisions, $pp \to \gamma + \text{jet} + X$ provides a testing ground for perturbative QCD in a cleaner environment than in jet production, since the photon originates directly from the hard interaction. The next-to-leading-order QCD calculations are compared to the measurements and provide a good description of the data, except for the case of the azimuthal opening angle.

4 Conclusion

Various measurements sensitive to the soft and perturbative SM processes have been considered. Their characteristics like total pp cross section, characteristics of the underlying events, jets, isolated prompt photon, photon and jet production cross sections were measured by the ATLAS detector and compared to the theoretical expectations and Monte-Carlo calculations. The results of the measurements are used or have a potential to test and tune PDFs and phenomenological model parameters.

Acknowledgments

This work was supported by the Slovak funding agency (The Ministry of Education, Science, Research and Sport of the Slovak Republic).

References

[1] ATLAS Collaboration, JINST 3 (2008) S08003
[2] ATLAS Collaboration, Eur.Phys.J. C74 (2014) 2965
[3] ATLAS Collaboration, submitted to EPJC, arXiv:1409.3433
[4] ATLAS Collaboration, Nature Commun. 2 (2011) 463
[5] ATLAS Collaboration, Eur. Phys. J. C72 (2012) 1926
[6] ATLAS Collaboration, submitted to Nuclear Physics B, arXiv:1408.5778
[7] ATLAS Collaboration, Eur. Phys. J. C (2014) 74:2895
[8] ATLAS Collaboration, submitted to EPJC, arXiv:1407.5756
[9] ATLAS Collaboration, JHEP05(2014)059
[10] ATLAS Collaboration, ATLAS-CONF-2014-045
[11] ATLAS Collaboration, Phys. Rev. D 89, 052004 (2014)
[12] ATLAS Collaboration, Nucl. Phys, B 875 (2013) 483–535

Measurements of vector-boson production in ATLAS and CMS

Manuella G. Vincter[1] on behalf of the ATLAS and CMS Collaborations

[1]Carleton University, 1125 Colonel By Drive, Ottawa, ON, K1S 5B6, Canada

DOI: http://dx.doi.org/10.3204/DESY-PROC-2014-04/213

Vector-boson production in $p-p$ collisions in LHC Run-1 has been extensively studied by ATLAS and CMS. Charged and neutral-current Drell-Yan cross sections are sensitive to the parton distribution functions of the proton and electroweak corrections. The measurements of the neutral-current Drell-Yan process in three distinct kinematic regions, i.e. at the Z boson mass peak, below, and above, are performed. The results are compared to NLO Monte Carlo simulations and to NNLO QCD predictions corrected for NLO EW effects calculated using various parameterisations of the parton distribution functions. An overview of these results is given.

1 Introduction

The proton-proton collisions at the Large Hadron Collider (LHC) are in fact parton-parton collisions, where the momentum fraction x carried by a parton can be described in terms of Parton Distribution Functions (PDFs). These colliding partons may undergo a hard-scattering process producing, for example, a Z boson in the final state. The production cross section for such a process may be factorised into the hard scattering between the partons and the PDF of each of the interacting partons. Via this hard scatter, one can test perturbative QCD (pQCD). Predictions for such processes are available at next-to-next-to-leading order (NNLO).

Drell-Yan (DY) production at the LHC probes the structure of the PDFs over a wide range of x and four-momentum transfer Q^2. The quark and gluon PDFs may be parameterised by functions that describe their shapes as a function of x. One can then use such processes to feed information into global QCD fits to extract these PDFs. The cross-section measurements available at the LHC have differing sensitivity to the proton's PDFs and so much may be gained by including, for example, electroweak boson production as such processes are sensitive to both the valence and sea quark distributions.

The recent measurements presented at this PANIC Conference included the transverse momentum $p_{\mathrm{T}}^{\ell\ell}$ and invariant mass $m_{\ell\ell}$ dependence of the production of $Z/\gamma^* \to \ell\ell$, where the lepton can be either an electron or a muon, as well as the charge asymmetry of $W^{\pm}$ production. The results from QCD analyses extracting PDF information were also discussed. A subset of this presentation is summarised in these proceedings.

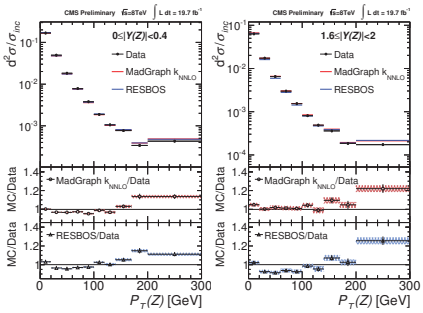

Figure 1: The CMS Z production cross section [1] as a function of $p_{\mathrm{T}}^{\ell\ell}$ in two illustrative bins of $Y_{\ell\ell}$ compared to MADGRAPH [2] normalised to NNLO (red) and RESBOS [4] (blue).

2 $p_{\mathrm{T}}^{\ell\ell}$ dependence of Z/γ^* production

Near the Z pole, single and double-differential cross-section measurements as a function of $p_{\mathrm{T}}^{\ell\ell}$ and Z-boson rapidity $Y_{\ell\ell}$ are reported. The region of low $p_{\mathrm{T}}^{\ell\ell}$ is that of initial state radiation and intrinsic k_{T} of the partons. This region may be modeled through either soft-gluon resummation or parton showers. The high $p_{\mathrm{T}}^{\ell\ell}$ region is that dominated by the radiation of high p_{T} gluons. This region may be modeled by fixed-order calculations available at NNLO. Several measurements have been made by ATLAS and CMS comparing to the predictions for a given choice of PDF. Only one example is illustrated here. Figure 1 shows the CMS measurement [1] of the double-differential cross section for DY dimuon production in two illustrative bins of the dimuon rapidity $Y_{\ell\ell}$. The ratios in these plots show comparisons of data to the leading order MADGRAPH [2] prediction scaled to NNLO with the FEWZ [3] calculation, and the NNLO RESBOS [4] prediction which models soft-gluon resummation at low $p_{\mathrm{T}}^{\ell\ell}$. Both predictions tend to overshoot the data for $p_{\mathrm{T}}^{\ell\ell}$ above approximately 80 GeV. RESBOS also tends to undershoot the data at lower $p_{\mathrm{T}}^{\ell\ell}$.

ATLAS also makes use of its differential cross-section measurements as a function of $p_{\mathrm{T}}^{\ell\ell}$ [5] and an angular variable ϕ_η^* [6] to produce a better tune for the parton shower model used (PYTHIA8 [7]) in conjunction with generators. This new tune called AZNLO is compared to an older tune labelled 4C in Figure 2. The new tune was obtained by modifying, e.g., the values of the primordial k_{T} within the proton and the value of the initial-state radiation cutoff in the parton shower. The tune shows agreement with data to better than 2% up to $p_{\mathrm{T}}^{\ell\ell}$ of 50 GeV.

3 $m_{\ell\ell}$ dependence of Z/γ^* production

Single and double-differential DY cross-section measurements as a function of $m_{\ell\ell}$ and $Y_{\ell\ell}$ are available from ATLAS and CMS in the $m_{\ell\ell}$ range of 15 GeV up to 2000 GeV. Low-mass DY production is dominated by the electromagnetic coupling of the photon γ^* to the quark-antiquark pair. This region exhibits different sensitivity to u and d-type quarks than on the Z pole which is dominated by the electroweak coupling of the Z. The measurements are compared to fixed-order calculations and to various generators and PDFs.

Figure 3 (left) shows the ATLAS measurement of the DY differential cross section at low $m_{\ell\ell}$ [8], compared to fixed-order FEWZ [3] calculations at next-to-leading order and NNLO.

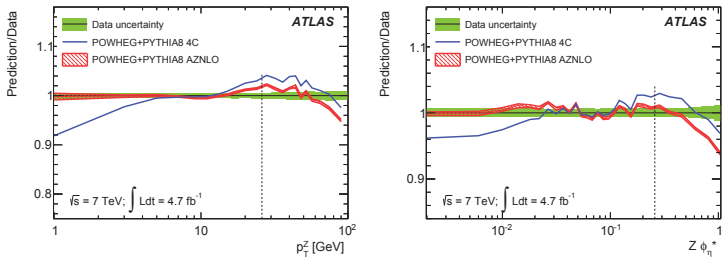

Figure 2: Comparison [5] of the tuned 4C (blue) and AZNLO (red) predictions to the $p_{\mathrm{T}}^{\ell\ell}$ (left) and ϕ_{η}^{*} (right) differential cross-section data from ATLAS.

It is evident at low $m_{\ell\ell}$ that NNLO-level calculations are needed to successfully describe the data. In this region of low $m_{\ell\ell}$, the CMS measurement [9] of the differential cross section as a function of $Y_{\ell\ell}$ is shown in Figure 3 (right) compared to a FEWZ prediction with several NNLO PDFs currently available. The agreement is good to the 10% level.

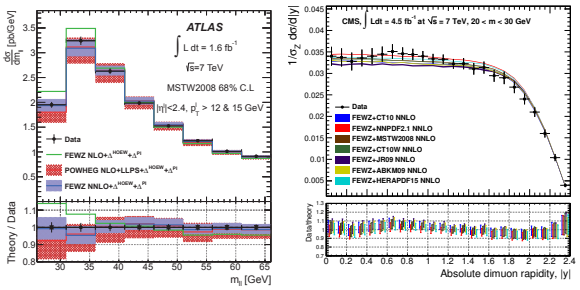

Figure 3: Left: The ATLAS cross-section measurement [8] as a function of $m_{\ell\ell}$ (points) compared to NLO and NNLO predictions. Right: Comparison of the CMS cross-section measurement [9] as a function of $|Y_{\ell\ell}|$ with theory expectations including NNLO PDF sets.

4 $W^{\pm}$ charge asymmetry

The dominant $W^{\pm}$ production mechanisms at the LHC are $d\overline{u} \to W^{-}$ and $u\overline{d} \to W^{+}$ and so the differential cross section charge asymmetry of $W^{\pm}$ production as a function of the lepton η can provide additional insight into the d/u PDF ratio as well as sea antiquark PDFs, including the poorly known strange sea. CMS has recently made a measurement of this $W^{\pm}$ charge asymmetry [10], shown in Figure 4 (left) compared to several PDF predictions. Best agreements are obtained with, e.g., the CT10 [11] PDFs while the MSTW2008 [12] family of PDFs shows significant deviations as the lepton η approaches zero. A global QCD fit was made by CMS [10], which used the HERA I inclusive data [13] and these charge-asymmetry results. Figure 4 (right) shows the prediction for d-valence quarks. Adding these new data to the global fit not only better constrains this PDF but also predicts a slight change in the shape of d_v as a function of x.

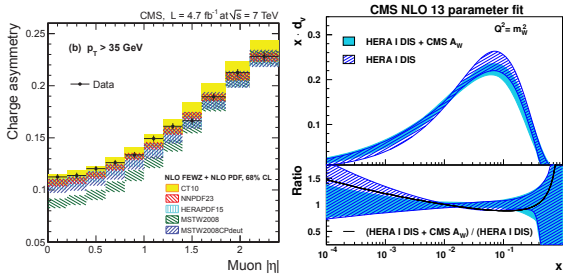

Figure 4: Left: Comparison of the CMS muon charge asymmetry [10] to predictions interfaced with several PDFs. Right: Distribution of d_v resulting from a global fit using HERA I deep inelastic scattering data [13] and CMS muon asymmetry [10] (shaded), and HERA only (hashed).

5 Conclusions

Vector-boson production at the LHC is interesting on many levels. It can be used as a probe of pQCD via the hard-scattering process as well as to better constrain PDFs, particularly valence quarks and poorly-known strange sea quarks. These proceedings presented a very brief overview of some of the ATLAS and CMS measurements that contribute to this new knowledge: the $p_{\mathrm{T}}^{\ell\ell}$ and $m_{\ell\ell}$ dependence of DY production as well as the $W^{\pm}$ production charge asymmetry.

References

[1] CMS Collaboration, CMS-PAS-SMP-13-013, cds.cern.ch/record/1700115.

[2] J. Alwall *et al.*, JHEP **06** 128 (2011).

[3] R. Gavin *et al.*, Comput. Phys. Commun. **182** 2388 (2011).

[4] G. Ladinsky and C. Yuan, Phys. Rev. **D50** 4239 (1994); F. Landry *et al.*, Phys. Rev. **D67** 073016 (2003); C. Balazs and C. Yuan, Phys. Rev. **D56** 5558 (1997).

[5] ATLAS Collaboration, arXiv:1406.3660 (2014).

[6] ATLAS Collaboration, Phys. Lett. **B720** 32 (2013).

[7] T. Sjöstrand, S. Mrenna, and P. Z. Skands, Comput. Phys. Commun. **178** 852 (2008).

[8] ATLAS Collaboration, JHEP **06** 112 (2014).

[9] CMS Collaboration, JHEP **12** 030 (2013).

[10] CMS Collaboration, Phys. Rev. **D90** 032004 (2014).

[11] H.-L. Lai *et al.*, Phys. Rev. **D82** 074024 (2010).

[12] A.D. Martin *et al.*, EPJ **C63** 189 (2009); A.D. Martin *et al.*, EPJ **C73** 2318 (2013).

[13] F.D. Aaron *et al.* (H1 and ZEUS Collaborations), JHEP **01** 109 (2010).

Higgs Boson in Lepton Decay Modes at the CMS Experiment

Somnath Choudhury[1] for the CMS collaboration

[1]DESY - Hamburg, Germany

DOI: http://dx.doi.org/10.3204/DESY-PROC-2014-04/120

The results on the standard model Higgs boson in lepton decay channels with tau pair and muon pair final states using 25 fb^{-1} of pp collision data at 7 and 8 TeV center-of-mass energies collected by the CMS detector at the LHC has been summarized. A direct evidence of the Higgs-lepton coupling is established with the tau pair decay mode. Searches for Higgs bosons decaying to leptons in scenarios beyond the standard model such as supersymmetry within the minimal extension of the model has also been reported.

1 Introduction

The ATLAS and CMS collaborations in July 2012 came out with the observation of a Higgs boson [1, 2] using proton-proton collision data from the LHC at CERN corresponding to integrated luminosities of around 5 fb^{-1} at 7 TeV and 5 fb^{-1} at 8 TeV center-of-mass energies. The LHC has completed its first run with the detectors having recorded about 95% of delivered collision data, among which about 90% were certified and used to obtain the results reported here. The final analysis is based on integrated luminosity of 20 fb^{-1} at 8 TeV in addition to the 5 fb^{-1} at 7 TeV collected by the CMS detector [3]. The observation of a Higgs boson around mass of 125 GeV in the high resolution boson decay channels motivates the search in major fermion decay modes as decays of the Higgs boson to tau pairs and bottom quark pairs have significantly large branching fraction in this mass regime. The 125 GeV Higgs boson opens an interesting avenue for its decays to fermions as this would provide an effective handle for the measurement of the Higgs coupling to fermions. The Higgs boson suffers from quadratically divergent self-energy corrections at high energies. Numerous extensions to the standard model (SM) have been proposed to address these divergences one of which is supersymmetry, a symmetry between fundamental bosons and fermions, which results in cancellation of the divergences. The Minimal Supersymmetric extension of the standard model (MSSM), outlays the introduction of 2 Higgs doublets leading to 5 physical Higgs bosons after electroweak symmetry breaking, where, h and H are the CP-even scalar bosons, A is the CP-odd pseudoscalar boson and H^+ and H^- are the charged bosons. If the discovered Higgs boson is the low mass Higgs within MSSM, then the search for its heavy partners gains a lot of interest in tau pair decay which has a branching fraction around 10% enhanced at all masses.

The CMS detector plays a crucial role in robustly identifying individual particles in the collision events. The detector subsystems employed for the analysis are the pixel detector and the silicon tracker forming the innermost component of the detector followed by the electromagnetic calorimeter of lead tungstate crystals and hadronic calorimeter of brass / scintillator

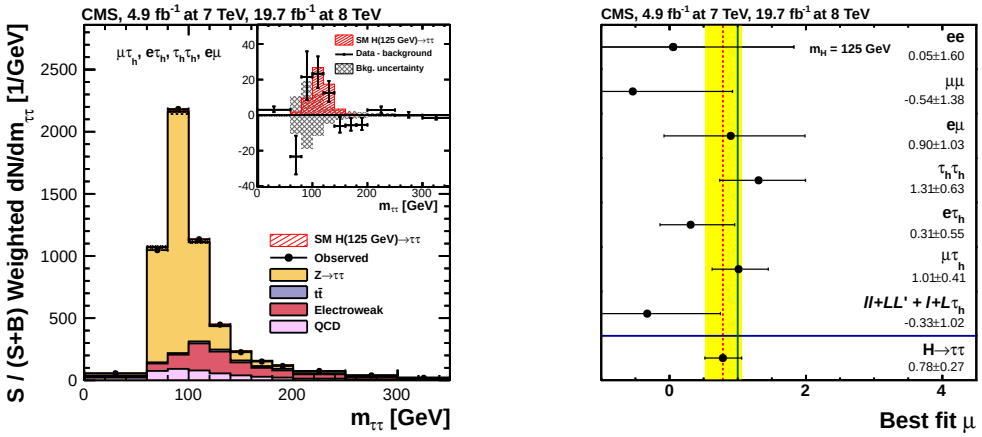

Figure 1: The di-tau invariant mass distribution combining all categories (on left) and the signal strength with respect to SM expectation in different di-tau decay channels and result of the combination (on right).

samplers which is enveloped by the 3.8 T superconducting solenoid. Outside the solenoid are the muon chambers which are gas ionization detectors in steel return yoke composed of cathode strip chambers, resistive plates and drift tubes. For the physics object reconstruction in a collision event, CMS uniquely employs a particle flow technique which provides event description in the form of mutually exclusive particles identifying all stable particles produced in the event by combining the capabilities of each sub-detector with the most precise measurement of the energy and direction for each particle and then individual measurements from each sub-detector are combined by a geometrical linking alogorithm providing particle identification on blocks of these linked elements. The experiment had to establish methods to cope with a high number of multiple collisions per beam crossing (pileup), which occurs at high luminosity. The average number of pileup events is about 9 and 21 interactions in the years 2011 and 2012 respectively. The successful mitigation of pileup was demonstrated and an almost uniform response of the missing transverse energy resolution as a function of the number of primary vertices in the event is achieved. The SM Higgs boson analysis utilises the major Higgs boson production mechanisms in pp collisions in order of decreasing cross-sections namely gluon fusion, vector boson fusion (VBF) and associated production with vector bosons (VH). The MSSM Higgs bosons search utilises the production in gluon fusion and in association with bottom quarks or in bottom quark fusion.

2 Higgs to Taus

The SM H$\rightarrow \tau\tau$ search [4] is performed using all possible decays in fully leptonic, semi-leptonic and fully hadronic states using the final-state signatures eμ, $\mu\mu$, ee, eτ_h, $\mu\tau_h$ and $\tau_h\tau_h$, where electrons and muons arise from leptonic τ-decays and τ_h denotes hadronic tau lepton decays. To enhance the sensitivity of the search, each of these categories is further divided into three exclusive sub-categories according to the nature of the associated jets in the event. The gluon-

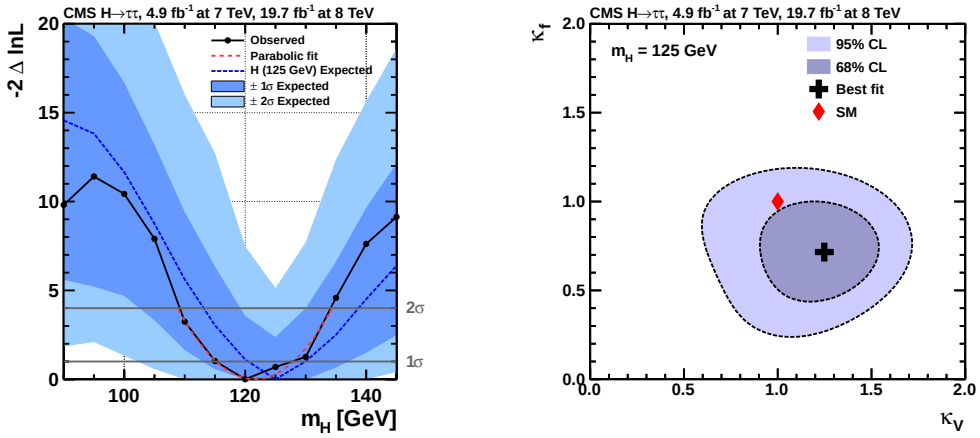

Figure 2: The measured mass from log-likelihood scan in the di-tau channel (on left) and the 2-D scan of couplings to vector bosons and fermions scaled to the SM expectation (on right).

fusion production mechanism has the largest production cross section. However, in the mass region of interest, background from Drell–Yan production of tau pairs overwhelms the expected Higgs boson signal. This search therefore relies strongly upon the signature of Higgs bosons produced via vector boson fusion (VBF) or in association with a high transverse momentum (p_T) jet recoiling against the tau pair. In the former case, the distinct topology of two jets with a large rapidity separation greatly reduces the background. In the latter, requiring a high-p_T jet both suppresses background, and improves the resolution of the tau-pair invariant mass. The search has been categorized into 0-jet, 1-jet and 2-jet VBF categories to extract the signal which are further split on the basis of hadronic tau p_T and di-tau p_T for 0 and 1 jet categories or di-tau p_T, di-jet invariant mass and di-jet pseudorapidity separation for 2-jet category. The 0-jet category constrains the background normalization, identification efficiencies and energy scales, the 1-jet category improves the resolution of Higgs boson mass and the VBF category has high signal over background ratio. The analysis is also performed in the VH category with lepton tagging from vector bosons along with the tau lepton pair.

To distinguish the Higgs boson signal from the background, the tau-pair mass is reconstructed using a maximum likelihood technique. The algorithm estimates the original momentum components of the two taus by maximizing a likelihood with respect to free parameters corresponding to the missing neutrino momenta, subject to kinematic constraints. Other terms in the likelihood take into account the tau-decay phase space and the probability density in the tau transverse momentum, parametrized as a function of the tau-pair mass. This algorithm yields a tau-pair mass with a mean consistent with the true value, and distribution with a nearly Gaussian shape. The relative $m_{\tau\tau}$ mass resolution estimated from simulation is 10–20% depending on the di-tau decay channel and category. The likelihood based mass reconstruction allows for a better separation between simulated 125 GeV Higgs signal and $Z\rightarrow \tau\tau$ background than the visible mass alone, yielding an improvement in the final expected significance of 40%.

In each of these categories, a search is performed for an excess of events in the reconstructed di-tau invariant mass distribution. The largest source of irreducible background is $Z\rightarrow \tau\tau$ which is estimated using an observed sample of $Z\rightarrow \mu\mu$ events, where the reconstructed muons are

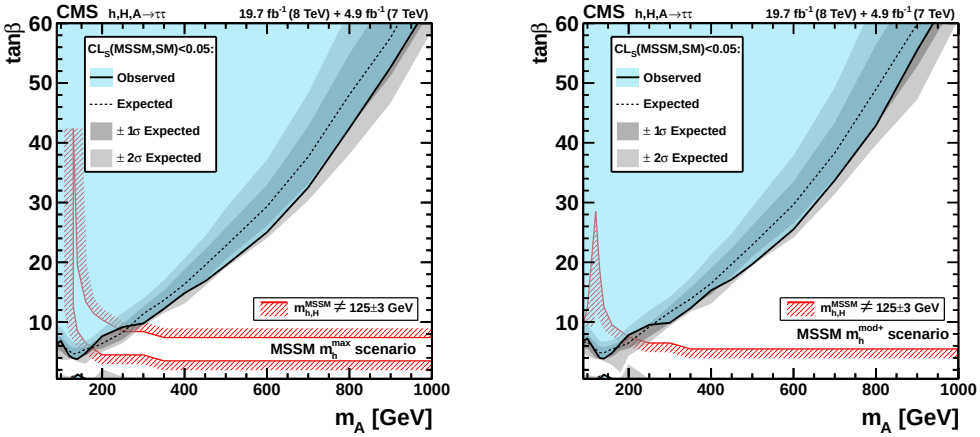

Figure 3: Region in the parameter space of tanβ versus m_A excluded at 95% CL in the context of the MSSM maximal mixing scenario (on left) and a modified mixing ${m_h}^{mod+}$ benchmark scenario (on right). The expected one- and two- standard deviation ranges and the mean expected 95% CL upper limits are shown together with the observed excluded region.

replaced by the reconstructed particles from simulated tau decays, a procedure called "embedding". The normalization for this process is determined from the measurement of the CMS measured cross section. The reducible backgrounds (W + jets, multijet production, Z + jets) are also evaluated from control samples in data. The QCD multijet background is evaluated using the ratio of opposite-sign (OS) to same-sign (SS) di-tau events and relaxed lepton isolation after an estimate of the W + jets background using the high transverse mass ($m_T^{\ell E_T^{miss}}$) side-band W boson enriched region and extrapolating it to the signal region. The Z + jets background is evaluated from fake rate and OS/SS ratio with the shape from simulation. The top pair produced events and diboson contribution are estimated using simulation.

Combining all event categories, a broad excess of events is observed in the tau pair invariant mass distribution as seen in Figure 1 over a range of the Higgs boson mass consistent with the 125 GeV scalar boson observed in the high resolution boson decay channels. The observed (expected) significance of the excess at Higgs boson mass of 125 GeV is 3.2σ (3.7σ). The best-fit value of the signal strength is μ=0.78±0.27, obtained in the global fit combining all channels included in this analysis where the H→WW process has been added as a background for the observed process. This result provides the first direct indication of the Higgs boson coupling to leptons. The mass of the Higgs boson measured in this channel is 122±7 GeV from a parabolic fit of the log-likelihood scan of the observed mass points in data shown in Figure 2. The measured couplings of the Higgs boson to vector bosons and fermions scaled with respect to SM, shows consistency within around one standard deviations from SM predictions where the H→WW process has been added as a signal for this measurement.

A Higgs-like state at 125 GeV is rather large for the light MSSM Higgs boson which can be achieved by maximizing the radiative corrections to Higgs mass at 1-loop level. The tau-pair decays of the neutral Higgs bosons in the MSSM, having a branching fraction of roughly 10%, serve as the best experimental signature for this search. The $b\bar{b}$ mode, though it has a much larger branching fraction, suffers from an overwhelming background from multi-jet production.

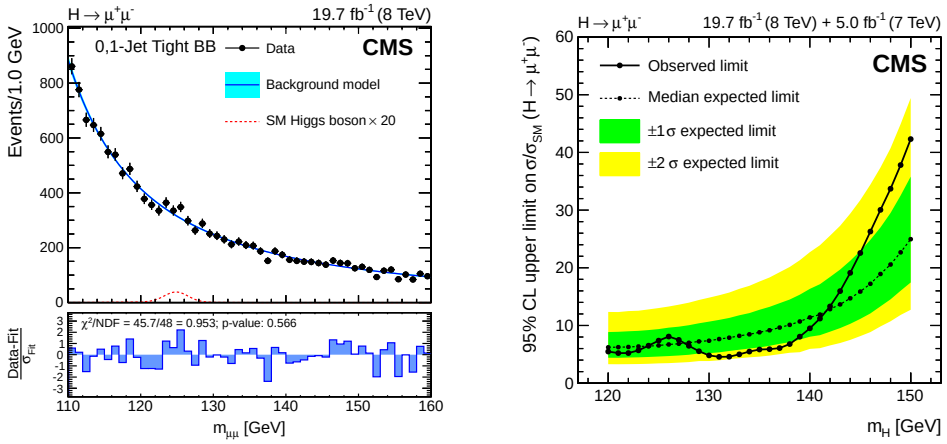

Figure 4: The di-muon invariant mass distribution combining all categories (on left) and 95% CL upper limits on cross section times the branching ratio normalized to the SM expectation as a function of Higgs boson mass (on right).

The MSSM Higgs bosons search [5] is performed using the di-tau final-state signatures eμ, $\mu\mu$, eτ_h, $\mu\tau_h$ and $\tau_h\tau_h$. The τ_h decay modes considered for the analysis are a single charged hadron, a charged hadron with neutral pion via the $\rho(770)$ resonance and three charged hadrons via the a_1 resonance. The data sample has been divided on the b-jet multiplicity into b-tag and non b-tag categories to enhance the sensitivity to bbΦ coupling:
• b-Tag category: At most one jet with p_T>30 GeV and at least one b-tagged jet with p_T>20 GeV.
• Non b-Tag category: At most one jet with p_T>30 GeV and no b-tagged jet with p_T> 20 GeV.
The di-tau invariant mass spectrum shows no evidence for a Higgs boson signal and hence 95% confidence level (CL) upper bound on the Higgs boson production cross-section times the branching fraction to tau pairs have been set using the mass shape of the tau pair mass spectrum and uncertainties from theory (parton distribution function and renormalization / factorization), normalization (luminosity and efficiency) and shape (energy scale). These limits are further interpreted in the MSSM parameter space on the m_A-tanβ plane as shown in Figure 3 in the maximal mixing scenario of the stop-top sector with a soft SUSY breaking mass of 1 TeV as the stop mass scale as well as a modified m_h mixing benchmark scenario [6]. It excludes all previously unexplored regions reaching as low as tanβ = 3.9 for mass of the pseudoscalar Higgs boson m_A=140 GeV.

3 Higgs to Muons

One of the properties of the Higgs boson that has to be checked is the couplings to first and second generation leptons. Indeed, the SM Higgs decays to fermions should not be universal. A search for H→ $\mu\mu$ [7] is performed with at total luminosity of the 7 and 8 TeV dataset from Run-1 LHC. In the SM, the decay H→ $\mu\mu$ presents a vary small branching ratio of $2.2\text{x}10^{-4}$ at m_H = 125 GeV. However, the search takes advantage of the clean signature in the detector and the excellent di-muon invariant mass resolution. The gluon fusion and VBF production

modes are utilized by the jet multiplicity of events in the final state. In addition, events are split into categories according to the p_T of the di-muon system, the properties of jets in the 2-jet category, and according to the detector regions (barrel, endcap, overlap regions) in which the two muons are reconstructed. The latter make use of the different experimental resolutions of the reconstructed di-muon mass for muons from different detector regions. The signal is extracted by means of a fit to the di-muon invariant mass distribution using signal and background shapes. The combined di-muon mass distribution is shown in Figure 4, weighted for the ratio of the signal and signal-plus-background distributions in the dfferent event categories. The background distribution is estimated using an analytic fit function, and, amongst others, systematic uncertainties are estimated by modifying the used fit function. Upper limits on the cross section times H$\rightarrow \mu\mu$ branching ratio have been derived and the observed (expected) limit is found to be 7.4 (5.1) times the SM prediction. The observed significance at 125 GeV is 1.1σ and no significant excess of events is expected in this channel at the Run-1 LHC luminosity.

4 Conclusion

A broad excess of events is observed for the SM Higgs boson search in the tau pair decay mode consistent with the 125 GeV Higgs boson signal from high resolution boson decay modes ($\gamma\gamma$ and ZZ$^\star\rightarrow 4\ell$) providing the first direct indication of the Higgs boson coupling to leptons. Combining tau pair and bottom quark pair decay modes, the significance for Higgs boson decay to fermions at 125 GeV is more than 3σ showing the first direct evidence of Higgs-fermion coupling [8] at the LHC. The mass of the Higgs boson measured in the di-tau channel is 122 ± 7 GeV from a parabolic fit of the likelihood scan of the Higgs mass. The results on the SM Higgs boson in di-tau and di-muon decays reveal lepton non-universality. The search for MSSM Higgs bosons in tau pair decay has set stringent bounds in the m_A-tanβ plane with different MSSM benchmark scenarios tested and reaching as low as tanβ=3.9 at m_A=140 GeV at a modified mixing scenario consistent with the observed Higgs boson at 125 GeV. In the Run-2 LHC, the measurement of properties of the Higgs-like state in tau decay would continue looking for deviations from SM as well as searches for Higgs bosons beyond the SM in lepton decays.

References

[1] The ATLAS Collaboration, Phys. Lett. **B 716** 1 (2012).

[2] The CMS Collaboration, Phys. Lett. **B 716** 30 (2012).

[3] The CMS Collaboration, JINST **3** S08004 (2008).

[4] The CMS Collaboration, JHEP **05** 104 (2014) and all references therein.

[5] The CMS Collaboration, arXiv: 1408.3316 [hep-ex] and all references therein.

[6] M. Carena et. al., Eur.Phys.J. **C73** 2552 (2013).

[7] The CMS Collaboration, CMS-PAS-HIG-13-007 and all references therein.

[8] The CMS Collaboration, Nat. Phys. **10**, 557 (2014) and all references therein.

The Higgs Physics Programme at the International Linear Collider

Felix Sefkow[1]

[1]DESY, Notketraße 85, 22607 Hamburg, Germany

DOI: http://dx.doi.org/10.3204/DESY-PROC-2014-04/122

The talk summarises the case for Higgs physics in e^+e^- collisions and explains how Higgs parameters can be extracted in a model-independent way at the International Linear Collider (ILC). The expected precision will be discussed in the context of projections for the experiments at the Large Hadron Collider (LHC).

1 Introduction

The discovery of a Higgs boson, honoured with the 2013 Nobel prize in physics, marks a turning point in particle physics, as the last missing building block of the Standard Model falls into place and opens the door to completely new studies of a particle unlike every other discovered before. Like in many earlier instances in the history of particle physics, it did not come as a surprise, but was anticipated and sought for. The Higgs mass had been predicted with increasing precision from the analysis of electro-weak quantum corrections, in which measurements at the previous generation of e^+e^- colliders played a prominent role.

Today, Higgs physics has been identified as one of the prime "drivers" of the field, as a compelling line of research with great promise, where surprises may be expected. The main question is to fully establish the profile of the Higgs particle, measure its quantum numbers and, above all, its precisely predicted couplings to almost all other fundmental particles, and to find out whether it fulfils its rôle in the Standard Model, or whether it holds the key to new physics beyond.

The accuracy, which is required in order to detect possible mechanisms behind electroweak symmetry breaking through deviations of the Higgs couplings from their pure Standard Model values, has been quantitatively investigated in the framework of the Snowmass study 2013 [1]. Popular models like two-Higgs doublet or composite Higgs schemes, which predict new particles at the TeV scale, and which are still compatible with recent limits from direct searches at the LHC, typically lead to such deviations in the per-cent or sub-percent range. This sets the scale of the future experimental challenges and demonstrates the discovery potential of precision measurements in the Higgs sector.

The ILC and its detectors

The ILC has been proposed as the next big high energy accelerator project. It is designed to have centre-of-mass energies ranging from 250 to 500 GeV and is upgradeable to reach 1 TeV. The delivered luminosity increases with energy and amounts to typically 100 – 300 fb^{-1}/y,

with beam polarisations of up to 80% and 30% for electrons and positrons, respectively. The superconducting technology is mature, as is demonstrated by the on-going construction of the European XFEL at DESY, which uses a very similar design at industrial scales. A technical design report (TDR) [2] for the ILC has been completed in 2012, a proposed site has been selected in the Kitakami mountains in the North of Japan, and the project is currently being discussed at ministerial levels.

Two detector concepts have been proposed [3] for the ILC, which have been optimised for precision, as radiation hardness and rate capability requirements are very relaxed with respect to those at the LHC. The detectors feature highly granular and compact calorimeters for particle flow reconstruction, ultra-thin and precise trackers, and vertex detectors capable of identifying not only beauty but also charm quarks. Detailed designs have been implemented in the simulations to evaluate the physics potential under realistic conditions, including beam-induced backgrounds.

2 Measurements of Higgs couplings

It is instructive to recall the necessary ingredients to a measurement of a coupling strength. The number of particles N observed in a given final state f, normalised to integrated Luminosity L, is given by the product of cross-section σ and branching fraction $\mathcal{B}$, which is the ratio of partial width Γ_f to total width Γ_T. The couplings to the initial and final state, g_i and g_f, enter via the production cross section and the partial width, such that one has

$$N/L = \sigma \cdot \mathcal{B} = \sigma \cdot \Gamma_f/\Gamma_T \sim g_i^2 \cdot g_f^2 \,/\, \Gamma_T \,. \tag{1}$$

In order to extract g_f, one needs a measurement of the inclusive cross section – to obtain g_i – and the total width. In the Z line shape analysis at LEP, the width of the Z resonance was directly observable, and the cross section in the e^+e^- final (and initial) state provided a normalisation of the couplings of the Z to fermions. The width of the Higgs particle, however, is expected to be about 4 MeV in the Standard Model and too narrow to be resolved experimentally, so it has to be extracted from the branching ratio of a channel, for which the coupling is already known, e.g. from a production measurement,

$$\Gamma_T = \mathcal{B}/\Gamma_f \sim \mathcal{B}/g_f^2 \tag{2}$$

At the LHC the total cross section and total width are poorly constraint, and in general the Standard Model values are assumed. At the ILC, however, one can make use of the unique features of an e^+e^- collider to obtain a self-contained set of observables.

2.1 Higgs production at the ILC

The dominant Higgs production processes at the ILC are Higgs strahlung and W fusion. [4]. Figure 1 shows the diagrams and the dependence of the cross-section on the centre-of-mass energy. Higgs strahlung as an s channel process dominates at threshold, whilst the cross section of the t channel process W fusion increases logarithmically with energy and takes over at about 450 GeV. Here, one has made use of the beam polarisation to enhance the cross section. Now, since at an e^+e^- machine one can control the energy of the incoming fermions, one can select the dominant process by tuning the beam energy.

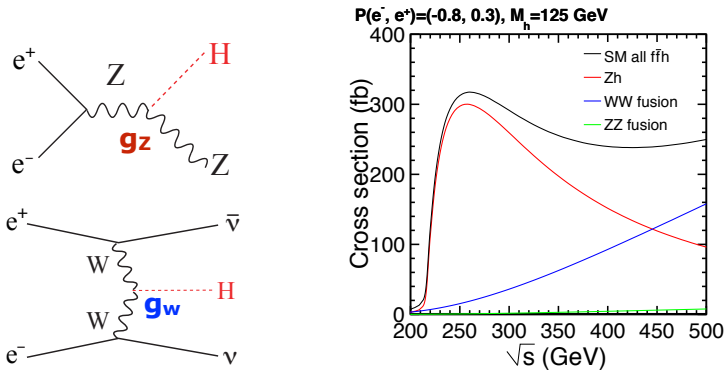

Figure 1: Higgs production diagrams and cross section vs. centre-of-mass energy.

Another consequence of the well-defined initial state is the possibility to apply kinematic constraints. In ZH events, a Higgs signal can be observed in the spectrum of recoil masses against the Z decay products,

$$M^2_{\text{recoil}} = E^2 - p^2 \text{ with } E = \sqrt{s} - E_Z \text{ and } p = p_Z$$

This works best for Z decays into muon pairs, as shown in Figure 2, but also well for the electron channel, whilst for hadronic Z decays it is more difficult. Here, no requirements whatsoever on the Higgs final state have been made, it can even be invisible, and thus the measurement is fully inclusive. It provides an absolute normalisation for all branching ratios into specific final states and a model-independent extraction of the absolute value of g_Z, the Higgs Z coupling, which is *the* central measurement of the Higgs coupling analyses.

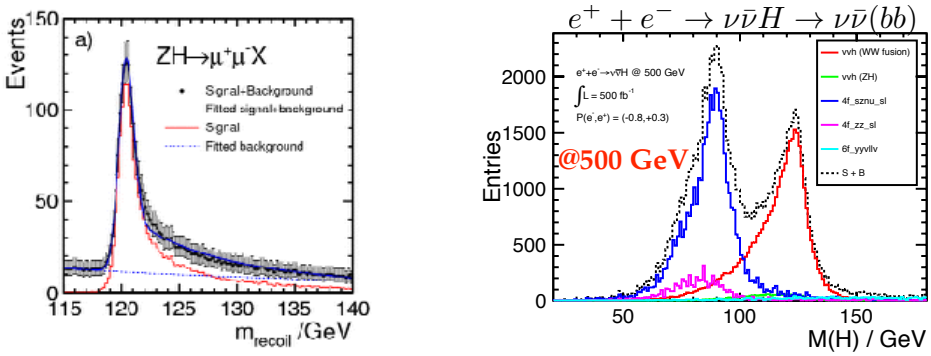

Figure 2: Higgs signal in the recoil mass spectrum (ZH production), and in the $b\bar{b}$ di-jet mass (W fusion).

2.2 The Higgs total width

The Higgs mass of 125 GeV is almost ideally suited for the study of a large number of decay modes with not too small branching ratios. However, the fraction of decays into Z pairs is only a few per-cent and the statistics for specific Z channels very small. An extraction of the total width, using Eq. 2 with g_Z and $\mathcal{B}(\mathrm{H} \to \mathrm{ZZ}^*)$ is in principle possible, but would suffer from large uncertainties of $\sim 20\%$.

It is more advantageous to use the W fusion cross section and the branching ratio $\mathcal{B}(\mathrm{H} \to \mathrm{WW}^*)$. Since in W fusion the Higgs is accompanied by two neutrinos, the recoil method cannot be applied for a decay-mode independent measurement, but a specific Higgs channel must be used. Both the $b\bar{b}$ and the WW^* channel are suited [5]; the $b\bar{b}$ signal is shown in Figure 2. Since these decay modes are also measured in HZ production, the ratio g_W/g_Z and thus g_W can be extracted and Γ_T from Eq. 2. Now one has all ingredients to convert also the other branching ratio measurements into absolute couplings,

2.3 Higgs couplings to fermions and the self-coupling

Thanks to the relatively benign beam conditions at the ILC vertex detector systems can be realised which can not only identify b flavoured hadron decays on the basis of the finite decay length, but can also tag charmed hadrons and disentangle prompt open charm from tertiary vertices, which originate from $b \to c$ decays. Particularly well suited are ZH events with Z decaying into neutrinos, such that the final state consists of the two jets from the Higgs only, giving a signal in the diet invariant mass. A multivariate analysis of the vertex topologies then yields a simultaneous measurement of $\mathcal{B}(\mathrm{H} \to b\bar{b})$, $\mathcal{B}(\mathrm{H} \to c\bar{c})$ and $\mathcal{B}(\mathrm{H} \to gg)$, and thus g_b, g_c and a model-dependent value for g_t, like the $\gamma\gamma$ mode.

The measurement of the coupling to the second quark generation is unique for testing the mass dependence of the Higgs coupling in the quark sector, since couplings to u, d and s quarks are unobservable. In the lepton sector, g_τ can be measured well, but in the H$\to \mu\mu$ channel only very few events can be observed and only at the highest energies attainable at the ILC, where luminosity and cross section are maximal.

The direct observation of the top Higgs Yukawa coupling is made though a production cross section measurement for the $t\bar{t}$H channel, where, e.g., a Higgs is radiated from one of the two quarks in a $t\bar{t}$ pair. This involves the analysis of complex 8 or 10 fermion final states, where eben after using flavour tags and di-jet masses, the signal basically consists of an excess over expectation without $t\bar{t}$H coupling. This is a particularly good example for cases where a large gain in precision can be obtained from a combined evaluation of ILC and LHC data, see below.

Finally, a measurement of the Higgs self-coupling would represent the last cornerstone in establishing the Higgs profile and demonstrating that it has the properties required for electroweak symmetry breaking. The strength g_{HHH} can be measured at the ILC, albeit with only moderate precision. This is due to the fact that ZHH events are not only produced with diagrams involving triple-Higgs coupling, but also through processes like double Higgs strahlung, which constitute an irreducible background. The situation is more favourable in the case of W fusion leading to $\nu\bar{\nu}$HH events, therefore the best precision is obtained at highest energies, where the dilution is less and luminosity and cross section are largest.

3 Global fits and achievable precision: Summary

In a staged running scenario, each centre-of-mass energy, 250, 500 and 1000 GeV, provides an independent set of measurements. Altogether, 33 measurements of $\sigma \cdot \mathcal{B}$ values are made and injected into a global fit with 10 free parameters – the couplings to W, Z and t, b, c, τ, μ fermions, indirect to gg, $\gamma\gamma$ pairs, and the total width Γ_T. The result is shown in Figure 3.

The precision has been compared to that expected for the LHC [6] and its high-luminosity upgrade [7]. In these studies consistent assumptions and constraints have been used for both colliders' data sets, which is important for a fair comparison. As the Figure 3 shows, with linear collider results the per-cent and sub-per-cent level precision can be reached, which is required to detect deviations from the Standard Model in the magnitude expected in theories for mechanisms behind electro-weak symmetry breaking.

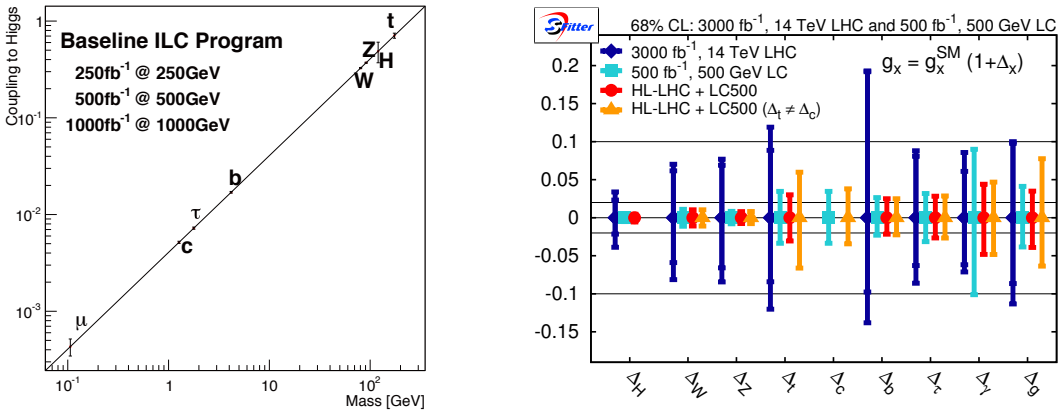

Figure 3: Higgs coupling strengts, mesurerd at the ILC, as a function of mass: relative precision for expected ILC and LHC results, including the luminosity upgrade, and combination of data.

References

[1] S. Dawson, A. Gritsan, H. Logan, J. Qian, C. Tully, R. Van Kooten, A. Ajaib and A. Anastassov *et al.*, arXiv:1310.8361 [hep-ex].

[2] C. Adolphsen, M. Barone, B. Barish, K. Buesser, P. Burrows, J. Carwardine, J. Clark and H. M. Durand *et al.*, arXiv:1306.6328 [physics.acc-ph].

[3] T. Behnke, J. E. Brau, P. N. Burrows, J. Fuster, M. Peskin, M. Stanitzki, Y. Sugimoto and S. Yamada *et al.*, arXiv:1306.6329 [physics.ins-det].

[4] H. Baer, T. Barklow, K. Fujii, Y. Gao, A. Hoang, S. Kanemura, J. List and H. E. Logan *et al.*, arXiv:1306.6352 [hep-ph].

[5] C. Dürig, K. Fujii, J. List and J. Tian, arXiv:1403.7734 [hep-ex].

[6] M. E. Peskin, arXiv:1312.4974 [hep-ph].

[7] M. Klute, R. Lafaye, T. Plehn, M. Rauch and D. Zerwas, Europhys. Lett. **101** (2013) 51001

Top Quark Precision Physics at Linear Colliders

Frank Simon[1] on behalf of the ILC Physics and Detector Study and the CLICdp Collaboration

[1]Max-Planck-Institut für Physik, Föhringer Ring 6, 80805 München, Germany

DOI: http://dx.doi.org/10.3204/DESY-PROC-2014-04/123

Linear e^+e^- colliders provide a rich set of opportunities for precision top physics, crucial for the understanding of electroweak symmetry breaking and for the search for physics beyond the Standard Model. A $t\bar{t}$ threshold scan in e^+e^- annihilation enables a precise measurement in theoretically well-defined mass schemes with small experimental and theoretical systematic uncertainties. Above the production threshold, the efficient identification of top pair events combined with polarized beams provides the potential to extract the form factors for the top quark couplings with high precision and in a model-independent way, resulting in excellent sensitivity to physics beyond the Standard Model. This contribution provides an overview of top physics at linear colliders based on results from full-simulation studies of top quark pair production in the detectors proposed for ILC and CLIC.

1 Introduction

As the heaviest particle in the Standard Model, the top quark has a special role. Due to its high mass, it has the the strongest coupling of all known particles to the Higgs field. It also takes a central role in many models of New Physics, and thus provides a high sensitivity for phenomena beyond the Standard Model.

To date, the top quark is the only quark that has been studied exclusively at hadron colliders. The clean experimental environment in e^+e^- collisions enables the study of all decay modes of the top quark with high resolution and very low background levels. The measurements at lepton colliders also profit from the high precision of theoretical calculations, which result in small overall systematic uncertainties.

At e^+e^- colliders, there are two different main programs for top physics. The first is the study of the threshold for top quark pair production, which provides access to the detailed properties of the top quark. The second is the use of the top quark as a tool for the search for physics beyond the Standard Model, for example by precisely measuring its coupling to the electroweak interactions. In the first case, collision energies at several different values around 350 GeV are necessary, while the second program requires energies substantially in excess of the threshold for top pair production, of the order of 500 GeV or higher. In particular, the energies above threshold are uniquely available at linear e^+e^- colliders.

Two such high-energy e^+e^- colliders are currently being developed in international collaboration, the International Linear Collider (ILC) [1] and the Compact Linear Collider (CLIC) [2]. They are based on different acceleration technologies, resulting in a different energy reach for the full projects. ILC is based on superconducting RF structures, and is planned as a 500 GeV collider with operation at different energies from 250 GeV to 500 GeV, including the region around the $t\bar{t}$ threshold, and the possibility for upgrades to one TeV. CLIC uses a

normal-conducting two-beam acceleration scheme, and is foreseen to be constructed in several stages. It has an ultimate energy of 3 TeV and two lower energy stages to maximise the physics potential, with the first stage covering the $t\bar{t}$ threshold. For ILC, the technical design report has been completed, while for CLIC a conceptual design report was delivered, with a technical design phase still ongoing until 2018.

In the following, the top physics program at these future colliders is illustrated based on two examples that have been studied with detailed simulations with realistic detector models, including physics and machine-related backgrounds. For the $t\bar{t}$ threshold scan, studies have been performed both in the context of ILC and CLIC, while the investigation of the physics potential for measurements of the electroweak couplings of the top quark have been performed for ILC at 500 GeV.

2 A top threshold scan at ILC and CLIC

The cross section of $t\bar{t}$ production close to the threshold strongly depends on the top quark mass. In addition, it receives contributions from the top quark width, from the strong coupling and from the top Yukawa coupling. The top width influences the shape of the would-be bound state of the $t\bar{t}$ pair. The strong coupling and the top Yukawa coupling, which both influence the interaction of the two top quarks, primarily affect the overall magnitude of the cross section. Beyond those effects connected to the $t\bar{t}$ system, the cross section also receives corrections due to initial state radiation (ISR) and due to the luminosity spectrum of the collider. The pure $e^+e^- \to t\bar{t}$ cross section can be calculated with high precision, resulting in clean theoretical predictions for the observables based on theoretically well-defined parameters, such as the 1S mass of the top quark.

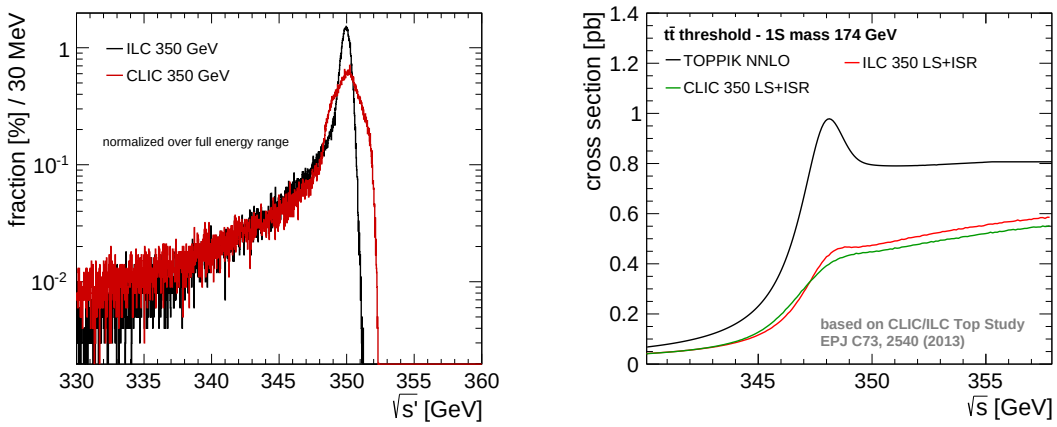

Figure 1: The luminosity spectrum for ILC and CLIC at 350 GeV (*left*) and the resulting total $t\bar{t}$ cross section in the threshold region based on TOPPIK NNLO calculations [3, 4] including ISR and luminosity spectrum effects.

Figure 1 shows the luminosity spectrum of both ILC and CLIC at an energy of 350 GeV, and illustrates the effect of these spectra together with initial state radiation on the pure $t\bar{t}$

production cross section calculated with NNLO QCD [3, 4]. The luminosity spectrum and ISR result in an overall reduction of the effective cross section since they shift a fraction of the luminosity below the threshold energy, and lead to a broadening of the threshold turn-on due to the low-energy tail and due to the width of the main luminosity peak. Since the beam energy spread is larger at CLIC than at ILC, the smearing is slightly more pronounced at CLIC.

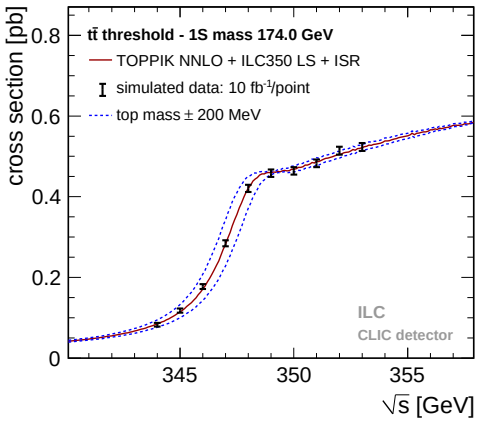

Figure 2: A simulated $t\bar{t}$ threshold scan at ILC with 10 points spaced by 1 GeV each, assuming an integrated luminosity of 10 fb^{-1} per point with unpolarised beams. For illustration purposes, the effect of a shift in the 1S top quark mass by $\pm$200 MeV is shown in addition to the simulated data points. Figure taken from [6].

With full detector simulations of the CLIC_ILD concept [5] the reconstruction efficiencies for $t\bar{t}$ events and the rejection efficiency for Standard Model background was determined in the threshold region. These efficiencies are used to simulate threshold scans at ILC and CLIC, as illustrated in Figure 2. From these scans, the top mass is determined via a template fit of the measured cross section. With a 10-point scan with a total integrated luminosity of 100 fb^{-1} assuming unpolarised beams, the top quark mass can be determined with a statistical uncertainty of 18 MeV in the case of ILC and 21 MeV in the case of CLIC [6]. The current precision of α_s of 0.0007 leads to a systematic uncertainty of equal magnitude (18 MeV for ILC, 20 MeV for CLIC), which is expected to improve in the future with a more precise determination of the strong coupling constant.

In addition, there are experimental systematic uncertainties from several sources, such as the beam energy and the reconstruction efficiency and background contamination, which are expected to have a total size below 50 MeV. On top of that, there are theoretical systematics due to the precision of the calculation of the total $t\bar{t}$ cross section. These depend on the details of the calculations, and are still being evaluated. With the simplified assumption of a 3% overall normalisation uncertainty, the resulting systematic uncertainty of the mass is around 50 MeV, making theoretical uncertainties potentially the leading source of systematics.

A potentially important source of experimental systematics is the knowledge of the luminosity spectrum. The impact of this has been studied for CLIC by reconstructing the luminosity spectrum from simulated measurements of large-angle Bhabha scattering [7]. In a preliminary study, the uncertainty resulting from the precision of the reconstructed luminosity spectrum

has been found to be of the order of 6 MeV, demonstrating that this is not a limiting factor for the overall precision of the top quark mass measurement. Since the luminosity spectrum at ILC is less complicated than the one at CLIC, even smaller uncertainties are expected for the ILC case.

Overall, a $t\bar{t}$ threshold scan at linear colliders is expected to provide the top quark mass in a theoretically well-defined mass scheme with sub-100 MeV total uncertainty, which would provide a knowledge of the $\overline{MS}$ mass of the top quark at the 100 MeV level or better. Given the dominance of systematics and the uncertainties involved in the conversion from the 1S to the $\overline{MS}$ mass, the small differences in statistical uncertainties between the different linear collider options are insignificant.

3 Electroweak couplings

The capability for polarised beams at linear colliders provides excellent conditions to probe the electroweak couplings of the top quark in $t\bar{t}$ production above threshold. These couplings are precisely determined in the Standard Model, but may receive substantial modifications in scenarios with physics beyond the Standard Model, such as extra dimensions and Higgs compositeness. The measurement of the total production cross section, the forward-backward asymmetry and the helicity angle, each for two different polarisation configurations, provides sufficient information to fully constrain the top quark couplings with high precision. Since the asymmetry and angle measurements require the identification of the top quark charge and rely on the correct association of W bosons and b jets to top candidates, these measurements profit from higher energy which provides a clean separation of the two top quarks in the $t\bar{t}$ system.

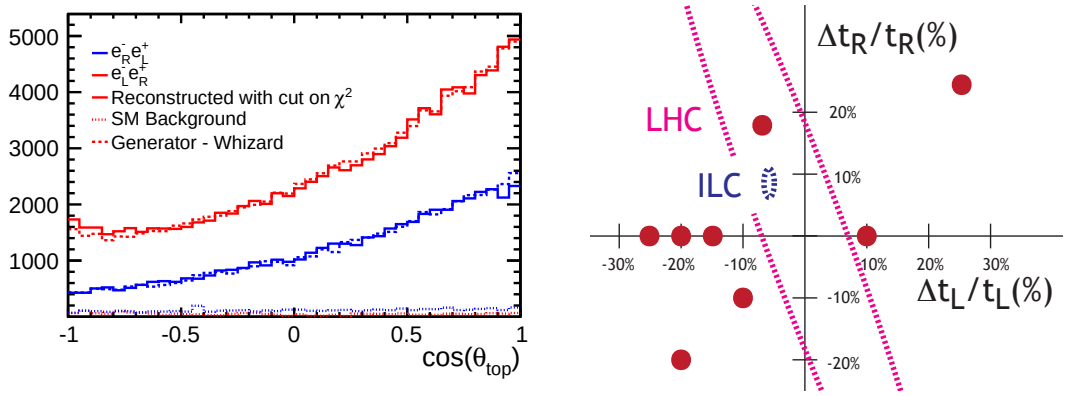

Figure 3: The forward-backward asymmetry of $t\bar{t}$ production at 500 GeV in a full simulation study for two different polarisation configurations of the beams ($\pm$ 80% e^-, $\mp$ 30% e^+ polaristion) (*left*). Figure taken from [8]. The precision achievable at ILC at 500 GeV with an integrated luminosity of 500 fb^{-1} for the left- and right-handed couplings of the top quark, compared to the expected precision achievable at the HL-LHC, together with the deviations from the Standard Model values in a variety of models with composite Higgs bosons [9, 10] (*right*).

Figure 3 *left* shows the forward-backward asymmetry in a full simulation study with the ILD

detector [11] for an integrated luminosity of 500 fb^{-1} at an energy of 500 GeV at ILC. The total integrated luminosity is equally split between two polarisation configurations of $\pm 80\%$, $\mp 30\%$ for electrons and positrons, respectively [8]. From this measurement, the forward-backward asymmetry is extracted with a $\sim$2% uncertainty including statistical and systematic contributions. Similarly, the helicity angle distribution can be extracted with a precision of 4%, and the total cross section with a 0.5% uncertainty. From these results, the left- and right-handed couplings can be extracted with a 0.7% and 1.8% precision, respectively [8, 9]. This precision is illustrated in Figure 3 *right* together with the predicted deviations from the Standard Model for several scenarios of New Physics with composite Higgs bosons and with the precision expected from the HL-LHC [9, 10]. This clearly illustrates the immense power of a polarised high-energy electron-positron collider not only to discover possible new phenomena in the top sector, but also to precisely pin down the underlying mechanism if deviations from the Standard Model are observed.

4 Summary

The future linear electron-positron colliders ILC and CLIC provide excellent opportunities for a precise study of the top quark sector. With polarised beams, the possibility for a scan of the $t\bar{t}$ production threshold and with measurements of the electroweak couplings of the top quark at energies substantially above the threshold they will provide high precision measurements of top quark properties and significant sensitivity for various physics scenarios beyond the Standard Model. A linear collider will determine the top-quark mass in the theoretically well-defined $\overline{MS}$ scheme with a total precision of 100 MeV or better, and is capable of a percent-level measurement of the top electroweak couplings, which provides sensitivity to new physics scales extending substantially beyond the direct reach of present colliders.

References

[1] T. Behnke *et al.*, arXiv:1306.6327 [physics.acc-ph].

[2] P. Lebrun *et al.*, arXiv:1209.2543 [physics.ins-det].

[3] A. H. Hoang and T. Teubner, Phys. Rev. D **60**, 114027 (1999).

[4] A. H. Hoang and T. Teubner, Phys. Rev. D **58**, 114023 (1998).

[5] L. Linssen *et al.*, arXiv:1202.5940 [physics.ins-det].

[6] K. Seidel, F. Simon, M. Tesar and S. Poss, Eur. Phys. J. C **73**, 2530 (2013).

[7] S. Poss and A. Sailer, Eur. Phys. J. C **74**, 2833 (2014).

[8] M. S. Amjad *et al.*, arXiv:1307.8102 [hep-ex].

[9] F. Richard, arXiv:1403.2893 [hep-ph].

[10] K. Agashe *et al.*, arXiv:1311.2028 [hep-ph].

[11] T. Behnke *et al.*, arXiv:1306.6329 [physics.ins-det].

Measurements with electroweak bosons at LHCb

Katharina Müller

Winterthurerstr. 190, CH-8057 Zurich, Switzerland

DOI: http://dx.doi.org/10.3204/DESY-PROC-2014-04/241

The LHCb measurements of electroweak boson production, either inclusive, or in association with a jet or a D meson at a centre-of-mass energy $\sqrt{s}$=7 TeV as well as Z boson production in proton-lead collisions are reported. The LHCb forward acceptance allows measurements complementary to the other LHC experiments.

1 Introduction

The LHCb detector [1] is a single-arm forward spectrometer instrumented in the pseudorapidity region $2 < \eta < 5$ and is optimised for the study of B and D mesons. Its unique kinematic coverage allows it perform measurements that are sensitive to both low and high values of Bjorken x and hence are complementary to those performed at the general purpose detectors, ATLAS and CMS. At energy scales typical for electroweak boson production, LHCb measurements are sensitive to values of x as low as 1.7 $\times 10^4$, where they can provide a fundamental input to parton distribution functions (PDFs) kinematic parametrisations of the partons within the colliding protons. The results presented here, except for Z production in proton-lead, are based on data collected at a centre-of-mass energy of 7 TeV with an integrated luminosity of about 1 fb^{-1}.

2 W boson production

A measurement of inclusive W boson production is performed at LHCb using the muonic decay mode of the W boson [2]. Events are selected which contain a muon with a transverse momentum, p_T, above 20 GeV/c and $2 < \eta^\mu < 4.5$. In addition, the muon is required to be isolated and consistent with production from the primary vertex. Furthermore it is required that there is no other muon in the event with $p_T > 2$ GeV/c. The signal purity is obtained by fitting the p_T distribution of the data sample in eight bins of muon pseudorapidity for both charges, simultaneously, to the expected shapes for signal and background. Background contributions are decay-in-flight of pions and kaons, semi-leptonic decays of heavy-flavour mesons, $Z \to \mu\mu$ events with one muon outside the LHCb acceptance and $Z \to \tau\tau$ events with a single muon in the final state. The templates are obtained from simulation for the signal and the electroweak backgrounds and from data for the other backgrounds. A total of about 8×10^6 W candidates are selected, with signal purities of about 77% for both charges of the muon. The signal yield is corrected for losses due to reconstruction and selection efficiency, acceptance and final-state radiation (FSR). The reconstruction and selection efficiencies are primarily estimated from data, while the acceptance and FSR corrections are determined with simulation. The total

cross-sections for W^+ and W^- production in the fiducial range defined as $p_T^\mu > 20$ GeV/c and $2 < \eta^\mu < 4.5$ are measured to be $\sigma(W^+ \to \mu\nu) = 861.0 \pm 2.0 \pm 11.2 \pm 14.7$ pb and $\sigma(W^- \to \mu\nu) = 675.8 \pm 1.9 \pm 8.8 \pm 11.6$ pb, where the first uncertainty is statistical, the second is systematic and the third is due to the luminosity. The W^+ and W^- cross-sections and the lepton charge asymmetry as a function of muon pseudorapidity are shown in Fig. 1, where many experimental and theoretical uncertainties cancel for the latter. The measurements are compared to theoretical predictions calculated at next-to-next-to-leading order (NNLO) in QCD [3] using different parameterisations of the PDFs. In general, the results are in good agreement with the predictions.

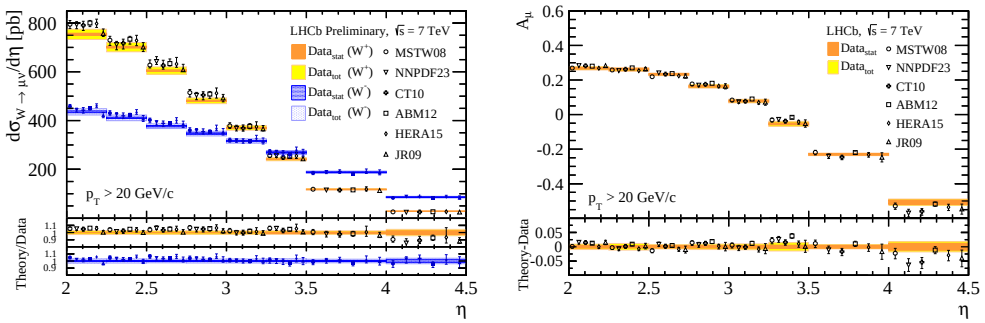

Figure 1: W^+ and W^- cross-sections (left) and lepton charge asymmetry (right) as a function of muon pseudorapidity [2]. The measurements, shown as coloured bands, are compared to NNLO predictions with different PDF sets. They are displaced horizontally for better visibility.

3 Z plus jet production

The production of a Z boson in association with a hadronic jet is studied with the Z decaying into two muons [4] with the same kinematic requirements for the muons as in the W analysis. In addition, the di-muon invariant mass is restricted to $60 < M_{\mu\mu} < 20$ GeV/c^2 and the event is required to contain a high-p$_T$ jet with $2 < \eta^{jet} < 4.5$ and $p_T^{jet} > 10$ or 20 GeV/c. The jets are reconstructed using an anti-k_T algorithm [5] with radius parameter of R=0.5. Reconstructed tracks and neutral clusters serve as charged and neutral inputs to the jet reconstruction algorithm and are selected using a particle flow algorithm. The jet energy scale is determined using simulation and cross-checked in data, with the jet energy resolution varying between 10 and 15% for the p_T^{jet} between 10 and 100 GeV/c. The fraction of $Z \to \mu\mu$ events containing a jet are determined to be $\sigma(Z + jet)/\sigma(Z) = 0.209 \pm 0.002 \pm 0.015$ for jet $p_T^{jet} > 10$ GeV/c and $\sigma(Z + jet)/\sigma(Z) = 0.083 \pm 0.001 \pm 0.007$ for jet $p_T^{jet} > 20$ GeV/c. The first uncertainty is statistical and the second systematic. The differential cross-section normalised to the inclusive Z cross-section for $p_T^{jet} > 20$ GeV/c is shown as a function of the azimuthal separation of the Z boson and the jet, $\Delta\phi$, in Fig. 2. The measurement is compared to theoretical predictions at up to $\mathcal{O}(\alpha_s^2)$ with parton showering and hadronisation effects included. As expected, the calculations performed at $\mathcal{O}(\alpha_s)$ fail to describe the distribution.

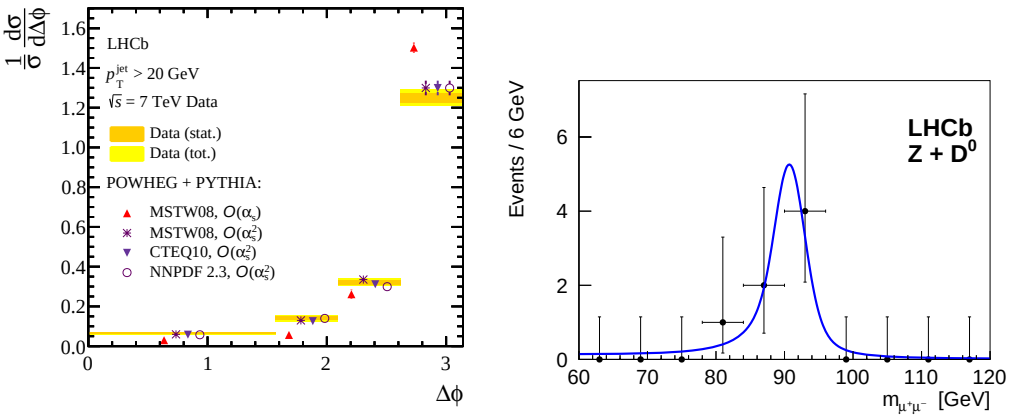

Figure 2: Z plus jet cross-section as a function of $\Delta\phi$ [4] (left). Invariant di-muon mass for the selected $Z + D^0$ candidates [6] (right).

4 Z plus D production

The $Z \to \mu\mu$ selection is also applied to search for the production of Z bosons in association with D mesons [6]. The D candidates are reconstructed using the $D^0 \to K\pi^+$ and $D^+ \to K\pi^+\pi^+$ decay modes and are restricted to the kinematic range of $2 < \eta^D < 4$ and $2 < p_T^D < 12$ GeV; together with the kinematic range of the muons of the Z decay, this also defines the fiducial volume of the measurement. The Z and the D are furthermore required to come from the same primary vertex. Backgrounds are taken into account from feed-down from beauty meson decays, which is the dominant contribution, combinatorics, and pile-up where the Z boson and the D meson are produced in different proton-proton interactions. The signal purity is determined to be about 95%. A total of 7(4) candidates are found for the $Z + D^0(Z + D^+)$ decay channel, corresponding to a combined significance of 5.1σ. The reconstructed mass of the Z boson for events in the $Z + D^0$ sample is shown in Fig. 2 (right). The production cross-sections are measured to be $\sigma(Z \to \mu\mu, D^0) = 2.50 \pm 1.12 \pm 0.22$ pb and $\sigma(Z \to \mu\mu, D^+) = 0.44 \pm 0.23 \pm 0.03$ pb, where the first uncertainty is statistical and the second systematic. The cross-sections receive contributions from single parton (SPS) and double parton scattering processes (DPS). The latter dominates in the kinematic range of the measurement. The measured cross sections are found to be in agreement with theoretical predictions[1] for the $Z + D^0$ but lower for $Z + D^{\pm}$. However, the large statistical uncertainties do not allow a firm conclusion.

5 Inclusive Z boson production in proton-lead collisions

Measurements in proton-lead collisions can serve as reference for future lead-lead collisions but can also provide significant constraining power for nuclear PDFs in unprobed regions of the phase space, at both low and high x_A, where x_A is the longitudinal momentum fraction of the parton in the nucleon. A search for Z boson production is performed based on two data samples corresponding to 1.6 nb^{-1} of proton-lead collisions at a centre-of-mass energy per

[1]The SPS contribution is calculated with MCFM [7], DPS as $\sigma = (\sigma_{Z\to\mu\mu}\sigma_D)/\sigma_{eff}$ with σ_{eff} from [8].

proton-nucleon pair of $\sqrt{s_{NN}}$ =5 TeV [9]. The two data samples correspond to two different beam configurations, with the proton (lead) beam into the direction of LHCb, referred to as forward (backward). The Z candidates are reconstructed in the di-muon final state. Background contributions from muon mis-identification and the decay of heavy flavour mesons are determined from data. A total of 15 candidates are selected with a purity of above 99%, corresponding to a significance of 10.4σ (6.8σ) for the Z signal in the forward (backward) direction. Figure 3 (left) shows the di-muon invariant mass of the Z candidates in the forward direction. The inclusive Z boson production cross-section is measured to be $\sigma(Z \to \mu\mu) = 13.5^{+5.4}_{-4.0} \pm 1.2$ nb in the forward and $\sigma(Z \to \mu\mu) = 10.7^{+8.4}_{-5.1} \pm 1.0$ nb in the backward configuration. Here, the first uncertainty is statistical and the second systematic. The measurements are compared to theoretical predictions calculated at NNLO using the FEWZ generator [3] and computed with and without considering nuclear effects based on the EPS09 nuclear PDF set [10] in Fig. 3 (right).

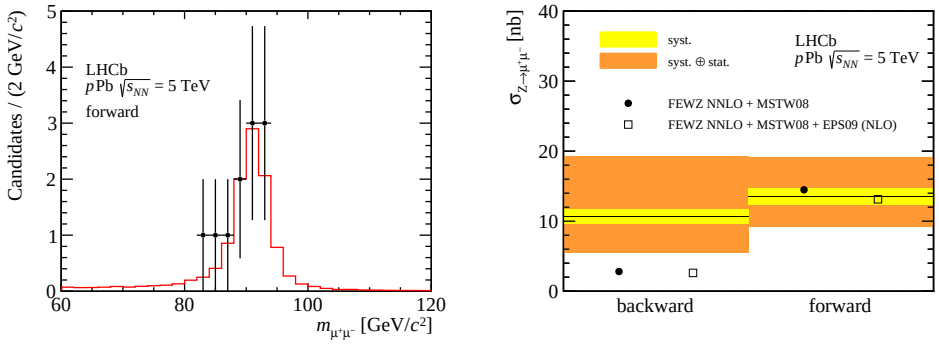

Figure 3: Left: Invariant di-muon mass of the Z candidates in proton-lead collisions. Right: Experimental results and theoretical predictions for the Z production cross-section in proton-lead collisions [9].

References

[1] Jr. Alves, A. Augusto et al. The LHCb Detector at the LHC. *JINST*, 3:S08005, 2008.

[2] R. Aaij et al. Measurement of the forward W boson cross-section in pp collisions at $\sqrt{s} = 7$ TeV. 2014.

[3] Ye Li and Frank Petriello. Combining QCD and electroweak corrections to dilepton production in FEWZ. *Phys.Rev.*, D86:094034, 2012.

[4] R. Aaij et al. Study of forward Z + jet production in pp collisions at $\sqrt{s} = 7$ TeV. *JHEP*, 1401:033, 2014.

[5] Matteo Cacciari, Gavin P. Salam, and Gregory Soyez. The Anti-k(t) jet clustering algorithm. *JHEP*, 0804:063, 2008.

[6] Roel Aaij et al. Observation of associated production of a Z boson with a D meson in the forward region. *JHEP*, 1404:091, 2014.

[7] John M. Campbell and R.K. Ellis. MCFM for the Tevatron and the LHC. *Nucl.Phys.Proc.Suppl.*, 205-206:10–15, 2010.

[8] F. Abe et al. Double parton scattering in $\bar{p}p$ collisions at $\sqrt{s} = 1.8$TeV. *Phys.Rev.*, D56:3811–3832, 1997.

[9] R. Aaij et al. Observation of Z production in proton-lead collisions at LHCb. *JHEP*, 1409:030, 2014.

[10] K.J. Eskola, H. Paukkunen, and C.A. Salgado. EPS09: A New Generation of NLO and LO Nuclear Parton Distribution Functions. *JHEP*, 0904:065, 2009.

Measurement of Properties of the Higgs Boson in Bosonic Decay Channels using the ATLAS Detector

Eleonora Benhar Noccioli[1] on behalf of the ATLAS Collaboration
[1]Université de Genève, 24 Quai Ernest-Ansermet, CH 1211 Genève 4, Switzerland

DOI: http://dx.doi.org/10.3204/DESY-PROC-2014-04/224

The paper reports the properties of the Higgs boson measured in bosonic decay channels ($H \to ZZ^* \to 4\ell$, $H \to \gamma\gamma$, $H \to WW^* \to \ell\ell\nu\nu$ and $H \to Z\gamma \to \ell\ell\gamma$) with 25 fb^{-1} of pp collision data from the LHC run-1 collected by the ATLAS detector. An improved mass measurement, as well as new fiducial and differential cross sections measurements are discussed.

1 Introduction

In the discovery of the Higgs boson, announced by ATLAS [1] and CMS [2] in July 2012, the analyses searching for bosonic decay channels played a crucial role among all channels accessible at the LHC. Since then, using two and a half times more data than was available for the discovery [3], more precise measurements of the properties of this particle have been achieved. Once again the $H \to ZZ^* \to 4\ell$, $H \to \gamma\gamma$ and $H \to WW^* \to \ell\ell\nu\nu$ decay modes have proven to be fundamental in testing the agreement between the observed results and the Standard Model (SM) predictions. Thanks to several refinements achieved in both the $H \to ZZ^* \to 4\ell$ and $H \to \gamma\gamma$ analyses, an improved measurement of the mass of the Higgs boson was recently published. The production modes and therefore the Higgs couplings were tested, and found to be in agreement with theory predictions. In addition, no significant deviations were found following new fiducial and differential cross section measurements, performed in both the $H \to ZZ^* \to 4\ell$ and $H \to \gamma\gamma$ decay channels. Furthermore, an indirect measurement of the Higgs width, Γ_H, was made exploiting the $H \to ZZ^*$ off-peak background interference effects. Finally, a combined measurement of the spin-CP properties of the boson is available. In the following sections the results obtained using approximately 25 fb^{-1} of pp collision data collected at 7 TeV and 8 TeV in 2011 and 2012 are reported.
While in the $H \to Z\gamma \to \ell\ell\gamma$ final state no signal has yet been observed, this channel will be particularly interesting in the coming years due to its sensitivity to the presence of new physics beyond the SM. The last section of this paper describes the analysis and the latest available results.

2 $H \to ZZ^* \to 4\ell$

The $H \to ZZ^* \to 4\ell$ channel provides good sensitivity to the measurement of the Higgs properties due to its high signal-to-background ratio (s/b), which is about two, and its excellent mass resolution varying from 1.6 GeV to 2 GeV depending on the final state.
The analysis searches for two pairs of same-flavor, oppositely charged electrons and muons. Only isolated leptons arising from the same vertex are considered, and they are required to fulfill kinematic cuts and identification quality criteria. In particular, the 2012 data were analysed using a more efficient electron reconstruction algorithm, and an improved likelihood-based electron identification that increased the background rejection by a factor of 2.
Photons originating from final-state radiation (FSR) are searched for and recovered. A kinematic fit is then used to constrain the mass of the leading lepton pair (including FSR photons) to the Z pole mass within the experimental resolution.
The reducible *Z+jets* and $t\bar{t}$ backgrounds are estimated using data-driven methods, while the main ZZ^* background is estimated from simulation and normalized to next-to-leading order calculations. A new boosted decision tree (BDT) discriminant is applied to suppress the ZZ^* contribution, which uses the transverse momentum and pseudorapidity of the four lepton system, and a matrix element kinematic discriminant.
An improved electromagnetic energy calibration and a reduced uncertainty on the muon momentum scale have resulted in a decrease of the systematic uncertainty on the Higgs boson mass. This is measured with a two-dimensional fit to the four lepton invariant mass $\mathrm{m}_{4\ell}$ and the ZZ^* BDT output. The new procedure provides approximately 8% extra sensitivity on the mass with respect to the past, when a simple $m_{4\ell}$ fit was used. The measured Higgs boson mass in the $H \to ZZ^* \to 4\ell$ the decay channel is: $m_H = 124.51 \pm 0.52(\mathrm{stat}) \pm 0.06(\mathrm{syst})$ GeV [4].

By categorising the events according to the characteristics of the different production modes, we can further explore the coupling structure of the Higgs and measure possible deviations from the SM expectations. Four categories are considered: VBF-like, hadronic VH-like, leptonic VH-like and ggF-like. New multivariate techniques are used in the VBF category and in the recently introduced hadronic VH, both characterised by two jets in the final state. An additional lepton is required for the leptonic VH, while the ggF category includes all events discarded by the others. The ratio between the observed and expected signal events, referred to as the signal strength, is extracted at the combined $H \to \gamma\gamma$ and $H \to ZZ^* \to 4\ell$ mass value, which will be presented in the following section. For production in gluon fusion or in association with $t\bar{t}$ or $b\bar{b}$ pairs the signal strength is found to be $1.7^{+0.5}_{-0.4}$, while for vector boson fusion combined with WH/ZH associated production it is $0.3^{+1.6}_{-0.9}$ [5].

The fiducial and differential cross sections of the Higgs boson production have been recently measured in the $H \to ZZ^* \to 4\ell$ decay channel. The extraction of the signal yield for the measurement of the fiducial cross section is performed using a fit to the $m_{4\ell}$ distribution. In the differential cross section measurements, given the low number of signal events expected in each bin, a simple cut-and-count method is used, subtracting the expected number of background events from the observed ones. The differential measurements are performed for several Higgs kinematic distributions, decay angles and jets-related variables. The measured cross sections, determined within a fiducial phase space and corrected for detection efficiency and resolution effects, are then compared to selected theoretical calculations of the SM expectations. No significant deviation from any of the tested predictions is found [6].

The measurement of the ZZ final state in the mass range above the $2m_Z$ threshold provides

a unique opportunity to measure the off-shell couplings strength of the observed Higgs boson. Assuming an identical coupling strength for on- and off-shell Higgs boson production and decay, one can reinterpret these measurements as a constraint on the total width Γ_H/Γ_H^{SM}. Given the assumptions detailed in Ref.[7], the observed 95% CL limit is found to be: $4.8 < \Gamma_H^{95\%}/\Gamma_H^{SM} < 7.7$.

3 $H \to \gamma\gamma$

The $H \to \gamma\gamma$ channel offers a clean signature due to the excellent mass resolution in the diphoton final state, allowing the observation of a narrow mass peak over a smoothly falling background determined from data. The typical mass resolution is 1.7 GeV, while the s/b is approximately 3%.
Higgs boson candidates are selected by requiring two photons fulfilling tight identification criteria based on calorimeter shower shapes, isolation requirements and kinematic cuts. The diphoton invariant mass $m_{\gamma\gamma}$ is computed using the measured energies and their opening angle, estimated from the production vertex and the photon impact points in the calorimeter. The vertex is selected by an algorithm that exploits the longitudinal segmentation of the calorimeter and information from the tracks associated to each vertex. Thanks to a revised photon energy calibration [8], a 10% improvement is achieved on the expected mass resolution.
To improve the accuracy of the mass measurement, events are separated into ten categories with different s/b, invariant mass resolutions and systematic uncertainties. The Higgs boson mass is extracted from a simultaneous signal-plus-background fit to the mass spectra of all categories where the parameters associated to the background model are allowed to vary. The measured mass in $H \to \gamma\gamma$ is found to be: $m_H = 125.98 \pm 0.42(\text{stat}) \pm 0.28(\text{syst})$ GeV [4].

The available data also allow a measurement of the fiducial and differential cross section in this channel. The general strategy is similar to that already described for the $H \to 4\ell$ channel: signal yields are extracted in a fiducial volume and then corrected for the effects of detector inefficiency and resolution. In this case, the number of signal events is estimated using a fit to $m_{\gamma\gamma}$. Differential cross sections as a function of variables related to the diphoton kinematics and the jet activity are measured and found to be broadly in line with SM expectations [9].

An improved mass measurement is obtained from the combination of the new results available for the $H \to ZZ^* \to 4\ell$ and the $H \to \gamma\gamma$ channels. The compatibility between the mass measurements from the two individual channels is now at the level of 2.0σ. The final measurement, $m_H = 125.36 \pm 0.37(\text{stat}) \pm 0.18(\text{syst})$ GeV, has significantly improved systematic uncertainty and supersedes the previous result [4].

4 $H \to WW^* \to \ell\ell\nu\nu$

The $H \to WW^* \to \ell\ell\nu\nu$ channel has the highest rate among the bosonic decays and its s/b ratio is $O(10)\%$, but it suffers from a limited mass resolution due to the presence of two neutrinos in the final state. The dominant backgrounds are WW, $t\bar{t}$ and Wt, all of which have two W bosons in their final state, *W+jets* and other diboson processes. In the analysis, events with two opposite-charge leptons and a large momentum imbalance from the neutrinos are split according to the jet multiplicity. This allows the control of the background from top quarks, as well as the extraction of the signal strengths for the ggF production process, populating mainly the 0- and 1-jet bin, and the VBF production process, ending up in the 2-jets category. An

excess of events relative to the background-only expectation is observed at $m_H = 125.5$ GeV with a local significance of 3.8σ and a measured signal strength of $\mu = 0.99^{+0.31}_{-0.28}$ [10].

Studies of the spin and parity of the Higgs boson have been carried out in all three channels introduced so far, and subsequently combined. These studies have shown that the new particle's quantum numbers are compatible with the SM spin-parity $J^P = 0^+$, whereas all alternative hypotheses are excluded at confidence levels above 97.8% [11].

5 $H \to Z\gamma \to \ell\ell\gamma$

The observation of the $H \to Z\gamma \to \ell\ell\gamma$ is extremely challenging, due to the low cross section, close to that of the $H \to 4\ell$, and the large background, which result in a s/b ratio ranging from 0.01 to 0.001. The event selection requires two opposite-sign leptons and one photon, satisfying very similar requirements to those of the $H \to \gamma\gamma$ and $H \to 4\ell$ analyses. The main backgrounds originate from continuum $Z + \gamma$, $Z + \ell\ell$ production, and from radiative $Z \to \ell\ell\gamma$ decays. To improve the signal sensitivity of this analysis, the selected events are classified into eight categories with different centre-of-mass energies, lepton flavours, s/b ratios and invariant-mass resolutions. The presence of a signal is tested using a likelihood fit to the $m_{\ell\ell\gamma}$ spectra, where the signal and the background are modelled by analytical functions independently in the eight event categories. No excess with respect to the background is found, and upper limits have been set on the cross section times branching ratio. The 95% CL limit for a Higgs mass of $m_H = 125.5$ GeV is found to be 11 times the SM expectation [12].

References

[1] ATLAS Collaboration, *The ATLAS Experiment at the CERN Large Hadron Collider*, JINST **3** S08003 (2008).

[2] CMS Collaboration, *The CMS Experiment at the CERN Large Hadron Collider*, JINST **3** S08004 (2008).

[3] ATLAS Collaboration, *Observation of a new particle in the search for the Standard Model Higgs boson with the ATLAS detector at the LHC*, Phys.Lett. **B716** 1-29 (2012).

[4] ATLAS Collaboration, *Measurement of the Higgs boson mass from the $H \to \gamma\gamma$ and $H \to ZZ^* \to 4\ell$ channels with the ATLAS detector using 25 fb^{-1} of pp collision data*, Phys.Rev. **D90** 052004 (2014).

[5] ATLAS Collaboration, *Measurements of Higgs boson production and couplings in the four-lepton channel in pp collisions at center-of-mass energies of 7 and 8 TeV with the ATLAS detector*, Submitted to Phys.Rev.D (2014).

[6] ATLAS Collaboration, *Fiducial and differential cross sections of Higgs boson production measured in the four-lepton decay channel in pp collisions at $\sqrt{s}$=8 TeV with the ATLAS detector*, Phys.Lett. **B 738** 234-253 (2014).

[7] ATLAS Collaboration, ATLAS-CONF-2014-042, https://cds.cern.ch/record/1740973

[8] ATLAS Collaboration, *Electron and photon energy calibration with the ATLAS detector using LHC Run 1 data*, Submitted to EPJC (2014).

[9] ATLAS Collaboration, *Measurement of fiducial and differential cross sections for Higgs boson production in the diphoton decay channel at $\sqrt{s} = 8$ TeV with ATLAS*, Submitted to JHEP (2014).

[10] ATLAS Collaboration, *Measurements of Higgs boson production and couplings in diboson final states with the ATLAS detector at the LHC*, Phys.Lett. **B726** 88-119 (2013).

[11] ATLAS Collaboration, *Evidence for the spin-0 nature of the Higgs boson using ATLAS data*, Phys.Lett. **B726** 120-144 (2013).

[12] ATLAS Collaboration, *Search for Higgs boson decays to a photon and a Z boson in pp collisions at $\sqrt{s}$=7 and 8 TeV with the ATLAS detector*, Phys.Lett. **B732** 8-27 (2014).

Inclusive Deep-Inelastic Scattering at HERA

Zhiqing Zhang on behalf of the H1 and ZEUS Collaborations

Laboratoire de l'Accélérateur Linéaire, Univ. Paris-Sud 11 and IN2P3/CNRS, Orsay France

DOI: http://dx.doi.org/10.3204/DESY-PROC-2014-04/259

This contribution covers three recent results on deep-inelastic scattering at HERA: (i) new measurements of the proton longitudinal structure function F_L from H1 and ZEUS experiments, (ii) a dedicated NC cross section measurement from ZEUS in the region of high Bjorken x, and (iii) preliminary combination results of all HERA inclusive data published up to now by H1 and ZEUS, taking into account the experimental correlations between measurements.

1 Introduction

At the electron-proton (ep) collider HERA, the inclusive neutral current (NC) differential cross sections in Bjorken x, the virtuality Q^2 and inelasticity y are connected with three different structure functions F_2, F_L and xF_3 as:

$$\tilde{\sigma}_{\rm NC}(x,Q^2,y) \equiv \frac{d^2\sigma_{\rm NC}}{dxdQ^2}\frac{xQ^4}{2\pi\alpha^2}\frac{1}{Y_+} = \left(F_2 - \frac{y^2}{Y_+}F_L - \frac{Y_-}{Y_+}xF_3\right) \quad (1)$$

where $Y_\pm = 1 \pm (1-y)^2$ and the fine structure constant $\alpha = \alpha(Q^2 = 0)$. The reduced cross section $\tilde{\sigma}$ differs from the full cross section by a kinematic factor. The F_2, corresponding to photon exchange, dominates. At high y, the F_L term, proportional to the absorption cross section for longitudinally polarized virtual photons by protons, is sizable. At $Q^2 \lesssim 1000\,\text{GeV}^2$, the xF_3 term, arising from Z exchange, is small. The similar relation also exists for the charged current (CC) process.

2 New F_L measurements

Using data taken with a lepton beam energy of 27.6 GeV and two proton beam energies of $E_p =$ 460 and 575 GeV corresponding to centre-of-mass energies of 225 and 252 GeV, respectively, the inclusive NC cross sections have been measured by H1 [1]. The measurements cover the region of $6.5\times10^{-4} \le x \le 0.65$ for $35 \le Q^2 \le 800\,\text{GeV}^2$ up to the highest accessible inelasticity $y = 0.85$. The measurements are used together with previously published H1 data at $E_p = 920\,\text{GeV}$ and lower Q^2 data at $E_p = 460, 575$ and 920 GeV to extract F_L in the region $1.5 \le Q^2 \le 800\,\text{GeV}^2$. The new measurement (Fig. 1(left)) extends the previous H1 measurements at low and medium Q^2 regions [2, 3] to higher Q^2 and improves the experimental precision in the region $35 \le Q^2 \le 110\,\text{GeV}^2$, thus the new measurement supersedes the previous H1 measurements [2, 3].

Similar measurements have also been performed by ZEUS but in a different kinematic region $0.13 \le y \le 0.75$ and $5 \le Q^2 \le 110\,\text{GeV}^2$ [6]. The new results supersede those in the previous

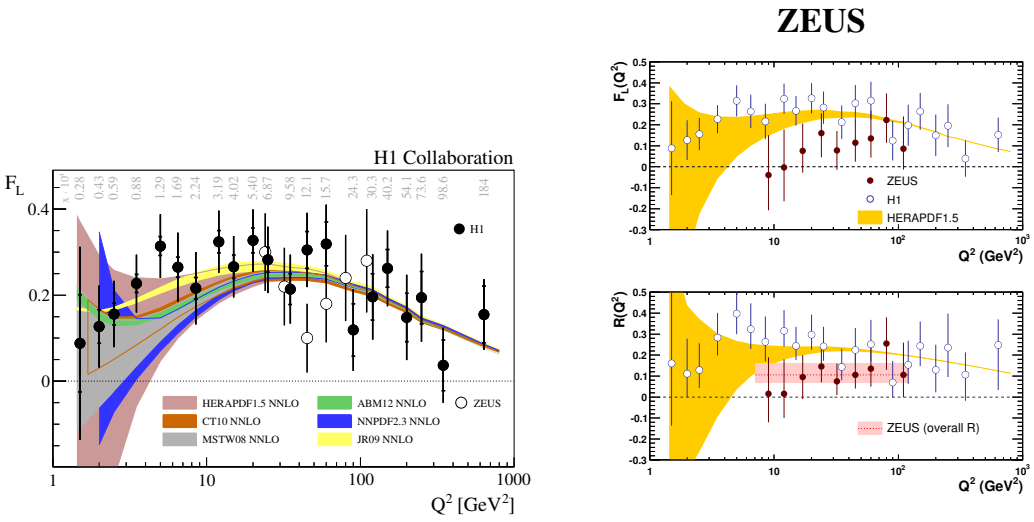

Figure 1: Left: new H1 F_L measurement (solid points) in comparison with previous ZEUS measurement (open points) [4] and a few selected NNLO predictions [5]. Right: new ZEUS F_L (a) and R (b) measurements (solid points) in comparison with H1 measurements (open points) and NNLO HERAPDF 1.5 prediction. The inner error bars represent the statistical uncertainties, the full error bars the total uncertainties. The shaded band labelled "ZEUS (overall R)" represents the 68% probability interval for the overall R.

publication [4]. The reduced cross sections were used together with those from the previous ZEUS data collected at $\sqrt{s} = 300\,\text{GeV}$ to extract F_L as well as F_2 for 27 values of x and Q^2. Relative uncertainties for F_L were in the range of $0.1 - 0.2$. In addition, F_L and the ratio, $R = F_L/(F_2 - F_L)$, have also been extracted as a function of Q^2 together with an overall value of $R = 0.105^{+0.055}_{-0.037}$. The results are shown in Fig. 1(right). The F_L measurements are lower than but compatible with those in the previous ZEUS and H1 publications and in reasonable agreement with the theoretical prediction.

3 High x measurement from ZEUS

Motivated by the large uncertainty of parton distribution functions (PDFs) at high x, NC $e^{\pm}p$ cross sections have been measured up to values of $x \simeq 1$ in a dedicated ZEUS analysis using an integrated luminosity of $187\,\text{pb}^{-1}$ of e^-p and $142\,\text{pb}^{-1}$ of e^+p collisions at $\sqrt{s} = 318\,\text{GeV}$ [7]. Differential cross sections in x and Q^2 are presented for $Q^2 \geq 725\,\text{GeV}^2$ (see Fig. 2 for the ratio of the e^-p measurements over the SM expectations based on a variety of recent PDFs). An improved reconstruction method and greatly increased amount of data allow a finer binning in the high-x region of the NC cross section and lead to a measurement with much improved precision compared to a similar earlier analysis. The agreement between the measurement and the predictions is non-trivial as the latter are mostly modeled with a $(1-x)^{\beta}$ parameterization.

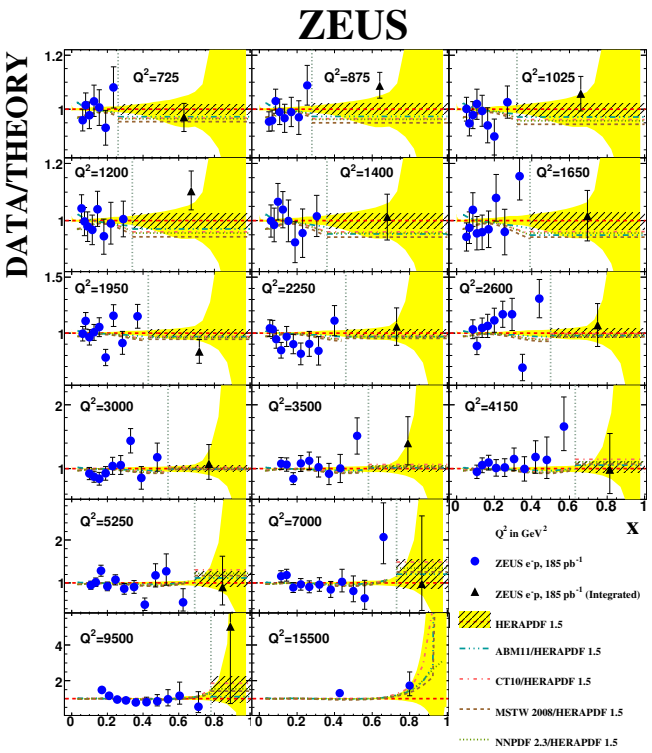

Figure 2: Ratio of the measured NC e^-p cross section over the SM expectation using the HERAPDF1.5 PDFs. The expectation for the integrated high x bin is shown as hatched box.

4 Preliminary combination results of full HERA data

A preliminary combination is performed of all inclusive deep-inelastic cross sections measured by the H1 and ZEUS collaborations in NC and CC $e^{\pm}p$ scattering [8]. The data correspond to an integrated luminosity of about $1\,\mathrm{fb}^{-1}$ and span six orders of magnitude in both Q^2 and x. They include data taken at proton beam energies of 920, 820, 575 and 460 GeV. The combination method used takes the correlations of systematic uncertainties into account, resulting in much improved accuracy. This is illustrated in Fig. 3 showing part of the combined dataset. The combined data are the inputs for the forthcoming HERAPDF 2.0 and will also have an important impact on other global PDF sets.

5 Summary

Recent results on deep-inelastic scattering at HERA have been presented. The H1 and ZEUS experiments each have determined new measurements of the proton longitudinal structure function F_L, making use of the HERA data recorded at reduced centre-of-mass energies. The results are in agreement with each other and with predictions derived from QCD fits. The region of high x is explored in a dedicated measurement by the ZEUS collaboration. All HERA inclusive

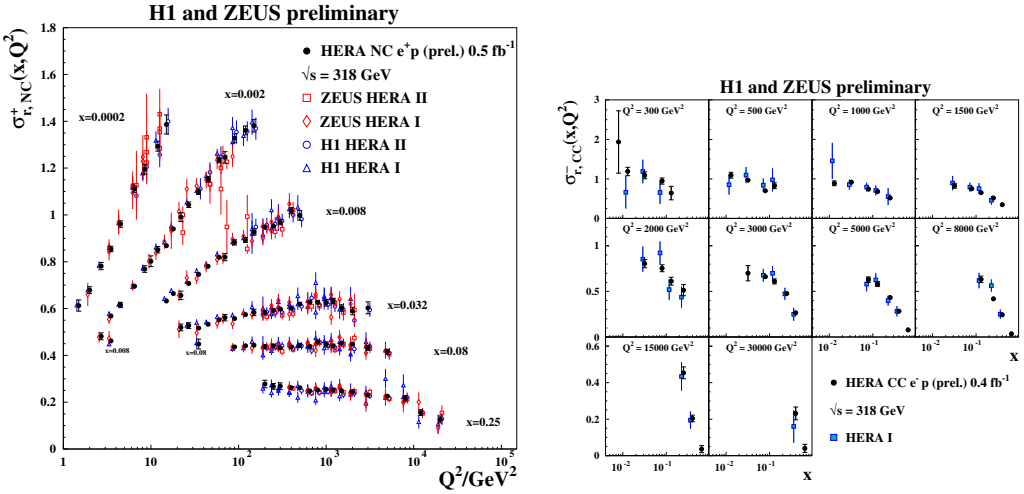

Figure 3: Left: Combined NC e^+p reduced cross section as a function of Q^2 for six selected x-bins compared to the separated H1 and ZEUS data which were input to the combination procedure. Right: Combined CC e^-p reduced cross section as a function of x for 10 Q^2 bins in comparison with the results from HERA I alone. The error bars represent the total uncertainties.

data published up to now by H1 and ZEUS are combined, taking into account the experimental correlations between measurements. The combined dataset includes measurements of neutral current and charged current cross sections recorded at different centre-of-mass energies, spanning up to six orders of magnitude both in momentum transfer Q^2 and in Bjorken x. The dataset is superior in precision compared to the previous HERA data combination which included a smaller fraction of the total integrated luminosity collected at HERA. Point-to-point uncorrelated uncertainties better than 1% are observed in certain kinematic regions.

References

[1] V. Andreev *et al.* [H1 Collaboration], Eur. Phys. J. C **74** (2014) 2814 [arXiv:1312.4821 [hep-ex]].

[2] F. D. Aaron *et al.* [H1 Collaboration], Phys. Lett. B **665** (2008) 139 [arXiv:0805.2809 [hep-ex]].

[3] F. D. Aaron *et al.* [H1 Collaboration], Eur. Phys. J. C **71** (2011) 1579 [arXiv:1012.4355 [hep-ex]].

[4] S. Chekanov *et al.* [ZEUS Collaboration], Phys. Lett. B **682** (2009) 8 [arXiv:0904.1092 [hep-ex]].

[5] HERAPDF 1.5 [H1 and ZEUS Collaborations], `http://www-h1.desy.de/publications/H1preliminary.short_list.html`; H. L. Lai *et al.*, Phys. Rev. D **82** (2010) 074024 [arXiv:1007.2241 [hep-ph]]; A. D. Martin, W. J. Stirling, R. S. Thorne and G. Watt, Eur. Phys. J. C **63** (2009) 189 [arXiv:0901.0002 [hep-ph]]; S. Alekhin, J. Bluemlein and S. Moch, Phys. Rev. D **89** (2014) 5, 054028 [arXiv:1310.3059 [hep-ph]]; R. D. Ball *et al.*, Nucl. Phys. B **867** (2013) 244 [arXiv:1207.1303 [hep-ph]]; P. Jimenez-Delgado and E. Reya, Phys. Rev. D **79** (2009) 074023 [arXiv:0810.4274 [hep-ph]].

[6] H. Abramowicz *et al.* [ZEUS Collaboration], arXiv:1404.6376 [hep-ex].

[7] H. Abramowicz *et al.* [ZEUS Collaboration], Phys. Rev. D **89** (2014) 072007 [arXiv:1312.4438 [hep-ex]].

[8] H1 and ZEUS Collaborations, *Combined measurement of inclusive $e^{\pm}p$ scattering cross sections at HERA*, H1prelim-14-041, ZEUS-prel-14-005.

Vector Boson + Jets Production at CMS

Yun-Ju Lu[1] on behalf of CMS Collaboration

[1]National Central University, No. 300, Jhongda Rd., Jhongli City, Taoyuan County 32001, Taiwan

DOI: http://dx.doi.org/10.3204/DESY-PROC-2014-04/182

Recent measurements of the production cross section of a vector boson in association with jets and a vector boson in association with heavy flavour quarks in proton-proton collision are presented. The collisions were recorded at $\sqrt{s} = 7$ and 8 TeV with the CMS detector at the LHC, for an integrated luminosity of 5.2 and 19.7 fb^{-1} respectively.

1 Introduction

Measurements of the production cross section of a vector boson in association with jets (V+jets, $V = W, Z, \gamma$) and a vector boson in association with heavy flavour quarks (V+HF) are fundamental tests of perturbative quantum chromodynamics (pQCD). These V+jets and V+HF productions also constitute important backgrounds to searches for rare standard model processes and to searches for particles predicted by new physics. With the LHC proton-proton collision data taken in 2011 and 2012, the CMS collaboration [1] measured the V+jets cross section to higher energies and jet multiplicities compared to previous results from CMS. The rapidity distributions in V+jet events and ratios of the cross sections of Z/γ^* plus jets and photon plus jets events are also measured to provide additional sensitivities to parton distribution functions (PDFs) and higher order effects.

Besides testing pQCD, measurements of W and Z production with b hadrons (Z+b and W+b) are particular important for searches of new particles. For Z+b process, both cross section and angular distribution are measured. For W+b process, previous measurements concentrating on W-boson production with at least one observed b-quark jet have shown various levels of agreement with theoretical calculation. The CMS measurement provides a complementary approach focusing on the observation of W-boson production with two well-separated b-quark jets. The study of associated production of a W boson and a charm (c) quark (W+c) production provides direct access to the strange-quark content of the proton. More precise knowledge of the PDFs is essential for many present and future precision analyses.

2 Vector boson + jets

The production cross sections of a photon and one or more jets in the final state with various angular configurations are sensitive to contributions from the QCD hard-scattering subprocesses and to PDFs of the proton. The main background for these processes comes from the decay of neutral hadrons into nearly collinear pairs of photons. These background is estimated using a data-driven method which exploits the distribution of energy in the vicinity of the photon. The

measurement is performed in four regions of pseudorapidity for the photon and two regions of pseudorapidity for the leading-transverse-momentum jet [2]. This kinematic region corresponds to x and Q^2 region of $0.002 \lesssim x \lesssim 0.4$ and $1600 \leq Q^2 \leq 9 \times 10^4$ GeV^2. Results are compared to theoretical predictions from the SHERPA [3] leading-order QCD event generator and the next-to-leading-order(NLO) perturbative QCD calculation from JETPHOX [4]. The predictions are found to be consistent with the data over most of the examined kinematic region.

Compared to γ+jets process, Z/γ^*+jets process has a much cleaner signature. Z/γ^*+jets cross sections with jet multiplicity up to six and seven for $\sqrt{s} = 7$ and 8 TeV respectively are measured [5],[6]. The differential cross section as a function of the transverse momentum of the leading jet is shown in Figure 1. The differential cross section as a function of jet multiplicity and H_T, the scalar sum of jet transverse momenta is also measured. The experimental results and their NLO theoretical predictions are generally consistent within uncertainties.

The measurements of the production cross section of W+jets events have a larger data-sample size however also higher systematic uncertainties compared to measurements of Z+jets events. The higher systematic uncertainties are mainly from a lager background contamination from $t\bar{t}$ decay. The data sample of proton-proton collisions at $\sqrt{s} = 7$ TeV was collected and corresponds to an integrated luminosity of 5.0 fb^{-1}. The measured cross sections [7] are compared to predictions from MADGRAPH [8] + PYTHIA [9] and SHERPA, and to NLO calculations from BLACKHAT+SHERPA [10]. The differential cross section as a function of the transverse momentum of the leading jet is displayed in Figure 1. The differential cross section are found to be in agreement with the predictions for most kinematic region.

The angular distributions of Z/γ^*+jet events and γ+jet events are measured with $\sqrt{s} = 7$ TeV data [11]. The rapidity of a particle is defined as $y = (1/2)\ln[(E + p_z)/(E - p_z)]$, where E is the energy and p_z is the momentum component along the direction of the counterclockwise circulating proton beam. The invariant rapidity difference can be written in terms of the measured quantities y_V and $y_{\rm jet}$ as $y_{\rm dif} = |y_V - y_{\rm jet}|/2$. The quantity $y_{\rm sum} = |y_V + y_{\rm jet}|/2$ is the boost from the laboratory frame to the center-of-mass frame of the V and jet. The distribution in $y_{\rm sum}$ depends mainly on the PDFs , while the distribution in $y_{\rm dif}$ reflects the leading order partonic differential cross section. The distribution for the sum of the V and jet rapidity is shown in Figure 1. It is best described by hybrid calculations that employ NLO PDF.

The measurement of the cross section ratio of Z/γ^*+jets and γ+jets provides an important information about possible contributions of large logs in higher-order effects. This measurement used data collected at $\sqrt{s} = 7$ TeV [12]. The results are compared to leading order prediction from MADGRAPH. The prediction agrees with data in shape, but overestimates the ratio.

3 Vector boson + heavy quarks

The measurement of the cross sections for the production of a Z boson in association with at least two b-jets is displayed in Figure 2 [13]. The measurement is of particular importance for search of higgs production associated with a Z boson. The result is compared to MADGRAPH in the five-flavour scheme, where b quarks are assumed massless, and the four-flavour scheme, where massive b quarks are used, as well as with the NLO predictions from amc@nlo [14]. With the tracker only b-tag, angular separation of the b hadrons and the Z boson is measured in [15]. The azimuthal separation($\Delta\phi$) between the b hadrons compared to theory is shown in Figure 2. Some differences are found between predictions and data in collinear region.

The production cross section for a W boson and two b-jets is measured at $\sqrt{s} = 7$ TeV [16].

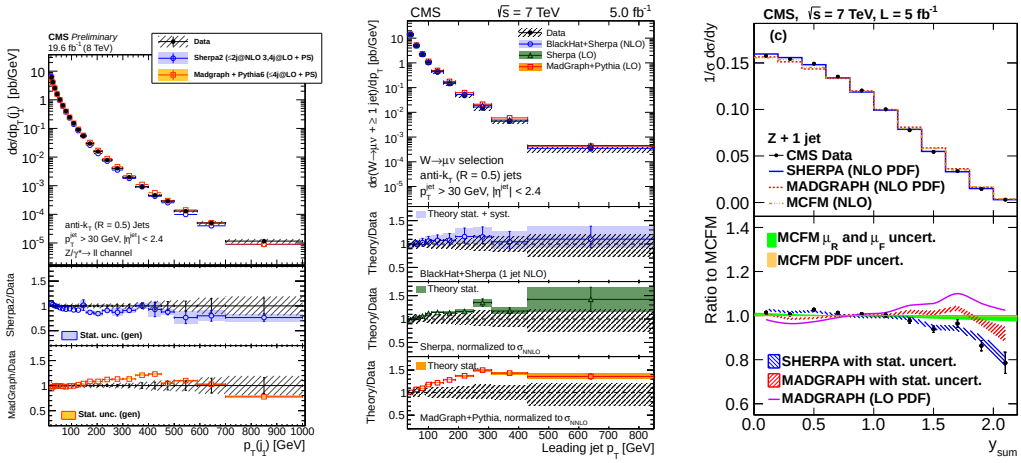

Figure 1: Differential cross sections of Z+jets at $\sqrt{s} = 8$ TeV(left) and W+jets at $\sqrt{s} = 7$ TeV(center) as a function of the transverse momentum of the leading jet. The distribution of y_{sum} in Z+jet channel(right).

Previous studies from hadron colliders are concentrated on W-boson production with at least one observed b-quark jet. Different level of agreements with theory is found in these analyses. The study of W boson and exactly two b-jets hence complements previous measurements. The measured fiducial cross section is in agreement with NLO prediction from MCFM at parton level.

The study of associated production of a W boson and a charm quark at hadron colliders provides direct access to the strange-quark content of the proton. The good measurement of charmquark jet charge is utilized in this measurement to disentangle the W+c signal component from most of the background processes [17]. The measured total cross section is compared with next-to-leading order calculation from MCFM [18] using four PDF sets, which is shown in Figure 2. Measurement of the cross section ratio of $\sigma(W^+ + \bar{c})/\sigma(W^- + c)$ is a test of $s - \bar{s}$ asymmetry hypothesis. The measured cross section ratios are around 95%. This result does not favour such hypothesis although the measurement is still dominated by experimental uncertainties.

4 Conclusion

Recent CMS results of V+jets and V+HF productions have been presented. Besides the measurements from different final states, new results also extend the kinematic coverage of previous measurements and probe additional observables. Overall, NLO predictions agree with the data rather well for most of the V+jets processes. Some disagreements exist for the variables sensitive to higher order term such as H_T. Some differences remain between theory and measurements in the production of V+HF such as angular distribution of the Z+b-jets process and differential cross section of W+chram process. These results provide input to MC tools and background estimation of different standard model measurements and beyond standard model searches.

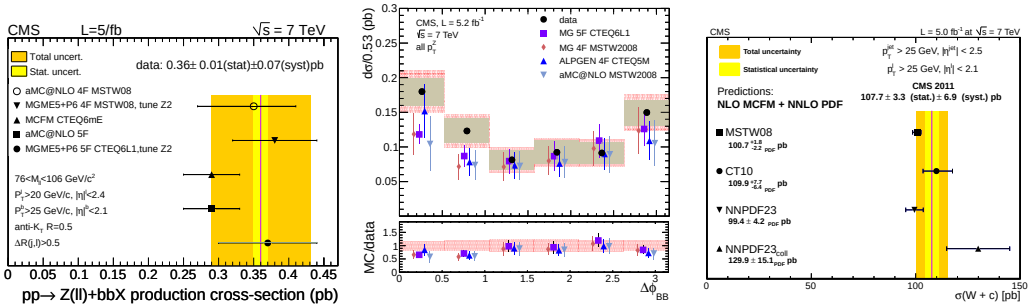

Figure 2: Cross sections for the production of a Z boson with at least two b-jets(left). Differential cross sections as a function of ϕ difference between two b quarks(center). Total cross section of W+c production compared with NLO MCFM using four different PDF sets(right).

References

[1] S. Chatrchyan et al. The CMS experiment at the CERN LHC. *JINST*, 3:S08004, 2008.

[2] Serguei Chatrchyan et al. Measurement of the triple-differential cross section for photon+jets production in proton-proton collisions at $\sqrt{s}$=7 TeV. *JHEP*, 1406:009, 2014.

[3] T. Gleisberg, Stefan. Hoeche, F. Krauss, M. Schonherr, S. Schumann, et al. Event generation with SHERPA 1.1. *JHEP*, 0902:007, 2009.

[4] S. Catani, M. Fontannaz, J.P. Guillet, and E. Pilon. Cross-section of isolated prompt photons in hadron hadron collisions. *JHEP*, 0205:028, 2002.

[5] Vardan Khachatryan et al. Measurements of jet multiplicity and differential production cross sections of Z+jets events in proton-proton collisions at sqrt(s)=7 TeV. 2014.

[6] CMS Collaboration. Measurement of the differential production cross section of Z bosons in association with jets in pp collisions at sqrt(s) = 8 TeV. 2014.

[7] Vardan Khachatryan et al. Differential cross section measurements for the production of a W boson in association with jets in proton-proton collisions at sqrt(s) = 7 TeV. 2014.

[8] Johan Alwall, Michel Herquet, Fabio Maltoni, Olivier Mattelaer, and Tim Stelzer. MadGraph 5 : Going Beyond. *JHEP*, 1106:128, 2011.

[9] Torbjorn Sjostrand, Stephen Mrenna, and Peter Z. Skands. PYTHIA 6.4 Physics and Manual. *JHEP*, 0605:026, 2006.

[10] Z. Bern, L.J. Dixon, F. Febres Cordero, S. Hche, H. Ita, et al. Ntuples for NLO Events at Hadron Colliders. *Comput.Phys.Commun.*, 185:1443–1460, 2014.

[11] Serguei Chatrchyan et al. Rapidity distributions in exclusive Z + jet and γ + jet events in pp collisions at $\sqrt{s}$=7 TeV. *Phys.Rev.*, D88:112009, 2013.

[12] CMS Collaboration. Measurement of the Z/gamma*+jets/photon+jets cross section ratio in pp collisions at sqrt(s)=8 TeV. 2014.

[13] Serguei Chatrchyan et al. Measurement of the production cross sections for a Z boson and one or more b jets in pp collisions at sqrt(s) = 7 TeV. *JHEP*, 1406:120, 2014.

[14] Rikkert Frederix, Stefano Frixione, Valentin Hirschi, Fabio Maltoni, Roberto Pittau, et al. W and $Z/\gamma*$ boson production in association with a bottom-antibottom pair. *JHEP*, 1109:061, 2011.

[15] Serguei Chatrchyan et al. Measurement of the cross section and angular correlations for associated production of a Z boson with b hadrons in pp collisions at $\sqrt{s}$ = 7 TeV. *JHEP*, 1312:039, 2013.

[16] Serguei Chatrchyan et al. Measurement of the production cross section for a W boson and two b jets in pp collisions at sqrt(s) = 7 TeV. *Phys.Lett.*, B735:204, 2014.

[17] Serguei Chatrchyan et al. Measurement of associated W + charm production in pp collisions at $\sqrt{s}$ = 7 TeV. *JHEP*, 1402:013, 2014.

[18] John M. Campbell and R.K. Ellis. MCFM for the Tevatron and the LHC. *Nucl.Phys.Proc.Suppl.*, 205-206:10–15, 2010.

Properties Measurement of New (Higgs) Boson

Shivali Malhotra on behalf of the CMS Collaboration

Department of Physics & Astrophysics, University of Delhi, Delhi - 07, India

DOI: http://dx.doi.org/10.3204/DESY-PROC-2014-04/186

The precise determination of the mass, couplings and other properties of the particle discovered in 2012 around 125 GeV is important to establish precisely if it is a Standard Model Higgs boson. CMS experiment has collected lot more data since the discovery of this particle in July 2012 and has performed many of its properties measurements. In this talk, I will present some of these measurements. These measurements are based on data samples corresponding to integrated luminosities of up to 5.1 fb^{-1} at 7 TeV and up to 19.7 fb^{-1} at 8 TeV in proton-proton collisions at the LHC. The combined result for the measured mass, the best-fit signal for all the channels and different fits for couplings, using all the studied Higgs boson decay modes, will be described.

1 Introduction

The Standard Model (SM) is the most successful theory which describes many of the experimental results and predicts all the properties of the interactions of the known elementary particles. The Higgs boson is one of the predicted corner stones in the SM theory and is responsible for giving mass to all the fundamental particles. The Higgs boson has been searched for few decades with different experiments like Large Electron Positron Collider, Tevatron, but success came with Large Hadron Collider (LHC). The spectacular observation of a scalar particle with a mass ∼125 GeV by both CMS [1] and ATLAS [2] Collaborations, opens a crucial chapter of properties measurement. The measurement of the properties of the 125 GeV boson is important not only to confirm whether this is the SM Higgs boson but also to look for hints of beyond SM physics. The combination of the different decay modes of this boson i.e. WW, ZZ, $\gamma\gamma$, $\tau\tau$ and $b\bar{b}$, as well as measurements of the $t\bar{t}H$ production mode [3, 4, 5], are exploited to measure its properties. To reconstruct the mass of the Higgs boson, high resolution channels i.e. H$\rightarrow ZZ \rightarrow 4l$ (with $l = e, \mu$) and H $\rightarrow \gamma\gamma$, are considered. The statistical methodology used for the combination of all the Higgs analysis was developed by the ATLAS and CMS Collaborations in the context of the LHC Higgs Combination Group [6]. Systematic uncertainties and their correlations are modelled by the introduction of nuisance parameters with their expected distributions.

2 Mass Measurement

The accurate measurement of the mass of the boson is done using the invariant mass distribution of two decay modes namely, H $\rightarrow \gamma\gamma$ and H $\rightarrow ZZ \rightarrow 4l$ that are the two high resolution channels. A fit to the data is performed separately profiling independent signal strengths in three final states i.e. H $\rightarrow ZZ \rightarrow 4l$, H $\rightarrow \gamma\gamma$ without Vector Boson Fusion (VBF) tag

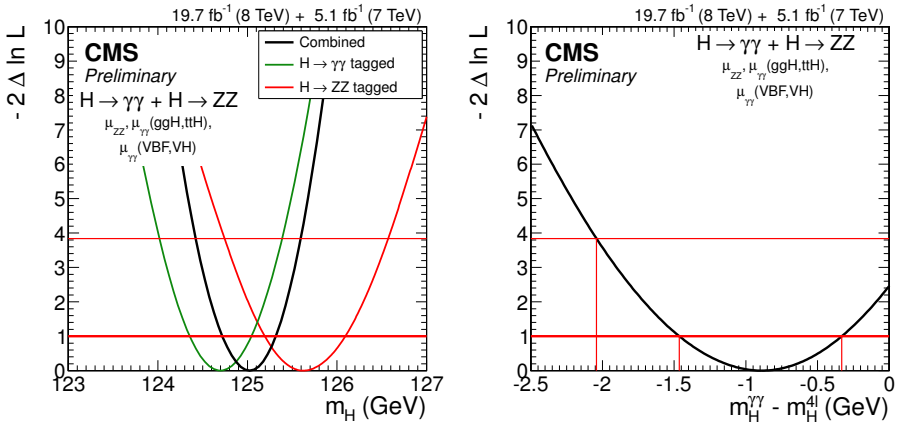

Figure 1: (Left) 1D test statistics $q(m_H)$ scan vs hypothesized Higgs boson mass m_H for the $\gamma\gamma$ (green) and $4l$ (red) final states separately and for their combination (black). (Right) Scan of the test statistic $q(m_H^{\gamma\gamma} - m_H^{4l})$ versus the difference between two individual mass measurements.

and H $\rightarrow$ $\gamma\gamma$ with VBF tag. The three signal strength are left free to reduce the model dependency of the mass determinations. Figure 1 (left) shows the likelihood scan as function of the mass of the H $\rightarrow$ ZZ and H $\rightarrow$ $\gamma\gamma$ channels and of their combination. The horizontal lines at 1.0 and 3.84 depicts the 68% and 95 % CL intervals. The mass is measured to be $m_H = 125.03^{+0.26}_{-0.27}(stat.)^{+0.13}_{-0.15}(syst.)$ GeV from the combination of the two high resolution channels.

Decay Channel	Expected (σ)	Observed(σ)
H $\rightarrow$ WW [7]	5.4	4.3
H $\rightarrow$ ZZ [8]	6.3	6.5
H $\rightarrow$ $\gamma\gamma$ [9]	5.3	5.6
H $\rightarrow$ $\tau\tau$ [10]	3.9	3.9
H $\rightarrow$ bb [11]	2.3	2.1

Table 1: Expected and observed significances of the excess for $m_H = 125.0$ GeV of the combinations of channels.

To quantify the compatibility of the two individual measurements, a scan of the test statistics $q(m_H^{\gamma\gamma} - m_H^{4l})$ versus the difference between two individual mass measurements from $\gamma\gamma$ and $4l$ final states is performed, Fig. 1 (right). The result comes out to be $m_H^{\gamma\gamma}$ - m_H^{4l} = $-0.87^{+0.54}_{-0.57}$ GeV and the two measurements agree at the 1.6σ level. Table 1, summarizes the expected and observed significance for individual channel for a SM Higgs boson mass of 125.0 GeV. We have used the combination of these five dominant decay channels for different compatibility tests of the Higgs boson.

3 Signal Strength

After the precise measurement of mass of the Higgs boson, the best fit value of the signal strength modifier, $\mu = \sigma/\sigma_{\rm SM}$ is calculated which quantifies the compatibility of an excess with the expectations from a SM Higgs boson. Evaluation of the signal strength by combining channels with respect to decay mode, Fig. 2 (left), or by combining with different production

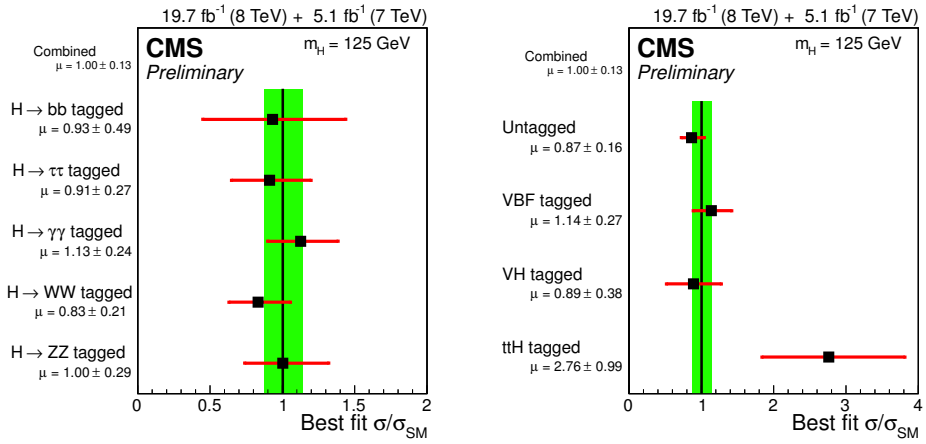

Figure 2: Values of the best-fit $\sigma/\sigma_{\rm SM}$ for sub-combinations by (left) predominant decay channels and (right) individual production modes. The vertical band shows the overall $\sigma/\sigma_{\rm SM}$ uncertainty while the horizontal bars indicate the ± 1 standard deviation uncertainties in the best-fit $\sigma/\sigma_{\rm SM}$ values for the individual modes; they include both statistical and systematic uncertainties.

tags, Fig. 2 (right), has been done. A slight excess in the $t\bar{t}$H-tagged sub-combination is due to the excesses in the $t\bar{t}$H-tagged H$\to\gamma\gamma$ and H$\to$leptons analyses. The combined best-fit signal strength for $m_H = 125$ GeV is found to be $1.00 \pm 0.09(stat.)\,^{+0.08}_{-0.07}\,(theo.) \pm 0.07(syst.)$.

4 Couplings to Fermions and Bosons

We map the vectorial and fermionic couplings into two scale factors, $\kappa_{\rm V}$ and $\kappa_{\rm f}$, respectively. Figure 3 (left) shows the likelihood scan as a function of $\kappa_{\rm V}$, $\kappa_{\rm f}$ with the cross indicating the best-fit values (1.01, 0.89) with respective uncertainties. The fit is compatible with the SM at the one sigma level with $\kappa_{\rm f}$ value being smaller than unity due to an excess in the VBF H $\to \gamma\gamma$ channel and deficit in the fermionic channels. The same $(\kappa_{\rm V}, \kappa_{\rm f})$ analysis is also performed separately for each Higgs boson decay mode to better visualize the contribution of individual channels, Fig. 3 (right).

5 Other Compatibility Tests

To test the custodial symmetry, we introduce two scaling factors $\kappa_{\rm W}$ and $\kappa_{\rm Z}$ that modify the SM Higgs boson couplings to the W and Z bosons and perform combination in two channels i.e. untagged pp$\to$H$\to$WW and pp$\to$H$\to$ZZ, to assess the consistency of the ratio $\lambda_{\rm WZ} = \kappa_{\rm W}/\kappa_{\rm Z}$ with unity. The result is $\lambda_{\rm WZ} = 0.94^{+0.22}_{-0.18}$ while assuming SM couplings to fermions, $\kappa_{\rm f} = 1$; which implies that the data are consistent with the SM expectation.

The asymmetry of couplings to fermions is checked by performing two combinations in which we allow for different ratios of the couplings to down/up fermions ($\lambda_{\rm du} = \kappa_{\rm d}/\kappa_{\rm u}$) or different

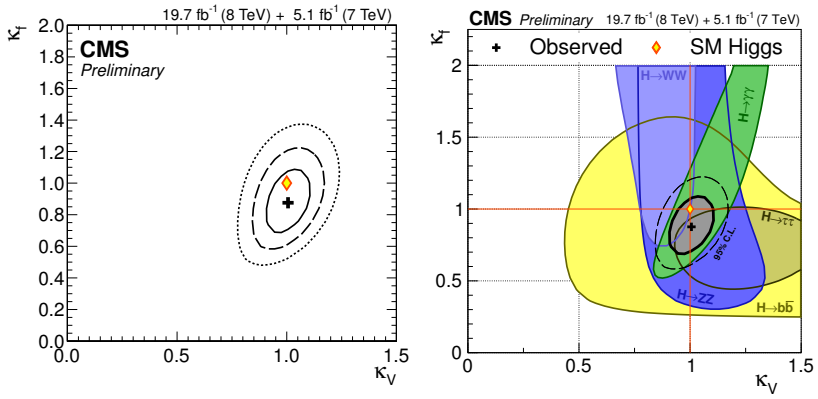

Figure 3: 2D test statistics $q(\kappa_{\rm V},\, \kappa_{\rm F})$ likelihood scan constrained to the (+,+) quadrant. The yellow diamond shows the SM point $(\kappa_{\rm V}, \kappa_{\rm f}) = (1,\, 1)$. (Left) The cross indicates the global best-fit values with the solid, dashed, and dotted contours showing the 68%, 95%, and 99.7% CL regions, respectively. (Right) The 68% CL contours for individual channels (colored swaths) and for the overall combination (thick curve) for the $(\kappa_{\rm V}, \kappa_{\rm f})$ parameters.

ratios of the couplings to leptons and quarks ($\lambda_{\rm lq} = \kappa_{\rm l}/\kappa_{\rm q}$) assuming $\Gamma_{BSM} = 0$. Both $\lambda_{\rm du}$ and $\lambda_{\rm lq}$ are found to be constrained within [0.66, 1.43] and [0.61, 1.49] respectively, at 95% CL.

We also explore a generic five-parameter model by making some assumptions with the scale factor for different couplings. The couplings to W and Z bosons are scaled by $\kappa_{\rm W}$ and $\kappa_{\rm Z}$, respectively; $\kappa_{\rm t}$ denotes the scale factor for couplings of up-type quarks; $\kappa_{\rm b}$ denotes the scale factor for couplings of down-type quarks; and κ_τ denotes the scale factor for all the charged leptons. The result of a model with five independent coupling scaling factors, assuming SM structure for loops is shown in Fig. 4.

Many other compatibility tests were also performed for checking beyond the SM physics scenarios [12].

6 Results

The excellent performance of the LHC machine and the CMS detector during Run I made the experiment able to collect data corresponding to an integrated luminosity of about 5 fb^{-1} at a collision energy of 7 TeV in 2011 and about 20 fb^{-1} at 8 TeV in 2012 and led to the discovery of a scalar particle. It was then required to understand its various properties and to check whether they are consistent with the Higgs boson predicted by SM. It was possible to measure the mass of the Higgs boson that resulted $m_H = 125.03^{+0.26}_{-0.27}(stat.)^{+0.13}_{-0.15}(syst.)$ GeV using the CMS detector, at this value the Higgs boson is allowed to decay in many different modes. For the mass measured at 125 GeV, the event yields obtained in the different analyses for specific decay modes and production mechanisms are consistent with those expected for the SM Higgs boson. The combined best-fit signal strength was also found compatible with the SM expectation. Searches for deviations of the couplings of the Higgs boson along with some other

compatibility tests were performed and no significant deviations were found. Run II of LHC may shed some more light with precision measurement of the above mentioned quantities while having more statistics in hand at higher energy and higher integrated luminosity.

References

[1] The CMS collaboration, arXiv:1207:7235 [hep-ex].

[2] The ATLAS collaboration, arXiv:1207:7214 [hep-ex].

[3] CMS Collaboration, "Search for the standard model Higgs boson produced in association with a top-quark pair in pp collisions at the LHC, JHEP **05** (2013) 145, doi:10.1007/JHEP05(2013)145, arXiv:1303.0763.

[4] CMS Collaboration, "Search for Higgs Boson Production in Association with a Top-Quark Pair and Decaying to Bottom Quarks or Tau Leptons, Technical Report CMS-PAS-HIG-13-019, CERN, Geneva, 2013.

[5] CMS Collaboration, "Search for the standard model Higgs boson produced in association with top quarks in multilepton final states, Technical Report CMS-PAS-HIG-13-020, CERN, Geneva, 2013.

[6] LHC Higgs Cross Section Working Group, "Handbook of LHC Higgs Cross Sections: 3. Higgs Properties", (2013). arXiv:1307.1347.

[7] CMS Collaboration, "Measurement of Higgs boson production and properties in the WW decay channel with leptonic final states", JHEP **01** (2014) 096, doi:10.1007/JHEP01(2014)096, arXiv:1312.1129.

[8] CMS Collaboration, "Measurement of the properties of a Higgs boson in the four-lepton final state", Phys. Rev. D **89** (2014) 092007, doi:10.1103/PhysRevD.89.092007, arXiv:1312.5353.

[9] CMS Collaboration, "Observation of the diphoton decay of the 125 GeV Higgs boson and measurement of its properties", CMS-HIG-13-001, CERN-PH-EP-2014-117, 2014. Submitted for publication in Eur. Phys. J. C.

[10] CMS Collaboration, "Evidence for the 125 GeV Higgs boson decaying to a pair of t leptons", JHEP **05** (2014) 104, doi:10.1007/JHEP05(2014)104, arXiv:1401.5041.

[11] CMS Collaboration, "Search for the standard model Higgs boson produced in association with a W or a Z boson and decaying to bottom quarks", Phys. Rev. D **89** (2014) 012003, doi:10.1103/PhysRevD.89.012003, arXiv:1310.3687.

[12] CMS Collaboration, "Precise determination of the mass of the Higgs boson and studies of the compatibility of its couplings with the standard model", CMS PAS HIG-14-009.

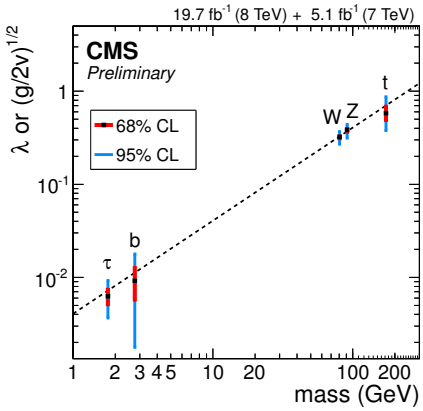

Figure 4: Summary of the fits for deviations in the coupling for the generic five-parameter model assuming SM structure for loops, expressed as function of the particle mass. The dashed line is taken from the fit to data with the model (M, ε)

Measurements of WV Boson Production and Limits on Charged aTGCs at CMS

Ilya Osipenkov on behalf of the CMS Collaboration

Department of Physics and Astronomy
Texas A&M University, College Station, TX, USA

DOI: http://dx.doi.org/10.3204/DESY-PROC-2014-04/184

We present a summary of the latest measurements of the WV production cross-sections, where V is either W or Z. The data sample(s) correspond to proton-proton collision events collected with the CMS detector at $\sqrt{s} = 7$ and 8 TeV. Subsequent searches for Anomalous Triple Gauge Couplings, which allow us to probe the non-Abelian structure in the Electroweak Sector, are described. We present exclusion limits on the corresponding couplings.

1 Introduction

Triple gauge boson couplings, which determine the self-interactions of W and Z bosons, are fixed by the gauge symmetry of the standard model (SM). Consequently, pair production of vector gauge bosons allows a direct test of the electroweak sector of the SM [1]. Observation of anomalous triple gauge boson couplings (aTGCs) would correspond to the presence of physics beyond the SM.

In this paper we summarize the measurements in the diboson final states $WZ \to \ell\nu\ell\ell$ [2], $WW \to \ell\nu\ell\nu$ [3] and $WV \to \ell\nu jj$ [4] in pp collisions in the Compact Muon Solenoid (CMS) detector at the Large Hadron Collider (LHC) [5]. Understanding of these processes is essential, as they serve as backgrounds for new physics searches and other measurements (*e.g.* Higgs production). Furthermore, for each channel we verify the Standard Model (SM) predictions by comparing the measured cross-section to the theory expectation. An additional enhancement of the spectrum in the high transverse momentum (p_T) region would correspond to nonzero aTGC values.

2 $WZ \to \ell\nu\ell\ell$

We present measurements of the $WZ \to \ell\nu\ell\ell$ production corresponding to the luminosities of 4.9 fb^{-1} collected at $\sqrt{s} = 7$ TeV and 19.6 fb^{-1} collected at $\sqrt{s} = 8$ TeV. In order to select the Z candidate the presence of two leptons of the same flavor (muons or electrons) and opposite charge with the transverse momentum $p_T > 20, 10$ GeV and mass near the Z resonance ($71 < m_{ll} < 111$ GeV) is required. In case of multiple pairs of candidates the one with the mass closest to the Z is selected. Likewise, in order to reconstruct the W, a lepton with $p_T > 20$ GeV, $MET > 30$ GeV are required. The remaining backgrounds can be separated into the non-peaking (*e.g.* $t\bar{t}$) and prompt lepton (real Z plus a lepton-like object) types, which are

taken from the Monte Carlo; as well as the real Z plus a jet faking a lepton, which is estimated from the sideband region in the data. Overall, we predict at total of 211 background out of the 1480 ($\sqrt{s} = 8$ TeV) events in the data after all of the cuts have been applied.

Upon subtracting the backgrounds a high purity signal is extracted. After accounting for the systematics, with the largest sources originating from the MET resolution as well as the data driven background estimates, cross section for each lepton combination is evaluated Fig. 1. The combined values are $20.8 \pm 1.3(stat.) \pm 1.1(syst.) \pm 0.5(lumi.)$, $24.6 \pm 0.8(stat.) \pm 1.1(syst.) \pm 1.1(lumi.)$ pb at $\sqrt{s} = 7$,8 TeV, while the $\sigma_{W^+Z}/\sigma_{W^-Z} = 1.94 \pm 0.25(stat.) \pm 0.04(syst.)$,$1.81 \pm 0.12(stat.) \pm 0.03(syst.)$. The measurements are consistent with the theory predictions of 17.8, 21.9 pb.

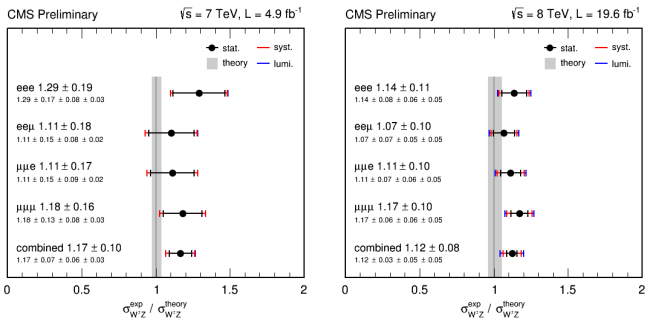

Figure 1: Ratio of measured inclusive cross-section to the theoretical prediction in the $WZ \to \ell\nu\ell\ell$ channel at $\sqrt{s} = 7$ TeV(left) and $\sqrt{s} = 8$ TeV(right).

3 $WW \to \ell\nu\ell\nu$

The $WW \to \ell\nu\ell\nu$ signal measurements correspond to the luminosities of 4.9 fb^{-1} collected at $\sqrt{s} = 7$ TeV and 4.92 fb^{-1} collected at $\sqrt{s} = 8$ TeV. We reconstruct W^+W^- signal by requiring two oppositely charged central leptons ($|\eta| < 2.4$,2.5 for muons, electrons) with $p_T > 20$ GeV. In order to further reduce background contamination the following cuts are implemented: remove events with jet $p_T > 30$ GeV and apply top-quark tagging techniques, require $MET > 45$ GeV (> 20 GeV in the μe channel), remove events with third lepton $p_T > 10$ GeV, reject photon-conversion electrons. The Top, Drell Yan and Diboson yields are determined from the data sideband region with the overall background contribution $\sim 30\%$ of the total event count.

We evaluate the cross section after subtracting the expected background contributions from the data. The main systematics are due to the jet veto uncertainty as well as the error in estimating the background yields. The measured cross sections are $52.4 \pm 2.0(stat.) \pm 4.5(syst.) \pm 1.2(lumi.)$, $69.9 \pm 2.8(stat.) \pm 5.6(syst.) \pm 3.1(lumi.)$ pb at $\sqrt{s} = 7$,8 TeV. Similarly to the WZ case, the results show a small ($\sim 1\sigma$) excess over the SM expectation, but overall are consistent with the theory predictions of 47.0, 57.3 pb.

In addition, we perform a search for the aTGCs based on the leading lepton p_T spectrum. The presence of anomalous signal would enhance the yield at high p_T values with an overall quartic dependence of the cross-section on the aTGCs. The systematic uncertainties are

incorporated into the likelihood function by introducing nuisance parameters with Gaussian constraints. We see no evidence for the anomalous signal and obtain 1-Dimensional limits of $-0.048 < \lambda < 0.048$, $-0.095 < \Delta g_1^Z < 0.095$, $-0.22 < \Delta\kappa_\gamma < 0.22$ at 95% C.L., with 2-D limits shown in Fig. 2.

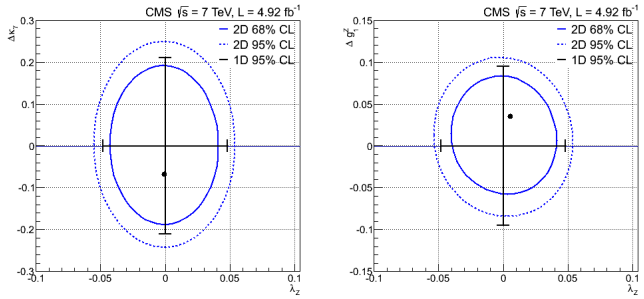

Figure 2: The 68% (solid line) and 95% C.L. (dashed line) aTGC limit contours, as well as the central value (point) for $\Delta g_1^Z = 0$ (left) and $\Delta\kappa_\gamma = 0$ (right). The corresponding 1-D 95% C.L. limits are shown along the axes.

4 $WV \to \ell\nu jj$

The first semileptonic channel measurement is performed for the 5.0 fb^{-1} CMS dataset collected at $\sqrt{s} = 7$ TeV. The analysis is particularly challenging due to the fact that vast majority of events in this final state originate from the $W + Jets$ irreducible background, but has a higher expected event count due to the larger branching fraction of W and Z bosons to quarks. We select events with on-shell W bosons by requiring lepton $p_T > 25$ GeV (35 GeV), $\eta < 2.1$ (2.4), W transverse mass > 30 GeV (50 GeV), $MET > 25$ GeV (30 GeV) and secondary lepton veto in the muon (electron) channel. Exactly two AK5 jets are reconstructed subject to PileUp corrections, isolation from leptons > 0.3, $p_T > 35$ GeV, $\eta < 2.6$ and jet b-tag veto on the secondary vertex. Additional requirements of dijet $p_{Tjj} > 20$ GeV, $|\Delta\eta_{jj}| < 1.5$ are placed in order to reduce the dominant $W + Jets$ background. A reasonable agreement between data and MC is observed.

In order to extract the cross section we perform an unbinned maximum likelihood for the dijet mass $40 < m_{jj} < 150$ GeV. The shape templates are taken from Monte Carlo (and multijet sideband), while the background yield contributions are free to float subject to Gaussian constraints. An empirical combination of default, alternate ME-PS and alternate QCD scale samples is used to describe the $W + Jets$ shape. The biases in the fit procedure and systematics are accounted for. A total of 2682 ± 482 $WW + WZ$ events is extracted out of 1.15×10^5 with a significance is 8.8σ using a simple likelihood ratio and 4.3σ using the profile likelihood ratio. The corresponding $WW + WZ$ cross section is $68.9 \pm 8.7(stat.) \pm 9.7(syst.) \pm 1.5(lumi.)$ pb, consistent with the SM prediction of 65.6 ± 2.2 pb.

Subsequently, limits on the aTGC parameters are set based on the hadronic $V \to jj$ p_T spectrum. We place an additional $75 < m_{jj} < 95$ GeV cut to enhance signal purity, normalize the backgrounds based on fit results and take $\Delta g_1^Z = 0$, since it is expected to be small. The

1-D limits of $-0.038 < \lambda < 0.030$, $-0.111 < \Delta\kappa_\gamma < 0.142$ at 95% C.L. are set, with 2-D limits shown in Fig. 3.

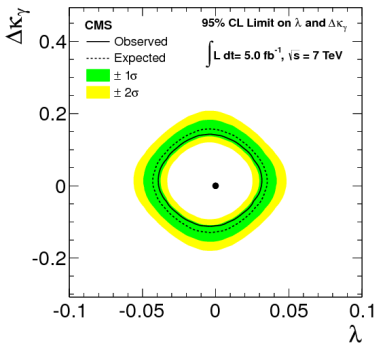

Figure 3: Observed (solid) and expected (dashed) exclusion limits at 95% CL for anomalous triple gauge couplings set based on the semileptonic WV final state $V \to jj$ p_T spectrum. The dark green(inner) and light yellow(outer) bands correspond to the one and two sigma intervals, respectively, in the expected limit distribution. The SM expectation is shown by the solid dot.

5 Summary

We implement the selections and measure the WV diboson productions for $WZ \to \ell\nu\ell\ell$, $WW \to \ell\nu\ell\nu$ and $WW + WZ \to \ell\nu jj$ final states at CMS. Excesses are observed for several channels, but no evidence for physics beyond SM is found. Furthermore, the presence of Anomalous Triple Gauge Couplings is expected to modify the spectrum at high values of p_T. We do not find evidence for such anomalous interactions between the charged vector bosons and set either competitive or the strongest limits to date.

References

[1] K. Hagiwara *et al.*, Low energy effects of new interactions in the electroweak boson sector. Phys. Rev. **D48** 2182 (1993).

[2] CMS Collaboration, Measurement of WZ production rate, CMS Physics Analysis Summary **CMS-PAS-SMP-12-006** (2012).

[3] S. Chatrchyan *et al.*, Measurement of the W^+W^- cross section in pp collisions at $\sqrt{s} = 7$ TeV and limits on anomalous $WW\gamma$ and WWZ couplings, Eur. Phys. J. **C73** 2610 (2013);
S. Chatrchyan *et al.*, Measurement of W^+W^- and ZZ production cross sections in pp collisions at $\sqrt{s} =$ 8 TeV, Phys. Lett. **B721** 190 (2013). (http://arxiv.org/abs/1301.4698).

[4] S. Chatrchyan *et al.*, Measurement of the sum of WW and WZ production with W+dijet events in pp collisions at $\sqrt{s} = 7$ TeV, Eur. Phys. J. **C73** 2283 (2013).

[5] The CMS Collaboration *et al.*, The CMS experiment at the CERN LHC. JINST **3** S08004 (2008).

Search for the Standard Model Higgs boson decaying to b quark with CMS experiment

Silvio Donato[1 2 3 4] on behalf of the CMS Collaboration

[1] Scuola Normale Superiore, Piazza dei Cavalieri, 7 - 56126, Pisa, Italy
[2] INFN Sezione di Pisa, Largo B. Pontecorvo, 3 - 56127 Pisa, Italy
[3] CERN, 1211 Geneve 23, Switzerland
[4] silvio.donato@cern.ch

DOI: http://dx.doi.org/10.3204/DESY-PROC-2014-04/188

A search for the standard model (SM) Higgs boson decaying to bottom quarks pairs is presented. Two production channels have been analyzed: vector-boson fusion and associated production with a vector boson decaying to leptons. The search is performed on data collected with the CMS detector at LHC during 2011 and 2012, at center-of-mass energies of 7 and 8 TeV, corresponding to integrated luminosities of about $5.\,\mathrm{fb}^{-1}$ and $19.0\,\mathrm{fb}^{-1}$, respectively. A 95% confidence level upper limit of 1.79 (0.89) times SM Higgs boson cross section has been observed (expected) at a Higgs boson mass of 125 GeV. An excess of events is observed above the expected background with a local significance of 2.2 standard deviations, which is consistent with the expectation from the production of the SM Higgs boson. The signal strength corresponding to this excess, relative to that of the SM Higgs boson, is 0.97 ± 0.48.

1 Introduction

In 2012, CMS [1] and ATLAS collaborations have observed a Higgs boson in the $\gamma\gamma$, ZZ, WW decay channels and its mass is about $m_H \approx 125\,\mathrm{GeV}$ [2, 3]. More recently, an evidence of the decay of the Higgs boson to a τ pair has been presented [4, 5]. This paper presents the search performed by CMS for the standard model (SM) Higgs boson decaying to bottom quarks, one of the most important decay channels not yet seen [6, 7].

Although the Higgs boson decay to b quark has a high branching ratio, the channel has a low sensitivity due to the large QCD background. Indeed the b-quark QCD production cross section is some 10^8 times larger than the Higgs boson cross section. In order to cope with such a large background, the topologies of two distinctive production modes have been exploited: the vector-boson associated production (VH) and the vector-boson fusion (VBF). These production modes have about one tenth of the cross-section of the gluon-gluon fusion dominant mode, but their topologies are useful to reduce the background.

2 Signal topologies

In the VH production, only the leptonic decays of the vector bosons are considered. Here, the topology is defined by the presence of two b jets from the Higgs boson decay, and at least one isolated charged lepton or large missing transverse energy (MET). These requirements make the QCD background negligible.

The VBF signal, is characterized by the presence of two b jets from the Higgs boson decay and two energetic quark-jets with a large η separation. No gluons participate in the interaction, so a low additional hadronic activity is expected. Nevertheless, in this channel the QCD background remains the main background.

3 Signal and background regions

The main processes that can simulate the VH signal topology are: W/Z + jets and $t\bar{t}$ production. Their shapes are taken from simulation whereas their normalizations are data-driven. The analysis is divided in six sub-channels, according to the vector-boson decay mode: $W \rightarrow e\nu\,, \mu\nu\,, \tau\,(1-\text{prong})\nu$ and $Z \rightarrow ee\,, \mu\mu\,, \nu\nu$. In addition, the channels are binned in two or three vector-boson p_T bins. In each bin a signal region is defined cutting on: jet kinematic variables, b-tagging discriminants, lepton momentum and/or MET, number of additional leptons and jets. Inverting some cuts, up to five control regions are defined for $t\bar{t}$ and W/Z + heavy/light quark jets backgrounds. They are used to evaluate up to seven scale factors to apply to $t\bar{t}$ and W/Z + 0/1/2b-jets background normalizations.

The main background in the VBF analysis is the multi-jet QCD production. This background is estimated directly from data. Minor backgrounds are W/Z + jets and $t\bar{t}$ productions and they are taken from simulation. The signal regions are defined using an Artificial Neural Network (ANN). It is trained to separate the signal from the backgrounds, using simulations. With the exception of the b-jets kinematic it exploits the most discriminants variables: $\Delta\eta$ between the most forward/backward jets, b-tagging discriminants and additional hadronic activity in the event. Five signal regions are defined using the ANN output, as shown in Figure 1. In each region the background and the signal yield are obtained with a fit to the $b\bar{b}$ jet mass distribution. The QCD background is extrapolated from the sidebands using a fifth-degree Bernstein polynomial, while the signal and the minor backgrounds shapes and are taken from simulations.

4 Multi BDT (VH)

In order to reduce the background in VH analysis, three specialized BDT are trained to reject the $t\bar{t}$, W/Z + jets and WW/WZ/ZZ backgrounds. The BDT variables are: Higgs boson candidate mass and p_T, b-tag discriminants, lepton momentum and MET, number of additional leptons and jets, other kinematic variables.

The final multi-BDT score distribution is realized as following. An event rejected by the $t\bar{t}$ BDT gets a score between -1 and -0.5. The other events that fail the W/Z + jets BDT have a score between -0.5 and 0. Again, the other events that fail the WW/WZ/ZZ BDT have a score between 0 and 0.5. A final BDT is applied to reject all backgrounds and it assigns a score between 0.5 and 1. In this way the combined multi-BDT is more powerful than the classic one-step BDT.

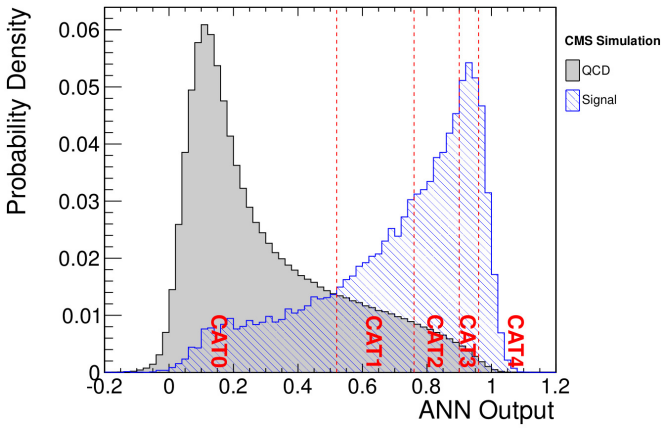

Figure 1: Probability distribution of the ANN output for signal and background, for VBF analysis. The vertical dashed lines define the signal regions used in the analysis.

The last step is the extraction of the signal. In the VH analysis this is obtained with a fit of the multi-BDT score distribution using the shapes from simulation and the data-driven scale factors.

5 Results

In the VH analysis an upper limits of 1.89 (0.95) times the SM Higgs boson cross section at 125 GeV with 95% C.L. has been observed (expected), as shown in Figure 2(a). Corresponding to an excess of events of 2.1 standard deviations and to a signal strength of $\mu = 1.0 \pm 0.5$. The Figure 2(b) shows the distribution of the bb dijet invariant mass for the VH analysis, combining all sub-channels.

In the VBF channel an upper limit of 3.6 (3.0) times the SM Higgs boson cross section at 125 GeV with 95% C.L. has been observed (expected), as shown in Figure 3(a). It corresponds to a signal strength of $\mu = 0.7 \pm 1.4$. The Figure 3(b) shows the bb dijet invariant mass distribution in the most sensitive signal region.

A combination of the two analysis gives a signal strength of $\mu = 0.97 \pm 0.48$. It corresponds to an excess of events of 2.2 standard deviations from the expected background.

6 Conclusions

A search for the SM Higgs boson decaying to bottom quarks has been presented. Two production channels have been studied: the associated production with vector boson decaying to leptons (VH) and the vector-boson fusion (VBF). An excess of events of 2.2 standard deviations at a mass of 125 GeV has been reported that corresponds to a signal strength of $\mu = 0.97 \pm 0.48$.

References

[1] S. Chatrchyan *et al.* [CMS Collaboration], JINST **3** (2008) S08004.

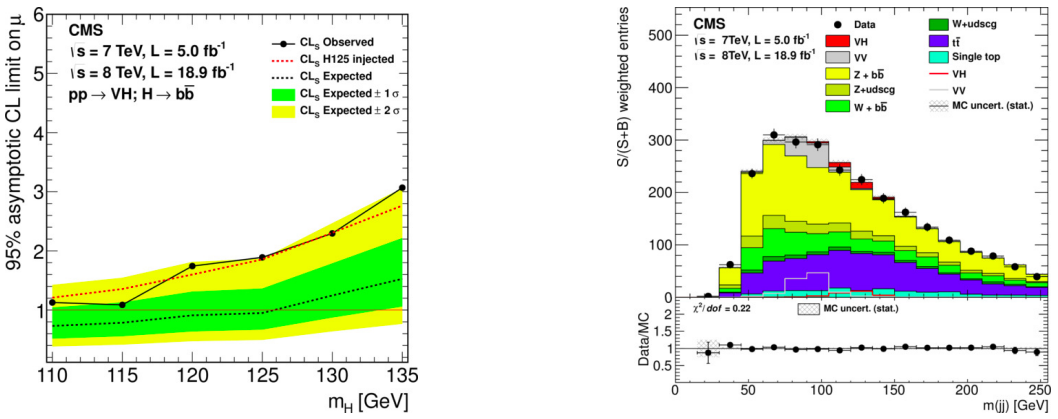

(a) (b)

Figure 2: On the left, the 95% CL upper limits on the signal strength for the SM Higgs boson hypothesis as a function of the Higgs boson mass, for the VH analysis. On the right, the b-jet pair invariant mass distribution in the VH analysis.

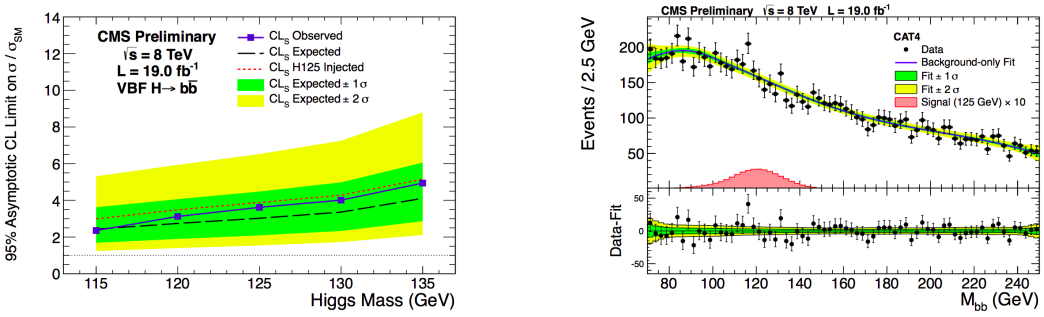

(a) (b)

Figure 3: On the right, the b-jet pair invariant mass distribution in the VBF analysis.

[2] S. Chatrchyan *et al.* [CMS Collaboration], Science **338** (2012) 1569.

[3] G. Aad *et al.* [ATLAS Collaboration], Science **338** (2012) 1576.

[4] S. Chatrchyan *et al.* [CMS Collaboration], CMS-HIG-13-004, CERN-PH-EP-2014-001.

[5] G. Aad *et al.* [ATLAS Collaboration], ATLAS-CONF-2013-108.

[6] S. Chatrchyan *et al.* [CMS Collaboration], Phys. Rev. D **89** (2014) 012003.

[7] S. Chatrchyan *et al.* [CMS Collaboration], CMS-PAS-HIG-13-011.

Recent theoretical and experimental results on top quark mass measurements

Roberto Franceschini

CERN, 1211 Geneve 23, Switzerland

DOI: http://dx.doi.org/10.3204/DESY-PROC-2014-04/317

In this contribution I will review recent experimental results on the measurement of the top quark mass. I will also review recent proposals about new methods proposed for the extraction of the top quark mass. Finally I will comment on recent detailed studies of the theoretical uncertainties in measurements based on templates fitting.

1 Introduction

The top quark mass is a key parameter of the Standard Model of particle physics. Indeed it is one of the free parameters of the theory that needs to be measured to fully define it. The top quark mass is also an input of many precision predictions of the Standard Model that are needed to assess its validity up to higher energy scales, possibly up to the Planck scale.

The great importance of the top quark mass for Standard Model and Beyond the Standard Model physics is motivation for the large efforts that the experimental community has put in its measurement. Remarkably, the LHC and TeVatron experiments have recently combined their results and obtained a combined measurement $173.34 \pm 0.27(stat) \pm 0.71(syst)$ GeV [1]. The uncertainty is dominated by systematic errors, in particular the measurement of hadornic jets, and is likely to not improve much when more data will be added to the analyses. The dominance of systematic errors in the current measurement is certainly a great motivation to think about new methods to mesure the top quark mass. At the end of Run-2 of the LHC it is foreseen to have few 1/ab of integrated luminosity, which would yield some *1 billion top pairs* produced at the LHC. The prospect to have such large sample of top quarks makes possible to consider measurement of the top quark mass that exploit very special final states (such as for instance J/ψ states or other exclusive decays) or exploit features of kinematic distributions that are not hugely populated (such as for instance end-point regions and tails). The hope is that among these alternative approaches to the top quark mass measurement one can find methods that are based on experimentally clean quantities and that exploit observables which are well under theoretical control. The balance of these two needs will be a key issue for the methods that will provide a reliable *precision* determination of the top quark mass.

The measurement of top quark mass through the measurement of the total inclusive $pp \to t\bar{t}$ cross-section is one instance of theoretically clean quantity, as it can be computed to high order in QCD, but, unfortunately, suffers of large uncertainties on the experimental side. The issue here has to do with the fact that the experiments measure the cross-section in the region of phase space accessible to their acceptance, not the total cross-section. The total cross-section

is obtained using MonteCarlo simulations to extrapolate from a fiducial region of phase-space to the total phase-space. Such extrapolation suffers of uncertainties that at the moment make impossible to measure the top quark mass better than a few GeV [2]. On the other hand the measurements that are more under control on the experimental side, and that has been possible to carry out with the current top quark sample, tend to be difficult to reliably interpret on a theory standpoint. One issue above all that can be mentioned is that the currently most precise measurement do require the construction of templates, whose matching with data, determines the top quark mass and its uncertainty. These templates can only be built from samples of exclusive events, that necessarily come from event generators. The accuracy of these events generators is often questioned when measurements at less than 1% are quoted; furthermore even the theoretical definition of the quantity that is measured with current template procedures might be not understood at this level of accuracy [3]. For these reasons it is useful to think about new quantities that can be used to measure the top quark mass having in mind from the very beginning the possibility to both compute and measure them *accurately*.

2 A portrait from different angles

One recent effort in the direction of measuring the top quark mass using a theoretically robust quantity is the measurement of the end-point of the invariant mass distribution of the lepton and the b-jet from the top decay [4]. The accuracy of this mass measurement is expected to reach a quite interesting sub-GeV level [5, 6]. Furthermore, by the end of the run of the LHC, with a luminosity of order 1/ab, other measurements are foreseen to become useful and to attain a similar level of accuracy [5, 6] thanks to the high statistics, reduced systematic errors and the improved theoretical calculations that will be available by then.

The fact that several new top quark mass measurement will be feasible with the large LHC top quark data set is extremely welcome. In fact to measure this mass with a precision well below the 1% level, one needs to carefully assess several delicate effects, most of which are particularly tough to control theoretically due to the nature of strong interactions and hadronic physics. The hope is that, by obtaining several independent measurements, each based on different experimental objects and possibly suffering of different theoretical uncertainties, we can obtain a *global* picture for the top quark mass measurement. In this picture it is likely that each single measurement will have a set of assumptions that can hardly be tested in the measurement itself or in other available data. For instance each measurement will have to deal in its own way with the many issues that exist in our *description* of hadronic physics: effect of higher order corrections, the estimation of theory uncertainties from scale variations and possible functional dependence of the scale on the kinematics, effect of finite width of unstable particles and radiation in the decay of resonances, effect of hadronization of partons and color neutralization. Each measurement will have different sensitivity to these effects and its interpretation will depend on our choice about how to address each of these issues. In the end the best knowledge of the top quark mass will emerge from the *combination* of truly independent, possibly uncorrelated, measurements. The variety of angles under which we will be able to observe the top quark will be the biggest strength of its mas measurement.

3 Issues with resonance reconstruction and templates

A very important issue with the top mass measurement has to do with the reconstruction of a resonance in the events that are used to measure the mass. Intuitively we expect that the most straightforward way to measure a resonance mass is to measure all its decay products and to compute the mass of the total four-vector. For instance for a Z boson one might want to look at $Z \to \mu^+\mu^-$ events and compute $\left(p_{\mu^+} + p_{\mu^-}\right)^2$. This procedure will definitively be good enough for most uses of the measured mass, however issues arise when one seeks *precision* and radiative corrections are added to this picture. In fact one has to remember that charged leptons come with an associated spectrum of emitted radiation that in reality makes the decay $Z \to \mu^+\mu^- +$ photons. The existence of these corrections to the naive (leading order) picture requires to move away from the simple picture outlined above and motivates complementary approaches to the mass measurement. In fact one can attempt to derive the Z boson mass from properties of just a subset of its decay products, even from just one of the leptons. This is a possibility actually very meaningful to entertain because it avoids to have to specify how the Z boson is reconstructed. This is even more true for the measurement of masses of particles where the final state is partly invisible, such as W bosons decaying leptonically and, as a consequence, top quarks. Furthermore, not having to reconstruct a resonance it is possible to measure the mass using more inclusive final states, which is a bonus for the accuracy of theory calculations. A recent attempt to obtain a mass measurement from inclusive single lepton distribution has been discussed in Ref. [7], which finds that the theory uncertainty on the top quark mass from such observable could be as low as 0.8 GeV.

Another interesting result from Ref. [7] has to do with the inherent uncertainties that should be evaluated when templates are used to extract the top quark mass. The fact is that templates are only as good as the approximation to real hadronic physics that has been put in the calculation or event generator used to obtain the templates. Therefore it is very important to scrutiny the effect on the measurement that arises from the several choices that one has to do in the making of the templates. For instance one needs to study the impact of the measurement of the presence of parton shower corrections, spin correlations treatment, and even the precise relation between the event kinematics and the choice of scales that are introduced in the calculation. Some of these effects my be not so relevant in other aspects of top quark physics, still, due to the differential nature of the information that is used in the top quark mass extraction, they might have a significant impact when one tries to extract the top quark mass better than 1% accuracy that is interesting nowadays. Ref. [7] discusses a few examples of leptonic observables that suffer from these *theory biases* and in particular highlights how in some cases even a higher order calculation seems to not help much to cure these largely unpredictable biases.

4 Phenomenological Lorentz invariants

The last issue discussed above motivates to consider observables that are as much as possible insensitive to the effects that are difficult to incorporate in the calculations used to produced the templates. In this respect observables that are invariant under Lorentz transformations are naturally interesting to look at. The reason is that many details about the events that produce the top quarks become irrelevant. In fact all the effects that amount to change the boost distribution of the top quark in the given production environment are not important.

One can simply compute these observables in the top quark rest frame and, by virtue of the invariance, carry the prediction to the laboratory frame. The example of the mass of the muon pair above perfectly displays the utility of Lorentz invariants. However, from the discussion above we also know that it is crucial to observe *all* the products of the decay, including the cloud of real photons (that can be energetic in some cases) that accompany the charged leptons.

A possible solution to this problem is to retrieve Lorentz invariant quantities from information encoded in the laboratory frame *distribution* of suitable Lorentz-variant quantities. The key idea is that distributions do retain the full information on the kinematics in the top quark rest frame and that, in suitable experimental conditions, one can reliably extract the top quark rest frame quantities from these distributions. Observables that have been considered so far are: a specially weighted median of the inclusive lepton energy distribution [8] and the position of the peak of the inclusive energy distribution of the b-jet [9]. The extraction of Lorentz invariants from the distribution of Lorentz-variants is potentially advantageous because can be carried out from the observation of a *single particle* among all the decay products of the top. This simplifies the issue of adding radiative corrections as one can base the top quark mass extraction on the study of a single distribution that is fully inclusive with respect to the presence of extra radiation. The further consequence of dealing with a single particle measurement is that there is no need to proceed to a resonance reconstruction. Furthermore a single particle observable avoids all the issues connected to the identification of the correct pair of particles to be combined to reconstruct a resonance from its invariant mass. The study of NLO corrections to the energy distribution of leptons and b-jets for the top mass measurement is currently underway.

5 Conclusions

The determination of the top quark mass with uncertainty below 1 GeV is a very challenging task both theoretically and experimentally. After the epoch of measurements based on a limited sample of top quarks, the LHC will make possible a variety of mass measurements that need large statistics. The combination of these measurement will provide a *global* assessment of the top mass, whose consistency will make us confident that the small error of these measurements is actually backed up by a solid *precision* understanding of QCD in top quark physics.

References

[1] ATLAS, CDF, CMS and D0 Collaborations. First combination of Tevatron and LHC measurements of the top quark mass. *ArXiv:1403.4427*.

[2] CMS Collaboration. Determination of the top quark pole mass and strong coupling constant from the $t\bar{t}$ production cross section in pp collisions at $\sqrt{s} = 7$ TeV. *Phys.Lett.*, B728:496–517(2013).

[3] A. H. Hoang and I. W. Stewart. Top Mass Measurements from Jets and the Tevatron Top-Quark Mass. *Nucl. Phys. B Proc. Supp.*, 185:220–226(2008).

[4] CMS Collaboration. Measurement of masses in the $t\bar{t}$ system by kinematic endpoints in pp collisions at $\sqrt{s}$ = 7 TeV. *Eur.Phys.J.*, C73:2494(2013).

[5] Juste et al. Determination of m_{top} circa 2013: methods, subtleties, perspectives. *ArXiv:1310.0799*.

[6] CMS Collaboration. Projected improvement of the accuracy of top quark mass measurements at the upgraded LHC. CMS-PAS-FTR-13-017

[7] S. Frixione and A. Mitov. Determination of the top quark mass from leptonic observables. *ArXiv:1407.2763*.

[8] Kawabataa et al. Weight function method for precise determination of m_{top} at the LHC. *ArXiv:1405.2395*.

[9] Agashe et al. A simple, yet subtle 'invariance' of two-body decay kinematics. *Phys. Rev. D*, 88(5):057701

Combined measurements of the properties of the Higgs boson using the ATLAS detector

Peter Kluit[1] on behalf of the ATLAS Collaboration

[1]Nikhef, Science Park 105 , 1098 XG Amsterdam , The Netherlands

DOI: http://dx.doi.org/10.3204/DESY-PROC-2014-04/227

The combination of the measurements of the Higgs boson properties by the ATLAS detector at the LHC will be presented. Firstly, the measurements of the spin and parity CP of the observed boson will be discussed. Secondly, the results for the production of the Higgs boson in different channels through the gluon-gluon and vector-boson fusion processes will be presented. Finally, coupling fits are performed to the data and the Standard Model symmetries and mass dependence are tested and discussed. It is concluded that the observed boson is compatible with one Standard Model CP-even Higgs boson.

1 Introduction

In this paper the combination of the measurements of the properties of Higgs boson by the ATLAS detector at the LHC [1] will be discussed. The Higgs boson is observed in several final states; initially it was discovered in the $\gamma\gamma$, ZZ and WW channels [2]. Here I will summarize what is currently known about the Higgs spin and CP properties and the Higgs couplings to bosons, quarks and leptons.

The Higgs spin and CP properties have been studied in the three di-boson channels. Subsequently, the analyses probing different CP and spin hypotheses have been combined [3]. The angular and momentum distributions of the bosons and their decay products are sensitive to the spin and CP of the produced boson. By fitting these distributions to the data for the hypothesis of a Standard Model (SM) Higgs boson (0^+) and an alternative spin CP hypothesis ($\mathrm{J^P} = 2^+, 1^+, 1^-$ or 0^-), exclusion limits are obtained. The results, shown in Fig. 1, are compatible with a CP-even scalar boson and the alternative hypotheses are excluded at 97.8% CL or higher.

In the following, I will discuss in more detail the combination of Higgs measurements in the $\gamma\gamma$, ZZ, WW [2], $\tau\tau$ [4] and $b\bar{b}$ [5] channels. The Higgs can be produced in gluon-gluon fusion (ggF), vector boson fusion (VBF) and W or Z associated production (VH). The channels were divided into categories that correspond to the production mode and final states. The di-boson channels included categories enriched in ggF and VBF; the $b\bar{b}$ channel was only analyzed in the VH final state. The paper will mainly focus on the results of the Higgs boson coupling measurements and their interpretation. A detailed description of the event selection, channels, categories and fit procedure can be found in Ref. [6].

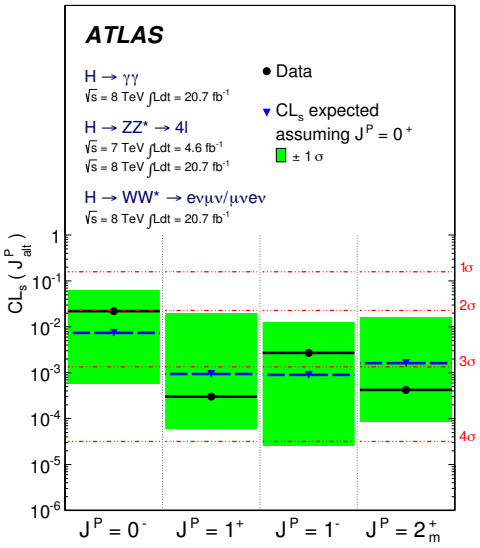

Figure 1: Expected (blue triangles/dashed lines) and observed (black circles/solid lines) confidence level CLs for alternative spin–parity hypotheses assuming a 0^+ signal. The green band represents the 68% CL expected exclusion range for a J^P signal. For the spin-2 hypothesis, the results for a specific 2^{+m} model, are shown.

2 Combination of the Higgs measurements

The inclusive signal strength μ normalised to the SM expectation, obtained by combining the five listed channels, is $\mu = 1.30^{+0.18}_{-0.17}$.

Because of the VBF enriched event categories, it is possible to measure the VBF fraction defined as: $\mu_{VBF}/\mu_{ggF+ttH} = 1.4^{+0.5}_{-0.4}(stat)^{+0.4}_{-0.3}$. This provides 4.1σ evidence for the production of Higgs bosons through VBF.

In the coupling fits $\kappa_i = g_i/g_i^{SM}$ is fitted, where g_i is the coupling of the Higgs boson to e.g. fermions (F) or bosons (V). The Higgs boson couplings are measured in simplified benchmark models. It is assumed that only one CP-even scalar Higgs boson with $m_H = 125.5\ GeV$ is produced. Its width is neglected, i.e. the narrow-width approximation is used.

In the first model the coupling ratios to fermions are put equal to κ_F and of all bosons to κ_V. This allows to test the SM difference of fermion and boson couplings under the assumption that there are no new physics contributions to the total width. The result is $\kappa_F = 1.15 \pm 0.08$ and $\kappa_V = 0.99^{+0.17}_{-0.15}$ as shown in Fig. 2. Note that the result is compatible with the SM, where one expects values of 1. It is possible to fit the ratio λ_{FV} defined as κ_F/κ_V. In that case no assumption on the total width is need. The result is $\lambda_{FV} = 0.86^{+0.17}_{-0.15}$ and shown in Fig. 2.

It is possible to test the custodial symmetry of the SM directly in the Higgs sector by fitting λ_{WZ} thus allowing different couplings to the W and Z bosons. The result is shown in Fig. 2: $\lambda_{WZ} = 0.94^{+0.14}_{-0.29}$, compatible with the SM expectation.

Many extensions of the SM predict different couplings to up- and down-type fermions. In that case λ_{ud} is constrained to the range 0.78 - 1.15 at 68% CL as shown in Fig. 2. It can be further shown that there is 3.6σ evidence for the coupling of the Higgs boson to down-type fermions.

Another test is the measurement of the lepton and quark couplings. Here λ_{lq} is constrained to the range 0.99 - 1.5 at 68% CL, shown in Fig. 2. A vanishing coupling of the Higgs boson to leptons is excluded at 4σ.

The loop contributions in SM processes are sensitive to possible new physics processes. To quantify this sensitivity, the couplings to gluons κ_g and photons κ_γ are measured to be: $\kappa_g = 1.08^{+0.15}_{-0.13}$ and $\kappa_\gamma = 1.19^{+0.15}_{-0.12}$. It is assumed that the $\kappa_{F,V}$ values are 1 and only SM particles contribute to the total width.

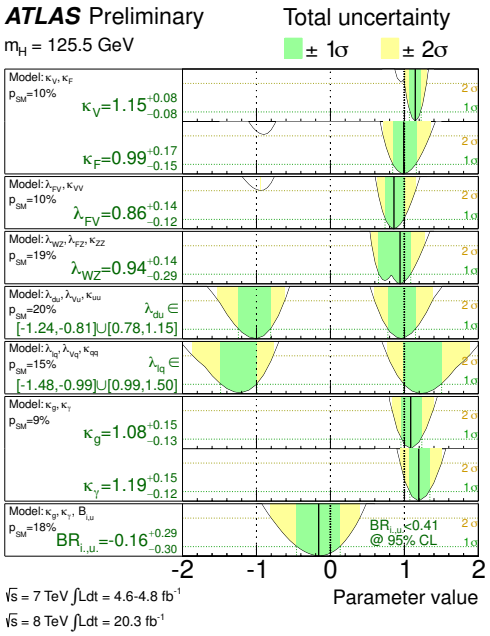

Figure 2: Summary of the coupling scale factor measurements for $m_H = 125.5\ GeV$. The best-fit values are represented by the solid black vertical lines. The measurements in the different benchmark models, separated by double lines in the figure, are strongly correlated, as they are obtained from fits to the same experimental data. For each model the compatibility of the SM hypothesis with the best-fit point is given by p_{SM}.

Finally, the mass scaling of the couplings is tested by parametrising deviations from the SM prediction in terms of two additional parameters ϵ and M in the formulae: $\kappa_{f,i} = v\frac{m^{\epsilon}_{f,i}}{M^{1+\epsilon}}$ and $\kappa_{V,j} = v\frac{m^{2\epsilon}_{V,j}}{M^{2+\epsilon}}$, where v is the vacuum expectation value of 246 GeV and $m_{f,V}$ denote to the fermion and boson masses. In the SM ϵ is zero and M equals v. The result of the fit is shown in Fig. 3. The deviation of the Higgs boson couplings to fermions (bosons) from a linear (quadratic) scaling with the particle masses is less than 10% [7].

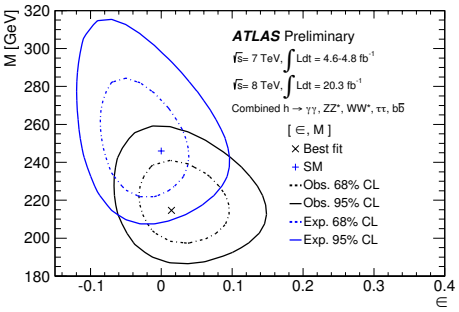

Figure 3: Two-dimensional likelihood scan of ϵ and M. The likelihood contours corresponding approximately to 68% CL (1σ) and 95% CL (2σ) respectively, are shown for both the data and the prediction for a SM Higgs boson. The best fit to the data and the SM expectation are indicated as $\times$ and $+$ respectively.

3 Conclusions

The spin and CP of the observed particle is consistent with a CP-even scalar boson. The boson is produced in ggF and VBF processes with cross sections and branching ratios that are consistent with a SM Higgs boson. The measured couplings are consistent with the SM predictions and the underlying symmetries and mass scalings have been measured. In the near future the final Run-1 Higgs analysis results will be published. We look forward to higher statistics Run-2 results for which the projections can be found in Ref. [8].

References

[1] ATLAS Collaboration, JINST **3** (2008) S08003, *The ATLAS Experiment at the CERN Large Hadron Collider.*

[2] ATLAS Collaboration, Phys. Lett. **B716** 1 (2012), *Observation of a new particle in the search for the Standard Model Higgs boson with the ATLAS detector.*

[3] ATLAS Collaboration, Phys. Lett. **B726** 120 (2013), *Evidence for the spin-0 nature of the Higgs boson using ATLAS data.*

[4] ATLAS Collaboration, ATLAS-CONF-2013-108, *Evidence for Higgs Boson Decays to the $\tau^+\tau^-$ Final State with the ATLAS Detector.*

[5] ATLAS Collaboration, ATLAS-CONF-2013-079, *Search for the bb decay of the Standard Model Higgs boson in associated (W/Z)H production with the ATLAS detector.*

[6] ATLAS Collaboration, ATLAS-CONF-2014-009, *Updated coupling measurements of the Higgs boson with the ATLAS detector using up to 25 fb^{-1}.*

[7] ATLAS Collaboration, ATLAS-CONF-2014-010, *Constraints on New Phenomena via Higgs Boson Coupling Measurements with the ATLAS Detector.*

[8] ATLAS Collaboration, ATL-PHYS-PUB-2013-014, *Projections for measurements of Higgs boson cross sections, branching ratios and coupling parameters with the ATLAS detector at a HL-LHC.*

Top-quark physics results from CMS

Jeremy Andrea for the CMS collaboration

Institut Pluridisciplinaire Hubert CURIEN, France

DOI: http://dx.doi.org/10.3204/DESY-PROC-2014-04/232

Recent results on top-quark physics from the CMS collaboration are presented. Among the many measurements performed by CMS, some of the most significant, related to the $t\bar{t}$ and single top production, top-quark mass and top properties measurements, are shown.

1 Introduction

The top quark is the heaviest particle observed. In many aspects, it is of a major interest in particle physics. It decays before it hadronizes, which allows for precise measurement of the top-quark properties. It also has the largest couplings to the Higgs boson, due to its large mass, and thus could play an special role in the electroweak symmetry breaking. While top-quark physic is crucial for our understanding of the Standard Model (SM), it is providing a very important window to potential new physics. Indeed, top-quark events have signatures comparable to many new physics prediction (BSM), and a good understanding of the top-quark background is mandatory for validating the detector performance and the simulation, but also for improving theoretical calculations and Monte-Carlo generation. Furthermore, precise measurements related to the top-quark can be used to indirectly probe new physics when searching for deviations with respect to the SM predictions.

While many major contributions to the top-quark physics were performed by the CMS collaboration [1], only some of the most significant results are presented in this proceeding. In the following, the top-quark pair and single-top-quark production cross section measurements will be first discussed. After discussing top-quark mass measurements, the top-quark properties, as well as the corresponding search for new physics, are discussed.

2 Top-quark production

The measurement of top-quark production cross sections are performed in both the $t\bar{t}$ and in single top channels, either inclusive [2], differential [3], or in association with additional particles [4, 5].

The most precise top-quark pair cross section measurement at 8 TeV is obtained in the dileptonic $e\mu$ channel, as it suffers from a very low background contamination, mainly the residual $Z/\gamma^* \to \tau\tau$ events with the τ decaying leptonically, and single-top-quark events in the tW channel. The event selection requires two isolated high p_T leptons with opposite signs, at least two high p_T jets with at least one b-tagged jet. The jet and b-tagged jet multiplicities after the event selection is presented in Fig.1.

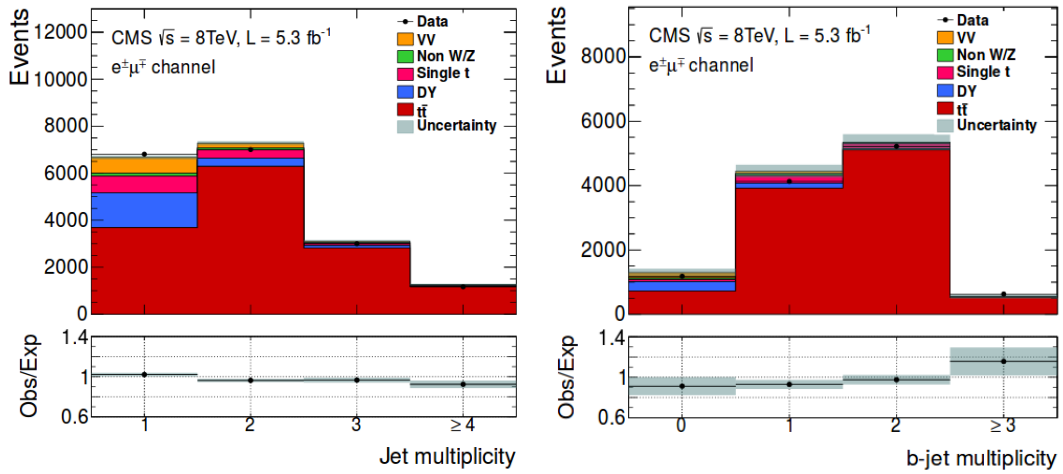

Figure 1: Jet and b-tagged jet multiplicities after the dilepton $e\mu$ event selection.

With the very large luminosity delivered by the LHC, the uncertainty is largely dominated by the systematics, with the largest contributions coming from the Jet Energy Scale (JES), the modelling of the $t\bar{t}$ signal and the luminosity. A simple counting experiment is already able to reach a very high level of precision, as demonstrated in [2]. The inclusive $t\bar{t}$ cross section is measured, with an overall precision of 5.8% , to be :

$$\sigma_{t\bar{t}} = 239.0 \pm 2.1(stat.) \pm 11.3(syst.) \pm 6.2(lumi.). \quad (1)$$

The top-quark production can also be studied through the single-top modes : the s-channel, the t-channel and the tW-channel, the two latest being observed at CMS [6]. The t-channel cross section is measured in the leptonic channel, after selecting events with one high p_T isolated lepton, at least one jet, a large missing transverse energy and a large transverse mass of the W candidates. The cross sections is extracted from the $|\eta|$ distribution of the recoiling jet in various signal and control regions, defined by different jet and b-tagged jet multiplicities, and by different reconstructed top-quark mass requirements. The measured cross section at 8 TeV is :

$$\sigma_{t-chan.} = 83.6 \pm 2.3(stat.) \pm 7.4(syst.). \quad (2)$$

The mains systematic uncertainties are related to the signal modelling, the jet selection and the b-tagging. Several other interesting measurements can also be performed using the same event selection and similar techniques, such as the top/anti-top cross sections ratio $\sigma_{t-chan.}(t)/\sigma_{t-chan.}(\bar{t})$ $(= 83.6 \pm 2.3(stat.) \pm 7.4(syst.).)$ which is sensitive to PDF, or the measurement of $|V_{tb}| > 0.92$, at 95% confidence level.

The first observation of the tW-channel was also performed for the first time by the CMS collaboration [7]. The measurement is performed in the dilepton channel, using an event selection similar to the $t\bar{t}$ inclusive cross section analysis. A boosted decision tree is used to discriminates signal against backgrounds, and fitted in various signal and background regions

(using categorization in jet and b-tagged jet multiplicities). The tW cross section is measured to be 23.4 ± 5.4, with a significance of 6.1σ.

3 Top-quark mass measurement

The top-quark mass is measured by the CMS collaboration through different channels and techniques. The most precise measurement is performed with the 8 TeV dataset with $t\bar{t}$ lepton+jets events [8] using the ideogram technique. The event selection ask for one isolated leptons with a high p_T (either a muon or an electron), at least 4 high p_T jets with two b-tagged jets. A high purity of events can be reached, and a kinematic fit is used to improve the rate of correct jet-to-parton assignments by cutting on the goodness of the kinematic fit.

The correction factor the the Jet Energy Scale (JSF) is fitted simultaneously with the top-quark mass using a likelihood fit technique. The measured mass and JSF are found to be :

$$m_t = 172.04 \pm 0.19(stat. + JSF) \pm 0.75(syst.) GeV, JES = \quad 1.007 \pm 0.002(stat.) \pm 0.012(syst.). \tag{3}$$

This result constitutes the most precise single measurement of the top-quark mass. The main systematic uncertainties are related to the JSF, the Jet Energy Resolution, the pile-up and the signal modelling. The different mass measurements performed within CMS are also combined[9] and improve slightly the overall precision.

4 Top-quark properties and search for new physics

As the top-quark decays before it hadronizes, the decay product of the top-quarks can be used to probe the top-quark properties. In particular, the $t\bar{t}$ spin correlation can be used to probe the $t\bar{t}g$ couplings and to search for new physics [10]. The signatures that carries most of the spin information is the $t\bar{t}$ in the dileptonic channel. Spin correlation, and the corresponding asymmetry, can be measured from the azimuthal angle $\Delta\phi(ll)$ between the two charged leptons in the $t\bar{t}$ rest frame. The differential $t\bar{t}$ cross section as a function of $\Delta\phi(ll)$, unfolded at parton level, can be seen in Fig.2 (left plot).

The differential cross section can also be used to probe new physics, by searching for chromomagnetic dipole-moment $\hat{\mu}_t$. By comparing the unfolded distribution to theoretical predictions, the real part of $\hat{\mu}_t$ was found to be within the range $-0.043 < Re(\hat{\mu}_t) < 0.0117$ at 95% confidence level.

New physics in top events can also be performed by searching for flavour changing neutral current (FCNC) interactions, which are highly suppressed by the GIM mechanism in the SM. Top-quark FCNC are searched for in top decays in $t\bar{t}$ events [11], when a top-quark decays into a c or an u quark and a Z boson. The search is performed in the three-lepton signature by asking for three isolated leptons (electrons or muons) with high p_T, and a pair of opposite-sign and same-flavour leptons compatible with the Z boson mass. At least two jets, with at least one b-tagged jet, is also required. No excess over the data is observed. Exclusion limits are calculated from the observed number of events with reconstructed top-quark masses compatible

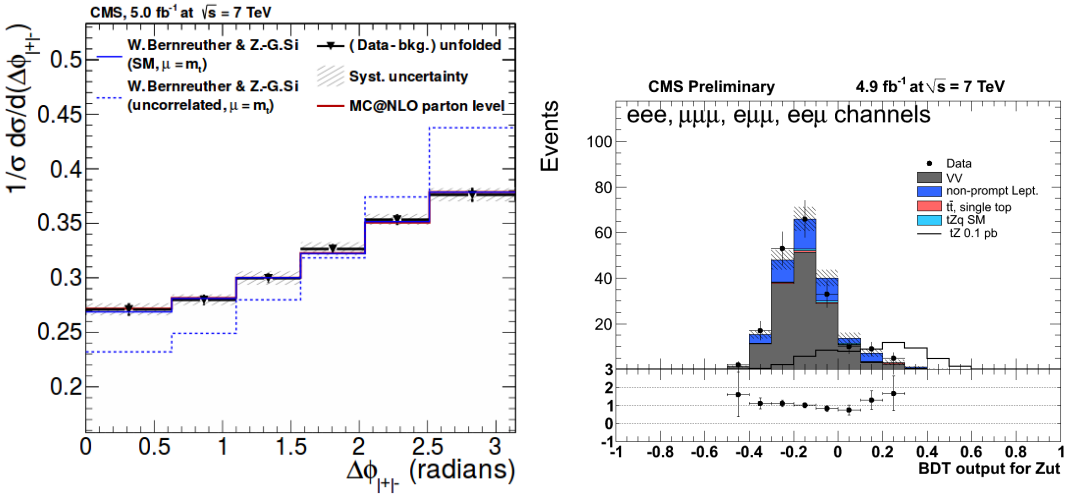

Figure 2: Left, $\Delta\phi(ll)$ differential cross section in $t\bar{t}$ events. Right : BDT distribution after the tZ selection.

with the known top-quark mass. Limit on the decay branching fraction of top quark into Zq is found to be $Br(t \to Zq) < 0.05\%$ at 95% confidence level.

Similar searches can be performed in the single top signature, as the search for a top-quark produced in association with a Z boson [12]. This channel has the advantage of being sensitive to the flavour of the quark q entering into the FCNC vertex tZq. The event selection is similar to [11], but with a looser jet selection. The analysis uses a BDT to extract the signal from the backgrounds, and to calculate exclusion limits. The BDT distribution in data and simulation can be found on Fig.2, right plot. Exclusion limits on the branching ratios are found to be $Br(t \to Zu) < 0.056$ and $Br(t \to Zc) < 7.12\%$. Similarly, on can probe $t\gamma q$ FCNC interactions by searching for a top quark produced in association with a real photon [13]. The corresponding limits on the top-quark branching fractions are $Br(t \to \gamma u) < 0.0279$ and $Br(t \to \gamma c) < 0.0161\%$.

5 Conclusion

The CMS collaboration covers a wide range of top-related topics and only a tiny fraction of the performed measurements is presented in this document. While these measurements correspond to a big step forward in our understanding of top-quark physics, there are still many open questions that need to be answered. Future runs of the LHC can provide the amount of data needed to perform those important investigations.

References

[1] The CMS collaboration, JINST 03 (2008) S08004

[2] The CMS collaboration, JHEP 02 (2014) 024

[3] The CMS collaboration, EPJ C73 (2013) 2339
[4] The CMS collaboration, Eur. Phys. J. C 74 (2014) 3014
[5] The CMS collaboration, Eur. Phys. J. C 74 (2014) 3060
[6] The CMS collaboration, JHEP 06 (2014) 090
[7] The CMS collaboration, PRL 112 (2014) 231802
[8] The CMS collaboration, CMS PAS TOP-14-001
[9] The CMS collaboration, CMS PAS TOP-14-015
[10] The CMS collaboration, CMS PAS TOP-14-004
[11] The CMS collaboration, PRL 112 (2014) 171802
[12] The CMS collaboration, CMS PAS TOP-12-021
[13] The CMS collaboration, CMS PAS TOP-14-003

Search for the Higgs boson decaying to two photons in CMS

Martina Malberti[1] on behalf of the CMS Collaboration

[1]University of California Riverside, USA

DOI: http://dx.doi.org/10.3204/DESY-PROC-2014-04/233

A search for Higgs bosons has been carried out in the Higgs to two photons decay channel with the CMS detector at the Large Hadron Collider. The analysis is based on proton-proton collision data collected in 2011-2012 at centre of mass energies of 7 and 8 TeV corresponding to integrated luminosities of 5.1 fb^{-1} and 19.7 fb^{-1}, respectively. The analysis strategy and measurements of the mass, couplings, and spin-parity are reported.

1 Introduction

In 2012, the ATLAS and CMS collaborations observed a new particle compatible with the Higgs boson postulated by the standard model (SM) [1, 2]. Here, the search through its decay to two photons is presented. Results based on the full CMS Run I dataset collected in 2011-2012 at centre of mass energies of 7 and 8 TeV are reported [3].

2 Analysis strategy

Despite the small branching ratio (0.23% for $m_{\text{H}} = 125$ GeV), the $H \to \gamma\gamma$ decay channel is characterized by a clean experimental signature, with two high transverse momentum isolated photons, which allow high precision for mass reconstruction. Photon candidates are reconstructed starting from energy deposits in the CMS electromagnetic calorimeter (ECAL). The ECAL single channel response is monitored and corrected for crystal transparency losses and is equalized between the different channels exploiting the $\phi-$simmetry of the energy flow, $\pi^0 \to \gamma\gamma$, $W \to e\nu$ and $Z \to ee$ decays [4]. Higher level corrections for shower containment, material and pileup effects are implemented through a multivariate regression, which provides also an estimate of the per photon energy resolution. Residual corrections, estimated from data to Monte Carlo (MC) comparisons in $Z \to ee$ events, are applied to correct the photon energy scale in data and to match the resolution of simulated events to the one observed in data.

A boosted decision tree (BDT), employing shower shapes and isolation variables, is used to discriminate prompt photons from jets misidentified as photons.

The di-photon vertex assignment is based on a multivariate approach with the transverse momenta of the tracks associated to the vertex, their correlation with the di-photon kinematics and the information from conversions as inputs. A further BDT is trained to estimate the

per event probability to assign the correct vertex (∼80% for an average pileup of about 20 interactions per bunch crossing).

To achieve the maximum sensitivity, events are splitted in categories exploiting their different mass resolution and signal-over-background ratio. The event information, including the kinematics, photon quality, mass resolution and probability to assign the correct vertex, is combined in a multivariate classifier (referred to as di-photon BDT), which is built in such a way to be mass independent and to have high values for events with good di-photon mass resolution and high probability of being signal rather than background. The output of the di-photon BDT is used to define untagged event classes. The boundary of the untagged categories are chosen to minimize the expected uncertainty on the signal strength measurement. In addition, categories tagged by the presence of additional objects in the final state are defined to target specific production modes: Higgs boson events produced via Vector Boson Fusion (VBF) have two jets with large rapidity gap; events from the associated VH (V = W, Z) production are tagged by the presence of one or more charged leptons, large missing transverse energy, or jets from the decay of the W or Z boson; and those from $t\bar{t}H$ production are characterized by the presence of b-jets and additional leptons or jets from the top decay. In total, 25 mutually exclusive event classes are defined: 14 in the 8 TeV dataset and 11 in the 7 TeV dataset.

For each event category, a signal and a background model are built. The signal model is obtained from a parametric fit of the simulated invariant mass of the two photons after having applied all the corrections derived from data to MC comparisons in $Z \to ee$ and $Z \to \mu\mu\gamma$ events. The background model is fitted from data. A smoothly falling background is expected, but the shape is *a priori* unknown. A discrete profiling method in which the choice of the function is included as discrete nuisance parameter in the likelihood to extract results is used. All reasonable families of functions are considered (exponentials, power laws, polynomials, Laurent series) and data are allowed to select the one which fits the best. The uncertainty resulting from the envelope around the negative log-likelihood curve of all the different functions takes therefore into account the model assumption.

3 Results

The inclusive di-photon invariant mass spectrum for all the selected events in the 7 and 8 TeV datasets is shown in Fig. 1-left. An excess of events is observed at a mass of 124.7 GeV with a significance of 5.7σ (Fig. 1-right). The corresponding measured signal strenght μ relative to the standard model expectation is $\mu = 1.14^{+0.26}_{-0.23} = 1.14 \pm 0.21(\text{stat.}) \, ^{+0.09}_{-0.05}(\text{syst.}) \, ^{+0.13}_{-0.09}(\text{theo.})$. The main sources of systematic uncertainties on the signal yield are the theoretical uncertainty on the production cross section and branching ratio, the shower shape modeling and the energy scale and resolution uncertainties.

The mass of the observed boson is determined via a 1-dimensional likelihood scan (Fig. 2-left) in which the relative signal strengths for couplings to fermions and bosons are floated to make the measurement less model dependent. The measured mass is $m_{\text{H}} = 124.70 \pm 0.31$ (stat.) $\pm$ 0.15 (syst.) GeV, where the main systematic uncertainties are due to the non-linearity in the extrapolation from the m_{Z} scale to the m_{H} scale and to imperfections in the modeling of the differences between electrons and photons in the MC simulation.

The measured signal strengths when considering different production modes separately are $\mu_{\text{ggH,t}\bar{\text{t}}\text{H}} = 1.13^{+0.37}_{-0.31}$ and $\mu_{\text{VBF,VH}} = 1.16^{+0.63}_{-0.58}$ (Fig. 2-right).

A test of the SM 0^+ hypothesis against a spin-2 graviton-like model with mininimal cou-

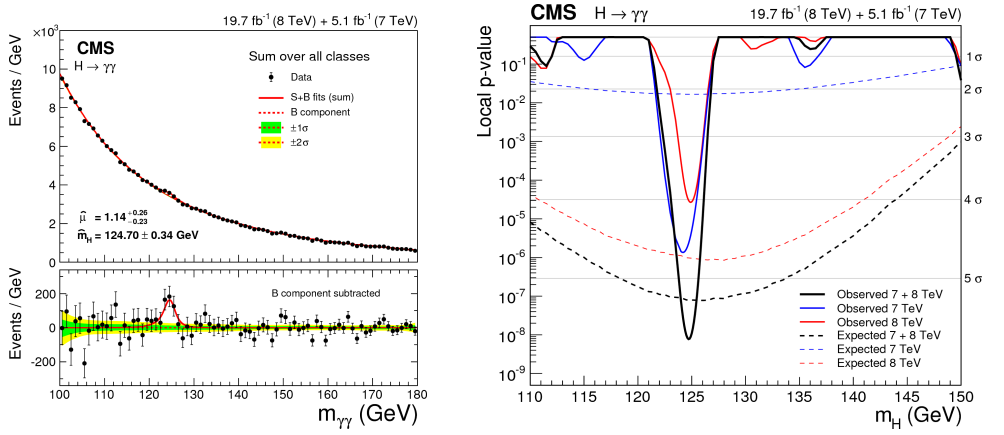

Figure 1: Left: invariant mass of the two photons for all the events selected in the 7 and 8 TeV datasets. Right: local p-values as a function of m_{H} for the 7 TeV, 8 TeV, and the combined dataset.

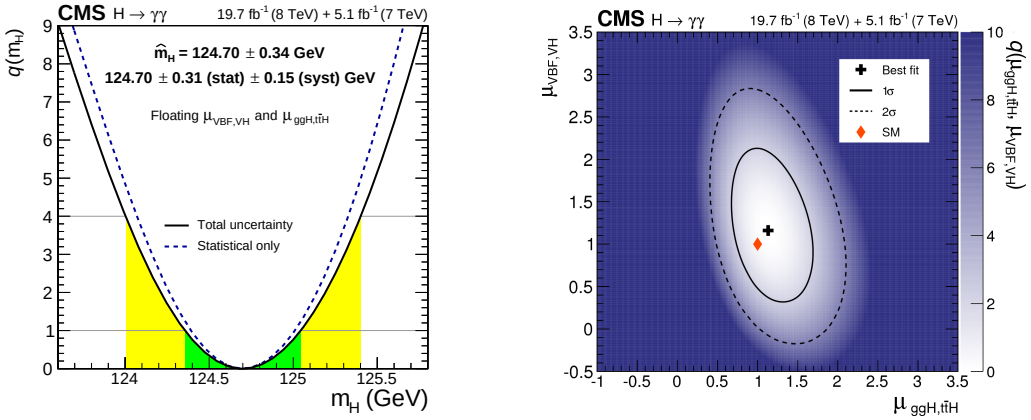

Figure 2: Left: likelihood scan as a function of the mass with $\mu_{\mathrm{ggH,t\bar{t}H}}$ and $\mu_{\mathrm{VBF,VH}}$ floated independently. Right: likelihood scan as a function of $\mu_{\mathrm{ggH,t\bar{t}H}}$ and $\mu_{\mathrm{VBF,VH}}$; the 1σ and 2σ uncertainty contours are shown, the cross indicates the best-fit values and the diamond represents the standard model expectation.

plings, 2^+_m [5], was performed. The variable used to discriminate between the two hypothesis is the cosine of the scattering angle in the Collins-Soper frame [6]. Figure 3 shows the test statistic $-2\ln(L_{2^+_m}/L_{0^+})$ as function of the fraction $f_{q\bar{q}}$ of $q\bar{q}$ production. The hypothesis 2^+_m is disfavoured at a 94% C.L. for pure gluon fusion production.

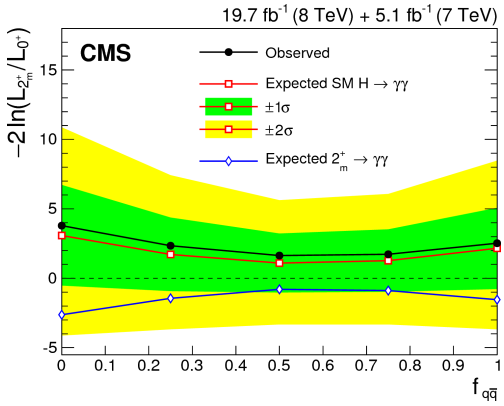

Figure 3: Test statistic for pseudo-experiments generated under the standard model 0^+ hypothesis (open squares) and the graviton-like 2^+_m hypothesis (open diamonds), as a function of the fraction $f_{q\bar{q}}$ of $q\bar{q}$ production. The full dots correspond to the observed distribution in the data.

4 Conclusions

The search for the Higgs boson through its decay to two photons in CMS was reported. The analysis is based on the full CMS Run I dataset collected at 7 and 8 TeV. A clear signal, with a local significance of 5.7σ, is observed at a mass of 124.7 GeV and the measured properties are consistent with the expectations from a standard model Higgs boson.

References

[1] ATLAS Collaboration, Phys. Lett. **B716** (2012) 1-29

[2] CMS Collaboration, Phys. Lett. **B716** (2012) 30

[3] CMS Collaboration, arXiv:hep-ex/1407.0558 (2014)

[4] CMS Collaboration, JINST **8** (2013) P09009

[5] Y. Gao et al. Phys. Rev. **D 81** (2010) 075022

[6] J. C. Collins and D. E. Soper, Phys. Rev. **D 16** (1977) 2219

Measurement of the angular production asymmetries in top quark pair lepton plus jets and dilepton final states

Kamil Augsten for the D0 Collaboration

Czech Technical University in Prague, Prague, Czech Republic

DOI: http://dx.doi.org/10.3204/DESY-PROC-2014-04/154

We present the measurement of the forward-backward asymmetry in the $t\bar{t}$ quark pair production in $p\bar{p}$ collisions in the lepton+jets and dilepton final states. Measurements use the full data set collected by the D0 detector in Run II corresponding to an integrated luminosity of 9.7 fb^{-1}. We present the most recent measurement of the lepton-based asymmetries both in lepton+jets and dilepton final states and their combination. We also present the top-quark based asymmetry as an inclusive measurement and differentially in $m_{t\bar{t}}$. These results are corrected for efficiency, acceptance and resolution effects to parton level. Measurements are compared to theory predictions.

1 Introduction

The top quark and its properties play an important role in the Standard Model (SM) and may probe for new physics. The forward-backward charge asymmetry was observed in fermion production in e^+e^- collisions in the 1980's, which was confirmation of the electroweak theory and observation of the mediation through Z-boson. Similar process might occur in strong sector as heavy mediators of strong interaction that have axial component, so called axigluons [1]. Top pair production in $p\bar{p}$ collisions mediated by axigluons would result in effect that as experimentally observable as a forward-backward asymmetry. Different models also suggest non-zero forward-backward asymmetry in top pair production.

In the SM, positive asymmetry appears at the α_s^3 level with numeric prediction of 9 % [2], which is next-to-leading order (NLO) QCD with the electroweak (EW) corrections. Recent preliminary NNLO calculation reported ~ 10 % asymmetry [3].

Asymmetry A_{FB} is defined as

$$A_{FB} = \frac{N_F - N_B}{N_F + N_B}, \tag{1}$$

where $N_F = N(x > 0)$ (forward events) and $N_B = N(x < 0)$ (backward events) for any angular variable x, for example η. The asymmetry $A_{FB}^{t\bar{t}}$ is defined with $x = \Delta y = y_t - y_{\bar{t}}$, a variable that is invariant under the boost along the beam axis. Similarly, the asymmetry A_{FB}^{l} in lepton direction is defined with the signed rapidity ($q_l y_l$) of the lepton from $t\bar{t}$ decay. Both asymmetries can be defined in the lepton+jets[1] (l+jets) and dilepton decay channels. Additionally for the

[1] By lepton are denoted here only electron and muon.

dilepton channel, the asymmetry A_{FB}^{ll} is defined based on the difference in rapidity between the positive and negative lepton.

This overview focuses on the latest measurements by the D0 experiment with the full Tevatron data set of 9.7 fb^{-1} in both l+jets and dilepton channels.

2 Asymmetry in Lepton Production from $t\bar{t}$ decay

2.1 Lepton + Jets Channel

The asymmetry A_{FB}^{l} in the l+jet channel [4] is measured in four sub-channels: l+3jets with 1 b-tag, l+4jets with 1 b-tag, l+3jets with 2 or more b-tags, and l+4jets with 2 or more b-tags. It includes l+3jets events, where one of the jets lost, to maximize the statistical sensitivity. It approximately doubles the statistics. However, this implies larger background, especially the production of W boson in association with jets. Leptons from the decay of the inclusively produced W bosons are produced asymmetrically in forward and backward direction. This effect is studied in Monte Carlo (MC) and analysis calibrates it using comparison of MC prediction and data in the orthogonal region, the W+jets background dominated 3 jets and 0 b-tag channel, which is not used for the measurement. The difference is accounted as systematic uncertainty. To maximize the analysis precision, the A_{FB}^{l} was measured separately in each sub-channel and combined afterwards. The result is corrected for the detector efficiency and resolution. The asymmetry is measured to be $4.2 \pm 2.3(\text{stat.})^{+1.7}_{-2.0}(\text{syst.})$ % and can be compared to MC@NLO prediction of 2.3 % or SM calculation of 3.8 ± 0.3 % [2]. The result is for leptons within rapidity range of 1.5. Fig. 1 (left) shows breakdown of the result to each sub-channel. The measurement of the A_{FB}^{l} in l+jets channel includes study of the asymmetry dependence on the transverse momentum of the lepton (p_T^l) from the $t\bar{t}$ decay. This provides an additional information that helps to distinguish between different models. The A_{FB}^{l} dependency measured in data after subtracting the contribution of the calibrated W+jets background as well as other background sources is shown in Fig. 1 (right) compared to the MC@NLO prediction.

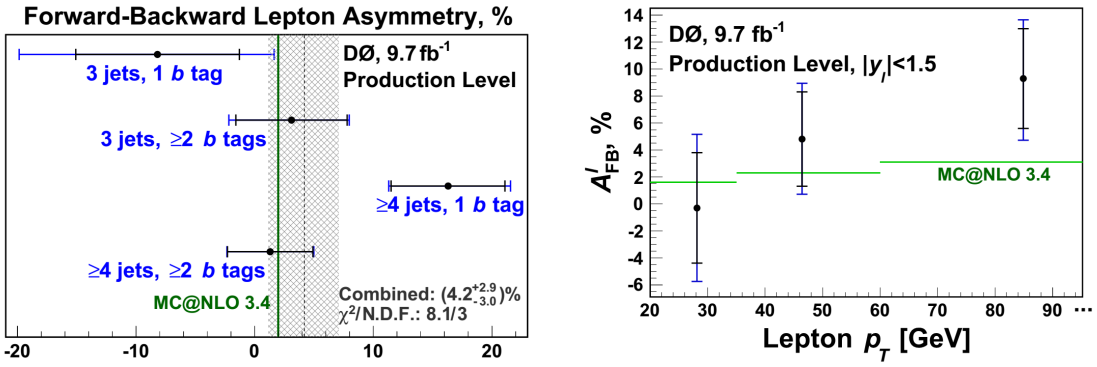

Figure 1: Left - Measured parton-level A_{FB}^{l} by sub-channel. The vertical line shows the MC@NLO prediction. Right - Predicted and observed parton-level asymmetries as a function of lepton transverse momentum. In both plots the statistical uncertainties are indicated by the inner, and the total uncertainties by the outer error bars.

2.2 Dilepton Channel

D0 performed measurements of asymmetry in lepton production in dilepton $t\bar{t}$ events [5], where two leptons (electrons or muons) are selected to have opposite charge and are accompanied by one jet in $e\mu$ channel and at least two jets in ee, $e\mu$, and $\mu\mu$ channels. Those four channels are treated separately to account for differences in purity and later combined together. Two asymmetry definitions are considered: A^l_{FB} with $x = q_l\eta_l$ and A^{ll}_{FB} with $x = \Delta\eta$. Additional acceptance cuts $|\eta| < 2.0$ and $|\Delta\eta| < 2.4$ are applied. The observed asymmetries are corrected for the detector efficiency and extrapolated to the full acceptance with scaling factor derived from MC@NLO. The corrected and extrapolated results are $A^l_{FB} = 4.4 \pm 3.7(\text{stat.}) \pm 1.1(\text{syst.})$ % and $A^{ll}_{FB} = 12.3 \pm 5.4(\text{stat.}) \pm 1.5(\text{syst.})$ % and can be compared to the SM NLO calculations [2] of $A^l_{FB} = 3.8 \pm 0.3$ % and $A^{ll}_{FB} = 4.8 \pm 0.4$ %.

2.3 Combination

To make a combination in A^l_{FB} for l+jets and dilepton channels we need first both results in the same lepton rapidity region. For the $|y_l| < 1.5$ region, the l+jets result has been already mentioned, $4.2 \pm 2.3(\text{stat.})^{+1.7}_{-2.0}$ (syst.) %, and dilepton channel gives $4.3 \pm 3.4(\text{stat.}) \pm 1.0$ (syst.) %. The combination is done using Best Linear Unbiased Estimator (BLUE) method [6] resulting in $A^l_{FB} = 4.2 \pm 2.4$ %. This value is extrapolated to cover the full phase space - $A^l_{FB} = 4.7 \pm 2.3(\text{stat.}) \pm 1.5(\text{syst.})\% = 4.7 \pm 2.7$ % and it is in agreement with the SM calculation $A^l_{FB} = 3.8 \pm 0.3$ % [2].

3 Inclusive $t\bar{t}$ Production Asymmetry in Lepton + Jets Channel

Similarly to the asymmetry in lepton production in l+jets channel the inclusive $t\bar{t}$ production asymmetry [7] is measured with addition of the l+3jets events. As this measurement requires the full reconstruction of the $t\bar{t}$ decay, partial reconstruction algorithm [8] with high probability of correct reconstruction of the sign is implemented. The reconstructed Δy distribution is unfolded accounting for the differences in the signal to background ratio in the measured subchannels. The measurement uses regularized unfolding (package TUnfold) and the asymmetry at the parton level is measured to be $A^{t\bar{t}}_{FB} = 10.6 \pm 2.7(\text{stat.}) \pm 1.3(\text{syst.})$ % which is consistent with the SM calculation $A^{t\bar{t}}_{FB} = 8.8 \pm 0.9$ % [2].

For the differential measurement a 2D unfolding algorithm was developed and the dependencies of the forward-backward asymmetry on the $|\Delta y|$ and on the invariant mass ($m_{t\bar{t}}$) of the $t\bar{t}$ system were studied and are shown on Fig. 2. The correlations between bins are taken into account in the fit of the measured asymmetry and slope is compared to the prediction from MC@NLO. The dependencies are in agreement with the SM predictions.

4 Conclusion

We present recent measurements of the angular production asymmetries in top quark pair lepton+jets and dilepton final states with the D0 detector in full 9.7 fb^{-1} data set. The asymmetry in lepton production from $t\bar{t}$ decay is combined for both channels and extrapolated

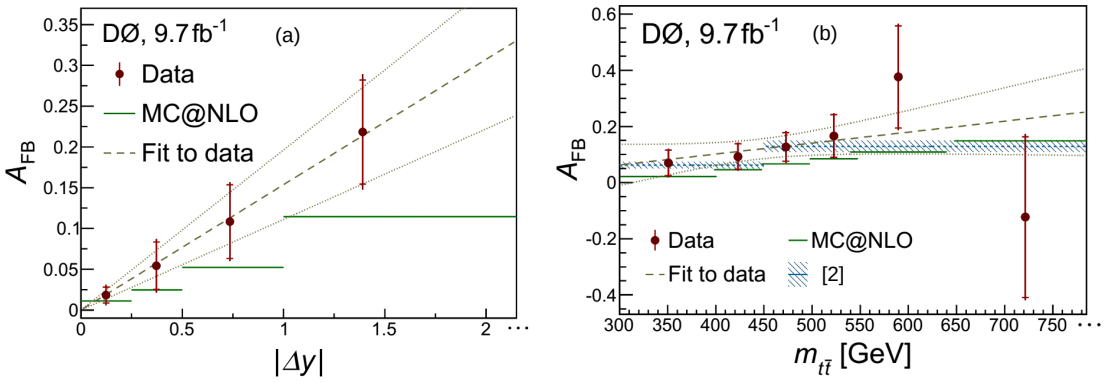

Figure 2: The dependencies of the forward-backward asymmetry on (a) the $|\Delta y|$ and on (b) the invariant mass of the $t\bar{t}$ system. The D0 data points are shown with total uncertainties and are compared to MC@NLO and [2] prediction. The dashed line shows the fit to the data with the dotted lines indicating the fit uncertainty. The last bin has no upper boundary.

to the full acceptance, $A^l_{FB} = 4.7 \pm 2.7$ %, while SM calculation predicts $A^l_{FB} = 3.8 \pm 0.3$ %. The inclusive $t\bar{t}$ production asymmetry in the l+jets channel corrected to the parton level as $A^{t\bar{t}}_{FB} = 10.6 \pm 3.0$ %. It agrees with SM prediction of $A^{t\bar{t}}_{FB} = 8.8 \pm 0.9$ % (NLO + QCD EW) and is in even better agreement with the recent NNLO + QCD EW prediction of ~ 10 %. The D0 results are consistent with SM-based calculations.

References

[1] P. H. Frampton, J. Shu and K. Wang, Phys. Lett. B **683**, 294 (2010).

[2] W. Bernreuther and Z.-G. Si, Phys. Rev. D **86**, 034026 (2012).

[3] M. Czakon, *Latest developments in generators and NNLO computations*, 7th International Workshop on Top Quark Physics, Cannes, France (2014).

[4] V. Abazov *et al.* (D0 Collaboration), Phys. Rev. D **90**, 072001 (2014).

[5] V. Abazov *et al.* (D0 Collaboration), Phys. Rev. D **88**, 112002 (2013).

[6] L. Lyons, D. Gibaut and P. Clifford, Nucl. Instrum. Meth. A **270**, 110 (1988); A. Valassi, Nucl. Instrum. Meth. A **500**, 391 (2003).

[7] V. Abazov *et al.* (D0 Collaboration), Phys. Rev. D **90**, 072011 (2014).

[8] R. Demina, A. Harel and D. Orbaker, arXiv:1310.3263 [hep-ex].

On a four dimensional formulation for dimensionally regulated amplitudes

A.R. Fazio

Departamento de Fisíca, Universidad Nacional de Colombia
Ciudad Universitaria, Bogotá, D.C. Colombia

DOI: http://dx.doi.org/10.3204/DESY-PROC-2014-04/149

We propose a pure four-dimensional formulation (FDF) of the d-dimensional regularization of one-loop scattering amplitudes. In our formulation particles propagating inside the loop are represented by massive internal states regulating the divergences. We present explicit representations of the polarization and helicity states of the four-dimensional particles propagating in the loop. They allow for a complete, four-dimensional, unitarity-based construction of d-dimensional amplitudes. Finally we show how the FDF allows for the recursive construction of d dimensional one-loop integrands, generalizing the four-dimensional open-loop approach.

1 Introduction

The recent development of novel methods for computing one-loop scattering amplitudes in gauge field theory has been highly stimulated by a deeper understanding of their kinematics enforced by on-shellness [1][2] and generalized unitarity [3][4]. Analyticity and unitarity of scattering amplitudes have then been strengthened by the complementary classification of the mathematical structures present in the residues of singular points.

The use of unitarity cuts and complex momenta for on-shell internal particles turned unitarity based methods into very efficient tools for computing scattering amplitudes. These methods exploit two general properties of scattering amplitudes such as unitarity and analyticity: the former granting that amplitudes can be reconstructed from the knowledge of their generalized singularity structures; the latter granting that the residues at singular points factorize in the product of simpler amplitudes [5][6][7].

However one-loop scattering amplitudes arising from a dimensionally regulated theory are the sum of one part containing polylogarithms, the so called "cut constructible" part, and the rational part, which is a rational function of the external spinors and polarizations. Contrarily to the cut-constructible, the rational part cannot be detected in four dimensions.

Based on the paper [8] this talk addresses the possibility of fully reconstructing a one loop amplitude in its cut-constructible and rational part in quantum chromodynamics (QCD) by just gluing tree level amplitudes. Such trees will be obtained by extending the definition of the helicity eigenstates entering the state sum in the propagators of quark and gluons, whithout leaving the four space-time dimensions.

This point of view combines the generalized unitarity cuts in $d = 4 - 2\epsilon$ dimensions with the Four Dimensional Helicity Scheme (*FDH*). The d-dimensional unitarity cuts detect also the

rational part by generalized on-shell conditions and generalized residues [9]. The former imply the vanishing of massive denominators, where the mass term depends both on the physical mass (vanishing or not) of the particle across the cut and on the effective mass parameter encoding the extra-dimensional dependence. Generalized residues computed on the cuts are generated by tree level amplitudes, which depend on the effective mass parameter, hence from the extra dimensions regulating the integrals, either from the generalized polarizations vectors associated to the cut particles, or from the extended algebra of the metric tensor and of the Dirac matrices in the definition of the Feynman rules.

In order to compute the constituting blocks of tree level amplitudes by using the helicity spinor formalism the *FDH* scheme will be used [10], in which the external particles are described by four dimensional Lorentz labels (momenta and helicities) and the internal particles (the so called "unobserved") have still the same numbers of helicity states like in four dimensions. In *FDH* scheme the momenta of the unobserved particles are kept in d dimensions as well as the metric tensor and the Dirac matrices, therefore in diagrammatic computations the algebraic manipulations are implemented by separating the four dimensional algebra from the extra-dimensional one.

In this talk we show that dimensionally regularized one-loop QCD amplitudes in *FDH* scheme can be simply calculated by generalizing the helicity eigenstates of the unobserved particles, by including an effective mass parameter in a pure four-dimensional formalism. The generalized four dimensional polarizations and propagators should be used for tree level and one loop computations avoiding any special decomposition of the particle running around the loop. We want to demonstrate that by an appropriate generalization of the cutted internal legs no supersymmetric decomposition [11] will be needed neither the introduction of new particles and new interactions [12] to afford separately the computation of the cut constructible and the rational part of a scattering amplitude.

2 Generalized internal legs

In this section we are going to provide the explicit expression of the cut legs of a one-loop amplitude involving fermion or vector particles in the loop. Those wave functions will be needed to compute the tree amplitudes to be merged in the reconstruction of the S-matrix elements by unitarity. Their dynamics is described by a pure four dimensional quantum field theory dual to the dimensionally regularised one. The following explicit construction of generalized spinors for fermions and polarization vectors for gluons is suitable for a numerical implementation of such an on-shell procedure of computation. In the following discussion we will decompose a d-dimensional momentum $\bar{\ell}$ as follows

$$\bar{\ell}^\alpha = \ell^\alpha + \mu^\alpha \qquad \bar{\ell}^2 = \ell^2 - \mu^2 = m^2, \tag{1}$$

while its four-dimensional component ℓ will be expressed in terms of the massless momenta $\ell^\flat$ and q_ℓ as

$$\ell = \ell^\flat + \hat{q}_\ell\,, \qquad \hat{q}_\ell \equiv \frac{m^2+\mu^2}{2\,\ell\cdot q_\ell} q_\ell\,. \tag{2}$$

Spinors – The legs of the cut fermion propagtors in the loop have to fulfill the following completness relation [8]

$$\sum_{\lambda=\pm} u_\lambda(\ell)\,\bar{u}_\lambda(\ell) = \ell + i\mu\gamma^5 + m \tag{3}$$

which is satisfied by the following four dimensional spinors

$$u_+(\ell) = \left|\ell^\flat\right\rangle - \frac{(m-i\mu)}{\left[\ell^\flat\, q_\ell\right]}\left|q_\ell\right], \quad u_-(\ell) = \left|\ell^\flat\right] - \frac{(m+i\mu)}{\left\langle\ell^\flat\, q_\ell\right\rangle}\left|q_\ell\right\rangle. \tag{4}$$

Polarization vectors – In the light-cone gauge the d-dimensional polarization vectors fulfill the following relation

$$\sum_{i=1}^{d-2} \varepsilon^\alpha_{i\,(d)}\left(\bar{\ell},\bar{\eta}\right)\varepsilon^{*\beta}_{i\,(d)}\left(\bar{\ell},\bar{\eta}\right) = -\bar{g}^{\alpha\beta} + \frac{\bar{\ell}^\alpha\ \bar{\eta}^\beta + \bar{\ell}^\alpha\,\bar{\eta}^\beta}{\bar{\ell}\cdot\bar{\eta}} - \frac{\bar{\eta}^2\bar{\ell}^\alpha\bar{\ell}^\beta}{(\bar{\eta}\cdot\bar{\ell})^2}, \tag{5}$$

where $\bar{\eta}$ is an arbitrary d-dimensional momentum such that $\bar{\ell}\cdot\bar{\eta}\neq 0$. Gauge invariance in d dimensions guarantees that the unitarity cuts are independent of $\bar{\eta}$. Assuming a four dimensional description we can take the vector μ fixed. The choice $\bar{\eta}^\alpha = \mu^\alpha$ allows for disentangling the four-dimensional contribution from the d-dimensional one:

$$\sum_{i=1}^{d-2} \varepsilon^\alpha_{i\,(d)}\left(\bar{\ell},\bar{\eta}\right)\varepsilon^{*\beta}_{i\,(d)}\left(\bar{\ell},\bar{\eta}\right) \quad = \quad \left(-g^{\alpha\beta} + \frac{\ell^\alpha\ell^\beta}{\mu^2}\right) - \left(\tilde{g}^{\mu\nu} + \frac{\mu^\alpha\mu^\beta}{\mu^2}\right). \tag{6}$$

The first term is related to the cut propagator of a massive gluon whose polarization vectors are

$$\varepsilon^\mu_+(\ell) = -\frac{\left[\ell^\flat\left|\gamma^\mu\right|\hat{q}_\ell\right\rangle}{\sqrt{2}\mu} \quad \varepsilon^\mu_-(\ell) = -\frac{\left\langle\ell^\flat\left|\gamma^\mu\right|\hat{q}_\ell\right]}{\sqrt{2}\mu} \quad \varepsilon^\mu_0(\ell) = \quad \frac{\ell^{\flat\mu} - \hat{q}^\mu_\ell}{\mu}. \tag{7}$$

3 Open loop

The FDF of d-dimensional one-loop amplitudes is compatible with methods generating recursively the integrands of one-loop amplitudes and leads to the complete reconstruction of the numerator of Feynman integrands as a polynomial in ℓ^ν and μ. Our scheme allows for a generalization of the current implementations of these techniques, reconstructing only the four-dimensional part of the numerator of the integrands, which is polynomial in ℓ. In the following we describe how the open-loop technique [13] has to be generalized within the FDF scheme. The subtrees $w^\beta(i)$ recursively merged by connecting their cut lines to vertices and propagators have the following form

$$w^\beta(i) = \frac{X^\beta_{\gamma\delta}(i,j,k)w^\gamma(j)w^\delta(k)}{p_i^2 - m_i^2 + i\epsilon}, \tag{8}$$

where $\frac{X^\beta_{\gamma\delta}}{p_i^2-m_i^2+i\epsilon}$ describes a vertex connecting i,j,k to a propagator attached to i. For one loop amplitudes the numerators of Feynman integrals can be computed by tree-level techniques. For the open loop with indices α and β where a single propagator has been cutted and the

denominator stripped out, the numerator of the amplitude's integrand satisfies the recursive relation

$$\mathcal{N}^{\beta}_{\ \alpha}\left(\mathcal{I}_n,\ell,\mu\right)=X^{\beta}_{\gamma\delta}\left(\mathcal{I}_n,i_n,\mathcal{I}_{n-1}\right)\mathcal{N}^{\gamma}_{\ \alpha}\left(\mathcal{I}_{n-1},\ell,\mu\right)w^{\delta}\left(i_n\right) \tag{9}$$

where w^{δ} is the expression related to the tree-level topology i_n. To achieve the Feynman diagrams expressions in FDH scheme by our FDF formulation the vertices $X^{\beta}_{\gamma\delta}$ are obtained by the Feynman rules in [8]

$$X^{\beta}_{\gamma\delta}=Y^{\beta}_{\gamma\delta}+\ell^{\nu}\,Z^{\beta}_{\nu;\,\gamma\delta}+\mu\,W^{\beta}_{\gamma\delta}\,. \tag{10}$$

Therefore the tensor coefficients of the covariant decomposition of the numerator in a given topology are obtained by the recursive relation

$$\mathcal{N}^{[a]\,\beta}_{\nu_1\cdots\nu_j;\,\alpha}\left(\mathcal{I}_n\right)=\left[Y^{\beta}_{\gamma\delta}\,\mathcal{N}^{[a]\,\gamma}_{\nu_1\cdots\nu_j;\,\alpha}\left(\mathcal{I}_{n-1}\right)+Z^{\beta}_{\nu_1;\,\gamma\delta}\,\mathcal{N}^{[a]\,\gamma}_{\nu_2\cdots\nu_j;\,\alpha}\left(\mathcal{I}_{n-1}\right)+W^{\beta}_{\gamma\delta}\,\mathcal{N}^{[a-1]\,\gamma}_{\nu_1\cdots\nu_j;\,\alpha}\left(\mathcal{I}_{n-1}\right)\right]w^{\delta}(i_n).$$

The recursive generation of integrands within the FDF can be suitably combined with public codes like Samurai and Ninja.

4 Conclusions and outlook

A four-dimensional formulation (FDF) of dimensional regularization of one-loop scattering amplitudes has been applied to generalized unitarity techniques. At one loop the cut-constructible part and the rational part of scattering amplitudes have been computed by the same on-shell methods. The inclusion of the fermion mass and the two loop case will be analysed elsewhere.

References

[1] F.Cachazo, P. Svrcek and E. Witten, JHEP 09 006 (2004).

[2] R. Britto, F. Cachazo, B. Feng, Nucl. Phys. B715 499 (2005).

[3] Z. Bern, L.J. Dixon, D.C. Dunbar, D.A. Kosower, Nucl. Phys. B425 217 (1994).

[4] R. Britto, F. Cachazo, B. Feng, Nucl. Phys. B725 275 (2005).

[5] C. F. Berger and D. Forde, Ann.Rev.Nucl.Part.Sci. 60,181 (2010).

[6] R. Britto, J.Phys. A44, 454006 (2011), 34 pages.

[7] R. Ellis, Z. Kunszt, K. Melnikov, and G. Zanderighi, Phys.Rept. 518 (2012) 141-250 (2011).

[8] A.R. Fazio, P. Mastrolia, E. Mirabella, W.J. Torres, arXiv:14044783 [hep-ph].

[9] Z. Bern and A. G. Morgan, Nucl. Phys., B467 479 (1996).

[10] A. Signer, D. Stockinger, Nucl.Phys. B808 88 (2009).

[11] A. Brandhuber, S. McNamara, B. J. Spence, G. Travaglini, JHEP 0510 11 (2005).

[12] R. Pittau, JHEP 1202 29 (2012).

[13] F. Cascioli, P. Maierhofer, S. Pozzorini, Phys. Rev. Lett. 108 111601 (2012).

Chapter 10

Beyond standard model

Search for electroweak supersymmetry production at CMS

Mario Masciovecchio[1] on behalf of the CMS Collaboration

[1] Institute for Particle Physics, ETH Zürich, 8093 Zürich, Switzerland

DOI: http://dx.doi.org/10.3204/DESY-PROC-2014-04/195

The latest results from the CMS experiment [1] at the LHC on searches for supersymmetry produced through electroweak production channels are presented using about 20 fb^{-1} of data from the 8 TeV LHC run. A variety of complementary final state signatures and methods are used, such as searches with Higgs, W, and Z bosons in the final state, to probe gaugino and slepton production.

1 Introduction

Many searches for supersymmetry (SUSY) at the LHC focused on models with strongly interacting new particles in final states with high levels of hadronic activity have constrained the squarks and gluinos to be heavier than several hundreds GeV. Other searches are focused on the direct electroweak production of charginos $\tilde{\chi}i^{\pm}$ and neutralinos $\tilde{\chi}^0$, i.e., mixtures of the SUSY partners of the gauge and Higgs bosons, and of sleptons $\tilde{l}$, i.e., the SUSY partners of leptons. Such production modes may dominate if the strongly interacting SUSY particles are heavy. A wide variety of signal topologies are targeted by electroweak SUSY searches at CMS. Here, searches are presented for electroweak pair production of neutralinos and charginos that decay to h^0h^0, h^0Z, and h^0W final states.

2 Gauge Mediated Supersymmetry Breaking models with Higgs bosons in the final state

A R-parity conserving gauge mediated SUSY breaking (GMSB) model is considered [2], in which the two lightest neutralinos $\tilde{\chi}_1^0$ and $\tilde{\chi}_2^0$, and the lightest chargino $\tilde{\chi}_1^{\pm}$ are higgsinos, approximately mass degenerate, with $\tilde{\chi}_1^0$ being the lightest of the three states. The lightest SUSY particle (LSP) is a gravitino $\tilde{G}$, i.e., the SUSY partner of the graviton. The $\tilde{\chi}_2^0$ and $\tilde{\chi}_1^{\pm}$ higgsinos decay to the lightest higgsino $\tilde{\chi}_1^0$, plus Standard Model (SM) particles with low transverse momentum. The $\tilde{\chi}_1^0$ is the next-to-lightest SUSY particle (NLSP) and it undergoes a two-body decay to a $h^0\tilde{G}$, or $Z\tilde{G}$, with $\tilde{G}$ being nearly massless and stable.

2.1 Search in the $\mathbf{h^0h^0 \to b\bar{b}b\bar{b}}$

With a branching fraction of about 0.56, Higgs decays to $b\bar{b}$ represent the most likely decay mode of the Higgs boson. Therefore, the $h^0(\to b\bar{b})h^0(\to b\bar{b})$ final state provides a sensitive

search channel for SUSY h^0h^0 production. Each Higgs boson is reconstructed in its decay to a $b\bar{b}$ pair. The data are consistent with the Standard Model predictions within uncertainties (Fig. 1).

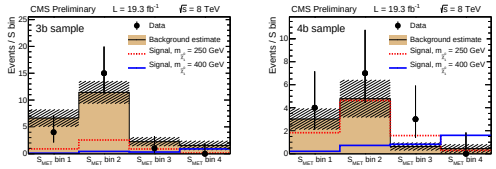

Figure 1: Results of search for $h^0(\to b\bar{b})h^0(\to b\bar{b}) + E_{\mathrm{T}}^{\mathrm{miss}}$ final states.

2.2 Search in the h^0h^0, h^0Z, h^0W channels with one $h^0 \to \gamma\gamma$

Searches for h^0h^0, h^0Z, h^0W states in channels with one Higgs boson that decays to photons are described. The other boson (h^0, Z, or W) decays to a final state with at least one lepton (electron or muon).

2.2.1 h^0Z, h^0W to $\gamma\gamma$ + jets

For the h^0Z and h^0W channels with $h^0 \to \gamma\gamma$ and either $W \to 2$ jets or $Z \to 2$ jets, the vector boson candidate is formed from two jets that yield a dijet mass m_{jj} consistent with the mass of a W or Z boson. The Higgs boson is reconstructed from a pair of photons. The data are consistent with the Standard Model predictions within uncertainties (Fig. 2).

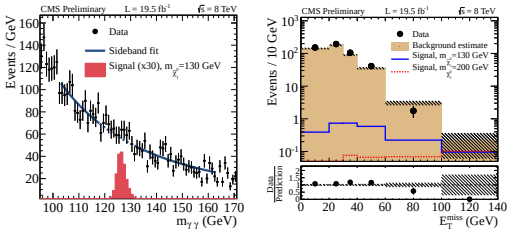

Figure 2: Results of search for h^0Z, h^0W to $\gamma\gamma$ + jets final states.

2.2.2 h^0h^0, h^0Z, h^0W to $\gamma\gamma$ + leptons

Searches for h^0h^0, h^0Z, h^0W states in channels with one Higgs boson that decays to photons are described. The other boson (h^0, Z, or W) decays to a final state with at least one lepton (electron or muon). A sample with at least one muon and an orthogonal sample with no muons but at least one electron are selected. For the muon channel, the data exhibit a small deficit with respect to the SM background estimate, while for the electron channel, there is an excess of 2.1 standard deviations (Fig. 3).

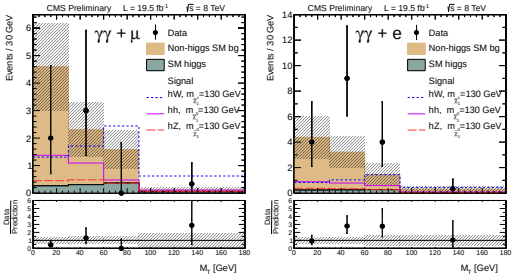

Figure 3: Results of search for h^0h^0 h^0Z, h^0W to $\gamma\gamma$ + leptons final states.

2.3 Search in the h^0Z channel with $h^0 \to b\bar{b}$ and $Z \to l^+l-$

A search in the h^0Z channel, with $h^0 \to b\bar{b}$ and $Z \to l^+l^-$ (with $l = e, \mu$) is presented. Events are required to contain exactly one same flavour opposite sign dilepton pair, with a dilepton invariant mass in the Z boson mass region. , and at least two tagged b jets, with the di-jet mass reconstructed from the two most b-like jets in the Higgs boson mass region. Data are in agreement with Standard Model prediction (Fig. 4).

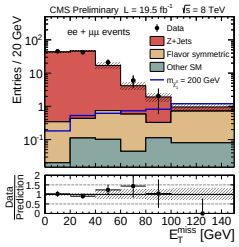

Figure 4: Results of search for h^0Z to $b\bar{b}$ + l^+l^- final states.

2.4 Interpretation

Figure 5 presents the 95% confidence level exclusion region for the GMSB higgsino NLSP scenario in the two-dimensional plane of the $\tilde{\chi}_1^0 \to h^0\tilde{G}$ branching fraction versus the higgsino mass $m_{\tilde{\chi}_1^0}$. The combination of the results discussed above exclude a significant fraction of the plane.

3 $h^0W + E_T^{miss}$

Searches for direct electroweak production of SUSY charginos and neutralinos in final states with a Higgs boson are presented [3]. A $\tilde{\chi}^{\pm}]\tilde{\chi}^0$ pair is produced, and decays to a W boson, a Higgs boson, and missing transverse energy from escaping lightest SUSY particles. Three channels are explored, depending on the particles detected in the final state: single lepton,

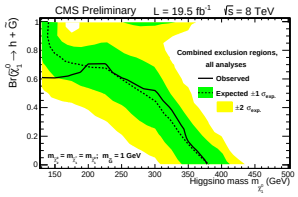

Figure 5: Observed and expected 95% confidence level exclusion regions for higgsino pair production.

same sign dilepton, and multilepton channels. The data are consistent with the Standard Model backgrounds (Fig. 6). Results are combined with the ones presented in Sec. 2.2.2 and

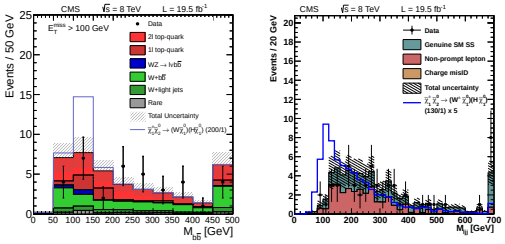

Figure 6: Results of searches for $h^0W + E_T^{miss}$ final states.

are used to set constraints on the mass of charginos and neutralinos up to 204 GeV (Fig. 7).

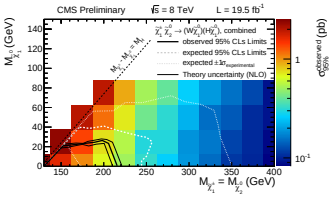

Figure 7: Interpretation of searches for $h^0W + E_T^{miss}$ final states.

References

[1] S. Chatrchyan et al. The CMS experiment at the CERN LHC. *JINST*, 3:S08004, 2008.

[2] Vardan Khachatryan et al. Searches for electroweak neutralino and chargino production in channels with Higgs, Z, and W bosons in pp collisions at 8 TeV. 2014.

[3] Vardan Khachatryan et al. Searches for electroweak production of charginos, neutralinos, and sleptons decaying to leptons and W, Z, and Higgs bosons in pp collisions at 8 TeV. *Eur.Phys.J.*, C74(9):3036, 2014.